DEVELOPMENT OF THE CONDITIONAL MOMENT CLOSURE METHOD FOR MODELLING TURBULENT COMBUSTION

by

Nigel Stuart Allen Smith

A thesis submitted in fulfilment of
the requirements for the degree of
Doctor of Philosophy

DEPARTMENT OF MECHANICAL & MECHATRONIC ENGINEERING
UNIVERSITY OF SYDNEY

October 1994

Summary

The conditional moment closure (CMC) method is developed from a recently proposed theoretical basis, into a series of computational models for use in predicting turbulent combustion processes.

The CMC method employs reactive species information that has been averaged conditionally upon the value of a chosen variable. This averaging process has the advantage over conventional unconditional averaging, in that instantaneous deviations from the resultant means are much smaller. The reduced level of instantaneous deviations allows the highly non-linear chemical reaction rate terms, which occur in the conditionally averaged species equations, to be closed with a first order approximation.

Two CMC models are developed for use in predicting nonpremixed turbulent combustion phenomena, whilst a third is proposed for simple premixed combustion systems. The great advantage of CMC models over other contemporary turbulent combustion models, is their ability to easily incorporate detailed chemical mechanisms into their predictions at very little computational cost.

The first of two nonpremixed models is derived for steady turbulent combustion, where the conditional mean reactive scalar field is neither a function of location or time. This Imperfectly Stirred Reactor (ISR) model is subjected to parametric studies to determine the influence of its governing parameters upon chemical yield. These parameters include the reactor residence time, the evolution of the mixture fraction probability density function (PDF) between the reactor inlet and outlet, and the choice of chemical mechanism.

The second nonpremixed CMC model is developed for axisymmetric turbulent jet flames. The predictions of this model are compared with existing experimental data measured in hydrogen and hydrogen-carbon monoxide turbulent jet flames.

Good agreement is found between the predicted and measured conditionally averaged data. Predicted peak conditional mean nitric oxide levels agree to within twenty percent of the measured values, but are consistently greater over the range of flow conditions studied. Predicted trends in nitric oxide emissions and radiation loss are compared with experimental findings over a range of flow conditions. Further, the importance of chemical mechanism detail is examined in relation to turbulent jet diffusion flame modelling.

A premixed CMC model is proposed for steady turbulent reactors with spatially independent conditional mean reactive scalar fields. A closure strategy for this model is proposed, and a discussion of the applications of the method is provided.

The future development of conditional moment closure methods is discussed, and tentative objectives for this ongoing research and development program are suggested.

Acknowledgements

This work has been made possible by the assistance and encouragement of Professor Robert W. Bilger, for which the author is profoundly grateful. Throughout the course of this investigation, the support and expert guidance of Prof. Bilger have allowed the author to build an appreciation of the complexities surrounding the field of turbulent combustion.

Many thanks are also due to Professor J.-Y. Chen and Dr Robert S. Barlow of the University of California at Berkeley and Sandia National Laboratories respectively. Whilst the former provided invaluable assistance in coming to grips with numerical modelling of combustion, collaboration with the latter insured that modelling efforts were always compared with accurate experimental measurements.

Many discussions with Dr Alex Yu. Klimenko and Dr Sten H. Stårner of the University of Sydney have been fruitful and have often aided the course of this investigation. The author is also thankful to Dr Assaad R Masri for making available his computational facilities.

This work could not have been possible without the generous support of the Combustion Research Facility, of Sandia National Laboratories which provided both computational resources and an environment that facilitated the productive exchange of ideas and concepts. The computational support of Australian Supercomputing Technology's Lucas Heights facility was instrumental in the completion of this investigation and is gratefully acknowledged.

This investigation is supported by the Australian Research Council, and the Office of Basic Energy Sciences within the United States Department of Energy.

The author would like to express his heartfelt thanks to Rachel, Colleen and Allen for their unfailing love, support, and understanding over the past years.

Contents

List of Figures

List of Tables

Nomenclature

Roman Symbols

A	area
c	reaction progress variable (RPV)
D	nozzle diameter
$\mathcal{D}_i$	ith species molecular diffusivity
EI_i	ith species emission index
f_{C-ox}	carbon oxidation fraction
f_{H-ox}	hydrogen oxidation fraction
f_{rad}	radiant fraction
G	conditional mean flux of reactive scalar
h	standardized specific enthalpy
h^s	sensible specific enthalpy
Δh	specific energy loss
k	turbulent kinetic energy
L_{st}	stoichiometric flamelength
L_{vs}	visible flamelength
$\dot{m}$	mass flow rate
P	probability density function (PDF)
Q_i	ith species conditional mean mass fraction
r	radial position
R	bounding radius
$R(\eta)$	conditional mean variance decrement
s	reactive species mass fraction sample space variable

$\mathcal{S}_c$	reaction progress variable source term
$\mathcal{S}_h$	radiation heat transfer rate
t	time
u	velocity
U_j	jet exit velocity
V	volume
w_i	ith species chemical production rate
W	molecular weight
x	spatial position
X_i	ith species mole fraction
Y_i	ith species mass fraction
y_i	ith species instantaneous deviation from mean

Non-Roman Symbols

β	conserved scalar
δ	incremental change
$\delta(\ldots)$	Dirac delta function
ϵ	turbulent kinetic energy dissipation rate
η	mixture fraction sample sapce variable
ζ	reaction progress sample space variable
χ	scalar dissipation rate
χ_q	critical extinction scalar dissipation rate
υ	special function consisting of Dirac delta functions
φ	special function consisting of Dirac delta functions
ϕ	special function consisting of Dirac delta functions
ψ	special function consisting of Dirac delta functions
ρ	density
σ_m^2	maximum variance
τ	residence time
ξ	mixture fraction

ω_t	turbulent mixing frequency
Ω	linear combination of sensible and standardized enthalpies
$\mho$	unmixedness

Subscripts

ad	adiabatic
b	burnt
eq	equilibrium
fu	fuel
g	global
in,$inlet$	inlet
j	jet
out,$outlet$	outlet
ox	oxidizer
r	reactor
R	bounding radius
rad	radiation
u	unburnt

Brackets

$< \ldots >$	unconditional ensemble average
$< \ldots \mid \ldots >$	conditional ensemble average (condition follows |)
$\{\ldots\}$	area average
$\{\ldots\}^*$	mass flow rate weighted area average
$\{\ldots\}^+$	PDF weighted area average
$\{\{\ldots\}\}$	volume average

Chapter 1

Introduction

Turbulent combustion can be defined as a process where an exothermic global chemical reaction takes place within a fluid that is subject to turbulent mixing. Turbulent mixing produces greatly enhanced heat and mass transfer rates compared to that resulting from molecular mixing alone. If a combustion device must provide maximum energy output within as short a time and as small a space as possible, it will typically be designed to take advantage of turbulent mixing.

Accordingly, turbulent combustion plays an essential role in modern civilisation, providing around $85-90\%$ of world energy production. Combustion of oil and petroleum products, natural gas, and solid fuels consumed approximately 285 trillion megajoules of chemical energy throughout the world in 1987, with consumption levels of 340 and 437 trillion megajoules projected for 1995 and 2005 respectively[1]. As a result of fossil fuel combustion, it is estimated that approximately 5.9 billion metric tonnes of carbon is annually released into the atmosphere[2].

Typical output efficiencies of fossil fuel power generation facilities are in the vicinity of $30-35\%$ (the transportation sector is even less efficient), implying that, annually more than 230 trillion megajoules of energy is wasted in production and 3.9 billion tonnes of carbon is emitted needlessly[2]. Apart from possible global climatic changes resulting from carbon dioxide emission, chemical and thermal pollution emission from combustion processes are serious problems. In 1985 the output of primary pollutants such as oxides of nitrogen, sulfur dioxide and volatile organic compounds came to approximately 67, 95 and 80 million tonnes respectively[3]. These compounds are biologically hazardous in themselves, but are also major contributors to

secondary pollution problems such as photochemical smog and acid rain.

With diminishing combustible resources and increasing concern over the environmental impact of energy generation, the requirement to improve combustion efficiency and reduce environmentally hazardous emissions is of paramount importance. Improved knowledge of combustion phenomena, improved high temperature materials, and power generation techniques such as co-generation are helping to increase output efficiencies to between 40 and 60%. It is expected that nationally averaged output efficiencies of modern electrical utilities could be around 55% within the next fifty years[2]. Regulations pertaining to pollutant emissions are becoming increasingly stringent. These regulations will only be met through a better understanding of how these pollutants are formed.

In order to meet current performance standards, designers and operators of combustion devices are increasingly required to employ sophisticated computational models of the combustion processes that they are designing and operating[4,5]. The design of a combustion device can be effected in a more efficient manner when aided by an appropriate computational model, since it obviates the need for prolonged and expensive prototype development programs. Computational models can also provide insight into the underlying principles of operation of combustion processes, which may not be apparent from an experimental testing program.

Computational models are constructed from sets of theories which are deemed applicable to the set of problems to be solved. Even the most detailed model cannot possibly include all the effects which constitute a combustion process. It is important to separate *a priori* those effects that are essential components of the target process, from those that can be treated in an approximate sense without compromising the validity of the model. This decision is made within the constraints imposed by available computational resources and development time, and the extent to which the various elements of the process are understood. Typically, more detailed models require more computational resources, more development time, and a better understanding of the component subprocesses. Naturally, the accuracy of a model cannot exceed the accuracy of the initial premises that it is based upon. If the constitutive theoretical framework of a model is inappropriate or insufficiently detailed for the problem under investigation, then the modelled solution will not display the key

characteristics of the target process.

In the past, the combustion models which have found industrial application have been those able to contend with the complex flow fields found in combustion systems. Many of these methods were evolved from non-reactive computational fluid dynamic models, such as $k - \epsilon$ and Reynolds stress closures, with combustion effects subsequently overlaid[5]. Equilibrium chemical results were simply matched to the computed flow field, given local values of chemically conserved scalar means and variances. The rationale for this approach was that chemical reactions were assumed to occur at a much faster rate than fluid mixing processes. According to this assumption, these *fast chemistry* methods allow for the effect of heat release upon the fluid flow through density fluctuations, but neglect the impact of the fluid flow upon chemical reaction rates and species production. This limitation excludes these models from the class of design problems where interaction between chemical reaction kinetics and the mixing of reactive species is important. This class of problems includes questions of flame propagation and stability, extinction and ignition behaviour, fuel efficiency and pollutant formation. It is clear that for combustion models to be useful in meeting current needs they must address this key aspect, the interaction between chemical reactions and turbulent mixing.

Unfortunately, the treatment of this interaction is one of the most difficult problems of combustion science. Turbulence is characterised by a wide physical separation between large scales, containing the bulk of the available turbulent kinetic energy, and small scales where viscosity smooths small velocity fluctuations into variations in molecular motion. Any discretization of a turbulent flow field, whether in a model or in the course of an experiment, involves temporal and spatial averaging to derive point values. If the resolution of a discretization is less than that required to resolve the diffusive molecular scales, then the resultant turbulent fluctuations about the averaged point values will be substantial. At the same time, combustion involves instantaneous chemical reactions whose rates display a highly non-linear dependence on instantaneous temperature and reactive species concentration. In the presence of turbulent fluctuations, it is not possible to estimate average reactive species production and consumption rates from the discretized values of temperature and species concentration. In a modelling context this presents a closure problem, and precludes

the accurate prediction of reactive species yield and sensible enthalpy production. A number of different models have been developed in an effort to accurately describe chemical kinetic effects in turbulent combustion, and these are discussed in more detail in the following chapter. Whilst these methods are successful in many cases, by and large they are constrained in terms of either general applicability or chemical complexity.

A new theoretical approach to the closure problem has been proposed in recent years[6,7,8,9], and is widely known as the Conditional Moment Closure (CMC) method. The purpose of the investigation, reported in this thesis, has been to develop the conditional moment closure method from an essentially untested theory into a fully implemented model, with applications to a diverse range of combustion systems. Whilst combustion can occur in all phases of matter, this investigation has been confined to combustion in the gas phase, such as would occur where gaseous fuels are mixed and burnt in air. Combustion in multiple phase environments, such as coal particles in air or diesel droplets in a compression ignition engine, are also excluded but the CMC model is readily applicable to the gas phase components of these processes.

The basic philosophy underpinning the CMC method is that by averaging reactive scalars conditionally upon an appropriate scalar or scalars, turbulent fluctuations about the resultant averages are much smaller than those resulting from conventional averaging. By reducing reactive scalar variance at each point in the conditioning scalar space, the conditional mean chemical reaction rates can be accurately estimated from conditional mean reactive scalar values. The choice of one or more conditioning variables depends upon the mode of combustion being investigated. If combustion is occuring as fuel and oxidizer mix together, in the so-called nonpremixed mode, then a conserved scalar such as the mixture fraction is the best choice of conditioning variable since it decribes the extent to which fuel and oxidizer are mixed. If on the other hand, combustion fronts are propagating through a flammable mixture in a premixed mode, then the conditioning variable must be one that describes the progress of the global reaction. In hybrid regimes where the distinction between these limiting modes of combustion is blurred, its is necessary to condition on both a mixedness variable and a reaction progress variable.

In the following chapter, a background of information relating to the current state of turbulent combustion modelling is provided. The principal advantages and disadvantages of the various methods are discussed so as to provide a gauge for the subsequent evaluation of the CMC method.

Chapter Three contains derivations of CMC models for general cases of premixed and nonpremixed turbulent combustion. The various closure assumptions involved in each derivation are discussed, and the constraints of applicability are outlined. Equations describing the relationship between conditioning variable probability density functions and conditional mean scalar dissipation are also derived.

In Chapter Four, a CMC model is described for the simplest possible case of nonpremixed turbulent combustion. The governing equations for an Imperfectly Stirred Reactor (ISR) are derived, and solution methods are discussed.

The ISR model was subjected to a series of parametric studies, the results of which are reported in Chapter Five. The general behaviour of the model was determined over a range of operating conditions for hydrogen (H_2) combustion in air. A further study was made of the detailed chemical processes which occur in the primary recirculation zone of a hypothetical methane-burning gas turbine combustor.

A CMC model for nonpremixed combustion in turbulent axisymmetric jet flames is described in Chapter Six. The simplifications afforded by this class of problems are discussed, and the resulting model equations are presented. A discussion of the methods required for the calculation of important scalar mixing parameters is presented, along with guidelines for the use of the jet flame model.

The results of jet flame calculations are presented in Chapter Seven for experimentally studied H_2 and $CO - H_2 - N_2$ turbulent diffusion flames. Various aspects of jet flame modelling are examined, including conditional mean chemical production and small scale transport, the effect of reduced chemical mechanisms upon flame predictions, and the nature of optically-thin radiation losses from jet flames. Trends in nitric oxide pollutant formation are compared with existing experimental data. The advantages and disadvantages of CMC jet flame modelling are discussed in relation to other contemporary modelling techniques.

Chapter Eight reports on the development of premixed conditional moment closure methods. A model for a steady zero-dimensional case of premixed combustion

is proposed. A strategy for the implementation of this model is outlined, and the closure problems associated with premixed CMC models are discussed.

Finally, Chapter Nine provides a general discussion of the current state of CMC modelling and the major findings of the preceding chapters. Speculations on the future development path for CMC modelling are made, and suggestions are provided to assist in this development.

Chapter 2

Background

In this chapter, the background is set for the introduction of the Conditional Moment Closure (CMC) method. This involves a brief preamble regarding the possible modes of combustion followed by a literature survey of contemporary models and their supporting theories. An effort is made to characterize these models according to general applicability, complexity and computational cost so that an assessment of the CMC method can be made in these same terms in subsequent chapters. Whilst this chapter provides a basic grounding in the current state of turbulent combustion modelling, it is by no means an exhaustive report. References to more authoritative sources are made throughout this chapter.

2.1 Modes of Combustion

Combustion will occur when chemically reactive species are mixed together in appropriate amounts, raised to a sufficiently high temperature and allowed to react. In a Lagrangian sense, the temporal delay between the formation of a reactive mixture and the subsequent reaction of that mixture plays a role in determining the global character of the ensuing combustion. The study of combustion has traditionally been divided into the separate study of the two limiting cases of this temporal delay, that of an infinitely long delay and an infinitely short delay. The former is referred to as premixed combustion, and is globally characterised by reactions occuring in fronts which propagate through a totally uniform reactive mixture. The latter is idealized to occur in nonpremixed (diffusion) flames, and is globally characterised by combustion occuring concurrently with the formation of flammable mixture in regions where

reactant mixing occurs.

The study of premixed combustion has applications to practical systems such as spark-ignition internal combustion engines, lean-premixed stationary/nautical gas turbines, aircraft afterburners, and a range of industrial processes. Nonpremixed combustion, on the other hand, is the conceptual model for systems such as compression-ignition internal combustion engines, gas turbines of all types, as well as furnaces and steam power boilers, to name only a few. Strictly speaking, neither truly premixed nor nonpremixed combustion ever occurs, only hybrids of the two where for each fluid particle there is always a finite non-zero delay time between the formation of a flammable mixture and the onset of reaction. For example, although a spark-ignition internal combustion engine can be treated as a premixed case, the limited amount of time available for the mixing of fuel and air prior to entering the combustion chamber causes substantial inhomogeneity in the resultant mixture. In modern applications, stratified compositions of the mixture are sought after, through the use of electronic fuel injection, to control ignition delay times and burning rates. Conversely, in non-premixed gas turbine applications reactant mixing can be so intense so as to locally extinguish a flame, and a zone of unburnt flammable mixture will then form in the absence of that flame. This reactive zone is then commonly re-ignited in a premixed mode by surrounding flame structures.

In order to deal with the hybrid nature of practical combustion, models should ideally take into account both variations in reaction progress and reactant mixedness. Whilst some models do this in a limited sense, most are restricted to one of the two limiting modes of combustion, and so it is neccesary to discuss the models for each mode separately.

2.2 Nonpremixed Turbulent Combustion

2.2.1 Decoupled Models

In one of the first studies of nonpremixed combustion, made by Burke and Schumann[10] in 1928, the principal assumption was that reaction zones could be treated as the locus of points upon the stoichiometric contour between the mixing reactant streams. Given the finite diffusion velocities of species through these reaction zones, it fol-

lowed that chemical reaction rates were assumed infinitely fast by comparison. As a result, the chemical composition at all points was simply a function of a fluid dynamic variable describing the mixedness between fuel and oxidizer. This marked the first appearance of a so-called *fast chemistry* approach, and provided a simple means of decoupling the chemical nature of the flame from its fluid dynamics, thereby reducing the problem to one of fluid mixing alone. In this first application, a single one-step irreversible chemical reaction was assumed, thus precluding dissociation effects and the existance of radicals and other minor species. Burke and Schumann's *fast chemistry* assumption yielded accurate predictions of major species yields and flamelength for the series of methane (CH_4), ethane (C_2H_6) and city gas (CO-H_2) fuelled laminar jet flames that they studied.

The *fast chemistry* approach has been subsequently employed by a number of researchers in modelling turbulent nonpremixed combustion[11,12,13,14,15]. In many cases the original approach was modified to allow for dissociation and the existence of minor species by assuming that all chemical species are in equilibrium at all values of the mixedness variable. As with the more primitive one-step approach[10], all instantaneous thermochemical quantities are a function of reactant mixedness alone, however unlike the earlier approach the reaction zone has a small non-zero thickness[16]. Distinct from laminar flames, turbulent diffusion flames are subject to turbulent fluctuations in reactant mixedness. The principal problem with *fast chemistry* methods is the frequent violation of the implicit assumption that all the elementary reactions rates of a combustion chemical mechanism are much more rapid than turbulent mixing processes. Commonly, the intense turbulent mixing that can occur in diffusion flames affects the progress of slower three-body recombination reactions. Where these mole consuming reactions are hindered to a greater extent than the faster two-body shuffle reactions responsible for radical formation, radical levels can exceed equilibrium by an order of magnitude or more. The associated depression in flame temperature due to the endothermicity of radical formation also cannot be predicted using these methods. In extreme cases, turbulent mixing rates can be great enough to impede even the fastest radical formation reactions and cause localized flame extinction. These difficulties preclude *fast chemistry* methods from the prediction of extinction and ignition, accurate temperatures and radical concentrations, or formation of chemical species that are strongly dependent on chemical

kinetic effects.

Efforts to deal with the shortfalls of *fast chemistry* methods has led some researchers to the develop methods where thermochemical properties are determined in terms of reactant mixedness and some other variable allowing for variation in reactedness. A choice of reactedness variable exists for these *two scalar* methods. In a chemical kinetics context, Dixon-Lewis[17] and others[18] employ a progress variable resulting from a linear combination of reactant and product species that are pertinent to simple hydrogen-air combustion. The linear combination of major species eliminates radical shuffle reactions from direct consideration and as a result the variable measures only the progress of three-body recombination reactions. The thermodynamic state and rate of change of state can be uniquely determined by this reaction progress variable for any given mixture fraction. Employing this variable in turbulent combustion modelling is problematic owing to the classic closure problem introduced in chapter 1, namely that the averaged rate of change of reactedness cannot be accurately estimated from the averaged reactedness, when in the presence of turbulent fluctuations.

Magnussen and Hjertager[19] employ a semi-empirical approach whereby the mean rate of change of reactedness variable is modelled as the product of local time-mean fuel. oxidizer, or mixed-reactant mass fraction, whichever is least, and the rate of large scale turbulent mixing with a premultiplying constant. This approach is similar to earlier models of Spalding[20,21] except that for those cases the rate of reaction was dictated by eddy-break-up timescales. In both cases, separate equations are solved for mixture fraction and reactedness, but the magnitude of the chemical source term in the reactedness equation is governed by mixing parameters. As with *fast chemistry* methods, these simple approaches cannot predict kinetically limited phenomena. In many cases, these semi-empirical methods have found industrial application because of constraints on computational resources, historical reasons. and the perception that no viable alternative method exists[22,23].

Janicka and Kollmann[18] account for turbulent fluctuations by employing a joint probability density function (PDF) for mixture fraction and reaction progress variable. This PDF has an assumed form, consisting of gaussian-like curves in mixture fraction space at three discretized locations in reaction progress space. Whilst this

approach correctly predicted radical concentrations and gave reasonable estimates of the nitric oxide in turbulent hydrogen-air diffusion flames, the assumed forms of the PDF were quite arbitrary and there is some doubt as to the applicability of the method in more chemically complex flames where the PDF would have a much higher dimensionality[5]. Correa and Shyy[24] have extended the two-dimensional PDF of Janicka and Kollmann to three dimensions to deal with CO-H_2 air combustion and have had some success.

Bilger[25] proposed a different approach where instead of modelling reaction progress, a system of equations governing individual species perturbation from chemical equilibrium were solved for a range of mixture fractions. Due to errors in reaction rate estimates, reaction progress variables may not predict chemical equilibrium given an infinite time to react under quiescent conditions. Perturbation variables do not incur this difficulty since the perturbations will tend to zero in the absence of turbulent interference, and chemical equilibrium is assured. In a study of hydrogen-air turbulent diffusion flames and isothermal atmospheric turbulent mixing layers, Bilger[25] was able to relate the individual species chemical formation rates to a local perturbation variable and solve the species perturbation equations. Whilst this method was feasible for the systems studied, simple relationships between species formation rates and perturbation variables for highly perturbed systems and chemically complex flames have not been forthcoming.

Another more promising class of *two scalar* methods has sought to retain some of the computational simplicity of *fast chemistry* methods afforded by the decoupling of mixing and chemical reaction, but gain greater applicability and accuracy for flames with significant departure from equilibrium. Usually referred to as the *flamelet* method, the basic simplifying assumption of this method is that turbulent flames consist of an ensemble of strained laminar flamelets[26,27,28,29]. The flamelets are assumed to exist in very thin one-dimensional zones where local mixing occurs by molecular diffusion alone. Where this assumption is valid, chemical production rates can be uniquely specified in terms of mixture fraction and scalar dissipation rate for statistically stationary flames. As with *fast chemistry* methods, *flamelet* methods reduce turbulent nonpremixed combustion to little more than a mixing problem. Chemical species yields can be precomputed or measured from laminar counterflow

diffusion flames for virtually any chemical system , and then matched to the turbulent flow field from a flamelet 'library'. Variation in the second scalar, the scalar dissipation rate, can account for states of chemical reactedness ranging from chemical equilibrium to extinction and thereby represent a vast improvement over simple *fast chemistry* techniques.

The difficulty with flamelet methods lies in their general applicability to turbulent combustion. Peters[28,29,30] and Williams[27,31] employ Crocco-type variable transformations in deriving flamelet equations, attaching a normal spatial coordinate to the stoichiometric mixture fraction contour. In their derivation, the criterion for flamelet viability was sufficient thinness of the flame zone in mixture fraction space, met in cases of high activation energy reactions and/or high ratios of mixing to chemical timescales (Damkohler number, Da). Given sufficient thinness, the one-dimensional equations for reactive species conservation were simplified to a simple balance between chemical reaction and scalar mixing rates at the stoichiometric contour. Outside of the flame zone, chemical reaction terms were assumed to be zero thereby making reactive species concentrations solely a function of mixing between the pure fuel, oxidizer, and stoichiometric fluid. Bilger[32] states that the criterion for flamelet viability is that the physical width of the flame zone must be much smaller than the smallest physical scale of turbulent mixing, namely the Kolmogorov microscale. It was further claimed, based on experimental measurement, that few combustion systems of practical interest meet this criterion[32]. Mell *eta al*[33,34] employed direct numerical simulation (DNS) results to verify the flamelet method in isothermal turbulence. It was demonstrated physical thinness does not neccesarily follow from thinness in mixture fraction space, contrary to what was assumed in the original derivation[27,28,29,30,31]. Rather, under conditions of low scalar dissipation rate, three dimensional effects can be significant and thereby invalidate the one-dimensional reaction zone structure inherent in flamelet models.

Dahm and coworkers[35,36,37,38] have derived flamelet equations through a different route, originating from the observation that instantaneous scalar dissipation structures are predominantly layer-like in low to moderate Reynolds number turbulence. The flamelet equations are claimed to have boundary conditions different from those of other derivations, and to be independent of any thinness constraints[38]. It

seems however, that because of an inability to specify these boundary conditions on reactive species concentration at each isopleth surface, a further assumption must be made which effectively renders the Bish and Dahm[38] model equivalent to other flamelet models. Buch *et al*[37] suggest that the thinness criterion of Bilger[32] may be too restrictive and derive alternative thinness scales based on strain rate arguments that are an order of magnitude greater than the well established Kolmogorov microscales. The general model derivation by Dahm and coworkers makes no allowance for sub-unity Schmidt number ($Sc < 1$) mixing of species[35,37,38]. Many important radical species, such as monatomic hydrogen H, display this mixing behaviour[39] and may result in multi-dimensional combustion zones that that cannot be accounted for by the model.

In an effort to account for poor predictions of chemical intermediates in some turbulent nonpremixed flames, transient flamelet models have been studied[40,41]. These studies suggest that chemical irreversibilities can lead to elevated time averaged intermediate concentrations compared to steady flamelet results. Criteria for the validity of the quasi-steady assumption employed in flamelet models[26,27,28,29,30,31] are suggested by Mell *et al*[33,34].

2.2.2 Coupled Models

As the controversy over flamelet applicability persists, it is appropriate to now consider the next generation of turbulent combustion models, namely those which address turbulence-chemistry interaction at all scales. Pope and coworkers[5,42,43,44,45,46,47] have developed successful modelling methods which involve the stochastic manipulation of a joint probability density function (PDF) for mixture fraction, velocity and key reactive scalars in a turbulent flow. Chen and others[48,49,50,51,52,53] employ a similar method, but do not include velocity in their joint PDF, and calculate the flow field through alternative methods. All of these PDF methods have the advantage that mean chemical production terms do not require approximation since they are exactly determined by the convolution of the joint PDF with production rates over all points in the composition/velocity domain[5,42,48]. The evolution of the joint PDF is typically handled using Monte Carlo methods where a large number of Lagrangian stochastic particles are operated on in fractional steps by modelled processes vari-

ously responsible for molecular mixing, chemical reaction and convection[5,42]. A stochastic formulation of the governing equations is necessary because deterministic approaches are only feasible for PDFs with low dimensionality. Even so the computational cost of PDF methods is high, and as a result the finite capability of modern computers places serious constraints on the degree of chemical and geometric complexity that can be modelled. For two dimensional turbulent jet flame calculations, on modern non-parallel supercomputers (such as Cray XMP/YMP series machines), the maximum number of independent chemical steps is limited to four or five and rate data must be precomputed and stored in 'look-up' tables. Efficient construction and usage of these tables can further limit computational tractability. Typical run times for PDF methods are of the order of $8-10$ CPU hours on a Cray YMP-1 for a three dimensional joint PDF in a turbulent hydrogen jet flame[51]. Recently, the advent of massively parallel supercomputers has allowed PDF methods to be expanded to handle much greater chemical complexity, but these calculations entail very large computation costs[44,53].

Aside from constraints on PDF dimensionality, the major problem associated with these methods is the modelling of molecular mixing terms[5]. Unless dissipation rates are explicitly included in the joint PDF[5], the rate of molecular mixing cannot be determined exactly and is usually modelled by lagrangian particle interaction[42] and pair exchange methods based on variants of Curl mixing models[5,54]. These models have a number of disadvantages, principally that they do not accurately predict mixing behaviour in the simple test case of isotropic turbulence, they are unable to predict mixing where different species diffuse at different rates (differential diffusion), and they have no firm empirical or theoretical basis[5]. Nevertheless, these models are employed because, with appropriate corrections, they yield plausible results for many cases [45,46,47,49,50,51,52,53,55,56] and work is continuing towards eliminating their disadvantages[5,57]. In principle, PDF methods can be applied to modelling turbulent combustion in all cases from the flamelet regime, where reaction scales are much smaller than the smallest turbulent scales, to the distributed regime where the converse is true. This flexibility represents a substantial step forward from the models described in the preceeding subsection, which depend upon there being a separation in scales between chemical reactions and turbulent mixing.

A more recent coupled model has been developed by Kerstein and coworkers [58,59,60,61,62,63,64,65], and has the potential to address some of the shortcomings of the PDF method. This method deals with turbulent mixing and reaction via a one dimensional description which, because of this dimensional reduction, allows diffusive scales to be resolved in the computation. The instantaneous scalar field is described as distribution of species along these line elements, and this distribution is simultaneously effected by the processes of reaction, molecular diffusion, and mixing due to turbulent eddies of different sizes. The method is now widely known as the linear-eddy model, reflecting the line description of the scalar field and the novel treatment of turbulent eddy interactions with that field[58]. The linear-eddy method is employed as a subgrid model for turbulent flow calculations. Turbulent flow field quantities which are resolved in the fluid dynamic calculation are passed as input parameters to the subgrid model which in turn provides a closure for the fine scale effects such as molecular diffusion, chemical reaction, and small scale turbulent mixing. Each of the many independent line elements in each subgrid are sufficiently resolved to allow instantaneous diffusion and reaction processes to be computed directly without any need for approximation. Subgrid scale turbulent mixing occurs at a rate dictated by the input mixing statistics and operates on the line elements causing them to undergo 'triplet mapping'[58,59,60.61,62], a heuristically designed process that seeks to mimic small scale eddy interaction with a scalar field. Exchange of line elements between subgrid cells occurs in 'splicing events', another stochastic simulation, which accounts for the effects of large scale turbulent eddies[63]. Mean species concentrations are returned to the fluid dynamic grid by averaging over all the individual line elements within each subgrid cell. The advantages of linear-eddy methods are that as with PDF methods the chemical reaction rate does not require approximation, and that molecular mixing is treated separately from small scale turbulent mixing. The latter allows molecular transport to be treated exactly, which is in contrast to the PDF method. Molecular transport can be calculated using multi-component diffusion velocity equations, thus allowing the calculation of differential diffusion effects[65]. The principal disadvantages of the linear-eddy method are that small scale turbulent mixing is approximated via the artificial construct of 'triplet mapping', and large scale mixing is simulated by 'splicing events'. Both of these processes may deviate substantially from physical reality. Nevertheless preliminary linear-eddy results have

been obtained by Calhoon *et al*[65] for a turbulent H_2/Ar-air jet flame, that include the effects of differential diffusion for chemical mechanisms up to 13 steps in size. These results show reasonable agreement with measurements, but as with chemically complex implementations of the PDF method they seem to have required a great deal of computation time on a massively parallel supercomputer.

Subgrid scale modelling of combustion processes, as is employed in Large Eddy Simulations (LES) of turbulent reactive flow, is subject to the same kinds of closure problems that are associated with large scale modelling[5]. Apart from linear-eddy methods (see above), subgrid scale models for turbulent combustion resemble simple large scale closure models such as fast chemistry methods and eddy-breakup formulations. In part, the lack of sophistication of many of the current subgrid models stems from constraints imposed by computational resources. In the large scale modelling methods mentioned above, such as joint PDF methods, solution of the turbulent flow field alone does not require a great deal of computational effort and thus more sophisticated turbulence-chemistry interaction models can be readily afforded. However, calculation of the turbulent flow field in an LES typically requires a great deal of computation time and memory capacity, so that it is simply not feasible to incorporate a detailed chemical model, whilst retaining the same level of spatial and temporal resolution. It would seem that with the current trend in increasing computational capability, subgrid models for turbulence-chemistry interaction will become increasingly sophisticated and variants of current large scale closure methods might find subgrid applications.

Direct Numerical Simulation (DNS) of turbulent reacting flow goes a step beyond LES, in that the very smallest scales of turbulent motion are spatially and temporally resolved. Sometimes DNS is referred to as being 'model-free'[66,67] in that it doesn't incorporate any turbulence closure models, but rather solves the Navier Stokes equations directly. Unfortunately, practically all combustion problems of interest, with realistic multi-step chemistry, contain a subset of very fast reactions. These reactions produce important structures at temporal and spatial scales below the smallest turbulent scales, and hence below DNS resolution levels. To date, direct numerical simulations of turbulent combustion have either been made with resolvable artificial chemistry, to provide a qualitative understanding of the ef-

fects of heat release upon detailed flow structure, or with one-step approximations of realistic chemical systems. In the case of the latter, subgrid chemical structure is neglected and these calculations are thus no longer 'model-free'. Future advances in computational capability will allow more sophisticated direct numerical simulations of turbulent reacting flow to be made. Two distinct routes of development are possible. Future DNS of combustion may become truly model-free by resolving the smallest chemical structures at a high computational cost, or subgrid models for turbulence-chemistry interaction may be employed instead. Whilst the latter is more likely to be adopted in common practice, given the similar efforts being made in LES and large scale modelling, the former technique would be an invaluable source of data for the verification of proposed subgrid models.

The Conditional Moment Closure (CMC) method, which is discussed in detail in subsequent chapters, is also characterised as a 'coupled' model since it explicitly treats turbulence-chemistry interaction at all scales. It will be seen that the CMC method has many of the advantages of the large scale methods discussed here, but requires only a tiny fraction of the computational effort. Although it has not been investigated in this thesis, CMC methods may prove useful in subgrid scale models for the LES and DNS applications discussed above.

2.3 Premixed Turbulent Combustion

Compared to the array of models available for the study of nonpremixed turbulent combustion, there are relatively few applicable to premixed turbulent combustion. This reflects the fact that due to the inherent complexity of flame-flow interaction in these cases, simplifying theories with practical accuracy have been slow in arriving[5,68,69].

In premixed combustion, flame fronts can be characterised as zones of intense chemical nonequilibrium where radical species are found in large numbers in a transition process between unburnt and fully burnt states. Unburnt mixture immediately adjacent to a flame zone is caused to react by an influx of heat and chemical radical species. thereby advancing the position of the front. In this way, the flame front describes the boundary between burnt and unburnt mixture and propagates into the

unburnt mixture at some finite rate. The rate of transfer of heat and radicals to a given unburnt volume is largely governed by the intensity of local mixing, the proximity and extent of the adjacent flame surface, and the mobility of the transported species. The passage of burning material through the flame front is accompanied by a large density decrease resulting from heat release. In accordance with conservation of momentum, this density decrease causes a large increase in fluid velocity and a concurrent decrease in static pressure. These fluid dynamic effects very strongly influence the nature of the flow field, which in turn effects the rate of local mixing, the shape of the flame front, and consequently, the speed of propagation.

Unlike nonpremixed combustion, where some headway can be made in some cases by decoupling turbulence-chemistry interactions, models for premixed combustion must address these complex flame-flow interactions if they are to have any practical relevance. The Bray-Moss-Libby (BML) model (descended from the Bray-Moss model) for premixed turbulent combustion has been successively improved since its inception[70,71,72,73,74] to include the majority of these interactions. The BML model takes into account flame-flow effects such as counter-gradient species transport and flame generation of turbulent kinetic energy, but as with most premixed models it does not incorporate the effects of instantaneous pressure fluctuations. Pope[69] suggests that these pressure fluctuations may act to diminish the differential-density driven counter-gradient transport effects. The BML model is applicable to combustion systems with unity Lewis and Schmidt numbers and low Mach number, where thermochemical state can be uniquely specified by a reaction progress variable. An assumed-form PDF for the reaction progress variable is adopted to determine the means, variances and correlations concerning velocity, reaction rate and reaction progress variable required for closure of the governing equations. Based largely on experimental evidence (see for example [75,76]), Bray and coworkers[68,70,73] concluded that the assumed form PDF is dominated by the fully burnt and unburnt reaction states and exploit this to greatly simplify the model. In applying this assumption, the BML model is restricted in application to cases where the Damkohler number Da is large and, due to assumptions made regarding turbulent transport, the Reynolds number Re is large. Thus the BML model is applicable to the flamesheet regime of turbulent premixed combustion as delineated variously by Peters[29], Bray[68], Pope[69] and others. It can be seen from these diagrams of premixed

regimes that flamelet combustion requires $Da >> Re^{0.5}$. This thinness constraint appears to be much less restrictive than in the case of nonpremixed combustion owing to the comparatively small width of premixed flames, even in cases of practical interest such as spark-ignited internal combustion[29,68].

Premixed laminar flamelet libraries are employed to determine the instantaneous rate of chemical production as a function of reaction progress variable, strain rate, mean pressure and unburnt reactant temperature[77]. The BML model determines mean reaction rates by multiplying a crossing frequency, which describes the number of times a flamelet crosses a unit length per unit time, with the reaction rate at each crossing which is in turn related to the flamelet library values[78].

A PDF method proposed by Pope and coworkers [69,79,80,81] can also employ flamelet library values, but unlike the BML formalism it does not employ an assumed form for the reaction progress variable PDF. Instead, a joint PDF for velocity and reaction progress variable is manipulated using Monte Carlo techniques. Mean chemical reaction and convection processes are closed in this methodology, and do not require modelling in contrast to the BML method. Molecular transport must still be modelled, with different schemes depending on whether the premixed combustion process is in the flamelet or intermediate regime[69,79,80]. The molecular transport modelling by and large involves the same kind of Curl mixing rules that are employed in nonpremixed PDF methods (see subsection 2.2.2) coupled with pressure-driven transport effects. Stochastic simulations of mixing require careful application since, as with thin nonpremixed combustion, unphysical mixing of stochastic particles from 'distant' locations in composition space can occur. Such mixing can lead to predictions of flame extinction events where none actually exist. The BML and PDF methods seem to produce plausible predictions when compared with each other and the limited amount of experimental data available[69,80,81].

In the forms described above, the PDF and BML flame-sheet methods do not explicitly treat flame front behaviour and as a result local burning rate predictions do not allow for the effects of flame surface orientation, curvature and cusps[82]. Subsequent development of the PDF and BML methods for premixed flamelet combustion has sought to include flame-surface density models[82,83,84] to calculate local burning rates as functions of not only local strain rate and reaction progress variable, as in

a flamelet library, but in accordance with local flamelet geometry. These preliminary models have been applied to cases of statistically-plane premixed flames in isotropic turbulence with constant density, but require further development to be more generally applicable[84]. Much of the difficulty involved in modelling turbulent premixed flames arises from the accurate prediction of flame surface behaviour and its influence upon local burning rates and speed of flame propagation. A substantial number of other modelling methods are under development (see for example [85,86,87,88,89,90]) but cannot feasibly be discussed here. Suffice to say that by and large their limitations are similar, with regard to mean and local burning rate prediction, to those of the PDF and BML models[82,84] discussed above.

Direct numerical simulation (DNS) of turbulent premixed combustion obviates the need for closure modelling of flame surface dynamics, provided the flame fronts are resolved. The discussion in the previous section relating to DNS resolution of chemical structures is even more relevant in premixed combustion, where these structures can be much thinner than their nonpremixed counterparts. Clearly, in the absence of adequate flame front resolution, the problems associated with modelling flame front dynamics remain. As with nonpremixed DNS, future advances in computational performance may allow wrinkled flamelets to be resolved in modest turbulence, or alternatively allow the development of more sophisticated subgrid models. Despite the difficulties mentioned above, DNS analysis of turbulent premixed flames continues to provide information, useful for the development of large scale models, such as flame surface density statistics[91].

In some idealized cases where spatial dimensionality is reduced to zero, such as in a stirred reactor, the need to predict turbulent burning rates is obviated since reactions occur in the distributed regime of premixed combustion. In these idealized cases, the influence of turbulent mixing on premixed distributed chemical reaction zones can be investigated with applications to some process reactors and lean premixed gas turbine combustors[92,93,94]. To date, the application of the Conditional Moment Closure (CMC) method to premixed turbulent combustion has been restricted to the degenerate case of stirred reactors, and will be reported on in subsequent chapters.

2.4 Summary

In summary, this chapter has introduced premixed and nonpremixed combustion as limiting cases of the temporal delay between the formation of a reactive mixture and the onset of reaction. In practical applications, hybrid modes of combustion frequently occur.

A great deal of model development has occurred for turbulent nonpremixed combustion with a gradual progression in sophistication from single scalar *fast chemistry* methods, to *two scalar* methods including nonpremixed steady laminar flamelet models, culminating in models such as the Joint PDF and Linear-Eddy models which account for turbulence-chemistry interaction at all physical scales. The CMC method, which is the subject of this thesis, belongs to this latter class of models. In general, coupled models require more computational resources than their decoupled counterparts but are much more widely applicable. The CMC method is a versatile new approach that required substantially less computational effort than other coupled models.

Premixed turbulent combustion models are substantially less developed than nonpremixed models, primarily because of the complicated flame-flow interactions which are present in premixed flames. The Bray-Moss-Libby (BML) and premixed joint PDF methods have been described as two examples of premixed models which have met with some success. These models both account for premixed combustion effects such as counter-gradient species transport and turbulent kinetic energy generation, but cannot treat the influence of the instantaneous pressure field. Apart from pressure field uncertainties, the principal difficulty facing premixed turbulent combustion modelling is the accurate prediction of flamesheet structure and speed of propagation. For the degenerate case of distributed regime turbulent premixed combustion in stirred reactors, modelling can proceed without facing this difficulty. Premixed CMC applications have so far been limited to this special case, and are described in a subsequent chapter.

Chapter 3

Model Derivation

In this chapter, Conditional Moment Closure (CMC) methods are mathematically described for premixed and nonpremixed turbulent combustion. The derivation for hybrid mode combustion is beyond the scope of this work, but some comments relevant to this type of CMC model are made in a later chapter. The derivations given here are generally applicable to any turbulent flow, but further simplifications are made for specific cases in subsequent chapters.

3.1 Conditional Statistics

The concept of conditional averaging is used extensively throughout the remainder of this thesis, and so it is appropriate to now provide a mathematical definition in the context of turbulent fluid flow. Consider an ensemble of N statistically independent realizations of a turbulent flow field, each with identical initial and boundary conditions. Within this field, a large number of different scalar and vector quantities fluctuate such that their instantaneous values at any point in space and time are unpredictable. Conventional unconditional averaging involves summing all instantaneous values, at a given point and time, for all realizations of the flow field and dividing the sum by the number of realizations. An example of this is given below for the scalar Y where an ensemble average value $< Y >$ is defined at the position $\underline{x}$ and time t.

$$< Y(\underline{x},t) > \equiv \lim_{N\to\infty} \frac{1}{N} \sum_{i=1}^{N} Y^i(\underline{x},t) \tag{3.1}$$

Individual realizations of the flow field can then be expressed in terms of the

ensemble average $< Y >$ and a deviatoric term y^i of unknown magnitude.

$$Y^i(\underline{x},t) =< Y(\underline{x},t) > +y^i(\underline{x},t) \tag{3.2}$$

When this averaging procedure is applied to the system of equations governing the spatial and temporal evolution of the turbulent field, the resulting set of equations contain mean values which can be predicted deterministically provided a closure exists for the unkown correlations of deviatoric terms. As first order closure approximations can only be formulated from mean value information, if the magnitude of deviations from the means are large compared to the mean values themselves it is unlikely that the approximations will be valid.

Conditional averaging upon a conditioning variable proceeds in a slightly different manner to that above, in that only those values of $Y(\underline{x},t)$ where an arbitrary condition is met will be included in the calculation of the average. Extending the example above, a conditional average for the scalar Y can be calculated upon the condition that the conditioning variable, say X, is equal to an arbitrary value X_a,

$$< Y(\underline{x},t) \mid X(\underline{x},t) = X_a >\equiv \lim_{N\to\infty} \frac{1}{N}\sum_{i=1}^{N} Y^i(\underline{x},t)\delta(X^i(\underline{x},t) - X_a) \tag{3.3}$$

where δ is the Dirac delta function. Correspondingly, the probability density function (PDF) for $X = X_a$ is defined as

$$P_{Xa}(\underline{x},t) \equiv \lim_{N\to\infty} \frac{1}{N}\sum_{i=1}^{N} \delta(X^i(\underline{x},t) - X_a) \tag{3.4}$$

and has the required property that

$$\int_{-\infty}^{\infty} P_{Xa}(\underline{x},t)dX_a = 1 \tag{3.5}$$

Unconditionally averaged values can be simply recovered from conditional values by convolution with the PDF as given below.

$$< Y(\underline{x},t) >= \int_{-\infty}^{\infty} < Y(\underline{x},t) \mid X(\underline{x},t) = X_a > P_{Xa}(\underline{x},t)dX_a \tag{3.6}$$

As with unconditional averaging, the values corresponding to individual realizations Y^i can be expressed as the sum of the conditional mean $< Y \mid X_a >$ and an unknown deviatoric contribution y^i_X.

$$Y^i(\underline{x},t) =< Y(\underline{x},t) \mid X(\underline{x},t) = X_a > + y_X^i(\underline{x}.t) \tag{3.7}$$

The statistical definition above (Eqns 3.3 - 3.6) can be readily extended to more complicated selection conditions involving any number of scalar values and corresponding joint PDFs. Intuitively, it is apparent that the greater the number of independent variables used in the conditional statement, the more specific the averaging process will be to a chosen subset of the statistical ensemble. It is evident that as the number of independent conditions increases, the relative magnitude of the deviatoric contribution will decrease, to the point where it is identically zero when all degrees of freedom are specified in the conditioning.

Clearly, if the instantaneous point quantities of the flow field cannot be predicted, perhaps due to computational limitations, then the problem remains intractable when all degrees of freedom are used in the conditional statement. However, it is possible to make the deviatoric terms appropriately small through the careful selection of a sufficient (hopefully small) number of critical degrees of freedom as conditioning statistics. These formulations allow accurate closure approximations to be made in terms of mean quantities, albeit at the expense of additional problem dimensionality compared to unconditionally averaged formulations. The minimization of deviatoric terms in exchange for increased problem dimensionality is characteristic of conditional moment closure methods.

3.2 Nonpremixed Model

In turbulent nonpremixed combustion, the degree to which instantaneous variations in reactive scalar values are due to fluctuations in mixedness can be estimated from the level of fluctuations present in a conserved scalar. Conserved scalars are variables, often combinations of species mass fractions and other scalars such as enthalpy, which have no chemical source terms. Selecting a conserved scalar such as mixture fraction, ξ, as a conditioning variable eliminates scatter due to mixedness variation from the conditionally averaged reactive scalar variables. This reduction in the magnitude of instantaneous deviations from mean values is well known[8] and will be exploited in closure approximations later in section 3.2.

Mixture fraction, ξ, is a normalized conserved scalar, that by convention is defined to have a value of unity in the designated fuel stream and zero in the designated oxidizer stream.

$$\xi(\underline{x},t) \equiv \frac{\beta(\underline{x},t) - \beta_{ox}}{\beta_{fu} - \beta_{ox}} \tag{3.8}$$

In Eqn 3.8, β is a conserved scalar such as an atomic mass fraction, and the subscripts fu and ox denote pure fuel and oxidizer values respectively. In the absence of differential diffusion, all conserved scalars mix at the same rate and consequently the value of ξ is independent of the choice of β[95]. In these cases, which occur where the diffusivities of all scalars are equal or effectively equal, mixture fraction ξ is a unique descriptor of the instantaneous state of mixedness between fuel and oxidizer. Where turbulent stirring is sufficiently intense, the characteristic length scales at which molecular transport is dominant are small, and thus differential diffusive separation of species is effectively insignificant. In the presence of significant differential diffusion, a unique mixedness descriptor no longer exists[39,95].

Since mixture fraction is a conserved scalar, the instantaneous governing equation is simply a balance between an instantaneous rate of change, fluid convection and molecular diffusion,

$$\rho\frac{\partial\xi}{\partial t} + \rho\underline{u}\cdot\nabla\xi = \nabla\cdot(\rho D_\xi\nabla\xi) \tag{3.9}$$

where ρ denotes density, $\underline{u}$ fluid velocity, and D_ξ the diffusivity of mixture fraction. The probability density function P_η for mixture fraction can be defined in the manner of Eqn 3.4.

$$P_\eta(\underline{x},t) \equiv < \psi(\underline{x},t) > \tag{3.10}$$

where the special function ψ is given by,

$$\psi(\underline{x},t) \equiv \delta(\xi(\underline{x},t) - \eta) \tag{3.11}$$

The governing equation for mixture fraction PDF evolution can be derived using the properties of ψ. The resultant equation is important in the calculation of scalar mixing behaviour in the nonpremixed CMC model, and the derivation serves as a useful introduction to the technique used by Klimenko[6,7] to derive the CMC

equations themselves. The following equations are in accordance with the properties of Dirac delta functions.

$$\frac{\partial \psi}{\partial t} = -\frac{\partial}{\partial \eta}(\psi \frac{\partial \xi}{\partial t}) \tag{3.12}$$

$$\nabla \psi = -\frac{\partial}{\partial \eta}(\psi \nabla \xi) \tag{3.13}$$

$$\nabla \cdot (\rho D_\xi \nabla \psi) = \frac{\partial^2}{\partial \eta^2}(\rho D_\xi (\nabla \xi)^2 \psi) - \frac{\partial}{\partial \eta}(\psi \nabla \cdot (\rho D_\xi \nabla \xi)) \tag{3.14}$$

Summing Eqns 3.12-3.14 and taking the instantaneous mixture fraction equation (Eqn 3.9) into account, the following expression results,

$$\rho \frac{\partial \psi}{\partial t} + \rho \underline{u} \cdot \nabla \psi - \nabla \cdot (\rho D_\xi \nabla \psi) = -\frac{\partial^2}{\partial \eta^2}(\rho D_\xi (\nabla \xi)^2 \psi) \tag{3.15}$$

which when averaged over the ensemble of realizations finally yields,

$$\begin{aligned} &< \rho \mid \eta > \frac{\partial P_\eta}{\partial t} + < \rho \underline{u} \mid \eta > \cdot \nabla P_\eta = \\ &\qquad \nabla \cdot (< \rho D_\xi \mid \eta > \nabla P_\eta) - \tfrac{1}{2} \tfrac{\partial^2}{\partial \eta^2}(< \rho \chi \mid \eta > P_\eta) \end{aligned} \tag{3.16}$$

where χ is the instantaneous scalar dissipation rate defined as.

$$\chi \equiv 2 D_\xi \nabla \xi \cdot \nabla \xi \tag{3.17}$$

As will be shown later, Eqn 3.16 provides the means for determining the form and magnitude of the critical mixing parameter $< \rho \chi \mid \eta >$, when given an assumed form of the mixture fraction PDF. The significance of conditional mean scalar dissipation rate $< \rho \chi \mid \eta >$ to the CMC model will become apparent in the derivations below, and the method for its determination will be explored in greater detail in the following chapters.

The derivation of the nonpremixed CMC equations presented here most closely follows the derivation of Klimenko[6,7] but observations will be made regarding the differences between this derivation and that of Bilger[8,9]. The equation governing the instantaneous evolution of a reactive species mass fraction Y_i is given below, and can be seen to differ from the conserved scalar equation (3.9) in that 1) it incorporates

a reactive source term w_i, and 2) the molecular diffusivity D_i does not neccesarily equal D_ξ.

$$\rho\frac{\partial Y_i}{\partial t} + \rho\underline{u}\cdot\nabla Y_i = \nabla\cdot(\rho D_i\nabla Y_i) + \rho w_i \tag{3.18}$$

By introducing a special function analogous to ψ, the derivation of the CMC equations can proceed in a manner similar to that given above for the mixture fraction PDF equation (3.16).

$$\phi(\underline{x},t) \equiv \delta(\xi(\underline{x},t)-\eta)\delta(Y_i(\underline{x},t)-s) \tag{3.19}$$

The joint PDF of reactive species mass fraction for species i and mixture fraction, $P_{\eta,s}$, is related to ϕ by ensemble averaging as before.

$$P_{\eta,s}(\underline{x},t) \equiv < \phi(\underline{x},t) > \tag{3.20}$$

The derivatives of ϕ are given below,

$$\frac{\partial\phi}{\partial t} = -\frac{\partial}{\partial\eta}(\phi\frac{\partial\xi}{\partial t}) - \frac{\partial}{\partial s}(\phi\frac{\partial Y_i}{\partial t}) \tag{3.21}$$

$$\nabla\phi = -\frac{\partial}{\partial\eta}(\phi\nabla\xi) - \frac{\partial}{\partial s}(\phi\nabla Y_i) \tag{3.22}$$

$$\begin{aligned}\nabla\cdot(\rho D\nabla\phi) &= -\frac{\partial}{\partial\eta}(\phi\nabla\cdot(\rho D\nabla\xi)) - \frac{\partial}{\partial s}(\phi\nabla\cdot(\rho D\nabla Y_i)) \\ &+\tfrac{\partial^2}{\partial\eta^2}(\phi\rho D(\nabla\xi)^2) + \tfrac{\partial^2}{\partial s^2}(\phi\rho D(\nabla Y_i)^2) + 2\tfrac{\partial^2}{\partial\eta s}(\phi\rho D(\nabla\xi\cdot\nabla Y_i))\end{aligned} \tag{3.23}$$

Summing Eqns 3.21-3.23 as in the earlier example, and by taking advantage of Eqns 3.9 and 3.18, the following results,

$$\begin{aligned}\rho\frac{\partial\phi}{\partial t} + \rho\underline{u}\nabla\phi - \nabla\cdot(\rho D_i\nabla\phi) &= -\frac{\partial}{\partial s}(\phi\rho w_i) \\ &-\tfrac{\partial}{\partial\eta}(\phi\nabla\cdot(\rho(D_\xi - D_i)\nabla\xi)) + \tfrac{\partial^2}{\partial\eta^2}(\phi\rho D_i(\nabla\xi)^2) \\ &+\tfrac{\partial^2}{\partial s^2}(\phi\rho D_i(\nabla Y_i)^2) + 2\tfrac{\partial^2}{\partial\eta s}(\phi\rho D_i(\nabla\xi\cdot\nabla Y_i))\end{aligned} \tag{3.24}$$

Ensemble averaging yields an equation for the joint PDF $P_{\eta,s}$ of the reactive scalar Y_i and the conserved scalar ξ.

$$\begin{aligned}&< \rho \mid \eta,s > \frac{\partial P_{\eta,s}}{\partial t} + < \rho\underline{u} \mid \eta,s > \nabla P_{\eta,s} - \nabla\cdot(< \rho D_i \mid \eta,s > \nabla P_{\eta,s}) = \\ &-\tfrac{\partial}{\partial s}(P_{\eta,s} < \rho w_i \mid \eta,s >) - \tfrac{\partial}{\partial\eta}(P_{\eta,s} < \nabla\cdot\rho(D_\xi - D_i)\nabla\xi \mid \eta,s >) \\ &+\tfrac{\partial^2}{\partial\eta^2}(P_{\eta,s} < \rho D_i(\nabla\xi)^2 \mid \eta,s >) + \tfrac{\partial^2}{\partial s^2}(P_{\eta,s} < \rho D_i(\nabla Y_i)^2 \mid \eta,s >) \\ &+2\tfrac{\partial^2}{\partial\eta\partial s}(P_{\eta,s} < \rho D_i(\nabla\xi\cdot\nabla Y_i) \mid \eta,s >)\end{aligned} \tag{3.25}$$

Multiplication through the left hand side of Eqn 3.25 by the scalar s followed by integration with respect to s between bounds (s_0,s_1) yields,

$$\int_{s0}^{s1} s[< \rho \mid \eta, s > \frac{\partial P_{\eta,s}}{\partial t} + < \rho \underline{u} \mid \eta, s > \nabla P_{\eta,s} - \nabla \cdot (< \rho D_i \mid \eta, s > \nabla P_{\eta,s})]ds =$$
$$\frac{\partial}{\partial t}(< \rho \mid \eta > Q_i P_\eta) + \nabla \cdot (< \rho \underline{u} Y_i \mid \eta > P_\eta) - \nabla \cdot (< \rho D_i \mid \eta > \nabla P_\eta Q_i) \quad (3.26)$$

where Q_i is the average of Y_i conditioned on mixture fraction as defined below,

$$Q_i(\underline{x}, t) \equiv < Y_i(\underline{x}, t) \mid \eta > \quad (3.27)$$

and P_η is the mixture fraction PDF introduced in Eqn 3.10.

Similar treatment of the s derivative terms on the right hand side of Eqn 3.25 yields,

$$\int_{s0}^{s1} s[\frac{\partial}{\partial s}(P_{\eta,s} < \rho w_i \mid \eta, s >)]ds =$$
$$s(P_{\eta,s} < \rho w_i \mid \eta, s >) \mid_{s0}^{s1} - P_\eta < \rho w_i \mid \eta > \quad (3.28)$$

$$\int_{s0}^{s1} s[\frac{\partial^2}{\partial s^2}(P_{\eta,s} < \rho D_i (\nabla Y_i)^2 \mid \eta, s >)]ds =$$
$$s(\frac{\partial}{\partial s}(P_{\eta,s} < \rho D_i (\nabla Y_i)^2 \mid \eta, s >) \mid_{s0}^{s1} - (P_{\eta,s} < \rho D_i (\nabla Y_i)^2 \mid \eta, s >) \mid_{s0}^{s1} \quad (3.29)$$

$$\int_{s0}^{s1} s[\frac{\partial^2}{\partial \eta s}(P_{\eta,s} < \rho D_i (\nabla \xi \cdot \nabla Y_i) \mid \eta, s >)]ds =$$
$$s\frac{\partial}{\partial \eta}(P_{\eta,s} < \rho D_i \nabla \xi \cdot \nabla Y_i \mid \eta, s >) \mid_{s0}^{s1} - \frac{\partial}{\partial \eta}(P_\eta < \rho D_i \nabla \xi \cdot \nabla Y_i \mid \eta >) \quad (3.30)$$

where groups followed by $\mid_{s0}^{s1}$ are understood to represent the difference between the upper and lower limiting values of the preceding term, for s tending towards the bounds.

The first term on the right hand side of Eqn 3.28 is equal to zero. The reason for this is that, either the joint PDF ($P_{\eta,s}$) or the conditional mean reactive scalar source term ($< \rho w_i \mid \eta, s >$) must be zero at a bound of reactive scalar space. If the conditional mean source term is non-zero at a bound, then the reactive scalar can only tend to that bounding value in the limit and cannot actually reach the bounding value. In this case, the joint PDF at this bound is equal to zero. On the

other hand, if the bounding conditional mean source term is zero (such as in the case of a hypothetical one-step irreversible reaction), then the influence of the source term can be such that totally reacted chemical species can exist. In this case, the joint PDF value at this bound will be greater than zero.

The dissipation terms containing $< \rho D_i(\nabla Y_i)^2 \mid \eta, s >$ and $< \rho D_i(\nabla\xi \cdot \nabla Y_i) \mid \eta, s >$ tend to zero in the limit as the reactive scalar s tends to either bound. The reasoning behind this claim is that the values of ∇Y_i, sampled at reactive scalar bounds, to form the conditional average terms, correspond with local extremum points and thus give a zero average. The s derivative term (first RHS term of Eqn 3.29) is zero due to the fact that there can be no gradient flux of reactive species beyond the prescribed bounding values. Based on the arguments given above, the first term on the right hand side of Eqn 3.30, and all of the RHS of Eqn 3.29 can be dropped from further analysis.

Treatment of the remaining term from Eqn 3.25 yields,

$$\int_{s0}^{s1} s[\frac{\partial^2}{\partial\eta^2}(P_{\eta,s} < \rho D_i(\nabla\xi)^2 \mid \eta, s >) - \frac{\partial}{\partial\eta}(P_{\eta,s} < \nabla \cdot \rho(D_\xi - D_i)\nabla\xi \mid \eta, s >)]ds =$$
$$\frac{\partial^2}{\partial\eta^2}(< \rho D_i(\nabla\xi)^2 Y_i \mid \eta > P_\eta) - \frac{\partial}{\partial\eta}(< \nabla \cdot \rho(D_\xi - D_i)Y_i\nabla\xi \mid \eta > P_\eta) \quad (3.31)$$

Combining Eqns 3.26-3.31 yields the expression,

$$\frac{\partial}{\partial t}(< \rho \mid \eta > P_\eta Q_i) + \nabla \cdot (< \rho\underline{u}Y_i \mid \eta > P_\eta)$$
$$-\nabla \cdot (< \rho D_i \mid \eta > \nabla P_\eta Q_i) = P_\eta < \rho w_i \mid \eta > + \frac{\partial}{\partial\eta}G_\eta \quad (3.32)$$

where G_η is a conditional mean flux term given by,

$$G_\eta \equiv \frac{\partial}{\partial\eta}(< \rho D_i(\nabla\xi)^2 Y_i \mid \eta > P_\eta) - 2 < \rho D_i(\nabla\xi \cdot \nabla Y_i) \mid \eta > P_\eta$$
$$- < \nabla \cdot \rho(D_\xi - D_i)Y_i\nabla\xi \mid \eta > P_\eta \quad (3.33)$$

No closure approximations have been made in the derivation of Eqns 3.32 and 3.33, they represent exact descriptions of conditional mean reactive scalar evolution in a turbulent nonpremixed combustion process. To understand the nature of Eqn (3.32), consider integrating the equation with respect to η between the limits η_1 and η_2. The left hand side of the resultant equation contains terms for the time rate of change, convection and molecular diffusion of reactive scalars located within the

band of isopleths between η_1 and η_2. The right hand side of the integrated equation contains a reaction rate term and the difference between G_η evaluated at η_1 and η_2. This latter term describes the transport of reactive scalars beyond the bounding isopleths by small scale processes.

Equations 3.32 and 3.33 are unclosed, and the form of the conditional mean flux term G_η must be modelled in order to yield the conditional moment closure (CMC) equations. The first closure assumption that will be made here is to assume that the mixing field is highly turbulent, such that the influence of molecular diffusion is negligible compared to turbulent mixing processes. This assumption allows molecular diffusivities to be approximated as being equal to the diffusivity of mixture fraction $D_i = D_\xi = D$, and allows the elimination of the differential diffusion term within G_η. Despite past erroneous claims to the contrary[96,97], CMC models have to date been unable to accurately account for the small scale transport effects resulting from differential molecular diffusion. A brief discussion of differential diffusion effects within the context of CMC modelling can be found in Chapter Nine. The assumed insignificance of molecular diffusion also allows the last left hand side term of Eqn (3.32) to be eliminated. Thus taking account of the above assumptions, Eqns 3.32 and 3.33 can be simplified to produce:

$$\frac{\partial}{\partial t}(<\rho \mid \eta> P_\eta Q_i) + \nabla \cdot (<\rho \underline{u} Y_i \mid \eta> P_\eta) = P_\eta <\rho w_i \mid \eta> + \frac{\partial}{\partial \eta} G_\eta \qquad (3.34)$$

$$G_\eta = 2 <\rho D(\nabla \xi \cdot \nabla Y_i) \mid \eta> P_\eta - \frac{\partial}{\partial \eta}(<\rho D(\nabla \xi)^2 Y_i \mid \eta> P_\eta) \qquad (3.35)$$

Closure of the remaining terms in G_η can be approached using two different sets of assumptions which then lead to the same set of equations. The first method uses a Brownian motion analogy for the movement of passive scalar particles in conserved scalar phase space and was proposed by Klimenko[6,7]. The second approach proposed by Klimenko[6,7] used the concept of local similarity between conserved and reactive scalar fields and resembles the approach of Bilger[8,9] in many ways. The following sections (3.2.1, 3.2.2) describe the two closure approaches, including their advantages and limits of applicability.

3.2.1 Flux Closure: Brownian Motion Analogy

Klimenko[6.7] provides a closure for the remaining terms in Eqn (3.35) by making an analogy between the small scale turbulent transport of a passive scalar in conserved scalar space, and the behaviour of small particles undergoing Brownian motion in physical space. Klimenko considers the movement in mixture fraction space of inertialess non-interacting tracer particles corresponding to some scalar Y. Initially ($t = t_0$) the particles are at a fixed location in mixture fraction space ξ_0 but then move around under the influence of small scale motion. According to theory of Kolmogorov[98] the mean square deviation in position from the initial mixture fraction ξ_0 is solely a function of the elapsed time and the mean scalar dissipation rate,

$$< (\xi(t) - \xi_0)^2 >= a < \chi > (t - t_0) \tag{3.36}$$

where a is some constant. Using Taylor's result[99] relating particle velocity correlation and mean square positional deviation,

$$< (\xi(t) - \xi_0)^2 >= 2 \int_{t_0}^{t} \int_{t_0}^{t} K_\xi(t' - t_0) dt' dt' \tag{3.37}$$

where $K_\xi \equiv < \dot{\xi}(t)\dot{\xi}(t_0) >$, Klimenko showed that the velocities of particles in mixture fraction space are uncorrelated over time periods greater than the Kolmogorov timescale t_k. In doing this, Klimenko was then able to apply the laws of Markovian processes to model small scale transport across isopleth surfaces.

It followed from Klimenko's argument that, for conditionally averaged reactive scalars Q with chemical characteristic times greater than the Kolmogorov timescale, the conditional mean flux G_η could be modelled in terms of first order diffusion and drift components.

$$G_\eta = A_1 \frac{\partial Q}{\partial \eta} + A_2 Q \tag{3.38}$$

The terms A_1 and A_2 are universal coefficients owing to the universal nature of small scale turbulence dynamics. The nature of the universal coefficients can be determined from the simplest case of Eqns 3.34 and 3.35, that is for statistically stationary homogeneous turbulence for an inert scalar Q that is simply a function of mixture fraction $Q(\eta) = a_1\eta + a_2$ where a_1 and a_2 are constants. For the case of $a_1 = 0$, Eqns 3.34, 3.35 and 3.16 (excluding molecular diffusion effects) yield,

$$A_2 = -\frac{1}{2}\frac{\partial}{\partial \eta}(< \rho\chi \mid \eta > P_\eta) \tag{3.39}$$

wheras the $a_2 = 0$ case yields,

$$A_1 = \frac{1}{2} < \rho\chi \mid \eta > P_\eta \tag{3.40}$$

The resultant closure equation for G_η is,

$$G_\eta = \frac{1}{2} < \rho\chi \mid \eta > P_\eta \frac{\partial Q}{\partial \eta} - \frac{1}{2}\frac{\partial}{\partial \eta}(< \rho\chi \mid \eta > P_\eta)Q \tag{3.41}$$

which when incorporated into Eqn 3.34 gives,

$$\begin{aligned}\frac{\partial}{\partial t}(< \rho \mid \eta > P_\eta Q_i) + \nabla \cdot (< \rho \underline{u} Y_i \mid \eta > P_\eta) = P_\eta < \rho w_i \mid \eta > \\ + \frac{1}{2}\frac{\partial}{\partial \eta}[< \rho\chi \mid \eta > P_\eta \frac{\partial Q_i}{\partial \eta} - Q_i \frac{\partial}{\partial \eta}(< \rho\chi \mid \eta > P_\eta)]\end{aligned} \tag{3.42}$$

Decomposing the conditional velocity reactive scalar correlation $< \rho \underline{u} Y_i \mid \eta >$ to give $< \rho \underline{u} \mid \eta > Q_i + < \rho \underline{u'} y_i \mid \eta >$, and taking account of Eqn 3.16 yields one form of the CMC equations:

$$\begin{aligned}< \rho \mid \eta > \frac{\partial Q_i}{\partial t} + < \rho \underline{u} \mid \eta > \cdot \nabla Q_i = < \rho w_i \mid \eta > \\ + \frac{1}{2} < \rho\chi \mid \eta > \frac{\partial^2 Q_i}{\partial \eta^2} - \frac{1}{P_\eta}\nabla \cdot (< \rho \underline{u'} y_i \mid \eta > P_\eta)\end{aligned} \tag{3.43}$$

In practical applications the final term on the right hand side of the equation is usually assumed to be negligible. Exceptions to this assumption occur, for example, in lifted diffusion flames. The Brownian motion flux closure approximations leading to the CMC equation (Eqn 3.43) are only strictly applicable in cases of locally homogeneous turbulence. This is a result of employing Kolmogorov theory[98] in the closure argument, which ignores large local fluctuations in instantaneous strain and scalar dissipation rates. Despite the fact that anisotropy can be present at smaller scales the assumption of local isotropy is widely used, particularly in one-point turbulence models[100].

3.2.2 Flux Closure: Local Field Similarity

Klimenko's second flux closure method is somewhat easier to grasp than the Brownian motion analogy and very nearly resembles Bilger's closure approach. To illustrate the closure method, the substitution (see below) of Bilger[8,9] will be employed for the terms within G_η.

$$Y_i(\underline{x}, t) \equiv Q_i(\underline{x}, t, \eta) + y_i \tag{3.44}$$

Klimenko[6,7] assumes that perturbations y_i from the conditional mean are small enough to be linearly approximated by a first order power series expansion about the mean. Further, by rationalizing that these small perturbations are statistically independent, from the large scale fluctuations which determine local scalar dissipation rate levels, it was claimed that:

$$< \rho D(\nabla \xi)^2 y_i \mid \eta > \approx 0 \tag{3.45}$$

$$< \rho D(\nabla \xi \cdot \nabla y_i) \mid \eta > \approx 0 \tag{3.46}$$

Substituting Eqn 3.44 into the conditional mean flux equation (Eqn 3.35) whilst taking the above argument into account yields,

$$G_\eta = < \rho D(\nabla \xi)^2 \mid \eta > \frac{\partial Q_i}{\partial \eta} P_\eta - Q_i \frac{\partial}{\partial \eta}(< \rho D(\nabla \xi)^2 \mid \eta > P_\eta) \tag{3.47}$$

which can be seen to be an identical result to that derived earlier using the Brownian motion analogy (Eqn 3.41).

The resulting equation is an identity for any scalars that are explicit functions of mixture fraction alone, such as in the case of passive scalar mixing or in fast chemistry approximations. Unlike the earlier Brownian motion analogy, this local field similarity approximation does not constrain chemical timescales to be greater than the Kolmogorov turbulent time scale t_k. However, Klimenko's assumptions require the magnitude of conditional scalar variance $< y_i^2 \mid \eta >$ to be small in order for them to be valid. In other words, the level of similarity between the conserved and reacting scalar fields must be good.

Bilger[8,9] does not explicitly assume any such local field similarity, rather the conditional deviation terms of G_η are collected, together with deviation terms arising elsewhere in the CMC equation (see for example the final term of Eqn 3.43), into a deviational error term $< e_y \mid \eta >$. It is then assumed that the error term makes a negligible contribution to the overall CMC equation shown below.

$$< \rho \mid \eta > \frac{\partial Q_i}{\partial t} + < \rho \underline{u} \mid \eta > \cdot \nabla Q_i = < \rho w_i \mid \eta > + \frac{1}{2} < \rho \chi \mid \eta > \frac{\partial^2 Q_i}{\partial \eta^2} + < e_y \mid \eta > + < e_Q \mid \eta > \tag{3.48}$$

Note that $< e_Q \mid \eta >$ is a collection of terms involving spatial derivatives of conditional means and is assumed to be negligible at high Reynolds number. In contrast

to the assumptions of Klimenko, the assumption of $< e_y \mid \eta > \approx 0$ seems to hold even in some cases of quite large conditional variance $< y_i^2 \mid \eta >$[34]. The reason for this is as yet unclear, but Bilger[101] suggests that although the individual components of $< e_y \mid \eta >$ are significant, their net effect is small. Appropriate constraints upon the validity of Bilger's assumptions are the subject of ongoing numerical and experimental investigations[101].

3.2.3 Chemical Closure Approximations

Closure of the conditionally averaged chemical production term is achieved by assuming that $< \rho w_i \mid \eta > \approx < \rho \mid \eta > w_i(Q_1, \ldots, Q_n)$ where there are n reactive scalars. In contrast to first order chemical closure for unconditional moment methods (see section 2.2.2), this closure approximation is accurate for nonpremixed combustion, provided it is not verging on extinction[8,34,96,102,103,104,105].

Unlike Bilger's zero-$< e_y \mid \eta >$ assumption above (section 3.2.2), the chemical closure approximation definitely requires $< y_i^2 \mid \eta >$ to be small. The definition of 'small' is determined by the desired model accuracy, and the particulars of the chemical reaction rates particpating in the formation of each species. Bilger[97] has derived Taylor series expansions for mean chemical reaction rates as functions of the means and variances of the contributing reactive scalars. These expansions are useful in determining the sensitivity of mean reaction rates, that are evaluated only in terms of mean reactive scalars, to different levels of conditional variance.

In cases where conditional mean chemical production rates cannot be closed using mean values conditioned upon mixture fraction alone, closure could be affected by either conditioning upon mixture fraction and a reaction progress variable, or by employing conditional variance terms. The former method is recommended for cases where local extinction and ignition may be present, whilst the latter may be required for predicting product yields from very high activation energy reactions (such as nitric oxide formation via the Zeldovich mechanism). Klimenko[7] and Li and Bilger[106] have derived appropriate expressions for the evolution of conditional variance which have been tested for isothermal chemical reactions in grid generated turbulence[106].

Both first order doubly conditional closures and second order singly conditional closures are beyond the immediate scope of this thesis. Some comments will be made

later regarding the future development of these approaches.

3.3 Premixed Model

In premixed turbulent combustion, chemical reactants are assumed to be uniformly mixed before undergoing reaction. Instantaneous fluctuations in chemical yield result from turbulent transport between burnt and unburnt fluid. By selecting a conditioning variable which describes the instantaneous degree of reactedness, scatter caused by variation in reactedness is eliminated from the conditionally averaged statistics. A number of reaction progress variables (RPVs) can be devised for multi-species chemical systems, but the RPV that will be employed here is based on specific standardized h and sensible enthalpy h^s. The reaction progress variable c, defined below, describes the instantaneous degree of reactedness for a global reaction scheme with radiation loss[97].

$$c(\underline{x},t) \equiv \frac{\Omega(\underline{x},t) - \Omega_{unburnt}}{\Delta h^s_{ad-u}} \tag{3.49}$$

where Ω is defined by,

$$\Omega \equiv h^s - 2h \tag{3.50}$$

and Δh^s_{ad-u} is the sensible enthalpy difference between adiabatic equilibrium and unburnt conditions. It can be seen that in the absence of radiation losses, c is bounded by zero and unity since standardized enthalpy is then a conserved scalar. However, when radiation losses are present, c will vary monotonically from an unburnt state $c = 0$, to near unity for peak temperature zones, and on to $c > 1$ values for radiatively cooled burnt product zones.

The maximum possible reaction progress variable in radiatively cooled cases is reached when the burnt products have the same temperature as their surroundings. The advantage of using a reaction progress variable such as the one defined here is that it allows post flamefront formation of kinetically limited species (such as nitric oxide) to be investigated. Note that standardized h and sensible h^s enthalpies are related by the sum of the enthalpies of formation $h_{i,0}$ of the species present,

$$h \equiv h^s + \sum_{i=1}^{n} (h_{i,0} Y_i) \tag{3.51}$$

so that Ω can be more conveniently written as

$$\Omega \equiv -[h + \sum_{i=1}^{n}(h_{i,0}Y_i)] \tag{3.52}$$

Using the instantaneous equation for species mass fraction Y_i (Eqn 3.18) and the following instantaneous equation for standardized enthalpy h,

$$\rho\frac{\partial h}{\partial t} + \rho\underline{u}\cdot\nabla h = \nabla\cdot(\rho D_h \nabla h) + \rho\mathcal{S}_h \tag{3.53}$$

the instantaneous equation for the RPV c can be constructed by linear superposition according to Eqn 3.51, assuming uniform molecular diffusivity $D_i = D_h = D$.

$$\rho\frac{\partial c}{\partial t} + \rho\underline{u}\cdot\nabla c = \nabla\cdot(\rho D\nabla c) + \rho\mathcal{S}_c \tag{3.54}$$

The source term $\mathcal{S}_c$ is defined as,

$$\mathcal{S}_c \equiv \frac{-1}{\Delta h^s_{ad-u}}[\mathcal{S}_h + \sum_{i=1}^{n}(h_{i,0}w_i)] \tag{3.55}$$

As with the nonpremixed derivation of Section 3.2 , the derivation of the premixed PDF equation for c begins by introducing a function Υ which is defined in terms of a Dirac delta function below.

$$\Upsilon(\zeta, \underline{x}, t) \equiv \delta(c(\underline{x}, t) - \zeta) \tag{3.56}$$

As before (see Section 3.2), the probability density function P_ζ for the RPV is related to Υ by averaging over the ensemble of independent realizations.

$$P_\zeta(\zeta, \underline{x}, t) \equiv < \Upsilon(\zeta, \underline{x}, t) > \tag{3.57}$$

Using the properties of Dirac delta functions under differentiation (see Eqns 3.12-3.14) the following equation can be derived.

$$\rho\frac{\partial\Upsilon}{\partial t} + \rho\underline{u}\cdot\nabla\Upsilon - \nabla\cdot(\rho D\nabla\Upsilon) = -\frac{\partial}{\partial\zeta}[\Upsilon(\rho\frac{\partial c}{\partial t} + \rho\underline{u}\cdot\nabla c) - \nabla\cdot(\rho D\nabla\Upsilon) + \frac{\partial}{\partial\zeta}(\Upsilon\rho D(\nabla c)^2)] \tag{3.58}$$

Taking Eqn 3.54 into account yields,

$$\rho\frac{\partial\Upsilon}{\partial t} + \rho\underline{u}\cdot\nabla\Upsilon - \nabla\cdot(\rho D\nabla\Upsilon) = -\frac{\partial^2}{\partial\zeta^2}(\Upsilon\rho D(\nabla c)^2) - \frac{\partial}{\partial\zeta}(\Upsilon\rho\mathcal{S}_c) \tag{3.59}$$

which when averaged over the ensemble gives the PDF equation for c,

$$< \rho \mid \zeta > \frac{\partial P_\zeta}{\partial t} + < \rho \underline{u} \mid \zeta > \cdot \nabla P_\zeta = \nabla \cdot (< \rho D \quad \zeta > \nabla P_\zeta)$$
$$- \frac{\partial^2}{\partial \zeta^2}(< \rho D (\nabla c)^2 \mid \zeta > P_\zeta) - \frac{\partial}{\partial \zeta}(< \rho \mathcal{S}_c \mid \zeta > P_\zeta) \qquad (3.60)$$

In contrast to PDF equations for conserved scalars, Eqn 3.60 contains a source term in addition to convective, diffusive and dissipative terms. The RPV PDF equation is useful in determining the form and magnitude of conditionally averaged reactive scalar dissipation profiles $< \rho D(\nabla c)^2 \mid \zeta >$ given the PDFs at points of interest within the reaction system. Equation 3.60 will be employed in this capacity in subsequent chapters.

Derivation of the premixed CMC equations employs the techniques described earlier in Section 3.2, in that the joint PDF $P_{\zeta,s}$ for a reactive scalar mass fraction Y_i and reaction progress variable c is related to a function composed of two independent Dirac delta functions.

$$\varphi(\zeta, s, \underline{x}, t) \equiv \delta(Y_i(\underline{x}, t) - s)\delta(c(\underline{x}, t) - \zeta) \qquad (3.61)$$

$$P_{\zeta,s}(\zeta, s, \underline{x}, t) \equiv < \varphi(\zeta, s, \underline{x}, t) > \qquad (3.62)$$

As in Section 3.2, the joint PDF equation can be derived by forming an evolution equation for φ from the properties of Dirac delta functions, followed by averaging the equation over the ensemble of independent realizations (taking Eqns 3.18 and 3.54 into account).

$$< \rho \mid \zeta, s > \frac{\partial P_{\zeta,s}}{\partial t} + \nabla \cdot (< \rho \underline{u} \mid \zeta, s > P_{\zeta,s}) - \nabla \cdot (< \rho D \mid \zeta, s > \nabla P_{\zeta,s}) =$$
$$- \frac{\partial}{\partial s}[< \rho w_i \mid \zeta, s > P_{\zeta,s} + \frac{\partial}{\partial s}(< \rho D (\nabla Y_i)^2 \mid \zeta, s > P_{\zeta,s})$$
$$+ 2\frac{\partial}{\partial \zeta}(< \rho D (\nabla c \cdot \nabla Y_i) \mid \zeta, s > P_{\zeta,s})] - \frac{\partial}{\partial \zeta}[< \rho \mathcal{S}_c \mid \zeta, s > P_{\zeta,s}$$
$$+ \frac{\partial}{\partial \zeta}(< \rho D (\nabla c)^2 \mid \zeta, s > P_{\zeta,s})] \qquad (3.63)$$

By multiplying Eqn 3.63 through by s and then integrating both sides with respect to the reactive scalar dimension yields,

$$< \rho \mid \zeta > \frac{\partial}{\partial t}(Q_i P_\zeta) + \nabla \cdot (< \rho \underline{u} Y_i \mid \zeta > P_\zeta) - \nabla \cdot (< \rho D \mid \zeta > \nabla Q_i P_\zeta) = + < \rho w_i \mid \zeta > P_\zeta + \frac{\partial G_\zeta}{\partial \zeta} \quad (3.64)$$

where for premixed cases Q_i is the conditional average mass fraction for species i ($Q_i \equiv < Y_i \mid \zeta >$), and G_ζ is the conditional mean flux term given below.

$$G_\zeta \equiv 2 < \rho D(\nabla c \cdot \nabla Y_i) \mid \zeta > P_\zeta - \frac{\partial}{\partial \zeta}(< \rho D(\nabla c)^2 Y_i \mid \zeta > P_\zeta) - < \rho \mathcal{S}_c Y_i \mid \zeta > P_\zeta \quad (3.65)$$

Closure of the flux term G_ζ requires the decomposition suggested by Bilger[8],

$$Y_i(\underline{x}, t) \equiv Q_i(\underline{x}, t, \zeta) + y_i \quad (3.66)$$

to be substituted into Eqn 3.65 to give Eqn 3.67.

$$\begin{aligned} G_\zeta = 2 < \rho D(\nabla c)^2 \mid \zeta > \frac{\partial}{\partial \zeta}(Q_i P_\zeta) - \frac{\partial}{\partial \zeta}(< \rho D(\nabla c)^2 \mid \zeta > Q_i P_\zeta) - < \rho \mathcal{S}_c \mid \zeta > Q_i P_\zeta \\ + 2 < \rho D(\nabla c \cdot \nabla y_i) \mid \zeta > \frac{\partial P_\zeta}{\partial \zeta} - \frac{\partial}{\partial \zeta}(< \rho D(\nabla c)^2 y_i \mid \zeta > P_\zeta) \\ - < \rho \mathcal{S}_c y_i \mid \zeta > P_\zeta + 2 < \rho(\nabla c \cdot \nabla Q_i) \mid \zeta > P_\zeta. \end{aligned} \quad (3.67)$$

After substituting Eqn 3.67 into Eqn 3.64, whilst taking account of Eqn 3.60, the following is obtained:

$$\begin{aligned} < \rho \mid \zeta > \frac{\partial Q_i}{\partial t} + < \rho \underline{u} \mid \zeta > \cdot \nabla Q_i = < \rho w_i \mid \zeta > \\ + < \rho D(\nabla c)^2 \mid \zeta > \frac{\partial^2 Q_i}{\partial \zeta^2} - < \rho \mathcal{S}_c \mid \zeta > \frac{\partial Q_i}{\partial \zeta} \\ + < e_y \mid \zeta > + < e_Q \mid \zeta > \end{aligned} \quad (3.68)$$

Where all terms containing y_i are collected within the deviational group $< e_y \mid \zeta >$.

$$< e_y \mid \zeta > \equiv \frac{1}{P_\zeta}[2 < \rho D(\nabla c \cdot \nabla y_i) \mid \zeta > \frac{\partial P_\zeta}{\partial \zeta} - \frac{\partial}{\partial \zeta}(< \rho D(\nabla c)^2 y_i \mid \zeta > P_\zeta) - \nabla \cdot (< \rho \underline{u} y_i \mid \zeta > P_\zeta)] - < \rho \mathcal{S}_c y_i \mid \zeta > \quad (3.69)$$

and $< e_Q \mid \zeta >$ contains the unclosed Q_i term from Eqn 3.67,

$$< e_Q \mid \zeta > \equiv < \rho(\nabla c \cdot \nabla Q_i) \mid \zeta > + \nabla \cdot (< \rho D \mid \zeta > \nabla Q_i P_\zeta) \quad (3.70)$$

The equations which must be derived for conditional mean standardized enthalpy Q_h are analogous to the equations given above for conditionally averaged species mass

fractions Q_i, except that the source term $\mathcal{S}_h$ describes a rate of energy loss instead of a chemical production rate w_i. The conditional mean reactive scalar equations given above for premixed combustion are essentially identical to those derived earlier by Bilger[8], and by Mantel and Bilger[107].

3.3.1 Closure Approximations

Closure of the conditionally averaged source terms within Eqn 3.68 is achieved by evaluating the relevant instantaneous expressions in terms of conditionally averaged reactive scalar values. This is analogous to the chemical closure described for the nonpremixed CMC equations (see section 3.2.3), and is likewise subject to the constraint that conditional variances $< y_i^2 \mid \zeta >$ be small. Bilger[97] defines 'small' as meaning that the effect of conditional variance terms, in the Taylor series expansions of any participating chemical reactions, is within arbitrary tolerances.

Compared to the equivalent nonpremixed conditional moment closure equation (Eqn 3.48), the magnitudes of the various terms of Eqns 3.68, 3.69 are not well known. It appears that the premixed CMC equation is no better suited to modelling general cases of turbulent premixed combustion than other methods, since the difficulty in modelling flame surface effects (see section 2.3) is manifested in determining accurate closures for $< e_y \mid \zeta >$ terms. Closure of the final two terms on the right hand side of Eqn 3.69 seems very difficult since velocity-RPV and RPV-source term correlations will depend on flame front proximity and topology. The same can be said for determining accurate values of conditional mean reactive scalar dissipation $< \rho D(\nabla c)^2 \mid \zeta >$ at points in physical space.

However, it is possible to develop the CMC model for a restricted class of turbulent premixed combustion problems where the spatial dependence of various terms is assumed to be small. By either assuming there is no dependence[97] or by volume averaging to get approximate values, it should be possible to gain useful information regarding chemical outputs without having to predict turbulent flame front dynamics. Bilger[97] suggests that a valid regime for this approximation exists for one dimensional flame zones at high Reynolds number but with moderate Damkohler number (≈ 3). In this investigation, a steady state turbulent premixed reactor model is proposed. Averaged conditional mixing statistics are determined from volume averaged

forms of Eqn 3.60, given that inlet and outlet area averaged RPV PDFs and reactor residence times are known. This reactor model can be thought of as a turbulent premixed generalization of the well known Perfectly Stirred Reactor (PSR), which was originally used in the study of chemical kinetics[108]. Under similar reactor assumptions but using different modelling methods, useful results have been obtained for simulated lean-premixed gas turbine combustor systems[92,93]. The further simplification of CMC equations for the specific case of a PTURCEL (*P*remixed *TU*rbulent *R*eactor *C*alculation with *E*nergy *L*oss) is delayed to Chapter 8.

3.4 Summary

In this chapter, Conditional Moment Closure equations have been derived for both nonpremixed and premixed turbulent combustion. The basic concept behind CMC methods is to reduce the variance of conditionally averaged statistics as much as possible through the judicious choice of as few conditional statements as possible. Since each additional conditional statement increases the problem dimensionality by one, it is important to choose conditioning variables appropriate to each case under investigation.

For nonpremixed combustion without extinction, conditioning upon mixture fraction alone is usually sufficient to reduce conditional variances so that first order closure of chemical reaction terms is accurate. Although the resultant CMC equations are identical, Bilger[8,9] and Klimenko[6,7] employ different closure assumptions in their derivation. Klimenko's Brownian motion analogy is strictly applicable to cases where the turbulence is locally isotropic and all scalars have chemical timescales longer than the Kolmogorov timescale of the turbulence. This method does not require there to be any similarity between reactive and conserved scalar mixing fields. Bilger's closure method does not explicitly require any similarity to be present despite being derived along similar lines to Klimenko's second closure method which does require local similarity. Numerical experiments have borne out the ability of Bilger's derivation to function in situations where there is minimal local similarity. The reason behind this ability is the subject of ongoing investigation.

A general turbulent premixed combustion model has been derived using a CMC

methodology similar to that used for nonpremixed combustion. In contrast to the nonpremixed CMC derivation, the premixed case is much more difficult to close, with a number of terms being very strongly dependent on unknown turbulent flame front dynamics. Development of this model is currently limited to the special case of a steady premixed turbulent reactor where conditional mean reactive scalars are spatially independent. This case will be addressed in Chapter 8.

In addition to the CMC equations, probability density function equations have been given for the appropriate conditioning variables in each case, namely mixture fraction ξ and reaction progress variable c. These latter equations have an important part to play in that they can be used to determine the conditionally averaged mixing statistics required by each set of CMC equations.

Chapter 4

Imperfectly Stirred Reactors

In this chapter, the CMC method is applied to the specific case of steady turbulent nonpremixed reactors. These Imperfectly Stirred Reactors (ISRs) are characterised as reaction zones where conditionally averaged reactive scalars are not dependent on spatial position or time. An ISR can be viewed as a nonpremixed generalisation of the better known PSR (Perfectly Stirred Reactor), and is naturally suited to steady state reactor modelling applications where there is significant reactant unmixedness.

Perfectly stirred reactors originally arose in the course of study of chemical kinetics. Based on experimental devices such as continously-stirred-flow tank reactors these PSR models emulate steady chemical reactions occuring in a contained volume where, ideally, reactants are uniformly mixed before entering the reactor[108]. Perfectly stirred reactor methods have been used in various circumstances to model carbon monoxide (CO) levels in methane flames[109], reactions in turbulent shear layers[110,111], core zones of turbulent jet diffusion flames[112], pollutant formation within internal combustion engines[113], and emissions from gas-turbine-like combustors[114,115], to name but a few.

In many cases these PSR models have been applied to essentially nonpremixed combustion processes with the rationale, that for the region under investigation, the reactants are very well mixed[110,111,112,115]. The degree of mixedness prior to reaction is not certain, and at best these applications of PSR methods are only rough approximations. Residual turbulent mixing of the reactants as the reaction progresses has a substantial effect on chemical yield, as mixing and reaction processes can be coupled. A simple model is required for cases where reactants are not perfectly mixed

so that these turbulence-chemistry interactions can be accounted for.

Recently, a class of Partially Stirred Reactor (PaSR) models have been developed for premixed[92,93,94] and nonpremixed[116] combustion applications. These methods involve stochastic PaSR simulations where solutions are determined through the evolution of the reactive scalar joint probability density function (PDF), via Monte Carlo techniques. Whilst these methods have yielded promising results, they are computationally intensive[93], and incorporate the traditional difficulties encountered when modelling molecular transport in joint PDF methods[116] (see also Section 2.2.2).

By employing an ISR (CMC) method, complex chemical systems can be modelled at a small fraction of the computational cost incurred by the PaSR approach, and much of the difficulty involved in modelling molecular transport is obviated. The CMC equations derived for ISR applications are the simplest of all nonpremixed applications, and serve as an ideal testbed for the development of submodels and implementation strategies for use with more complicated applications.

The remainder of this chapter is sectioned as follows. Section 4.1 contains the derivation of the ISR equations from the general CMC equations of Section 3.2. Section 4.2 analyzes the conditional mixing statistics of the ISR model, and the following section (4.3) discusses these statistics in connection with model applicability to combustion systems of practical interest. In the following chapter, the results of parametric studies of the ISR model are presented for both hydrogen and methane combustion systems. Some discussion of ISR behaviour and applications is delayed to the end of Chapter 5, following the presentation of the study findings.

4.1 ISR Equation Derivation

For the purposes of this analysis, an Imperfectly Stirred Reactor (ISR) is conceptualized as being a volume (V) of statistically stationary turbulent mixing where all reactive scalar statistics, averaged conditonally upon mixture fraction, are spatially independent. The mixture fraction field may not be homogeneous however, and the conditionally averaged reactive scalar profiles at the reactor inlet ($Q_{i,0}(\eta)$) are not necessarily the same as those elsewhere in the reactor ($Q_i(\eta)$). Streams of fuel and

oxidizer are introduced to the ISR through an inlet area or areas (A_{in}) and mixed products are removed via an outlet area or areas (A_{out}). The possibility of partial mixing of fuel and oxidizer prior to entering the ISR is not ruled out and will be discussed at a later stage of the derivation.

Following the derivation of the preceding chapter, the ISR equations are most easily produced by operating upon the nonpremixed CMC equation that retains explicit reference to the mixture fraction PDF (Eqn 3.42). By integrating Eqn 3.42 across the core volume V for stationary turbulence, and making use of the divergence theorem, the following equation results.

$$A_{out}\{< \rho \underline{u} \mid \eta > P_\eta Q_i\}_{outlet} - A_{in}\{< \rho \underline{u} \mid \eta > P_\eta Q_{i,0}\}_{inlet} =$$
$$V\{\{P_\eta(< \rho w_i \mid \eta > + \tfrac{1}{2} < \rho\chi \mid \eta > \tfrac{\partial^2 Q_i}{\partial \eta^2}) - \tfrac{1}{2} Q_i \tfrac{\partial^2}{\partial \eta^2}(< \rho\chi \mid \eta > P_\eta)\}\} \quad (4.1)$$

In Eqn. (4.1), single braces represent quantities averaged over inlet or outlet areas A_{in}, A_{out} of the reactor and double braces represent quantities averaged over the volume V of the reactor.

$$\{\underline{X}\} \equiv \frac{1}{A}\int_A \underline{X} \cdot \underline{dA} \quad (4.2)$$

$$\{\{X\}\} \equiv \frac{1}{V}\int_V X dV \quad (4.3)$$

The averaged evolution equation (Eqn 4.1) can be simplified given the definition of an ISR, which states that all conditional reactive scalar statistics are uniform within the ISR.

$$Q_i A_{out}\{< \rho \underline{u} \mid \eta > P_\eta\}_{outlet} - Q_{i,0} A_{in}\{< \rho \underline{u} \mid \eta > P_\eta\}_{inlet} =$$
$$V[\{\{P_\eta\}\} < \rho w_i \mid \eta > + \tfrac{1}{2}\{\{P_\eta < \rho\chi \mid \eta >\}\}\tfrac{\partial^2 Q_i}{\partial \eta^2} - \tfrac{1}{2} Q_i \tfrac{\partial^2}{\partial \eta^2}\{\{< \rho\chi \mid \eta > P_\eta\}\}] \quad (4.4)$$

Volume averaging of the conditionally averaged conservation equation for the PDF of mixture fraction (Eqn 3.16), in conjunction with the divergence theorem yields,

$$A_{out}\{< \rho \underline{u} \mid \eta > P_\eta\}_{outlet} - A_{in}\{< \rho \underline{u} \mid \eta > P_\eta\}_{inlet} = -\frac{1}{2} V\{\{\frac{\partial^2}{\partial \eta^2}(< \rho\chi \mid \eta > P_\eta\}\} \quad (4.5)$$

Given that there is no variation of conditional means across the inlet and outlet area(s) and throughout the reactor core, the above result can be used to further simplify Eqn 4.4.

$$(Q_i - Q_{i,0})\frac{\{P^*_\eta\}_{inlet}}{\tau_r} = \frac{\{\{P_\eta\}\}}{\{\{\rho\}\}}[< \rho w_i \mid \eta > + \frac{1}{2}\{\{< \rho\chi \mid \eta >\}\}\frac{\partial^2 Q_i}{\partial \eta^2}] \tag{4.6}$$

The symbol $\{P^*_\eta\}$ denotes a mass flow rate weighted mixture fraction PDF defined by,

$$\{P^*_\eta\} \equiv \frac{A}{\dot{m}}\{P_\eta < \rho\underline{u} \mid \eta >\} \tag{4.7}$$

$\dot{m}$ is the total mass flow rate through the reactor, and the reactor residence time τ_r is given by,

$$\tau_r \equiv \frac{\{\{\rho\}\}V}{\dot{m}} \tag{4.8}$$

Since the mean density $\{\{\rho\}\}$ is not known *a priori*, it is initially estimated from chemical equilibrium data, and then updated as the solution converges towards the steady state. The estimated value of mean density changes by only a small fraction during the course of computation.

The boundary conditions on Q_i, in Eqn 4.6, are that it is equal to the pure fuel and oxidizer values for $(\eta = 1, 0)$, and all source and scalar transport terms are zero at these bounds. As was indicated in Section 3.2.3, closure of the chemical production rate term $< w_i \mid \eta >$ is achieved by evaluating the instantaneous Arhenius rate expressions in terms of conditionally averaged reactive species and temperature. The corresponding equation for the evolution of conditional mean standardized enthalpy Q_h can be seen to be,

$$(Q_h - Q_{h,0})\frac{\{P^*_\eta\}_{inlet}}{\tau_r} = \frac{\{\{P_\eta\}\}}{\{\{\rho\}\}}[< \rho\mathcal{S}_h \mid \eta > + \frac{1}{2}\{\{< \rho\chi \mid \eta >\}\}\frac{\partial^2 Q_h}{\partial \eta^2}] \tag{4.9}$$

where the source term $< \rho\mathcal{S}_h \mid \eta >$ is a conditional mean rate of radiative energy loss. This term is also evaluated using conditional mean reactive scalar values.

It is clear from Eqn 4.5, that the evolution of the mixture fraction PDF from inlet to outlet of the ISR determines the magnitude and form of the core averaged conditional mean scalar dissipation rate $\{\{< \rho\chi \mid \eta >\}\}$.

$$\{\{< \rho\chi \mid \eta >\}\} = -\frac{2}{\tau_r}\frac{\{\{\rho\}\}}{\{\{P_\eta\}\}}[\int_0^\eta \int_0^{\eta'} \{P^*_{\eta''}\}_{outlet} - \{P^*_{\eta''}\}_{inlet} d\eta'' d\eta'] \tag{4.10}$$

The bounding conditions used in Eqn 4.10 are that $\{\{< \rho\chi \mid \eta >\}\} = 0$ at $\eta = 0, 1$. Note that this equation is overdetermined in that the slopes of $\{\{< \rho\chi \mid \eta >\}\}$ are also supposed to be zero at the bounds[117]. It is considered more important to insure zero bounding values rather than zero bounding slopes of $\{\{< \rho\chi \mid \eta >\}\}$.

If the PDFs include end intermittencies, that is delta function contributions at $\eta = 0, 1$, then it is not possible to ensure both zero value and zero slope boundary conditions. For PDFs with end intermittencies, Eqn 4.10 must have an additional right hand side term ($C_1(\eta)$) appended that is equal to the difference between the $\eta = 0$ intermittencies (γ_0) integrated across mixture fraction space.

$$C_1(\eta) \equiv -\frac{2}{\tau_r}\frac{\{\{\rho\}\}}{\{\{P_\eta\}\}}[\{\gamma_0^*\}_{outlet} - \{\gamma_0^*\}_{inlet}]\eta \tag{4.11}$$

It can be seen from Eqn 4.6 that the form of the inlet weighted PDF of mixture fraction determines the significance of the conditional mean difference in reactive scalar values across the reactor. For regions of mixture fraction space where the inlet PDF is zero, the conditional mean difference term has no influence on the solution. Only those portions of the inlet conditional mean reactive scalar profiles, where the inlet PDF is nonzero, need be specified. In the limiting case of pure fuel and oxidizer input streams to the ISR, the inlet PDF takes on the following form.

$$\{P_\eta^*\}_{inlet} = (1 - \overline{\xi})\delta(\eta) + \overline{\xi}\delta(1 - \eta) \tag{4.12}$$

where $\overline{\xi}$ is the mean mixture fraction and is determined by the oxidizer mass flow rate $\dot{m}_{ox}$ and the fuel mass flow rate $\dot{m}_{fu}$ (which sum to give the total mass flow rate $\dot{m}$) as follows:

$$\overline{\xi} = (1 + \frac{\dot{m}_{ox}}{\dot{m}_{fu}})^{-1} \tag{4.13}$$

In these instances, the inlet conditional mean reactive scalar profile need not be specified at all for non-bounding values of mixture fraction. The following CMC equations apply in this case for non-bounding mixture fractions,

$$< \rho w_i \mid \eta > + \frac{1}{2}\{\{< \rho\chi \mid \eta >\}\}\frac{\partial^2 Q_i}{\partial \eta^2} = 0 \tag{4.14}$$

$$< \rho \mathcal{S}_h \mid \eta > + \frac{1}{2}\{\{< \rho\chi \mid \eta >\}\}\frac{\partial^2 Q_h}{\partial \eta^2} = 0 \tag{4.15}$$

where the conditional mean scalar dissipation is determined by the following.

$$\{\{< \rho\chi \mid \eta >\}\} = \frac{2}{\tau_r}\frac{\{\{\rho\}\}}{\{\{P_\eta\}\}}[(1 - \bar{\xi})\eta - \int_0^\eta \int_0^{\eta'} \{P_{\eta''}^*\}_{outlet} d\eta'' d\eta'] \tag{4.16}$$

The governing reactive scalar equations for the pure-inlet ISR (Eqns 4.14, 4.15) bear a remarkable resemblance to the steady equations used to model turbulent flames burning in a flamelet regime. Given this resemblance, it is plausible to expect there to be applicability constraints on the pure-inlet ISR equations that are akin to those relating to flamelet models[28]. This seems to be the case, it will be seen later that one of the constraints on usage of the above equations is that conditional mean scalar dissipation must not exhibit such spatial dependence so as to cause large spatial dependence in the conditionally averaged reactive scalar fields. This is somewhat analogous to the definition of the flamelet regime in turbulent combustion, where scalar dissipation within the width of the flamelet reaction zone must be approximately uniform (see Section 2.2.1).

Wherever the conditional mean reactive scalar fields exhibit substantial spatial dependence, the ISR model cannot be used with confidence. Examples of systems where this spatial dependence probably exists include those with very strong spatial variations in conditional mean scalar dissipation rates and those with significant spatial flow development. In either of these exceptional cases, the ISR method may still be applied as a rough approximation.

A more accurate means of treating a reactor system with strong spatial dependence is to arbitrarily partition the reactor into spatially uniform zones and treat each zone with its own ISR. In this way, output statistics from pure-inlet ISR calculations or measurements, are passed as inlet parameters to subsequent calculations (using Eqns 4.6, 4.9 and 4.10) in the ISR 'chain'. Interconnected zone modelling of a similar type, using PSRs, has been applied in the past to gas turbine combustors[114,115] and spark ignition engines[113].

Whether it is used in a chain or individually, the maximum departure from spatial homogeneity that can be tolerated within an ISR calculation is difficult to quantify in a generic sense. This issue will be discussed in the following sections.

Aside from spatial independence constraints, the use of singly conditioned CMC methods in the ISR implementation limit the model to cases where the combustion system is devoid of extinction behaviour (see Section 3.2.3). The similarity between Eqn 4.14 and laminar flamelet equations, allows extinction conditions for the latter to be used as a guide to the extinction conditions for the pure-inlet ISR model. Impor-

tant differences between the ISR and flamelet equations, such as different treatment of molecular diffusivity and different scalar dissipation profiles, cloud this analogy to some extent.

4.2 Analysis of Mixing Statistics

The mixing behaviour of the ISR model is determined by four inputs, namely the weighted mixture fraction probability density functions at the reactor inlet $\{P_\eta^*\}_{inlet}$ and outlet $\{P_\eta^*\}_{outlet}$, the core averaged PDF $\{\{P_\eta\}\}$, and the residence time of the reactor. Whilst the former three determine both the magnitude and shape of the conditional mean scalar dissipation profile within the reactor, the latter merely influences the magnitude of the scalar dissipation.

To illustrate the effects of inlet-outlet PDF form on conditional mean scalar mixing, as dictated by Eqn 4.10, it is useful to introduce the nondimensional variable R,

$$R(\eta) \equiv \{\{<\rho\chi \mid \eta>\}\}\frac{\{\{P_\eta\}\}\tau_r}{2\{\{\rho\}\}\sigma_m^2} = -\frac{1}{\sigma_m^2}[\int_0^\eta \int_0^{\eta'} \{P_{\eta''}^*\}_{outlet} - \{P_\eta^*\}_{inlet} d\eta'' d\eta'] \quad (4.17)$$

where σ_m^2 is a scaling factor equal to the maximum mixture fraction variance $\overline{\xi}(1-\overline{\xi})$. It can be seen that when $R(\eta)$ is integrated across the width of mixture fraction space, the result is identically equal to to the fractional change in mixture fraction variance through the reactor. Thus the variable $R(\eta)$ can be thought of as the conditional mean contribution at η to this fractional decrement in variance. In this form, the conditional mean variance decrement $R(\eta)$ henceforth simply referred to as variance decrement, does not include the effects of the core averaged PDF or reactor residence time.

In Figure 4.1, variance decrement profiles are plotted in mixture fraction space for a variety of inlet and outlet PDF combinations. In the figure, the inlet and outlet PDFs have a clipped Gaussian form and a mean mixture fraction of $\overline{\xi} = 0.028$ (corresponding to the stoichiometric mixture fraction for hydrogen combustion in air). There is no need to use assumed form PDFs in practice, instead it is more likely that PDFs will be derived from measurement or computational fluid dynamics (CFD) calculations. However, for the generic cases studied here clipped Gaussian PDFs are an appropriate representation. The mixture fraction PDFs used in Fig.

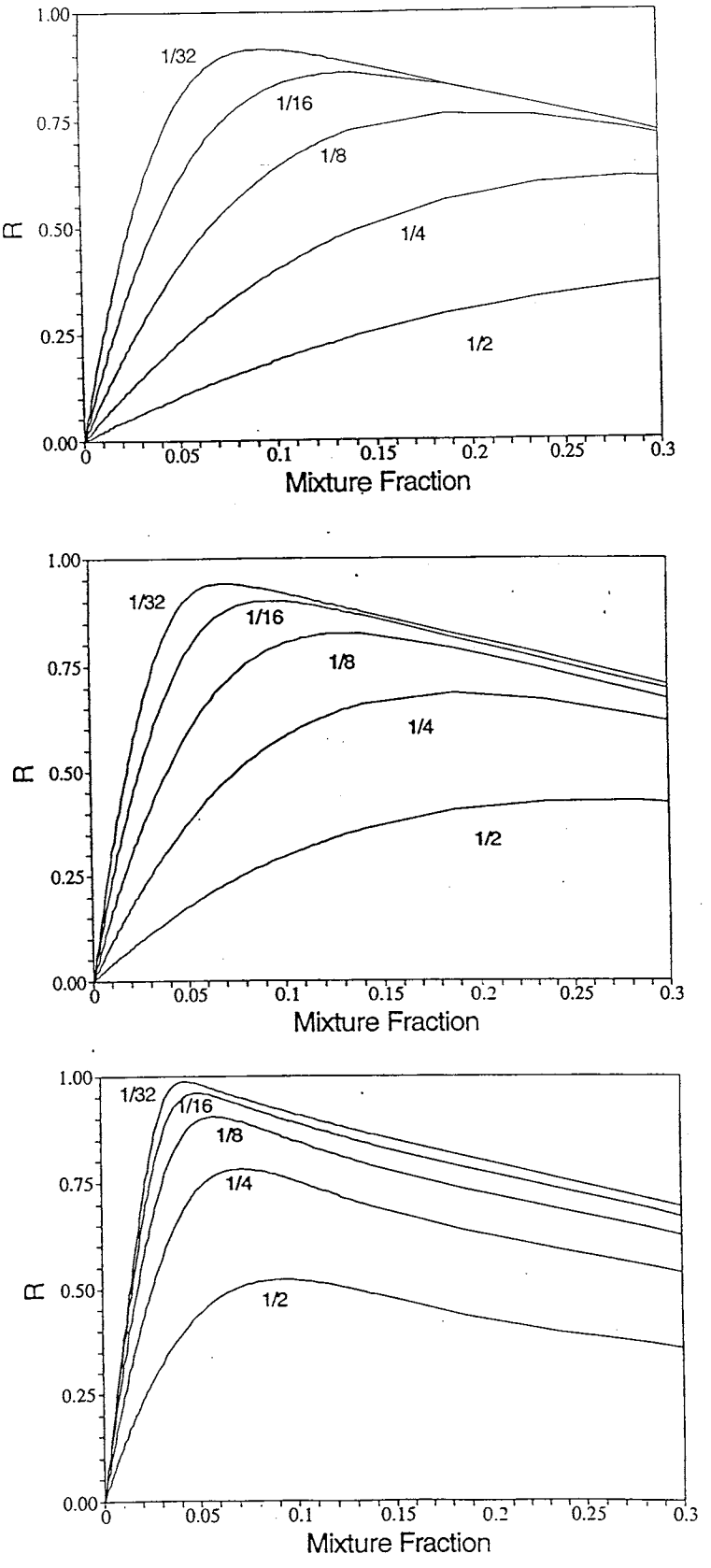

Figure 4.1: Conditional mean variance decrement $R(\eta)$ versus mixture fraction for different inlet-outlet PDF combinations. In each case annotations denote outlet unmixedness as a fraction of inlet unmixedness where the inlet unmixednesses are for each part: a) $\mho = 1.0$, b) $\mho = 0.5$, c) $\mho = 0.1$

4.1 are described in terms of their unmixedness, where unmixedness $\mho$ is defined below.

$$\mho \equiv \frac{\{\bar{\xi''^2}\}}{\sigma_m^2} \tag{4.18}$$

Unmixedness can be seen to be the ratio of actual variance to maximum possible variance, and thus is bounded by zero and unity.

From Fig. 4.1 it is evident that irrespective of inlet unmixedness, decreasing levels of outlet unmixedness cause the peak of the variance decrement profile to increase in value and shift in mixture fraction space from rich zones towards the mean mixture fraction. For the pure-inlet case (inlet $\mho = 1.0$) the variance decrement profile asymptotically approaches a triangular shape with its upper vertex located at $R(\eta) = 1.0$ and $\eta = \bar{\xi}$, as the outlet unmixedness tends to zero[103]. In all cases the integral under the $R(\eta)$ profile is equal to the fractional decrease in mixture fraction variance between the inlet and outlet of the ISR. Decreasing levels of inlet unmixedness tend to shift the locations of the profile peaks closer towards the mean mixture fraction and the increase peak values.

The form of the conditional mean scalar dissipation profile is also influenced by the core averaged mixture fraction PDF. The core averaged PDF must necessarily have a variance that lies between the values of the inlet and outlet mixture fraction variances. The influence of the core averaged mixture fraction PDF $\{\{P_\eta\}\}$ upon conditional mean scalar dissipation can be seen in Fig. 4.2, for cases corresponding to the same inlet-outlet PDF combinations as in Fig. 4.1.

In Fig. 4.2, the conditional mean scalar dissipation profiles have been calculated using core averaged clipped Gaussian PDFs with core averaged means and variances that are equal to the outlet means and variances in each case. There is no requirement for these variances to be equal, and in the presence of strong recirculation the core variance can be substantially greater than the outlet variance.

Furthermore, despite the simple clipped Gaussian PDFs used in this analysis the form of the core averaged PDF can be very much different with higher valued tails, shifted mean values, multiple-modality and so on. Future ISR investigations will determine the form of typical core averaged PDFs determined from experimental measurement and CFD calculation in laboratory and industrial reactors. Indeed, tailoring core averaged PDFs in real reactors to match the optimum form determined

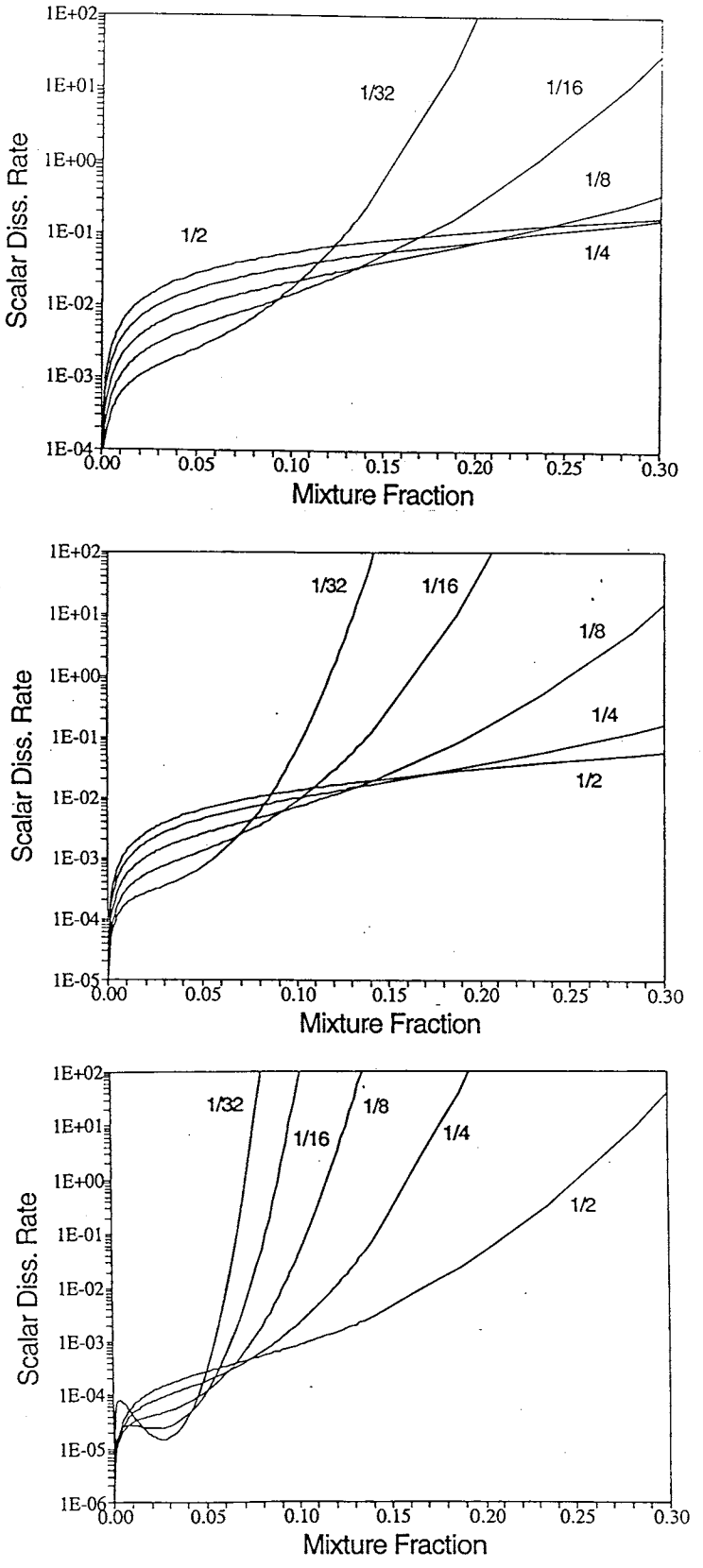

Figure 4.2: Conditional mean scalar dissipation rate versus mixture fraction for a residence time of one second. Cases and annotation are the same as for Fig. 4.1

from ISR calculations may prove useful in practical design and modification processes.

Due to the exceedingly small values that can occur in the core averaged PDFs, the resultant $\{\{<\rho\chi \mid \eta>\}\}$ values can be very large indeed. however at all points in mixture fraction space the profiles remain finite and furthermore are identically zero at $\eta = 0, 1$. The general behaviour of conditional mean scalar dissipation and R-like functions are discussed at length by Klimenko and Bilger[117].

The conditional mean scalar dissipation profiles of Fig. 4.2 all have the same basic form. In contrast with the variance decrement profile variations of Fig. 4.1, variations in the core averaged PDF can cause scalar dissipation changes of many orders of magnitude. Increasingly mono-modal core averaged PDFs give rise to the observed high valued zones in the scalar dissipation profiles at low probability mixture fractions. It can be seen that scalar dissipation variation with mixture fraction is relatively small in zones with similarly high probabilities.

In general, increased fractional reduction in unmixedness through an ISR leads to a reduction in the width of the scalar dissipation plateau in high probability mixture fraction space, and a decrease in the magnitude of scalar dissipation upon the plateau. Agreement to within an order of magnitude is found between different inlet PDF cases with the same core averaged PDF (see for example. 1/4 curve for $\mho = 1.0$ case and 1/2 curve for $\mho = 0.5$ case), again indicating the dominant role of the core averaged PDF in determining $\{\{<\rho\chi \mid \eta>\}\}$.

In a sense, the inlet PDF unmixedness influences the core averaged PDF unmixedness in that the core averaged variance is constrained to be less than or equal to the inlet averaged variance. This constraint is manifested in Fig. 4.2 for the $\mho = 0.1$ case where the low variance core averaged PDFs lead to particularly narrow and low valued scalar dissipation plateaux. In the 1/32 reduction curve for the $\mho = 0.1$ case, the influence of the core PDF peak shifting to the mean mixture fraction is evident from the formation of a scalar dissipation trough.

From the definitions for the averaged PDFs given in Section 4.1 it is clear that the core averaged PDF $\{\{P_\eta\}\}$ is not constrained to have the same mean value as the inlet and outlet PDFs. Indeed its structure will typically be quite different since unlike the other two PDFs it is not weighted by mass flow rate. If the assumption that conditional mean mass flow rate is uniform across mixture fraction space, is

abandoned then it is difficult to predict what kind of variations might be encountered in practice. This difficulty arises from the fact that the conditional mean mass flow rate depends both upon the conditional mean mass flux ($< \rho u \mid \eta >$), and the conditional mean area through which the flux passes.

A rationale for the assumption of a uniform mass flow rate profile, is that decreases in density resulting from heat release are accompanied by corresponding increases in conditional mean flux area with little or no changes to conditional mean velocity. In practical applications of ISR modelling, these questions of the influence of mass flow rate weighting will be resolved through experimental measurement or supplementary CFD calculations. A parametric study of the influences, upon conditional mean scalar dissipation, of using core averaged and area averaged (mass flow rate weighted) PDFs of different form is planned in the near future.

4.3 Model Applicability

In section 4.1, the constraints on the validity of the ISR model were stated, namely that the conditional mean reactive scalar fields should not depend on location or time. It was further stated that in order to effect a first order closure of chemical source terms using a CMC method, conditionally averaged reactive scalar variances should be small (see Section 3.2.3). Thus reactors displaying extinction and ignition behaviour must be precluded from the ISR analyses presented here.

Reactors with substantial flow development from inlet to outlet, such as where there is minimal fluid recirculation, are prone to display significant conditional mean reactive scalar dependence on position. If this is the case, a single ISR is an inappropriate model. It is difficult to conceive of a physical reactor where a decrease in unmixedness $\mho$ of more than an order of magnitude can be present from inlet to outlet without there necessarily being substantial flow development. Consequently, it is perhaps unrealistic to expect that scalar dissipation profiles like those in Fig. 4.2 corresponding to large unmixedness reductions (eg: 1/32 reduction example) will be encountered in practice. Rather it is more appropriate that large unmixedness reductions in steady nonpremixed reactors be treated by ISR chains, where each calculation in the chain accounts for a more modest $\mho$ reduction.

An effective means of testing the validity of applying an ISR model to a zone within a target reactor, is to ensure that core averaged statistics are not unduly sensitive to the location of the physical boundaries of the zone. If, for example, outward advancement of zone boundaries in physical space over small distances lead to a proportional increase in the core averaged mixture fraction variance, then a single ISR is probably not the best method for modelling the target zone. In this example the zone should be subdivided and treated with chained ISRs. If a zone cannot be effectively subdivided to provide adequate spatial independence for reactive scalar statistics, then another model should be chosen which reflects the influence of flow development.

One of the principal advantages of employing volume averaged models, such as ISRs and PSRs, over methods with higher spatial dimensionality is that they are capable of utilizing much more detailed chemical mechanisms to describe the target process. In many instances, the advantage gained from enhanced chemical detail more than compensates for inaccuracies arising from approximations relating to the flow field[103,115].

Chapter 5

ISR Parametric Study

This chapter is a presentation of results derived from a parametric study of the Imperfectly Stirred Reactor (ISR) model proposed in the preceding chapter. In the absence of comprehensive experimental data relating to turbulent combustion in steady reactors of practical interest[93,116], a parametric study of ISR performance is required for conditions that are commensurate with practical reactors. Impending investigations are intended to involve joint ISR and laboratory analyses of nonpremixed combustors[118].

The parametric study presented here was undertaken in two parts. The first part dealt with testing simple hydrogen-air combustion systems over a wide range of operating conditions (see Section 5.1). The second part (Section 5.2) involved simulating the primary recirculation zone of a practical gas turbine combustor burning methane in air, to investigate the importance of chemical mechanism detail. A general discussion of the study findings can be found in Section 5.3.

5.1 Hydrogen Calculations

A series of adiabatic ISR calculations were made for the mixing cases examined in Section 4.2 to determine the effect of these mixing conditions upon the relatively simple hydrogen-air chemical system. Aside from varying inlet, outlet and core averaged unmixednesses, the influence of varying reactor residence time was also investigated. The full list of specifications for the H_2 test cases is given in Table 5.1. In all cases, the overall equivalence ratio of the ISR was unity. Hydrogen combustion calculations

Designation	*Residence Time (ms)*	*Outlet Unmixedness*	*Inlet Unmixedness*	*Mean Scalar Dissipation* (s^{-1})
H1	100	0.5	1.0	0.14
H2	50	0.5	1.0	0.27
H3	25	0.5	1.0	0.55
H4	12.5	0.5	1.0	1.1
H5	6.25	0.5	1.0	2.2
H6	3.125	0.5	1.0	4.4
H7	1.5625	0.5	1.0	8.8
H8	0.78125	0.5	1.0	18
H9	100	0.25	1.0	0.21
H10	50	0.25	1.0	0.41
H11	25	0.25	1.0	0.82
H12	12.5	0.25	1.0	1.6
H13	6.25	0.25	1.0	3.3
H14	3.125	0.25	1.0	6.6
H15	1.5625	0.25	1.0	13
H16	0.78125	0.25	1.0	26
H17	100	0.125	1.0	0.24
H18	50	0.125	1.0	0.48
H19	25	0.125	1.0	0.96
H20	12.5	0.125	1.0	1.9
H21	6.25	0.125	1.0	3.8
H22	3.125	0.125	1.0	7.7
H23	1.5625	0.125	1.0	15
H24	0.78125	0.125	1.0	31
H33	100	0.25	0.5	0.068
H34	50	0.25	0.5	0.14
H35	25	0.25	0.5	0.27
H36	12.5	0.25	0.5	0.55
H37	6.25	0.25	0.5	1.1
H38	3.125	0.25	0.5	2.2
H39	100	0.125	0.5	0.10
H40	50	0.125	0.5	0.21
H41	25	0.125	0.5	0.41
H42	12.5	0.125	0.5	0.82
H43	6.25	0.125	0.5	1.6
H44	3.125	0.125	0.5	3.3
H45	1.5625	0.125	0.5	6.6

Table 5.1: Hydrogen ISR Calculations at $p = 1atm$ and $T_{inlet} = 300K$

were made using a chemical mechanism consisting of 12 species and 25 elementary reaction steps. The mechanism is listed in Table A.1 (Appendix A) as reactions $1-17$ and $28-34$. It contains the non-carbon steps of a skeletal methane mechanism used in subsequent methane calculations, and includes thermal NO formation pathways. The hydrogen mechanism originates from Warnatz[120], and has been used successfully a number of times in the past[96,102,103,104] for modelling turbulent nonpremixed hydrogen combustion. Thermo-chemical data and reaction rate calculations were provided by CHEMKIN-II subroutines[121] and the two point boundary value problem (Eqn 4.6) was solved using the TWOPNT subroutine developed by Kee *et al* [122]. Typical computation times using this simple 25 step mechanism were of the order of $6-10$ CPU seconds on a $\sim 15 Mflop$ DEC Alpha workstation. A listing of the ISR code (FIREBALL) can be found in Appendix C.

5.1.1 Chemical Response to Turbulent Mixing

In order to understand and interpret the results of this parametric study, it is appropriate at this point to briefly describe the typical behaviour of nonpremixed combustion systems in the presence of turbulent mixing.

Small scale turbulent mixing processes simultaneously transport fresh reactant to reactant deficient zones and product species away from zones with high product concentrations. Under intense mixing conditions, these transport processes can impede reaction progress by swamping the reaction zone with an influx of cold reactants, while rapidly dispersing the reaction-sustaining exothermic products and intermediate species into less reactive surroundings.

Increased mixing rates lead to smaller proportions of the transported fluid taking part in the chemistry as it is mixed through the reaction zone. Where the rate of mixing is comparable to a particular characteristic chemical reaction rate, that reaction will have insufficient time to progress to completion before the fluid is removed from the reaction zone.

The pool of principal radical species (H,O,OH) is formed and reversibly regulated by rapid two body reactions (eg: reactions 1-4). This pool is depleted by slower three body recombination reactions (eg: reactions 5,15-17) which decrease the overall number of molecules present. Since radical recombination reactions are typically two

orders of magnitude slower than radical formation/shuffle reactions at atmospheric pressure[55], they are more greatly impeded by turbulent mixing processes. As a result of this hinderance to the slower radical recombination reactions, whilst the faster two body reactions are relatively unaffected, radical concentrations tend to far exceed equilibrium levels. Further, due to the endothermic nature of radical formation and the exothermic nature of radical consumption, excess radical levels coincide with flame temperatures that are depressed below equilibrium levels.

5.1.2 Effect of Residence Time

A plot of conditional mean temperature, at the reactor outlet, versus mixture fraction at various residence times for an outlet unmixedness of $\mho = 0.5$ can be found in Fig. 5.1 (Cases H1-H6 of Table 5.1). From Eqn 4.10 it can be seen that halving of the reactor residence time (τ_r) corresponds to a doubling of the conditional mean scalar dissipation profile at all mixture fractions. A comparison of cases with varied reactor residence times but similar outlet unmixedness (H1-H6, H9-H14, H17-22) suggests that successive halving of residence time gives rise to nearly linear drops in the peak conditional mean temperature. Irrespective of outlet unmixedness, an eight-fold reduction in reactor residence time leads to an approximate $\sim 200K$ decrease in the peak conditional mean temperature.

In all of the cases studied, the temperature profiles lie well below the adiabatic equilibrium curve which has a similar form but peaks at approximately $2399K$, some two hundred degrees above the longest residence time case ($\tau_r = 100ms$). From the mean outlet temperatures for stoichiometric PSR calculations, given in Table 5.2, it can be seen that in each case (H1-H6) the peak conditional mean ISR temperatures lie at least $200K$ below perfectly stirred values. The conditional mean temperature profiles shown in the figure agree well with laminar flamelet cases with corresponding levels of local scalar dissipation[123,124,125,126,127].

As with the temperature profiles of Fig. 5.1, the conditional mean monatomic hydrogen radical profiles tend towards adiabatic equilibrium levels with increasing reactor residence time. Superequilibrium radical levels are present in all of the cases presented here, with the peak conditional mean mass fraction ranging between being six and twenty times greater than the peak equilibrium value of $Y_{H,eq} \approx 1.3e-4$. The

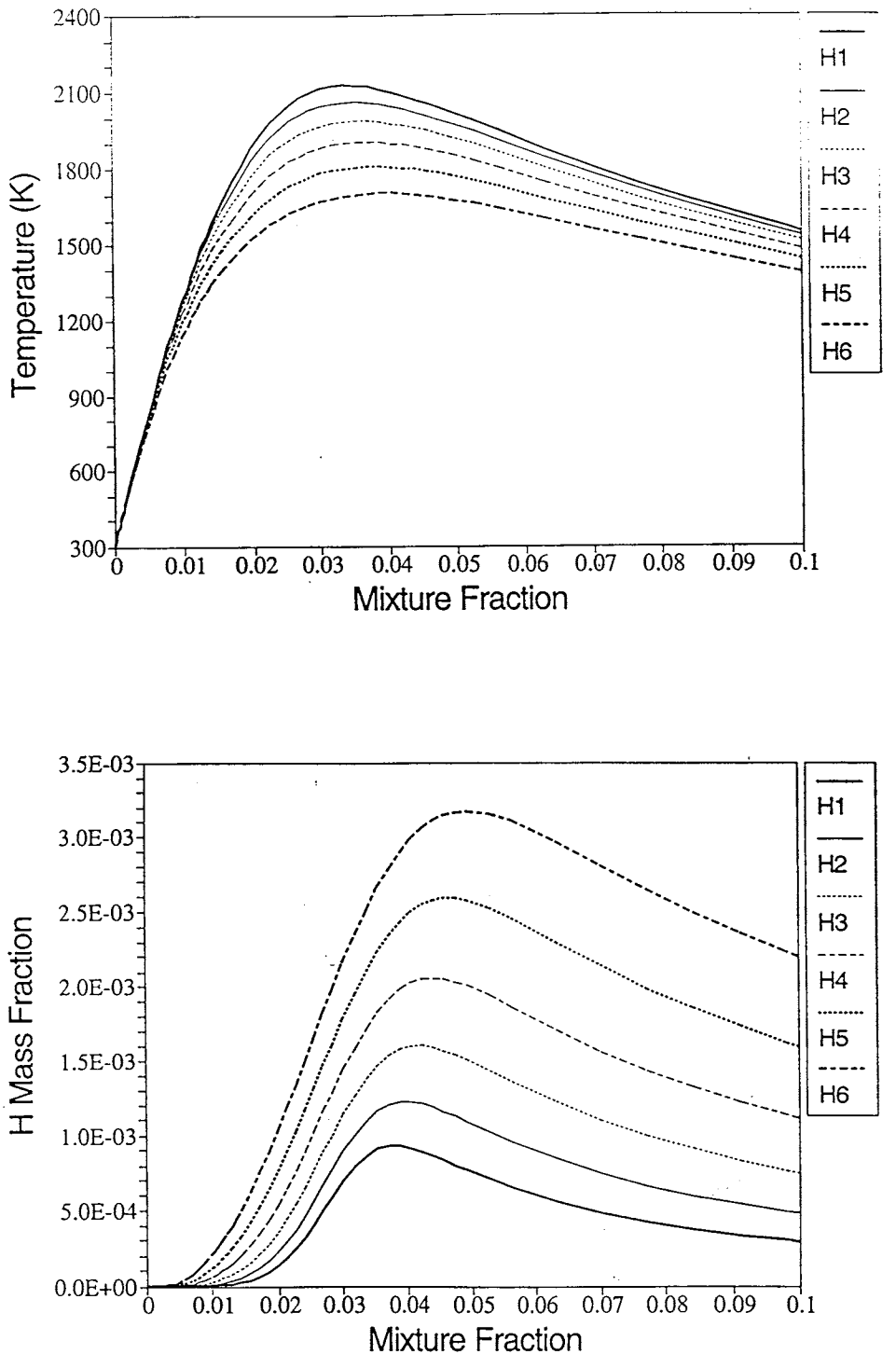

Figure 5.1: Conditional mean temperature and H mass fraction profiles for various residence times at an outlet unmixedness of $\mho = 0.5$. Legend labels correspond with entries in Table 5.1.

Residence Time (ms)	*Outlet Temp. (K)*	*Outlet H Mass Frac.*	*Outlet O Mass Frac.*	*Outlet OH Mass Frac.*	*Outlet NO Mass Frac.*
100	2347	8.08e-5	3.90e-4	4.93e-3	2.34e-3
50	2335	9.49e-5	4.65e-4	5.32e-3	1.92e-3
25	2316	1.20e-4	5.93e-4	5.90e-3	1.42e-3
12.5	2288	1.61e-4	7.99e-4	6.66e-3	9.23e-4
6.25	2248	2.26e-4	1.11e-3	7.54e-3	5.25e-4
3.125	2196	3.26e-4	1.58e-3	8.50e-3	2.59e-4
1.5625	2128	4.72e-4	2.21e-3	9.39e-3	1.09e-4
0.78125	2045	6.79e-4	3.07e-3	1.01e-2	3.77e-5

Table 5.2: Stoichiometric PSR calculated outlet values for residence times corresponding to cases H1-H24.

ISR values at stoichiometric in Fig. 5.1 are consistently greater than stoichiometric PSR values at corresponding reactor residence times (see Table 5.2). This is an indication of the importance of turbulence-chemistry interaction.

It is clear that the H profile substantially broadens when subjected to the increased scalar dissipation rates that arise from decreased residence time. At the same time, increased mixing rates seem to cause a rich shift in the location of the profile peak. This broadening trend has been observed in laminar hydrogen flamelet calculations with increasing rates of strain [123,124], but the shift of the profile peak is opposite to that seen for flamelets. This discrepancy can be attributed to differing scalar dissipation profiles, and the absence of differential diffusion in the ISR calculations. Peak H mass fractions agree to within twenty percent of flamelet values[123,126,127], but tend to be consistently greater, a fact which may also be due differences in the nature of scalar transport.

Similar elevation and broadening trends can be observed in Fig. 5.2 for the monatomic oxygen radical (O), but the location of its peak value shifts to leaner mixture fractions with increased scalar dissipation. This shift is qualitatively in line with flamelet results[124]. The peak conditional mean O mass fractions calculated here also agree to within twenty percent of the values reported for various hydrogen flamelet calculations[55,124,125], and range from six to fifteen times in excess of the peak equilibrium mass fraction of $Y_{O,eq} \approx 3.5e-4$.

In contrast to the other radical species, the hydroxyl radical (OH) profile does not monotonically increase with increasing local scalar dissipation rate (see Fig. 5.2).

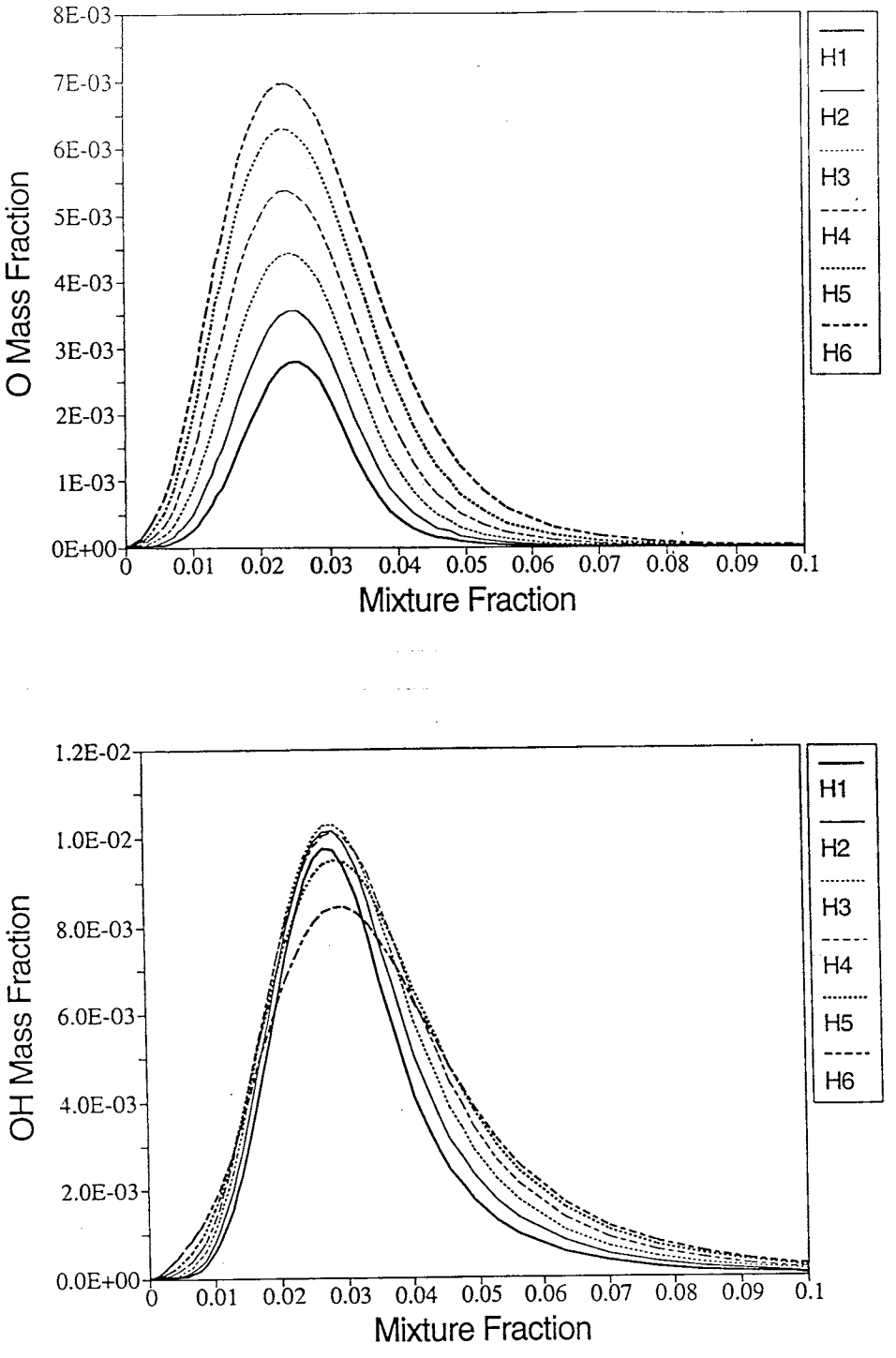

Figure 5.2: Conditional mean O and OH mass fraction profiles for various residence times at an outlet unmixedness of $\mathcal{U} = 0.5$. Legend labels correspond with entries in Table 5.1.

Whilst the profile peak is consistently around double the adiabatic equilibrium value of $Y_{OH,eq} \approx 4.5e-3$, increasing scalar dissipation rates cause it to increase until a critical value is reached before declining thereafter. It is evident that the variation in the hydroxyl profile with differing local mixing rates is substantially smaller than the variations observed for monatomic hydrogen and oxygen. As with the other radicals, reasonable agreement between ISR values and flamelet results exists for OH.

Departures from equilibrium similar to those found in Figs 5.1 and 5.2. can be produced in perfectly stirred reactors, but only with much shorter residence times than those tabulated in Table 5.2. This point highlights the crucial difference between perfectly and imperfectly stirred reactors, namely that the former are completely premixed and thus chemical reactions are only impeded when their characteristic timescale is comparable to the reactor residence time. Being nonpremixed, not all of an ISR reactor volume is comprised of fluid with a flammable composition, and as a result the residence times of the chemically reactive zones are more closely related to small scale turbulent mixing timescales, rather than the residence time of the entire reactor volume. It can be inferred from Eqn 4.6 that ISRs behave in a more PSR-like fashion when inlet-outlet variation of the mixture fraction PDFs is very small. In these instances, scalar mixing rates are much slower than the rate of reactor throughput, and the ISR reactive scalar profile becomes identically equal to that generated by an ensemble of PSRs at different input stoichiometries.

5.1.3 Effect of Outlet Unmixedness

Comparing ISR cases with equal reactor residence times but with different outlet unmixedness (see Fig. 5.3), reflects the influence of the conditional mean scalar dissipation trends discussed in Section 4.2. Lower outlet unmixedness cases are subject to correspondingly lower conditional mean scalar dissipation levels in the vicinity of the stoichiometric mixture fraction (see Fig. 4.2). These lower scalar mixing rates around stoichiometric allow the system to relax closer to chemical equilibrium.

Lower outlet unmixedness also gives rise to much higher scalar mixing rates in the less probable rich zones of mixture fraction space. Since chemical source terms are exceptionally weak in these zones, profile curvature is minimal even for low mixing rates. As a result large increases in scalar dissipation in these mixture fraction zones

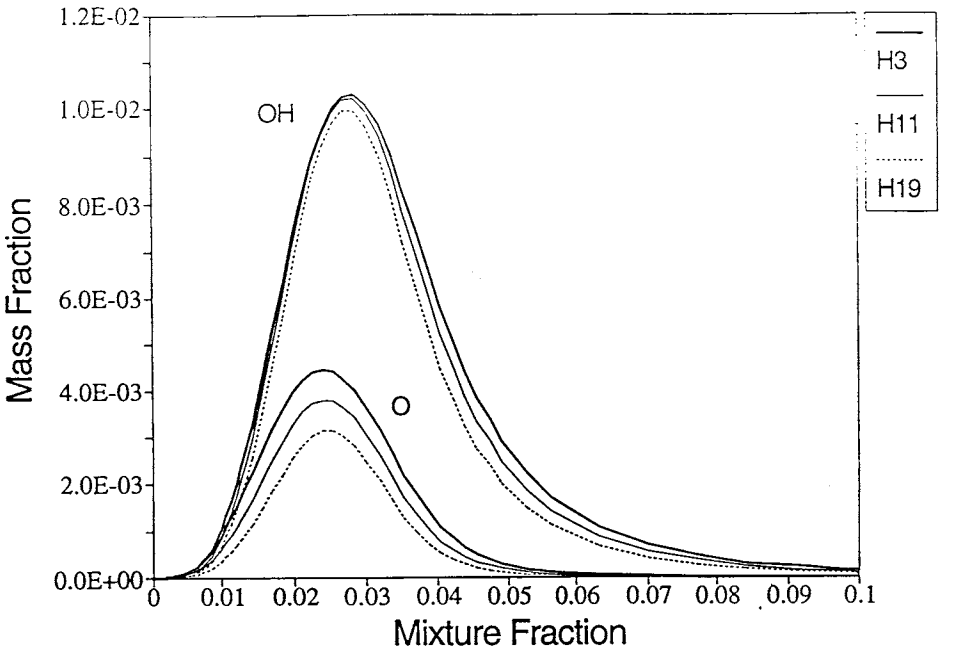

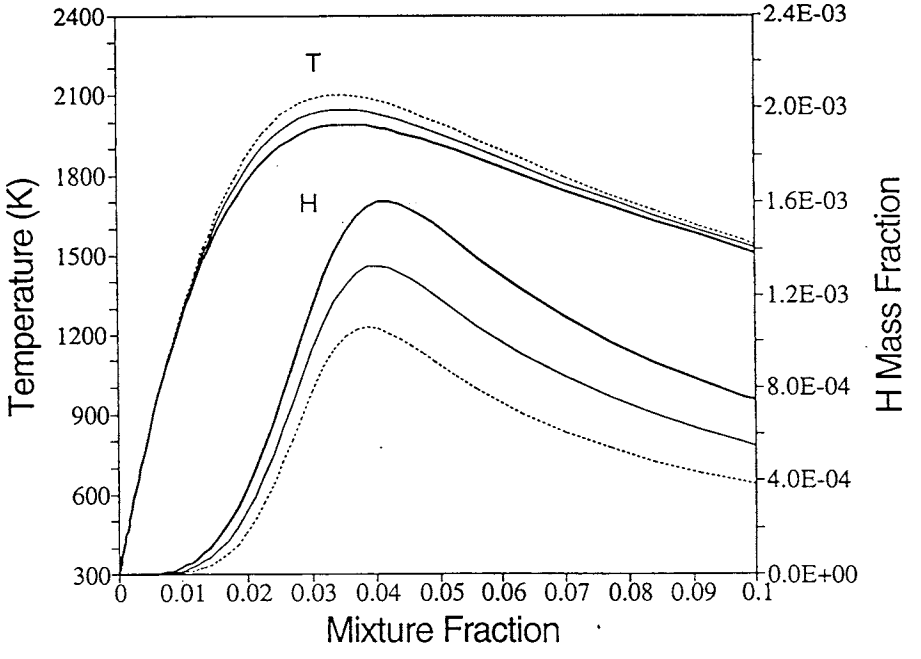

Figure 5.3: Conditional mean temperature, H, O and OH mass fraction profiles for varying levels of outlet unmixedness, with a residence time of $\tau_r = 100ms$. Legend labels correspond with entries in Table 5.1.

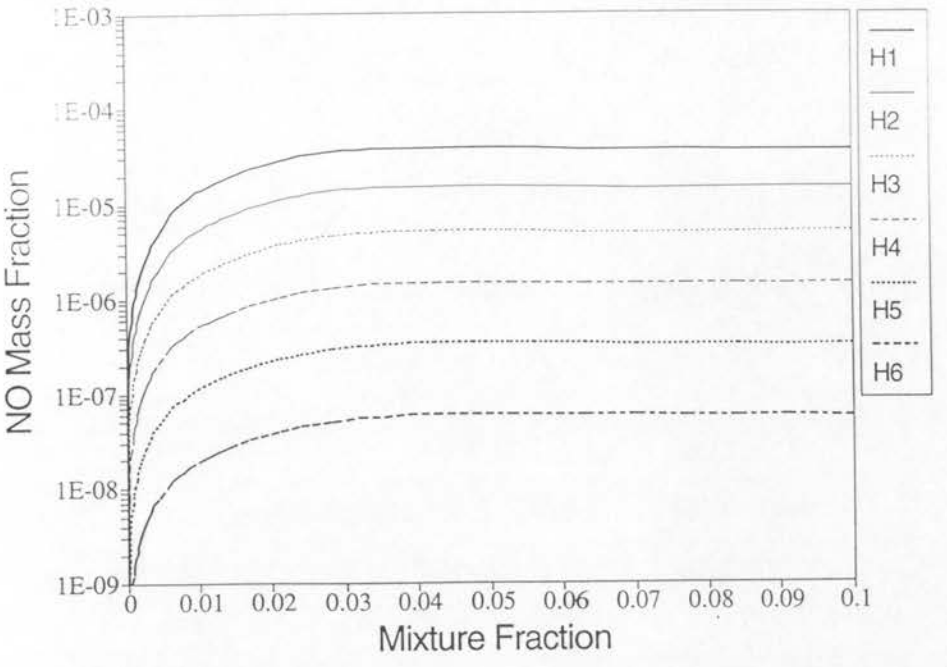

Figure 5.4: Conditional mean nitric oxide (NO) mass fraction profiles at various residence times for an outlet unmixedness of $\mho = 0.5$. Legend labels correspond with entries in Table 5.1

have only a relatively small effect on the reactive scalar statistics.

5.1.4 Nitric Oxide Formation

Nitric Oxide (NO) production via the Zeldovich thermal mechanism[128] is approximately rate limited by reaction 30 of Table A.1, and is thus strongly influenced by variations in flame temperature and monatomic oxygen (O) concentration. The net effect, upon NO mass fraction, of variations in these scalars with unmixedness and residence time can be seen in Fig. 5.4. It is evident that conditional mean NO profiles subside with decreasing reactor residence times (and increasing outlet unmixedness though not shown), thereby illustrating the dominance of flame temperature over O radical concentration as a controlling parameter.

It appears that the magnitude of the conditional mean NO profile is approximately an exponential function of the conditional mean flame temperature. Comparison of peak conditional mean values with tabulated PSR values for corresponding residence times show that the ISR values are two orders of magnitude lower for the

$100ms$ cases (H1,H9,H17). This discrepancy further widens such that for 1/32 of that residence time (cases H6,H14,H22), the ISR peak values are three to four orders of magnitude lower than the corresponding PSR value.

Meeting regulated limits on the formation of polluting nitrogen oxides (NO_x) is a critical criterion in the design of practical combustors[129], and so it is important to understand the effect of unmixedness and residence time upon unconditional mean NO_x emissions. Figure 5.5 is a plot of unconditional outlet area averaged temperature depression below equilibrium ($\{T - T_{eq}\}_{outlet}$), and NO mass fraction ($\{Y_{NO}\}_{outlet}$) as functions of residence time, upon lines of constant outlet unmixedness. The influence of the outlet mixture fraction PDF upon the unconditional area averaged temperature is evident from this figure. Decreased outlet unmixedness corresponds to a narrowed outlet PDF which, when convoluted with the conditional mean temperature profile, will weight temperature values near the mean mixture fraction more heavily than those at the mixture fraction bounds. Consequently, the upward relaxation of conditional mean temperature with increasing residence time is more apparent in the outlet averages for low outlet unmixedness cases than for high unmixedness cases.

The exponential dependence of outlet NO mass fraction upon residence time is clearly observed in Fig. 5.5, and is similar to the power law dependence discovered by Chen and Kollmann[49] and Smith *et al*[96] for nonpremixed combustion in turbulent jets (see also Chapter 7). Area averaged NO emission can be seen to be an exponential function of outlet unmixedness at constant residence time, which agrees with the results of Smith and Bilger[103], and Chen[116].

5.1.5 Extinction Conditions

The similarity between the pure-inlet ISR equations (Eqns 4.14,4.15) and laminar flamelet equations is borne out by the results presented here. There are substantial differences in profile shape between ISR and flamelet results owing to differing scalar dissipation profiles, and the the presence of differential diffusion in the latter. Despite this, peak values near stoichiometric agree reasonably well when stoichiometric scalar dissipation values are matched. The variation in conditional mean scalar dissipation rate at stoichiometric, with reactor residence time and outlet unmixedness, can be

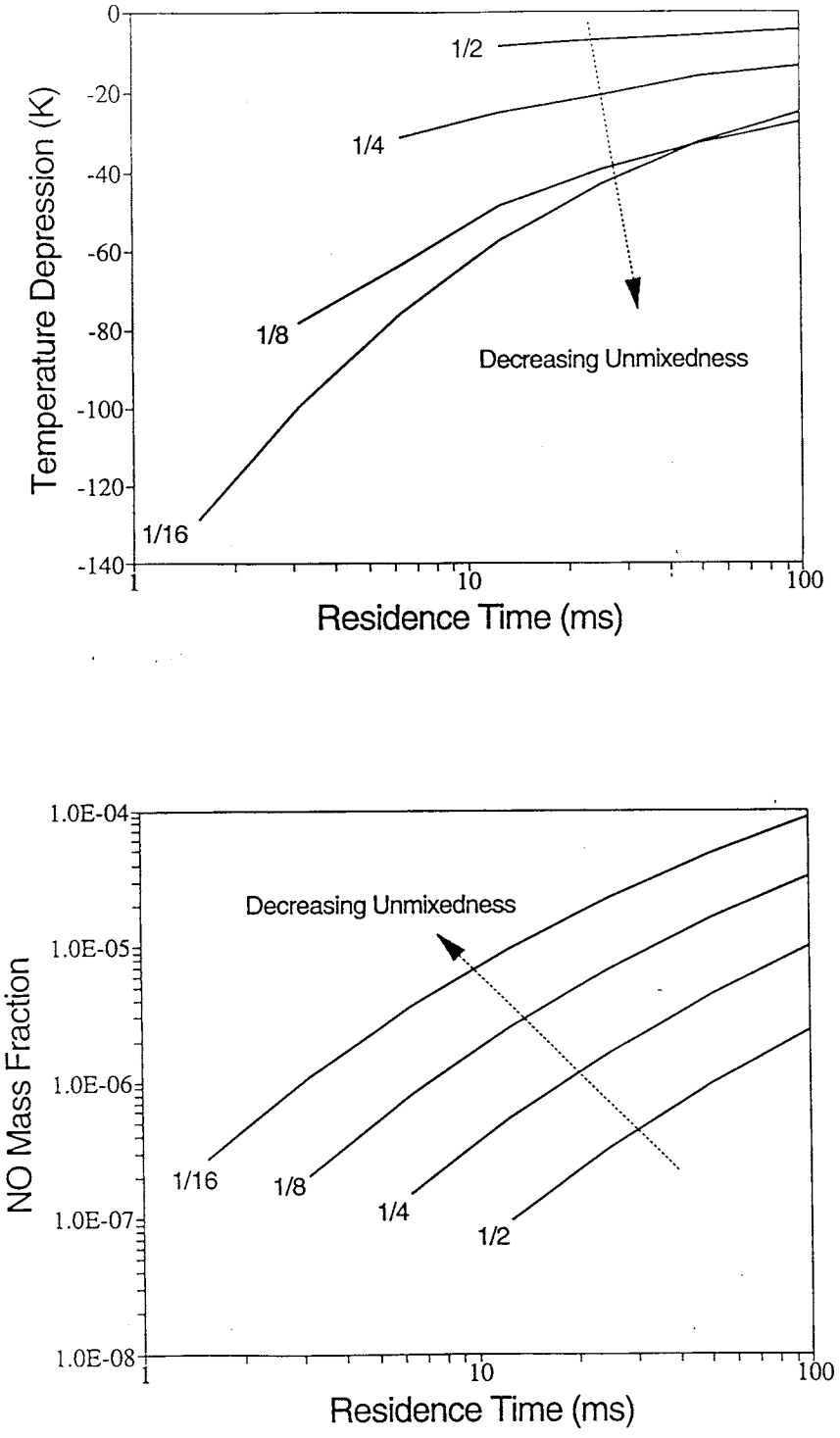

Figure 5.5: Unconditional outlet area averaged temperature and nitric oxide (NO) mass fractions as functions of outlet unmixedness and residence time for pure-inlet H_2 ISR combustion.

seen for pure-inlet hydrogen-air combustion in Fig. 5.6.

As was mentioned in preceding sections, extinction behaviour cannot be tolerated within a singly conditioned CMC implementation of an imperfectly stirred reactor. Extinction will occur where turbulent mixing processes are so rapid that they impede radical formation reactions. In these instances, conditionally averaging upon mixture fraction alone does not reduce instantaneous deviations sufficiently to allow a first order chemical closure.

In Fig 5.7, conditional mean profiles for OH radical mass fraction and temperature are plotted for a number of pure-inlet cases with intense mixing rates. The profiles display many of the features found in laminar flamelets at strain rates near the extinction limit. The temperature profiles are greatly depressed below chemical equilibrium levels, with the most intensely mixed case (H8) having a peak conditional mean temperature within $50K$ of the peak temperature for a flamelet on the verge of extinction[126]. Hydroxyl levels are further depressed below those in Fig. 5.2, to the point where the H8 profile is close to adiabatic equilibrium values.

The separation between monatomic hydrogen profiles with halved residence times is greatly narrowed for H7-H8 compared to more quiescent cases (H1-H6). At even smaller residence times the H profile reaches a maximum value and then declines thereafter. This decline can be found in laminar flamelet calculations prior to extinction [124,126], although in those cases the maximum H value reached is some twenty percent below that found in the ISR case. Monatomic oxygen profiles are also in decline and qualitatively agree with flamelet results near extinction[124,126].

Extinction behaviour in laminar flamelet calculations occurs when a critical value of scalar dissipation χ_q is attained at the stoichiometric mixture fraction. Drake[130] and others[123,125] suggest that flamelet extinction in a hydrogen-air laminar diffusion flame occurs in the vicinity of a strain rate of $a = 12000s^{-1}$ which, via the following equation[28],

$$\chi = 4a\,(\bar{\xi})^2\,[erfc^{-1}(2\bar{\xi})]^2 \tag{5.1}$$

yields an estimated extinction scalar dissipation rate of $\chi_q \approx 100s^{-1}$. This value is also in agreement with the values reported by Gutheil *et al*[126], and Gutheil and Williams[127].

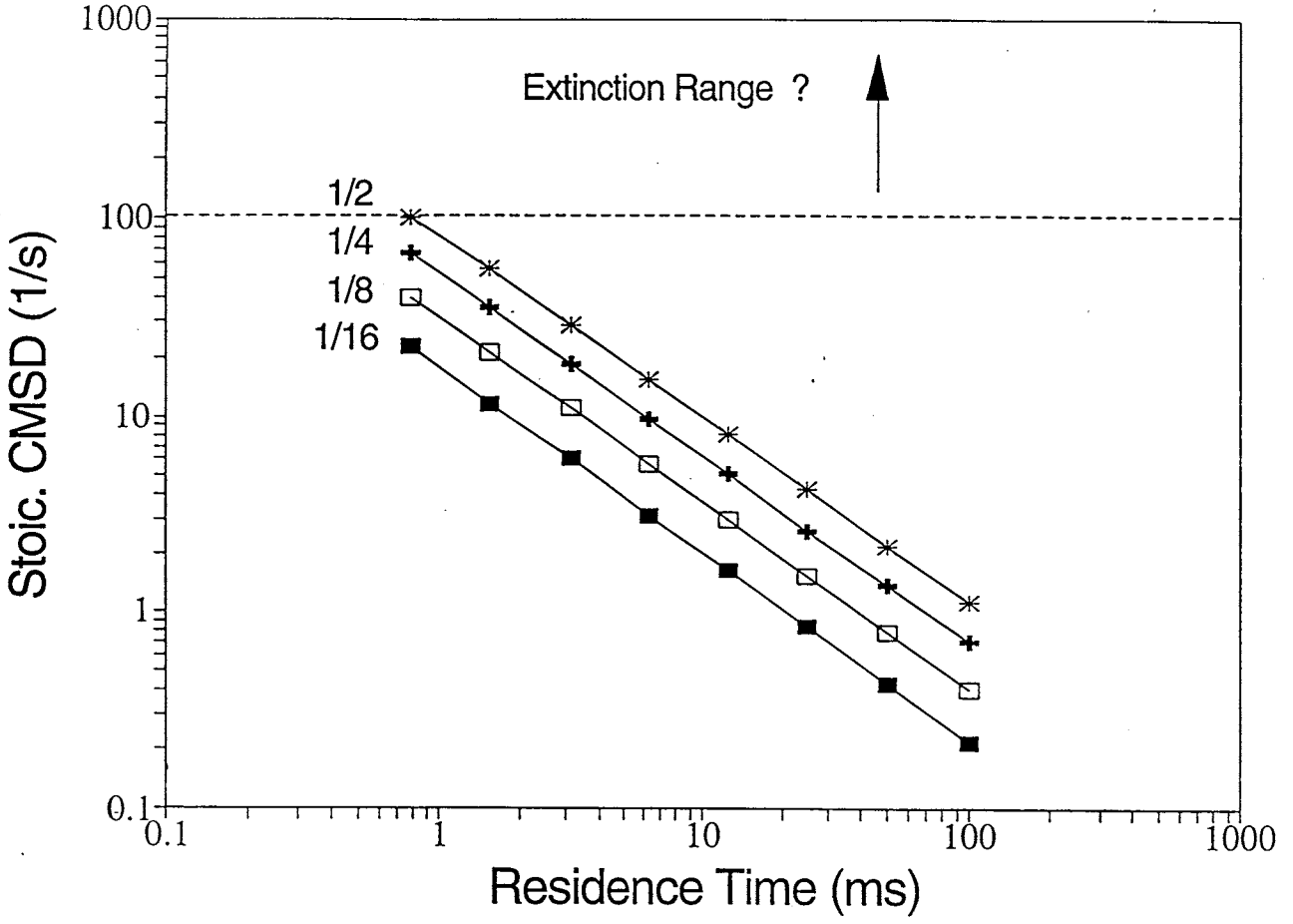

Figure 5.6: Conditional mean scalar dissipation rate at stoichiometric as a function of reactor residence time and outlet unmixedness for pure-inlet hydrogen burning ISRs.

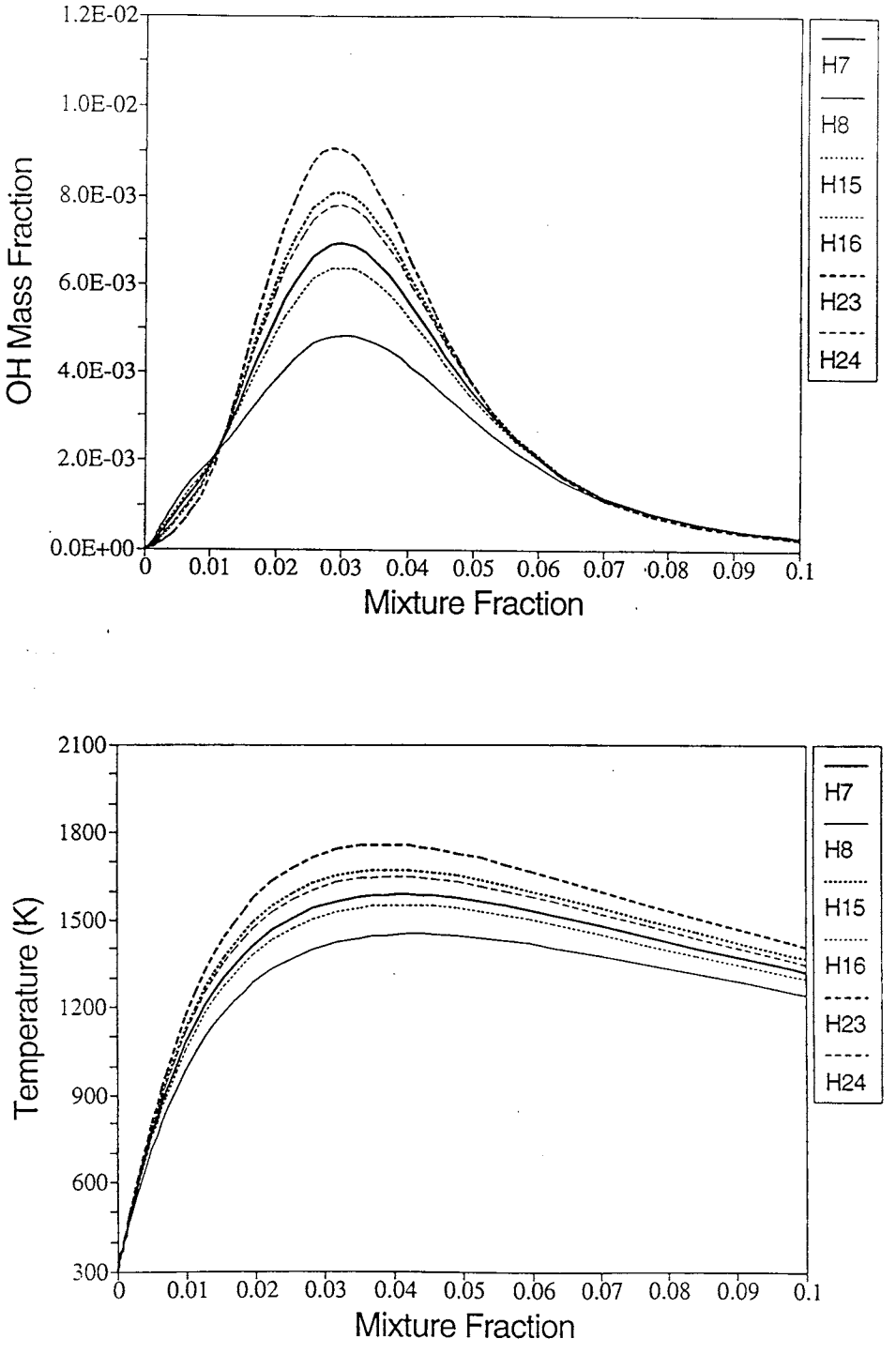

Figure 5.7: Conditional mean OH mass fraction and temperature profiles for intensely mixed pure-inlet ISR cases.

It can be seen that the temperature and radical mass fraction profiles for case H8, which has an extinction-inducing conditional mean scalar dissipation rate at stoichiometric ($\{\{<\chi \mid \eta>\}\} \approx 100s^{-1}$), are in good agreement with those reported elsewhere for hydrogen-air laminar flamelets near extinction[123,125,126,127]. This agreement between pure-inlet ISR and laminar flamelet results suggests that the critical scalar dissipation rate given above can be used as an indicator for the onset of extinction in pure-inlet ISR calculations. Due to the chemical closure limitations mentioned above, ISR results for conditions close to this critical value must be treated with caution. In Fig. 5.6 this critical value is plotted as an approximate upper bound upon singly conditioned CMC applications of the pure-inlet ISR method, for stoichiometric hydrogen air combustion at one atmosphere pressure with an inlet temperature of $300K$.

5.1.6 Partially Premixed Inlet Cases

Various ISR calculations have been performed to determine the effect of the governing parameters upon systems with non-unity inlet unmixedness (see H33-H45 of Table 5.1). In each of these cases, the conditionally averaged reactive scalar profiles at the ISR inlet were assumed to be frozen, that is as if cold fuel and oxidizer had been allowed to mix in the absence of chemical reaction. These inlet conditions correspond to the situation where either the reactants mix before entering chemically reactive zones, or they mix at the inlet point to the reaction zone at such a rapid rate that combustion cannot be not supported.

As was indicated earlier (see Sections 4.1-4.3), the inlet reactive scalar profiles are not restricted to the assumed form employed here and can alternatively be either measured or calculated for each application of the ISR model.

Figure 5.8 is a plot of conditionally averaged reactive scalar profiles for the pure and partially-premixed inlet cases of H9, H33 and H40. As with the profiles resulting from pure-inlet calculations, the partially premixed profiles tend towards chemical equilibrium with increasing residence time and/or decreasing outlet unmixedness. However, in comparison with the pure-inlet results, the conditional mean reactive scalar profiles are closer to chemical equilibrium for corresponding cases of outlet unmixedness and reactor residence time.

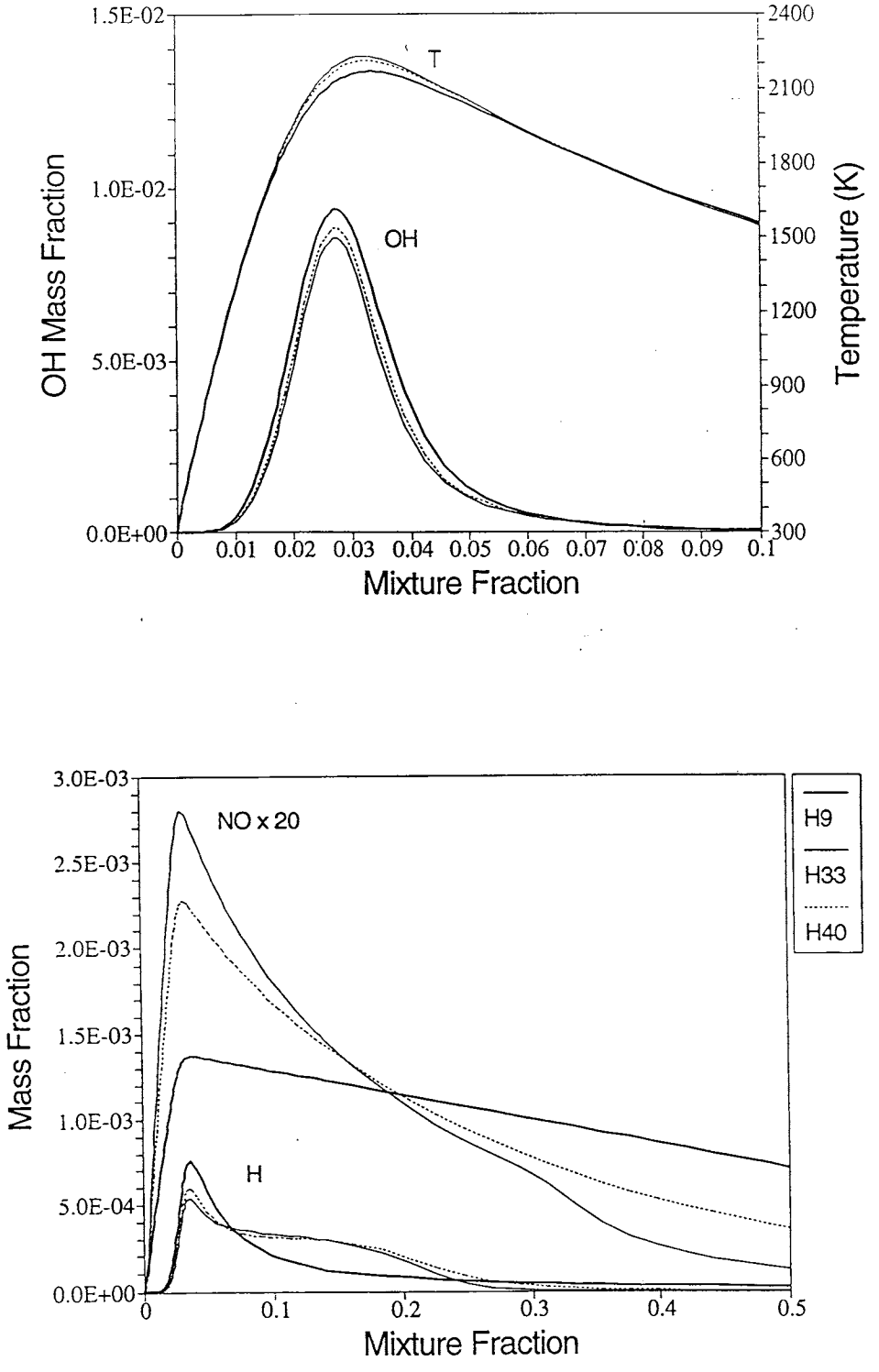

Figure 5.8: Conditional mean temperature and OH, H and NO mass fraction profiles for various outlet unmixednesses and residence times. Legend labels correspond with entries in Table 5.1

The reason for this behaviour lies principally with the differing form and magnitude of the conditional mean scalar dissipation profiles around stoichiometric in each case. Comparing cases H9 and H33 on Table 5.1, which have equal residence times and outlet unmixedness, it can be seen that the mean scalar dissipation of the former pure-inlet case is three times that of the latter. Correspondingly, the threefold difference in mean scalar dissipation is approximately transferred to the conditional mean profiles (see Fig. 4.2) at stoichiometric mixture fractions. The ratio of stoichiometric scalar dissipation rates is not exactly three owing to the differences in R profile shape for the two cases (see Fig. 4.1, 1/2 curve for $\mho = 0.5$ case and 1/4 curve for $\mho = 1$ case). This difference in conditional mean scalar dissipation is reflected by the reactive scalar profiles of Fig. 5.8, with the more quiescent H33 case being closer to chemical equilibrium near stoichiometric.

Comparing cases H9 and H40 which have identical mean scalar dissipation rates, the influence of differences in the core averaged PDF upon the conditional mean scalar dissipation profile is evident. The ratio of conditional mean scalar dissipation rates near stoichiometric for H9 to H40 is around ~ 2.5. This disagreement arises from the differing R and $\{\{P_\eta\}\}$ values at these mixture fractions, with the local R value being ~ 4 times greater for H34, but the core PDF value being an order of magnitude greater. The effect of these differences in conditional mean scalar disspation rate can be seen in Fig. 5.8, with the H40 profiles being subject to less mixing interference near stoichiometric.

The additional inlet-outlet difference term, which appears in Eqn 4.6 compared to Eqn 4.14, has a marked influence upon conditional mean reactive scalar profiles at richer mixture fractions. This additional term is analogous to the PSR inlet-outlet difference term and will only have a significant effect on the chemical reaction system in those regions of mixture fraction space where either scalar transport or chemical reaction terms are small by comparison. It would seem from Fig. 5.8 that at mixture fractions away from the reaction zone where chemical activity is small, the difference term is balanced by the scalar transport term. For still smaller changes in mixture fraction variance through the ISR, with a fixed residence time, reactive scalar profiles tend to frozen limits at chemically inert mixture fractions.

With the inclusion of the inlet-outlet difference term, the ISR equations are

no longer directly analogous to 'flamelet' like equations where a simple reactive-diffusive balance of terms exists. It can be seen that, depending upon the relative strength of the different terms in the full ISR equation (Eqn 4.6), flamelet-type models and PSR models are both subsets of the ISR parameter space. The three-way balance of a difference term, scalar transport and chemical reaction terms, introduced here, is an inherent characteristic of subsequent CMC applications such as transient nonpremixed reactors (not presented in this thesis) and steady two dimensional jet flames. In the latter application, the difference term is a mean convective one and will be discussed in that context in Chapter 7.

5.2 Methane Calculations

In an effort to emulate conditions similar to those encountered in the primary recirculation zone of a gas turbine combustor, ISR calculations were made for methane (CH_4) combustion in air at an absolute pressure of ten atmospheres and an inlet temperature of $600K$. Correa[129] estimates that for a land-based gas turbine combustor with mean flow velocity of $\sim 100m/s$, the integral time scale of the turbulent flow is of the order of $\sim 500\mu s$ with an integral length scale of $\sim 5mm$. Corresponding estimates of the integral scale velocity fluctuation u' and the mean turbulent kinetic energy dissipation rate ϵ, were $\sim 11m/s$ and $\sim 2.0e5m^2/s^3$ respectively. Employing a simple gradient mixing assumption,

$$\chi \approx c_\chi \frac{\epsilon}{(u')^2} \bar{\xi''^2} \tag{5.2}$$

where the constant $c_\chi \approx 4/3$, mean scalar dissipation can be estimated as being $\{\{\chi\}\} \approx 2000\{\{\bar{\xi''^2}\}\}$. It is reasonable to assume that the inlet PDF can be approximated as a double delta function ($\mho = 1.0$) since little or no premixing of fuel and oxidizer occurs in nonpremixed gas turbine combustors. Given this assumption and the volume averaging of the mixture fraction variance equation it can be shown that,

$$\{\{\chi\}\} = \frac{1}{\tau_r}[\sigma_m^2 - \{\bar{\xi''^2}\}_{outlet}] \tag{5.3}$$

which incorporating the above estimate of $\{\{\chi\}\}$ and the approximation that $\{\bar{\xi''^2}\}_{outlet} \approx \{\{\bar{\xi''^2}\}\}$ becomes,

$$\mho \approx \frac{1}{2000\tau_r + 1} \tag{5.4}$$

Designation	*Equivalence Ratio*	*Residence Time* (ms)	*Outlet Unmixedness*	*Mean Scalar Dissipation* (s^{-1})
B10	1.0	1.0	0.33	34
C10	1.0	1.5	0.25	26
D10	1.0	5.0	0.09	9.4
B15	1.5	1.0	0.33	50
C15	1.5	1.5	0.25	38
D15	1.5	5.0	0.09	14
B20	2.0	1.0	0.33	65
C20	2.0	1.5	0.25	49
D20	2.0	5.0	0.09	18

Table 5.3: Methane ISR Calculations at $p = 10atm$ and $T_{inlet} = 600K$

It can be seen that given a fixed turbulent time scale $3/2((u')^2)/\epsilon$, the outlet unmixedness is roughly a function of residence time alone, with scalar dissipation being given by the expression below.

$$\{\{\chi\}\} \approx 2000\mho\sigma_m^2 \tag{5.5}$$

Note that in the foregoing analysis, pure fuel and oxidant streams are assumed to enter the zone of ISR applicability directly. This may not be the case in reality and as ISR 'chain' may be more appropriate (see Section 4.3.

A series of ISR calculations were made for a range of different primary zone residence times and overall air-fuel ratios as is indicated in Table 5.3. The different residence times were selected to be two, three and ten times longer than the integral time scale of the flow. These values are still substantially less than the combustor residence time of $10ms$ estimated from the mean flow velocity of $100m/s$ and the typical land-based combustor length of $1m$ [129]. Other calculations were made for cases with the primary zone residence time equal to the integral timescale, but due to the high rate of mixing, combustion could not be supported.

Two different chemical mechanisms were employed in the methane calculations. an augmented skeletal mechanism (similar to that introduced by Smooke[119]) containing 34 steps and 19 chemical species (see Table A.1 in Appendix A), and the complete mechanism of Miller and Bowman[131] which includes C_2 chemistry and prompt NO_x formation with 259 steps and 51 species. Thermochemical data was obtained from CHEMKIN II as in the case of the hydrogen air system. and the solution methods for the ISR equations were identical. The calculations were made

on a Fujitsu VP2200 Supercomputer, and convergence required $3-6$ CPU minutes for the skeletal mechanism, and $20-30$ CPU minutes for the full mechanism at an estimated computation rate of ~ 20 Mflops. Using a PaSR approach for premixed methane combustion with a 77 step mechanism, Correa and Braaten[93] required approximately ten hours of dedicated CPU time on an Intel iPSC/860 hypercube running at ~ 70 Mflops. For a nonpremixed system with the same chemical mechanism, ISR convergence takes two orders of magnitude less computation time, even given the disparity in computation rates. It was found that existing solutions, for slightly different mixing and stoichiometry cases, proved to be superior initial estimates compared to the chemical equilibrium profiles normally used. Often the computation times stated above could be reduced by up to a factor of four, when using the solution to a different case as an initial estimate.

In contrast to the parametric study of hydrogen combustion, the methane calculations were not adiabatic, rather they allowed for radiation losses from gaseous products (H_2O and CO_2) using a model described by Kuznetzov and Sabelnikov[26] (see Appendix B). The formation of soot is an important feature of combustor performance under the fuel rich conditions found in primary recirculation zones. Soot particles typically cause large radiative losses in the combustion systems in which they appear, but due to their being in the solid phase, they are not treated in this analysis.

The influence of radiation losses on the outlet enthalpy level of a steady state reactor is proportional to the duration over which these losses act on the fluid in transit. For short residence times, such as those typical of primary recirculation zones, the effect of radiation losses upon the outlet results is small. In a test calculation made under adiabatic conditions for case D10 (see Table 5.3) the discrepancy from the non-adiabatic result in terms of peak conditional mean temperatures was only $6K$ out of $2333K$. The virtually insignificant effect of radiation losses from gas phase sources at the residence times studied here suggests that soot radiation losses will also be of little consequence. This is not to say that these radiation effects can be ignored in other parts of the combustor, downstream of the recirculation zone. Comparative calculations carried out for a much longer residence time case ($\tau_r = 50ms$) resulted in peak temperature differences of $60K$ which lead to $80-90\%$ discrepancies in peak

NO levels.

The effect of varying the overall equivalence ratio is an important consideration in applications where the operational power setting of a gas turbine combustor is variable, such as in aero-propulsion units, and non-baseline stationary and nautical units. The equivalence ratios modelled here range from unity, through to double the fuel mass flow required to completely react with the available air. This range roughly covers the typical values found in practical and laboratory combustors[132,133]. It will be seen later how changing the overall equivalence ratio strongly effects ISR outlet statistics such as mean fuel consumption, temperature, and CO and NO_x yield.

Despite these large unconditional mean effects, the influence upon the conditional mean reaction zone composition is remarkably small. For the high outlet unmixedness cases studied here, doubling the mean mixture fraction causes less than five percent variation in the magnitude of the conditional mean scalar dissipation profile in the $0 \leq \eta \leq 0.15$ range of mixture fraction space. Larger differences are present at higher mixture fractions, but these differences have no effect upon the reaction zone. This insensitivity of $\{\{< \rho\chi \mid \eta >\}\}$ to equivalence ratio variations naturally diminishes with decreasing unmixedness as the core and outlet averaged PDFs become distinctly mono-modal, and shifting the mean value causes very large changes in PDF value at nearby points in mixture fraction space.

5.2.1 Effects of Residence time on the Full Mechanism

The effect of different residence times upon conditional mean reaction zone structure can be seen in Figs 5.9-5.11 for calculations B10-D10 made with the full Miller-Bowman mechanism[131]. In Fig. 5.9, conditional mean temperature and mass fractions for the reactants (CH_4,O_2), major products (CO_2,H_2O), major intermediates (CO. H_2) are plotted versus mixture fraction. It is clear that increasing the primary zone residence time leads to a relaxation of the temperature and reactant profiles towards adiabatic equilibrium. The peak conditional mean temperatures are around $130K$ and $250K$ below the equilibrium temperature ($T_{eq} = 2411K$) for the D10 and B10 cases respectively. Increasing the reactor residence time by a factor of five leads to a $106K$ increase in the peak conditional mean temperature and a

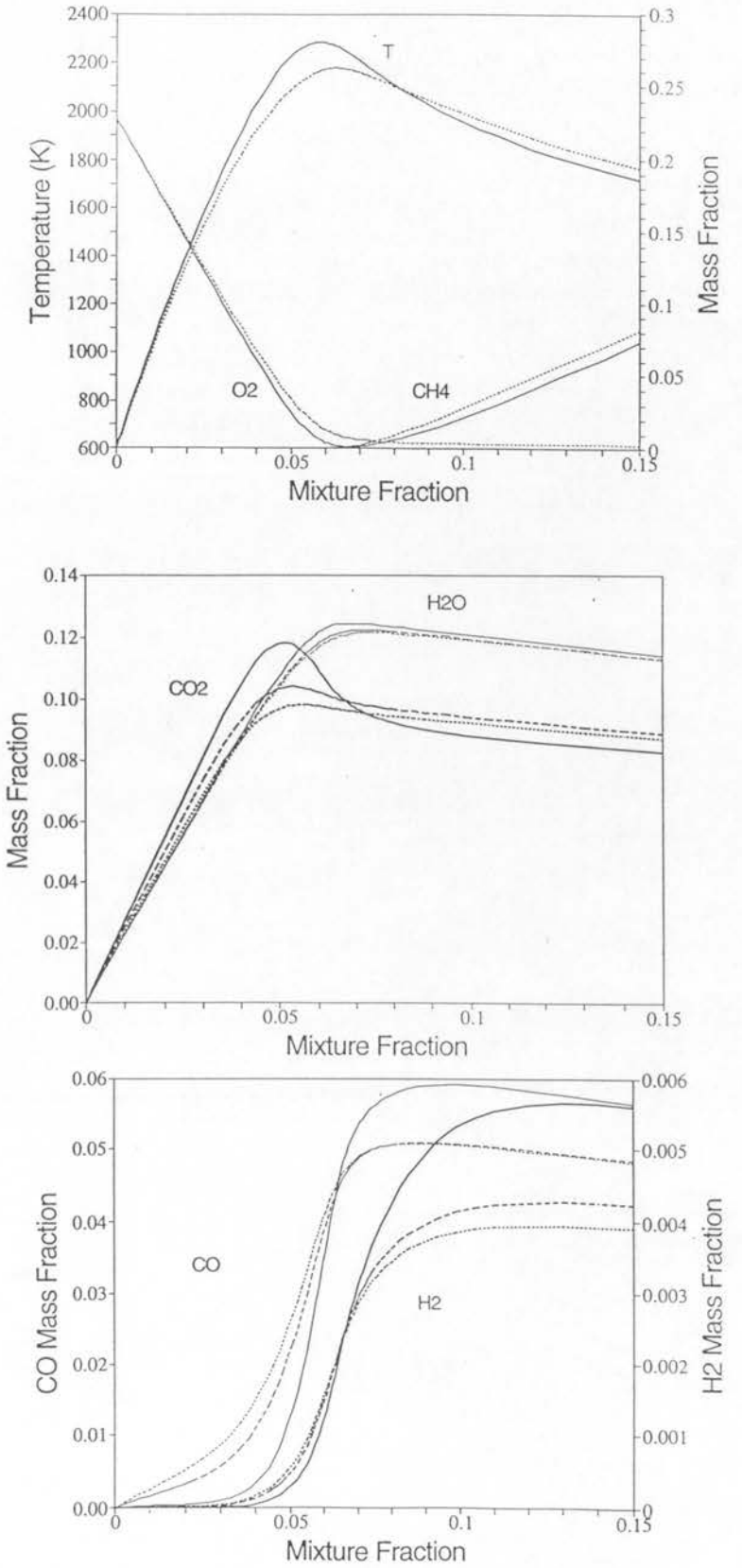

Figure 5.9: Conditional mean reactive scalar profiles for a methane burning ISR at various residence times. Line types denote residence time, solid - $\tau_r = 5ms$, dashed - $\tau_r = 1.5ms$, dotted - $\tau_r = 1ms$

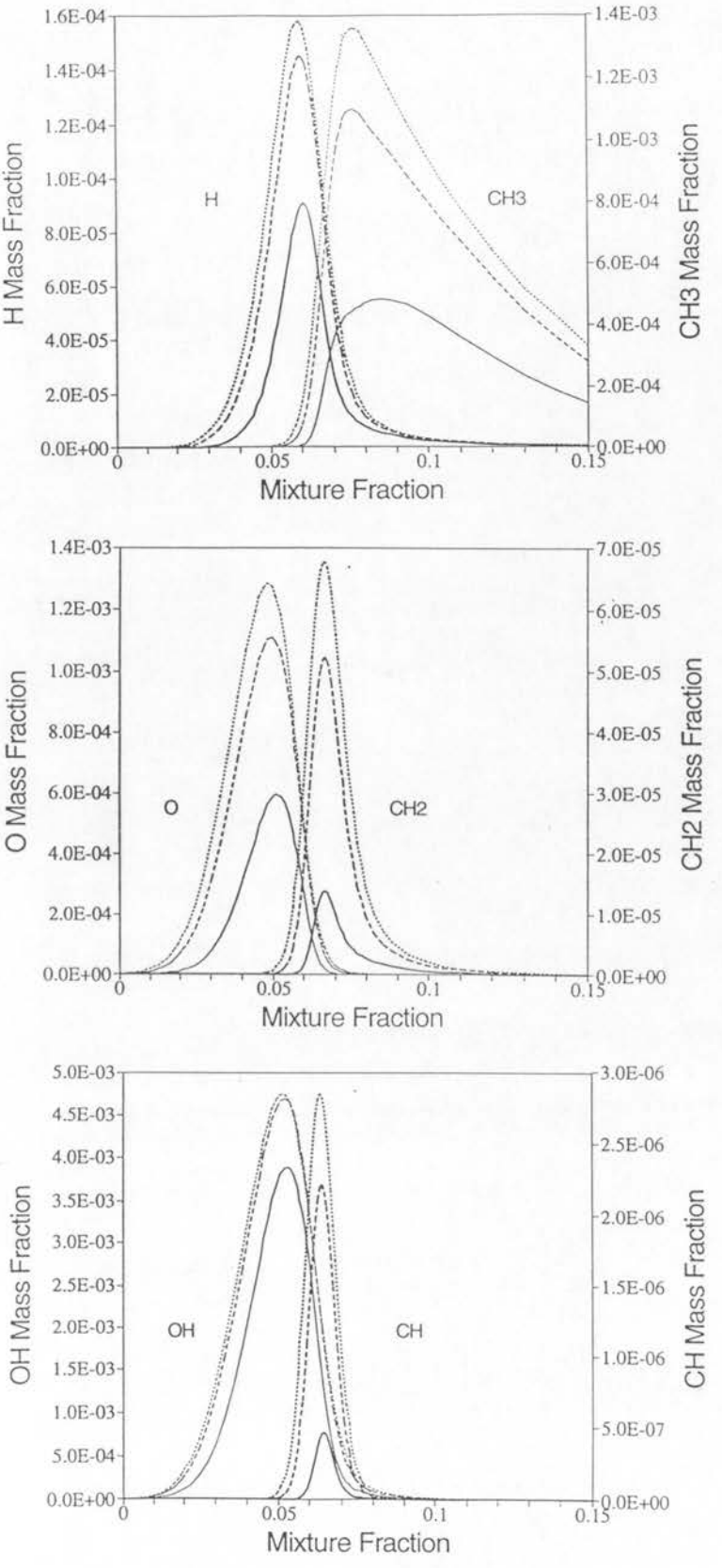

Figure 5.10: Conditional mean reactive scalar profiles for a methane burning ISR at various residence times. Line types denote residence time, solid - $\tau_r = 5ms$, dashed - $\tau_r = 1.5ms$, dotted - $\tau_r = 1ms$

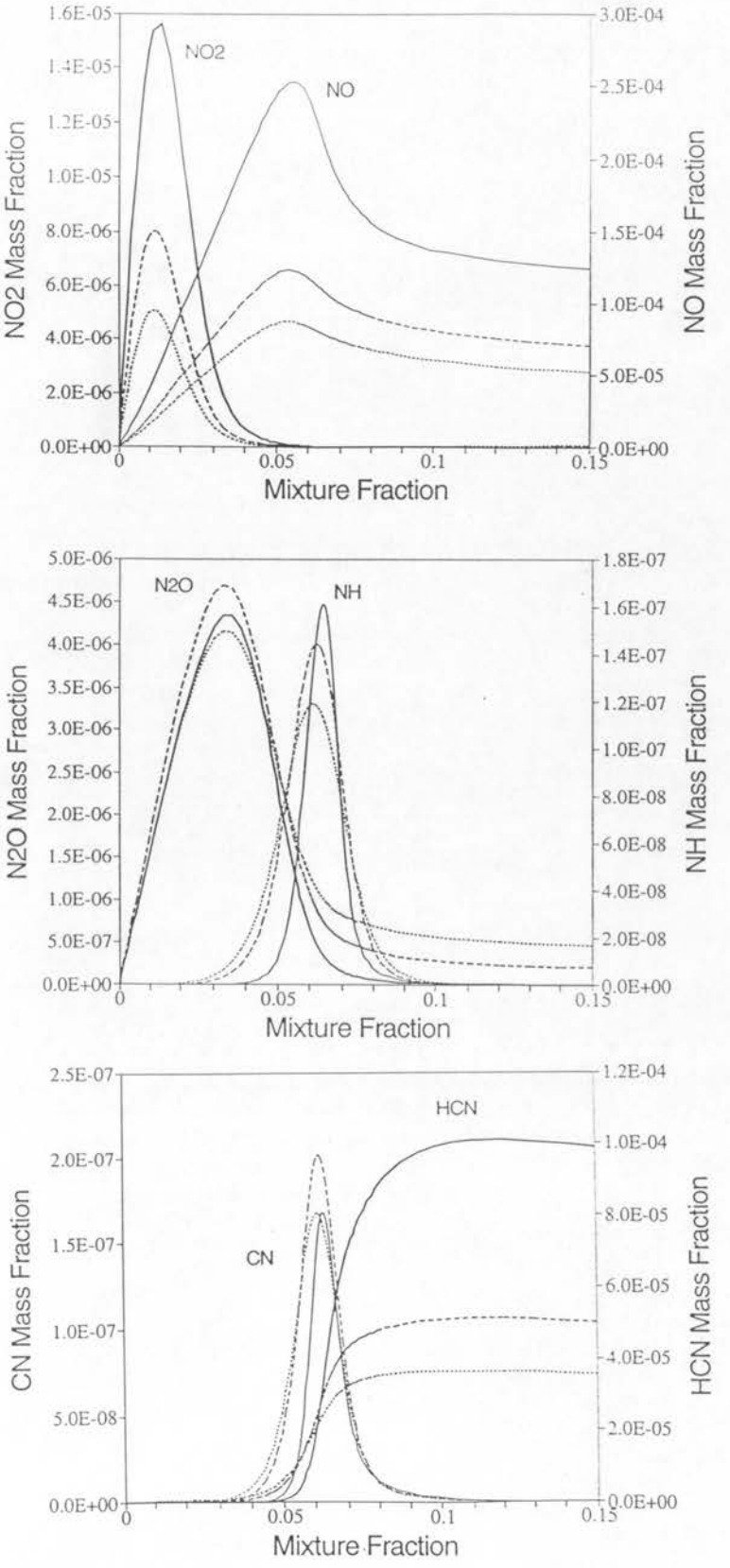

Figure 5.11: Conditional mean reactive scalar profiles for a methane burning ISR at various residence times. Line types denote residence time, solid - $\tau_r = 5ms$, dashed - $\tau_r = 1.5ms$, dotted - $\tau_r = 1ms$

shift in the location of the peak value from $\eta = 0.058$ to $\eta = 0.063$. The discrepancy between peak conditional mean ISR calculated temperatures and PSR calculated values narrows with increasing residence time from being $167K$ lower for B10 to only $100K$ lower for D10. This trend illustrates the significant role played by turbulence-chemistry interactions in causing departures from equilibrium beyond that resulting from the interactions between chemistry and reactor fluid transfer alone.

It is apparent from Fig. 5.9 that decreased reactor residence times allow proportionally less fuel and oxidizer to react, and correspondingly more O_2 leaks though the stoichiometric zone into richer mixture fractions. Conditional mean product mass fractions behave somewhat differently with decreasing residence time. Water (H_2O) levels are relatively unchanged over the range of residence times studied here, with conditional mean mass fractions peaking on the rich side with values around twelve percent, very close to the equilibrium value of $Y_{eq,H2O} = 0.119$. This perhaps indicates that H_2O formation reactions are quite fast compared to turbulent mixing processes.

On the other hand, carbon dioxide (CO_2) levels change substantially with decreasing residence time. The peak conditional mean mass fraction decreases from ~ 0.12 for the D10 case to ~ 0.10 for the B10 case, and the location of the peak moves slightly towards stoichiometric from the lean side. This decrease in peak CO_2 mass fraction seems to be a result of the interference in the progress of CO oxidation reactions (eg. reaction 18 of Table A.1) by turbulent mixing on the lean side of stoichiometric. This supposition is lent weight by the increased level of the CO mass fraction profiles on the lean side of stoichiometric for shorter residence times. On the rich side of the reaction zone, CO_2 levels rise and fall over the range of residence times presented here. This trend can be explained in terms of there being relatively little oxidation of CO to CO_2 in these rich zones, primarily because there are insufficient levels of the requisite oxidizing radical species[32]. As a result of this quasi-inert behaviour, rich CO_2 levels are principally determined by mixing from the lean side profile peak. This is supported by the fact that in the absence of scalar transport, such as in a chemical equilibrium calculation, rich side CO_2 levels are around half the values shown in Fig. 5.9. Under low scalar mixing conditions, the lean side CO_2 peak has a high value but little of this peak is transported to rich mixture fractions. For higher mixing rates, the lean side peak is depressed and more CO_2 is transported

to the rich side.

The major intermediate species ($CO.H_2$) are formed in rich mixture fraction zones from 'alkane attack' reactions (21-29 of Table A.1) which break down the alkane fuel species whilst consuming radicals. The increased turbulent mixing rates associated with decreased residence times clearly impede these alkane attack reactions and thus limit CO and H_2 formation. In the absence of turbulence-chemistry interaction, both CO and H_2 equilibrium mass fractions are double the rich side peak values shown in Fig. 5.9. Lean side H_2 and CO mass fractions exceed equilibrium values by a substantial margin due to the transport of these species from rich to lean mixture fractions.

Increased turbulent mixing rates in a methane reaction system cause elevations in the principal radical species (H, O and OH) similar to those found for the hydrogen-air reactions of Section 5.1. The major difference between the two reaction systems being that in the methane case, monatomic hydrogen is vigorously consumed on the rich side by alkane attack reactions instead of being mixed in an inert fashion to rich mixture fractions (see Fig. 5.10). Products of alkane attack reactions such as methyl (CH_3), methylene (CH_2) and methylidyne (CH) are plotted in Fig. 5.10 against the principal radicals to illustrate how the formation of the former group essentially consumes the latter. As with principal radical formation, the net formation of CH_3, CH_2 and CH is enhanced through increased turbulent mixing. In contrast to the principal radicals, the conditional mean mass fractions of CH_3, CH_2 and CH are more than six orders of magnitude greater than equilibrium values for the cases shown here.

The behaviour of nitrogen chemistry in the presence of increasing mixing rates can be seen in Fig. 5.11. Conditional mean mass fraction profiles for the regulated pollutants nitric oxide (NO) and nitrogen dioxide (NO_2) both decrease significantly with shortened residence times. Nitric oxide is formed via many different reaction pathways in hydrocarbon combustion[131], principally by the nitrous oxide (N_2O) pathway, the Zeldovich thermal mechanism[128], and the so-called prompt mechanism involving hydrogen cyanide (HCN) at stoichiometric and slightly rich mixture fractions. It is evident from Fig. 5.11 that the prompt and thermal mechanisms make large contributions to the NO profile in the range $0.045 \leq \eta \leq 0.065$, but that

outside these zones relatively little NO is formed and the levels there are mainly dependent upon scalar transport from the reaction zone.

Hydrogen cyanide formation supposedly results from a reaction between methylidyne (CH) and diatomic nitrogen. A comparison of Figs 5.10 & 5.11 supports this notion with a large increase in HCN levels, with increasing mixture fraction, being coincident with the occurence of the conditional mean CH spike. Hydrogen cyanide rapidly forms NO in stoichiometric mixture fraction zones by reacting to form monatomic nitrogen which then is oxidized by OH or O_2. Miller and Bowman[131] state that nitric oxide levels decrease somewhat at rich mixture fractions because of a tendency for NO to be recycled back to hydrogen cyanide via the cyano radical (CN). This process is evident in Fig. 5.11, where for rich mixture fractions the HCN profile has a negative curvature and the corresponding NO profile has a positive curvature.

Nitrous oxide (N_2O) is formed in lean zones primarily by a reaction between N_2 and monatomic oxygen[131], and can be seen to have peak values at a mixture fraction of $\eta \approx 0.035$ for the cases shown here. At richer mixture fractions, N_2O seems is consumed in increasing amounts with increasing reactor residence time. As one of the principal reactions for NO formation from N_2O also produces imidogen (NH)[131], it would seem that the N_2O consumption and imidogen formation in Fig. 5.11 at $\eta \approx 0.06$ is indicative of the nitrous oxide pathway in action.

Nitrogen dioxide is formed in very lean zones by reaction with HO_2 and NO, but is eliminated at richer mixture fractions by reacting with H, O and OH radicals to form NO. Both NO and NO_2 peak mass fractions are orders of magnitude lower than equilibrium and PSR calculated values.

5.2.2 Importance of Chemical Mechanism Detail

As was stated in Section 4.3, it is plausible that in many cases the added chemical detail afforded by employing an ISR approach over a method with higher dimensionality can more than compensate for the fluid dynamic approximations inherent in the model. In the following, a comparison is made between results obtained from the full Miller-Bowman mechanism and those obtained from the much simpler mechanism listed in Table A.1, for cases B10-D10.

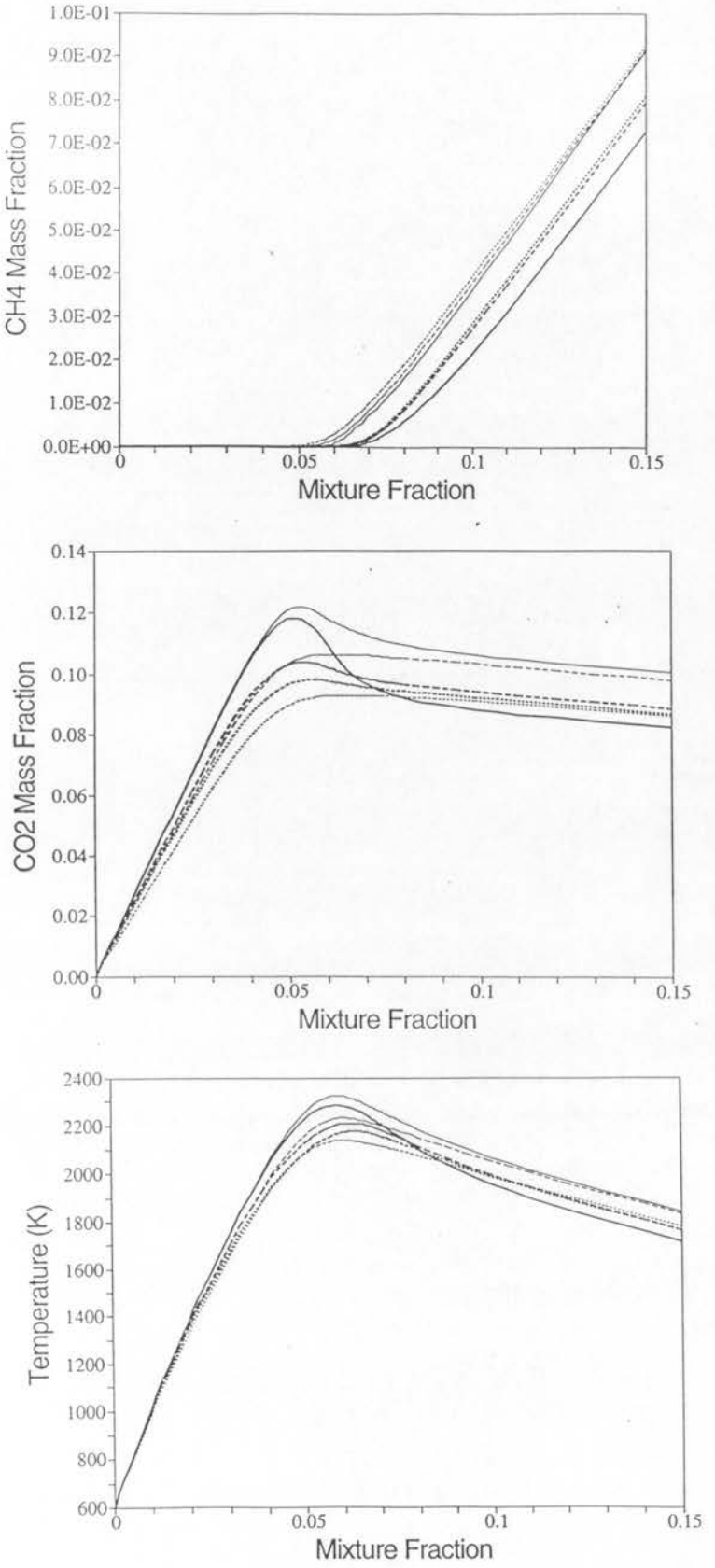

Figure 5.12: Conditional mean reactive scalar profiles for a methane burning ISR at various residence times, based on full and skeletal mechanisms. Line width denotes mechanism, bold - Miller and Bowman, plain - Skeletal. Line types denote residence time, solid - $\tau_r = 5ms$, dashed - $\tau_r = 1.5ms$, dotted - $\tau_r = 1ms$

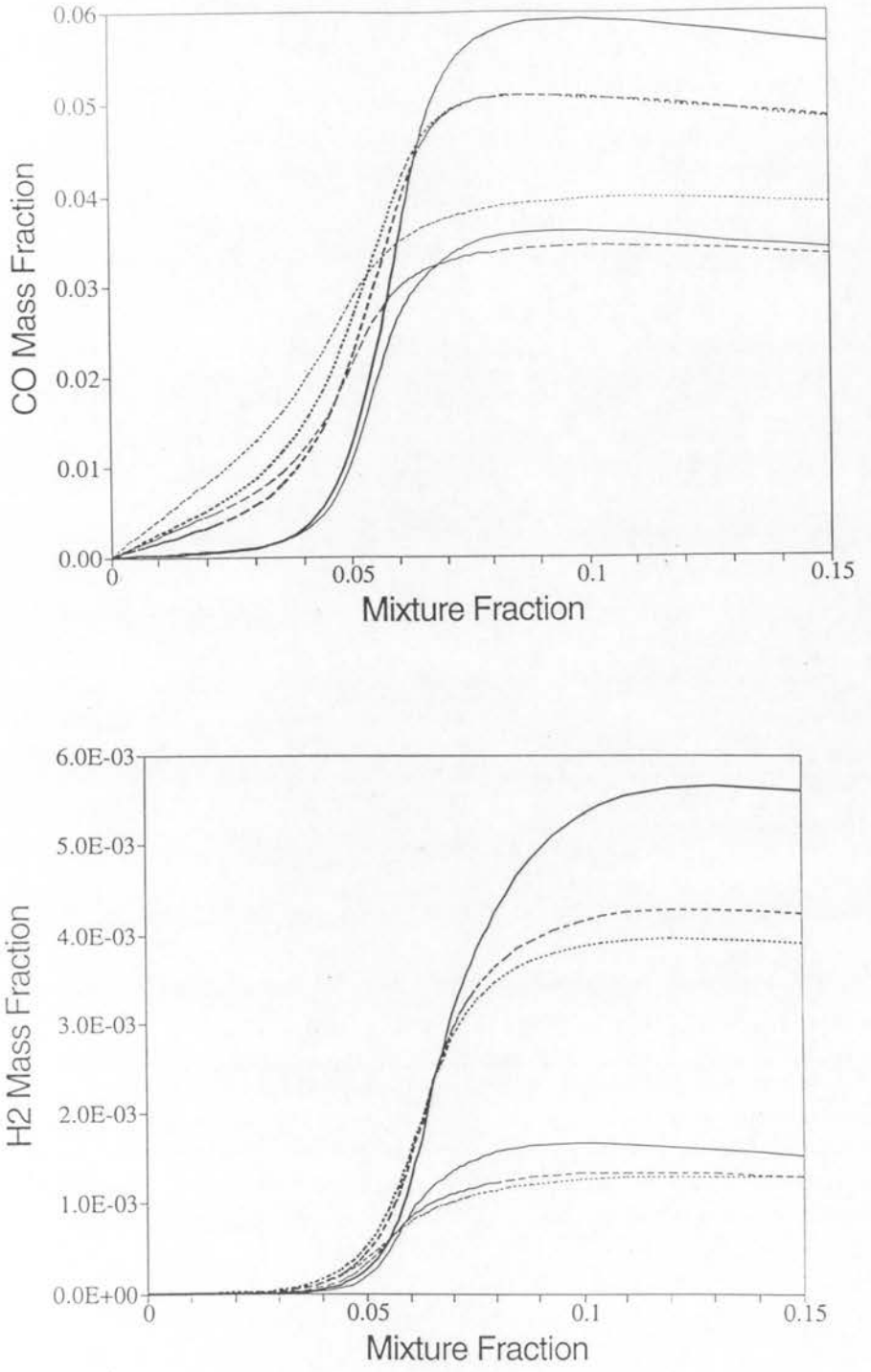

Figure 5.13: Conditional mean reactive scalar profiles for a methane burning ISR at various residence times, based on full and skeletal mechanisms. Line width denotes mechanism, bold - Miller and Bowman, plain - Skeletal. Line types denote residence time, solid - $\tau_r = 5ms$, dashed - $\tau_r = 1.5ms$, dotted - $\tau_r = 1ms$

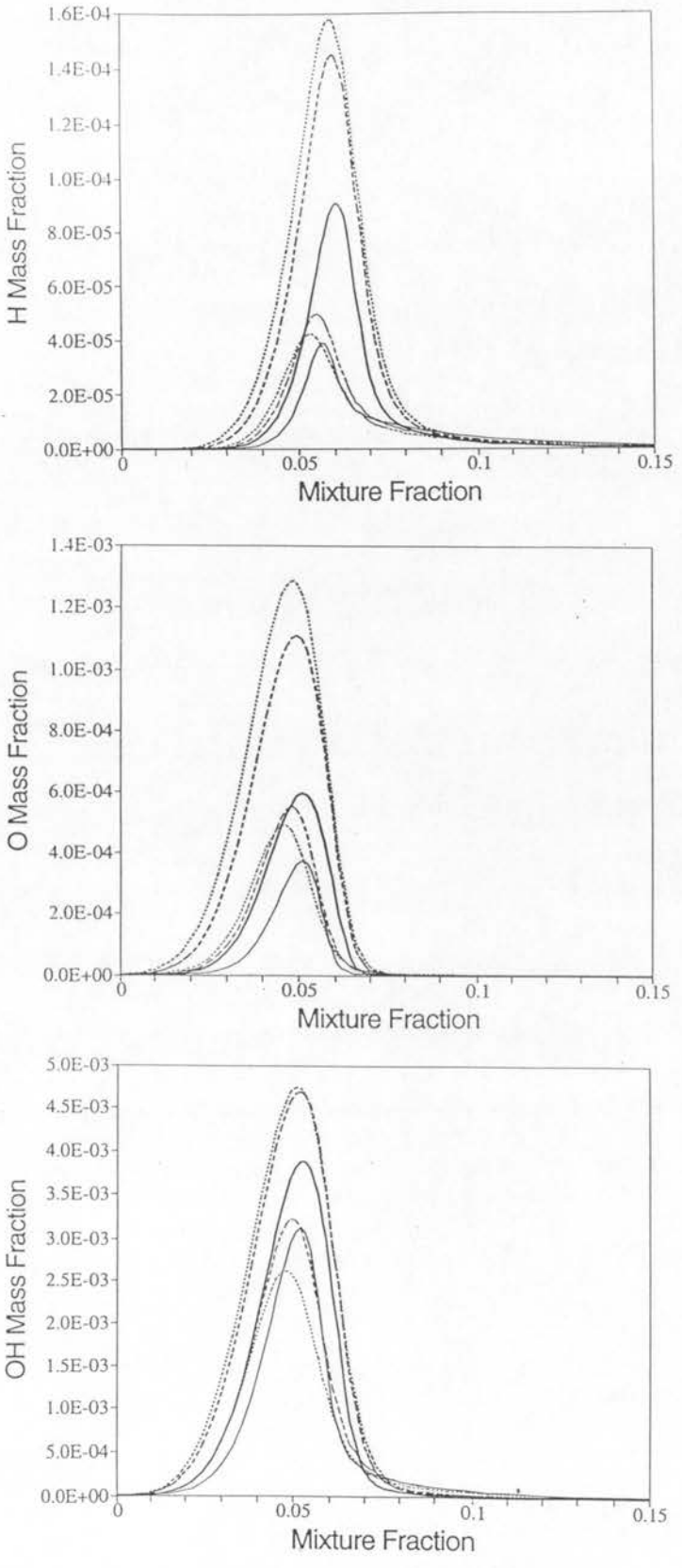

Figure 5.14: Conditional mean reactive scalar profiles for a methane burning ISR at various residence times, based on full and skeletal mechanisms. Line width denotes mechanism, bold - Miller and Bowman, plain - Skeletal. Line types denote residence time, solid - $\tau_r = 5ms$, dashed - $\tau_r = 1.5ms$, dotted - $\tau_r = 1ms$

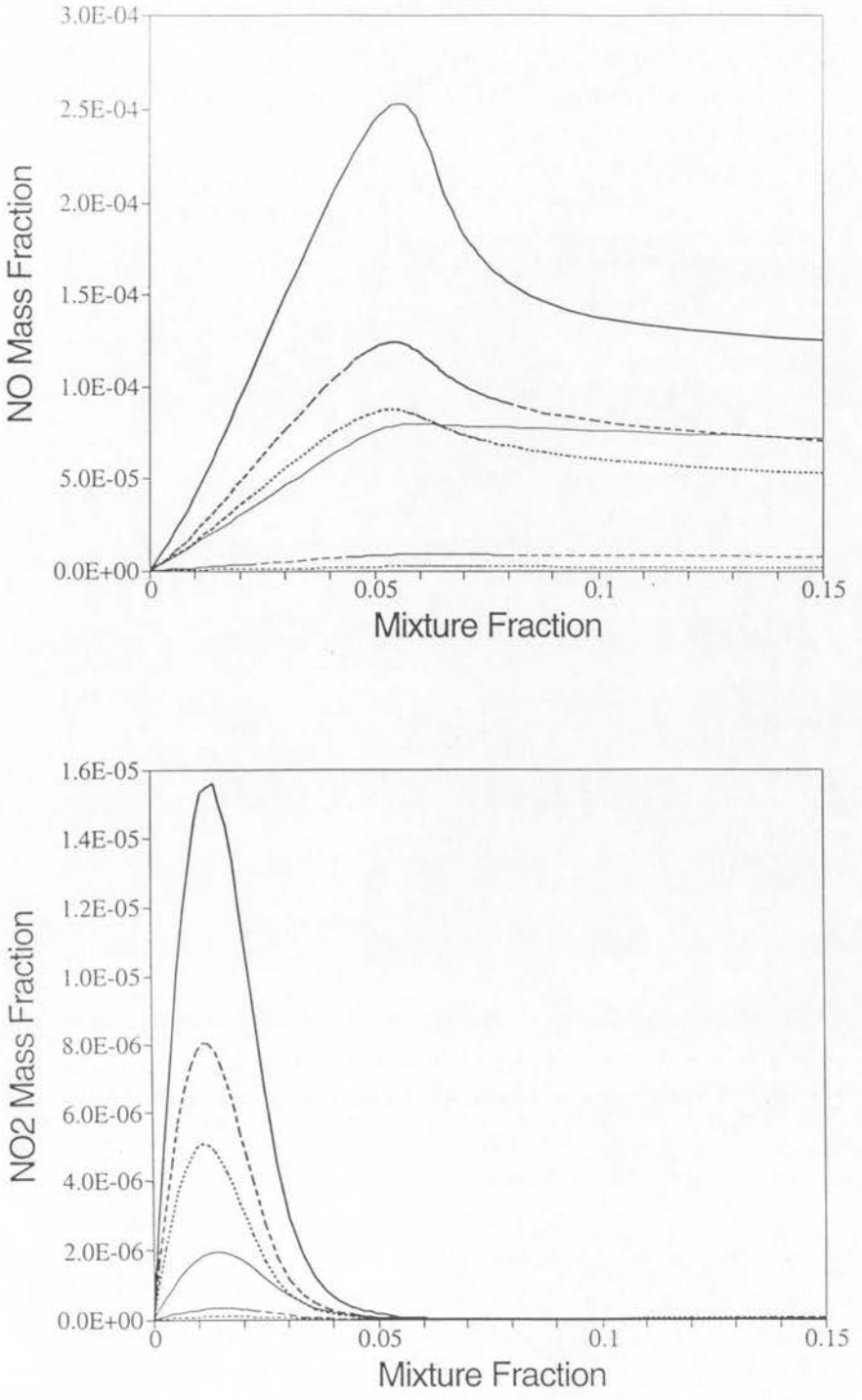

Figure 5.15: Conditional mean reactive scalar profiles for a methane burning ISR at various residence times, based on full and skeletal mechanisms. Line width denotes mechanism, bold - Miller and Bowman, plain - Skeletal. Line types denote residence time, solid - $\tau_r = 5ms$, dashed - $\tau_r = 1.5ms$, dotted - $\tau_r = 1ms$

Both chemical mechanisms predict that methane consumption is impeded by turbulence chemistry interactions. The full mechanism consistently predicts higher CH_4 consumption than the skeletal mechanism, and increasing residence time causes substantially greater variation in the full mechanism predictions. From Fig. 5.12 it is observed that the peak conditional mean flame temperature, calculated for the D10 case with a skeletal mechanism, is around $\sim 50K$ higher than that calculated with the full mechanism. At richer mixture fractions, the discrepancy further increases to be in the vicinity of $\sim 150K$. For the shorter residence time cases, the temperature predictions of the skeletal mechanism become closer to that of the full mechanism to the point where, for the B10 case, the skeletal profile falls slightly below the full profile. The higher temperatures predicted by the skeletal mechanism are largely due to the higher predictions for the formation exothermic products such as CO_2, and the lower predicted rates of endothermic consumption of the major reactants. In other words, a higher proportion of the consumed reactant mass is yielded as exothermic end-products by the skeletal mechanism compared to the full mechanism.

It is evident that the skeletal mechanism predicts higher rich-side CO_2 levels for the longer residence time cases, but underpredicts full mechanism values for the B10 case. For all cases, the predicted peak conditional mean CO_2 mass fractions are depressed below the peak equilibrium value of $Y_{eq,CO2} \approx 0.13$. The fact that skeletal CO_2 mass fraction and temperature predictions are depressed further, than the full mechanism predictions, over the same range of increasing mixing rates suggest that the skeletal mechanism is more susceptible to the influence of turbulent mixing.

Carbon dioxide is formed through the oxidation of CO, and as such CO_2 mass fraction predictions depend upon the net rate of this oxidation and indirectly upon the net rate of formation of CO. It can be surmised from Figs 5.12 & 5.13 that the CO levels predicted by the skeletal mechanism for cases C10 and D10 are lower than full mechanism predictions due to proportionally faster oxidation rates. Yet for B10, the CO oxidation steps of the skeletal mechanism are apparently impeded to a greater extent than the CO formation reactions, thus leading to a drop in CO_2 levels whilst the CO profile is slightly elevated. It can be seen that a similar phenomenon is occuring in the full mechanism calculations to a lesser extent, in that CO levels are relatively constant from C10 to B10, but CO_2 predictions drop over

the same change in residence time. The mass fraction profiles predicted by the full mechanism for the major intermediate species ($CO.H_2$) are substantially greater than the skeletal predictions. The skeletal mechanism cannot be used with confidence if these intermediate species levels are to be predicted accurately, such as in designing a combustor to meet CO emission regulations.

Differences between principal radical (H,O,OH) predictions from the two mechanisms are also apparent in Fig. 5.14, with the Miller-Bowman mechanism predicting much higher peak mass fractions. Also, whilst the full mechanism predicts monotonic increases in radical levels with increasing mixing intensity, this is not the case for the skeletal predictions. For each of the radicals species, the skeletal predictions for peak mass fraction are greatest for the intermediate mixing case C10, with lower levels for the faster and slower mixing cases of B10 and D10. Declining O and OH radical profiles were encountered in some of the more intensely mixed hydrogen cases of Section 5.1, and this behaviour suggests that the skeletal mechanism is closer to extinction compared to the full mechanism under the same mixing conditions. The skeletal variation in peak mass fractions is accompanied by a lean shift in the locations of the peaks. A similar shift can be seen in the full mechanism predictions and is perhaps due to the different nature of radical consumption on rich and lean sides of the reaction zone. Lean side consumption is rate limited by the three-body recombination reaction found also in the hydrogen-air system (reaction 5 of Table A.1), but rich side consumption results from the alkane attack and CO production reactions (21-29) which are mainly two-body in nature and significantly faster. It follows that with increased turbulence-chemistry interference, rich side radical consumption will be less impeded than lean side rates and so radical levels will be proportionally lower at higher mixture fractions.

Full and skeletal mechanism predictions for the conditional mean mass fraction profiles of NO and NO_2 show little quantitative agreement (see Fig. 5.15). The lack of nitrous oxide and prompt NO formation pathways in the augmented skeletal mechanism results in a predicted peak mass fraction for the D10 case that is only one quarter of the full mechanism prediction. Even greater discrepancies result for the more rapid mixing cases of C10 and B10. The strong lean side peak and rich side positive curvature attributed to prompt and nitrous oxide pathways, in the

preceeding section, are clearly absent from the predictions made with the thermal pathway alone. Nitrogen dioxide predictions are even more disparate than for NO, no doubt being in part due to the dependence of NO_2 formation on the different NO concentrations at very lean mixture fractions.

5.2.3 Mean Outlet Statistics

The influence of varying the overall fuel air equivalence ratio of the ISR can be seen for cases B10-D20 in Figs 5.16 & 5.17, where calculations have been made with both the full and skeletal mechanisms. Increasing the reactor residence time leads to greater proportional fuel consumption and higher outlet temperatures, irrespective of the overall air fuel ratio. In a gas turbine combustor, the remaining fuel will be burnt beyond the recirculation zone as more air enters through the primary holes in the surrounding liner. As the fuel is burnt, the mean temperature will increase somewhat before the fully burnt products are mixed with dilution air from secondary holes. The outlet temperatures calculated here are of the same order as those reported by Samuelson and coworkers for various laboratory operated optical-access gas turbine combustors[132,133]. For increasing fuel air equivalence ratios, proportional fuel consumption decreases somewhat despite the fact that absolute fuel consumption rates increase. The reduction in proportional fuel consumption becomes more apparent with increasing residence time, due to the greater departure of the CH_4 conditional mean profiles, from the notional 'zero-consumption' line, at lower mixing rates. Increased equivalence ratios give rise to greater outlet temperatures due to the diminished importance of the $600K$ unmixed oxidizer stream in the convolution of the mixture fraction PDF with the conditional mean temperature profile.

An aggregate mass fraction for NO_x is calculated from NO and NO_2 mass fractions by assuming that the former species is completely converted to the latter under atmospheric conditions, thus,

$$Y_{NOx} \equiv Y_{NO2} + \frac{W_{NO2}}{W_{NO}} Y_{NO}. \tag{5.6}$$

Unconditional mean NO_x mass fraction clearly increases with reactor residence time. It is also clear that the skeletal mechanism's lower NO_x predictions close upon the full mechanism predictions with increasing residence time, a result of the increased

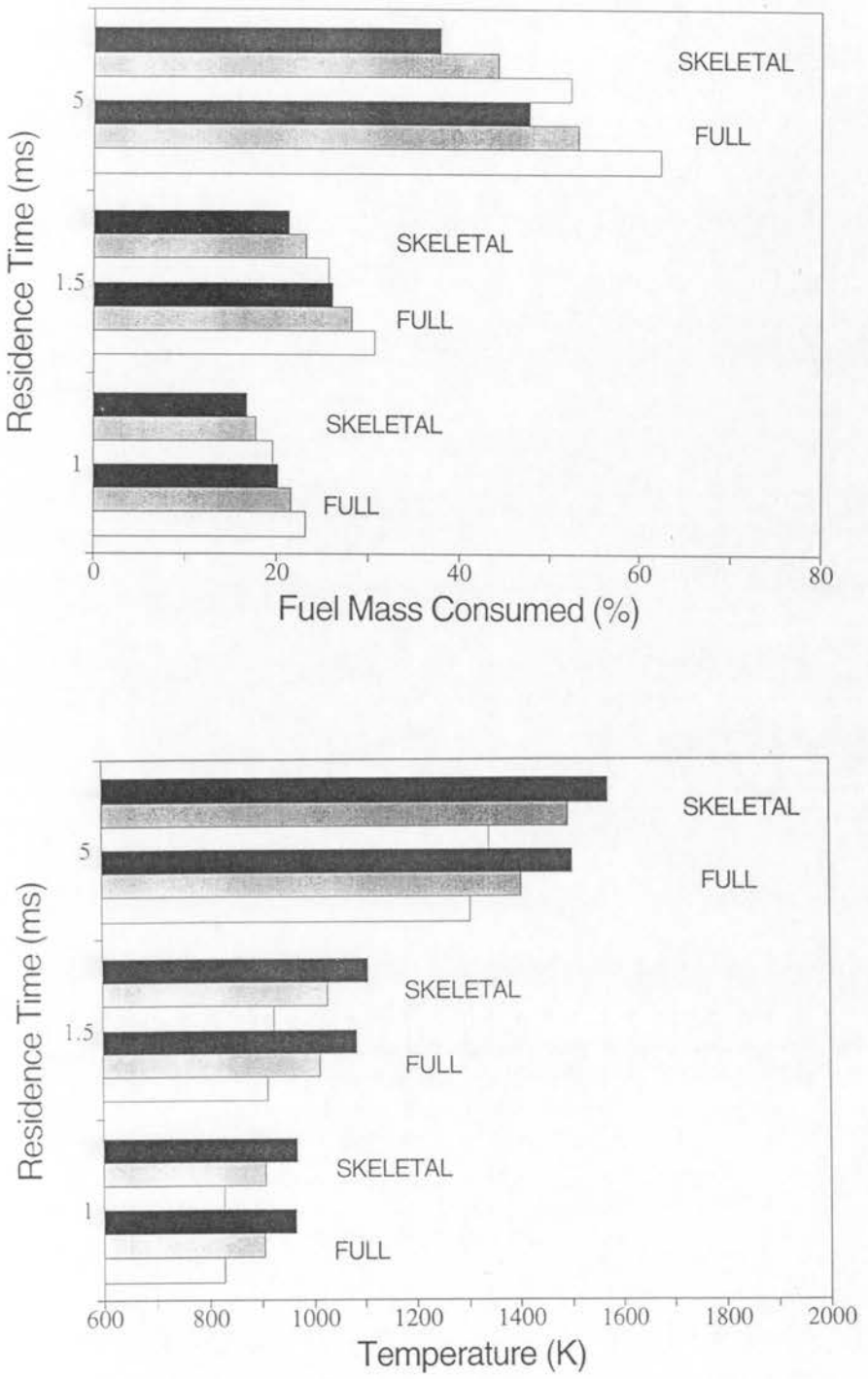

Figure 5.16: Unconditional mean outlet temperature and proportional fuel mass consumption from a methane burning ISR for different residence times and equivalence ratios. Bar colours denote equivalence ratio; white - 1, gray - 1.5, black - 2

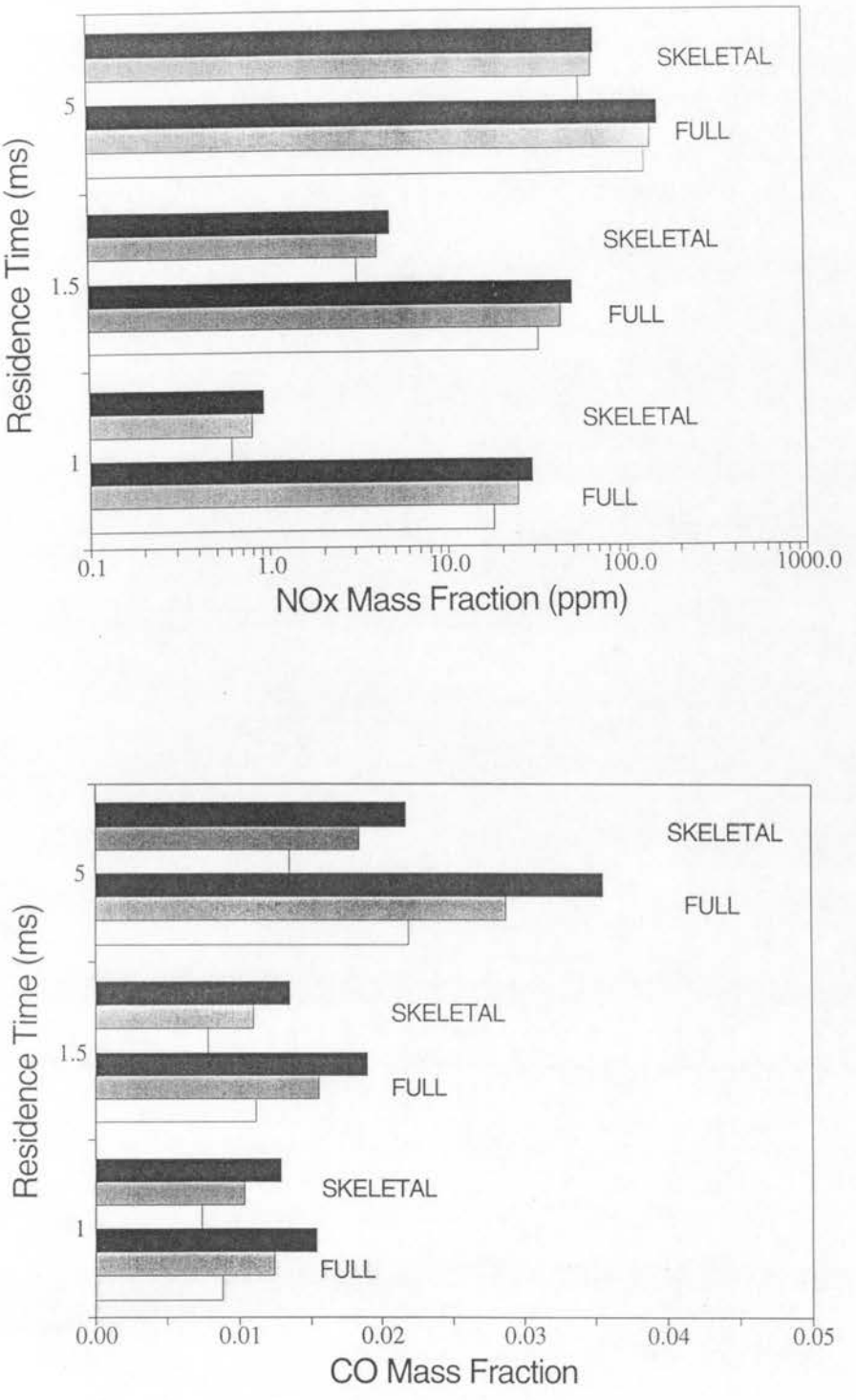

Figure 5.17: Unconditional mean outlet CO and NO_x mass fractions from a methane burning ISR for different residence times and equivalence ratios. Bar colours denote equivalence ratio; white - 1, gray - 1.5, black - 2

significance of the thermal Zeldovich pathway to overall NO production at higher flame temperatures. Increased fuel air ratios cause relatively modest increases in NO_x emission. This is no doubt due to the decreased weight of the NO_x-free oxidizer stream in the determination of the unconditional mean for higher equivalence ratio cases. It is likely that far more NO_x will be generated downstream of the recirculation zone as primary air is mixed in and the flame temperature increases.

In contrast, carbon monoxide levels will decrease somewhat downstream as the species is gradually oxidized to CO_2 in the dilution zones. As the bulk of the emitted CO is formed in the recirculation zone and immediately thereafter, the results plotted in Fig. 5.17 are of some interest. It is evident that CO emission levels increase with residence time and equivalence ratio. The former effect is due to the trends observed in the conditional mean profiles earlier, whilst the latter can be attributed to the diminishing levels of pure air in the unconditional mean calculation. Clearly, the skeletal mechanism seriously underpredicts CO levels, particularly for longer residence time cases.

Acetylene (C_2H_2) is the principal C_2 species produced by the ISR using the full Miller-Bowman mechanism. As was mentioned earlier, soot formation is not treated in this analysis despite its importance both as a radiation sink and as a regulated combustor emission species. Acetylene combustion is typically associated with soot formation, and so the unconditional mean C_2H_2 mass fractions presented here are both an indicator of C_2 species formation and the predisposition towards soot. It is clear that C_2H_2 emission increases with both increasing residence time and equivalence ratio. As with the other emitted pollutants described above, it is clear that the skeletal mechanism cannot be used to predict C_2 species and soot formation.

5.3 Discussion

The results of the hydrogen and methane calculations demonstrate the effect of varying the principal governing parameters, upon nonpremixed combustion systems. It is evident that reducing the reactor residence time, or increasing the core averaged unmixedness (υ), or the change in mixture fraction variance through the reactor, causes increased levels of conditional mean scalar dissipation to occur. As a result of the

increased scalar dissipation rates, chemical systems become increasingly perturbed from equilibrium.

Further departures can result from the convective difference term on the left hand side of Eqn 4.6, which depends in part upon the conditional mean reactive scalar profiles at the reactor inlet. Together, the terms of the full ISR equation equation form a three-way balance between the processes of chemical reaction, turbulent mixing and fluid inflow and outflow. Depending upon the conditions existing in a target reaction zone, ISR modelling can resemble a flamelet-like arrangement with a diffusive-reactive balance of source terms, or PSR-ensemble case with a purely reactive-convective balance, or more commonly a hybrid of these two. In this way, the Imperfectly Stirred Reactor model can be viewed as a super-set containing both perfectly stirred reactors (PSRs) and flamelet models as special cases.

Zone models such as ISRs and PaSRs have a significant advantage over fluid dynamically more precise multi-dimensional formulations in modelling nonpremixed combustion devices. These dimensionally degenerate methods are capable of applying far more complex chemical mechanisms to the problem within the constraints imposed by available computational resources.

By employing a conditional moment closure methodology, the ISR model can comfortably handle much larger mechanisms than the largest that can be employed by PaSR methods. Being approximately two orders of magnitude faster than PaSR methods for similarly complex calculations, ISR modelling can be facilitated on workstation-sized computers rather than incur the expense of supercomputing. This kind of low cost computing with detailed chemistry is important if reactor models are to be used in practical design applications. The importance of chemical mechanism detail has been demonstrated in the previous section for a parametric study of a methane burning gas combustor recirculation zone.

It is clear that significant discrepancies exist between the full mechanism of Miller and Bowman[131] and the skeletal mechanism. This is to be expected, since the skeletal mechanism was reduced from the complete set of reactions under the stipulation that it would be accurate for lean combustion only[119]. Given the substantial saving in computation time afforded by the latter, the skeletal approximation gives good agreement particularly for conditionally averaged statistics in the lean zone of

mixture fraction space. It is reasonable to assume then, that due to the large overall excess of air in the combustor as a whole, the differences between the unconditional mean predictions using the two mechanisms may be diminished at the combustor outlet.

However, the importance of C_2 chemistry is evident in the rich zone and it appears that the accurate prediction of intermediate carbon species, such as carbon monoxide (CO), may require the full mechanism. A peak conditional mean CO mass fraction of 6% is predicted by the full mechanism calculation, which is substantially greater than the skeletal prediction of 3%. The skeletal underprediction may partially explain the 'CO overshoot' of experimental measurements in turbulent methane jet flames compared to predictions by steady laminar flamelet methods using C_1 chemistry schemes[40,51]. Chen and Dibble[51] performed steady and transient PSR calculations, using C_1 chemistry, to explain the existence of superflamelet CO in turbulent nonpremixed flames. The findings of this chapter suggest that C_2 chemical effects should also be incorporated.

The prompt and nitrous oxide pathways for NO_x formation are clearly very important in the cases studied here. By itself, the Zeldovich thermal mechanism cannot account for the differences between full and skeletal chemistry NO predictions. The former predicts much higher NO levels whilst the latter has a much higher temperature prediction, albeit with lower monatomic oxygen levels. The preliminary evidence presented in this chapter suggests that the relative importance of thermal NO_x formation compared to other pathways decreases with increasing mixing intensity.

Chapter 6

Axisymmetric Jet Flames

In this chapter, nonpremixed conditional moment closure methods are applied to turbulent reacting flows that are two-dimensional in the mean. Whilst some comments made towards the end of the chapter are made in relation to these flows in general, the bulk of this chapter is devoted to steady axisymmetric nonpremixed jet flames. Over the last decade, the axisymetric jet flame has been a paradigm of nonpremixed turbulent combustion research. This type of flame has been attractive because whilst being relatively simple in form, with only a small number of specifying parameters, it has many features in common with complex flames of more practical significance.

Axisymmetric jet flames are well suited to both experimental and numerical analysis. In the case of the former, axisymmetric jet flames have only a small number of controlling parameters, namely nozzle diameter, jet mass flow rate fuel type and coflow velocity, thereby making them independently reproducible. In addition these flames need not be physically confined and so allow easy access to physical and optical diagnostic tools. From a numerical modelling standpoint, jet flames involve the essential elements of turbulence-chemistry interactions without requiring the solution of an elliptical set of partial differential equations. Typically, these streaming flows can be solved using boundary layer-like approximations to the Navier-Stokes equations and much of the turbulence modelling techniques, used in non-reactive boundary layer modelling, such as Reynolds stress closures and $k-\epsilon$ methods can be carried over with only minor modifications. The comparative simplicity of the steady axisymmetric flow arrangement has allowed more developmental and computational effort to be devoted to improving general combustion models, and has provided a

wealth of experimental data with which to evaluate model predictions.

In due course, the combustion models developed and tested in axisymmetric jet flames must be applied to more complex flames, like unsteady axisymmetric and asymmetric bluff-body and swirl stabilized flames, if they are to be of a practical interest. This process has begun in past years with, for example, a variant of the joint PDF method (see Section 2.2.2) being applied to a steady bluff-body stabilized flame[46]. Application of the nonpremixed CMC method to structurally more complex flows is beyond the immediate scope of this thesis but comments will be made in later a chapter which are directly relevant to this next stage of development.

In the following section, the CMC equations appropriate to the specific case of nonpremixed axisymmetric jet flames will be derived. In Section 6.2, the means by which conditional mean mixing and convection statistics are determined from unconditional data will be described and the general mixing characteristics of turbulent jet flames will be analyzed. This chapter concludes with a short discussion of the conditions under which the singly conditioned CMC jet flame model is applicable.

The effects of turbulence-chemistry interactions in turbulent hydrogen (H_2) and hydrogen-carbon monoxide ($H_2 - CO$) fuelled jet flames will be analyzed in Chapter 7. Aside from a study of the influence of mixing rates upon chemical reactions, analyses of the effects of reduced chemical mechanisms upon general flame structure and overall emissions are included. Subsequent to these analyses, points of interest are discussed in relation to overall model performance, and future development issues are briefly introduced.

6.1 Jet Flame Equation Derivation

The derivation of the appropriate CMC equations for axisymmetric jet flames, begins with Eqn 3.48 of Chapter Three which is reproduced below.

$$< \rho \mid \eta > \frac{\partial Q_i}{\partial t} + < \rho \underline{u} \mid \eta > \cdot \nabla Q_i = < \rho w_i \mid \eta > + \frac{1}{2} < \rho \chi \mid \eta > \frac{\partial^2 Q_i}{\partial \eta^2} + < e_y \mid \eta > + < e_Q \mid \eta > \tag{6.1}$$

The effects of inhomogeneous conditional means embodied by the grouped error term $< e_Q \mid \eta >$ diminish with increasing Reynolds number[9] and these effects are excluded from further analysis under the assumption that the flow is sufficiently

turbulent. In the presence of substantial mean mixture fraction and reactive scalar gradients, the relative influence of the instantaneous deviational term $< e_y \mid \eta >$ is likely to be small and is also neglected. This term cannot be neglected in cases where significant premixing of reactants are in evidence, like that which occurs in extinguished mixtures that are reignited in intensely mixed jet flame combustion. In these instances $< e_y \mid \eta >$ is one of the principal term responsible for mixing burnt and unburnt fluid. Nonpremixed flames exhibiting extinction and ignition behaviour are beyond the predictive capability of singly conditioned moment closure in any case, as was mentioned in Section 3.2.3.

By restricting this analysis to steady axisymmetric jet flames, the first term on the left hand side of Eqn 6.1 is eliminated and the convective term can also be substantially simplified. One of the principal advantages of the jet flame formulation is that despite large spatial variations in unconditional mean data, conditionally averaged statistics appear to be almost independent of radial position within the jet. The theoretical basis for this property was first noted by Klimenko[6,7], and experimental measurements of reactive species concentrations in jet flames were cited in evidence by Bilger[8,9]. The small degree of radial dependence, exhibited by conditionally averaged statistics in jet flames with simple boundary layer structures, allows Eqn 6.1 to be reduced to a quasi one-dimensional problem with conditional averages being calculated as functions of mixture fraction and axial location x alone. The first implementation of CMC methods in jet flames neglected radial dependence altogether[96] and solved the following equation for $Q_i = Q_i(x, \eta)$.

$$< \rho u \mid \eta > \frac{\partial Q_i}{\partial x} =< \rho w_i \mid \eta > + \frac{1}{2} < \rho \chi \mid \eta > \frac{\partial^2 Q_i}{\partial \eta^2} \qquad (6.2)$$

The conditionally averaged statistics ($< \rho u \mid \eta >$, $< \rho \chi \mid \eta >$) required for the solution of Eqn 6.2 were estimated by approximating them as being equal to the average of known unconditional mean statistics ($< \rho u >$, $< \rho \chi >$) at radial locations where the mean mixture fraction $\bar{\xi}$ was equal to the sample space variable η.

Since that first approximation, improvements have been made such that the existence of small radial dependence is acknowledged and radial convection is dealt with by solving cross-stream averaged equations. These equations (see Eqn 6.6), proposed by Klimenko[6], incorporate the influence of small radial variations in conditional mean mass flux $< \rho u \mid \eta >$ and scalar dissipation $< \rho \chi \mid \eta >$ to produce

averaged statistics which are then used to calculate radially representative conditional reactive scalars. The averaging operator $\{\ldots\}_R$ is defined below for cylindrical polar coordinates using any arbitrary function $M(r)$,

$$\{M\}_R \equiv \frac{2}{R^2}\int_0^R M(r) r dr \tag{6.3}$$

The bounding radius R is typically assumed to be large so that the bulk of the overall mass flow lies within its circumscribed perimeter, and radial gradients are very small.

Cross stream averaging of the divergence form of the CMC equation, which retains explicit reference to the mixture fraction PDF (Eqn 3.42), yields

$$\frac{\partial}{\partial x}(\{<\rho u \mid \eta> Q_i P_\eta\}_R) = \{<\rho w_i \mid \eta> P_\eta\} + \frac{1}{2}\{\frac{\partial}{\partial \eta}[<\rho\chi \mid \eta> P_\eta \frac{\partial Q_i}{\partial \eta} - Q_i \frac{\partial}{\partial \eta}(<\rho\chi \mid \eta> P_\eta)]\}_R \tag{6.4}$$

where the steady state assumption has been applied to eliminate time derivatives. The cross-stream convection term is eliminated for $\eta > 0$ due to mixture fraction PDF behaviour for large values of the bounding radius R [6,117]. A PDF weighted area average $\{M\}_R^+$ can be defined for any arbitrary function $M(r)$ as follows:

$$\{M\}_R^+ \equiv \{M(r)P_\eta(r)\}_R / \{P_\eta(r)\}_R \tag{6.5}$$

Using this definition and the conservation of the mixture fraction PDF, Eqn 6.4 becomes.

$$\{<\rho u \mid \eta>\}_R^+ \frac{\partial Q_i}{\partial x} = <\rho w_i \mid \eta> + \frac{1}{2}\{<\rho\chi \mid \eta>\}_R^+ \frac{\partial^2 Q_i}{\partial \eta^2} \tag{6.6}$$

where conditional mean reactive scalars are assumed to be radially independent.

The cross-stream averaging defined above is not dissimilar, in concept, to the volume averaging employed for the ISR model of Chapter 4. In this case however, the flow retains its evolutionary character between the jet nozzle and downstream zones. Further, in the case of ISRs, spatial independence of the conditional mean reactive scalar fields required demonstration before the model could be applied to a target system. In contrast, the absence of substantial radial dependence in axisymmetric jet flames is generally accepted and is not at issue[1].

Using Eqn 6.6, conditional mean reactive scalar quantities can be determined at any point in a steady axisymmetric jet flame provided the conditional mean mass

[1] New evidence suggests that this may not be the case in the near-field, see Section 6.4

flux and scalar dissipation profiles can be calculated. The boundary conditions for Eqn 6.6 are given below,

$$Q_i(x, \eta = 0) = Y_{i,ox}(x) \tag{6.7}$$

$$Q_h(x, \eta = 0) = h_{i,ox}(x) \tag{6.8}$$

$$Q_i(x, \eta = 1) = Y_{i,fu}(x) \tag{6.9}$$

$$Q_h(x, \eta = 1) = h_{i,fu}(x) \tag{6.10}$$

$$\tag{6.11}$$

where the possibility exists that the pure fuel and oxidizer stream values may be capable of varying with axial location as a result of radiative cooling or pyrolysis and the like. The conditional mean profiles are unknown at the nozzle exit plane ($x = 0$), with only the bounding mixture fractions ($\eta = 0, 1$) being present. A starting estimate of the conditional mean profiles is usually taken from adiabatic chemical equilibrium calculations, however the form of the starting profiles appears to have no influence on calculated results at locations more than a fraction of a nozzle diameter downstream.

Equation 3.16 of Section 3.2 provides the means for determining $\{< \rho\chi \mid \eta >\}_R^+$, after appropriate simplification and cross-stream averaging.

$$\frac{\partial}{\partial x}(\{< \rho u \mid \eta > P_\eta\}_R) = -\frac{1}{2}\frac{\partial^2}{\partial \eta^2}(\{< \rho\chi \mid \eta > P_\eta\}_R) \tag{6.12}$$

The cross stream convective terms associated with the PDF conservation equation are eliminated due to the behaviour of the PDF at large bounding radii[6,117]. Given mixture fraction probability density functions within the jet, the cross-stream averaged conditional mean scalar dissipation profile can be determined by double integrating both sides of Eqn 6.12 with respect to mixture fraction.

The unknown cross-stream averaged conditional mean scalar mass flux profiles are estimated from,

$$\{< \rho u \mid \eta >\}_R^+ \approx \{< \rho u >\}_R^+ \tag{6.13}$$

which neglects fluctuations in the longitudinal velocity component. The calculation of conditional mean mass flux and scalar dissipation profiles entails certain practical problems that make it a non-trivial exercise. The properties of these quantities and the difficulties that arise in their calculation are discussed in the following section.

6.2 Calculation of Mixing Statistics

In order to solve the CMC equation governing reactive scalar evolution in a turbulent nonpremixed jet flame (Eqn 6.6), the conditional mean scalar dissipation ($\{< \rho u \mid \eta >\}_R$) and mass flux ($\{< \rho u \mid \eta >\}_R$) profiles must be determined from the available unconditional mean information.

In the jet flame model used in this investigation, a FORTRAN code known as JFLAME, unconditional mean information is provided by a block tridiagonal (BTD) solver which uses a Reynolds stress closure to model the turbulence dynamics. This solver was written by Chen *et al*[134], has been used extensively in the past[48,50,51,52,56]. The BTD solver is not specific to CMC methods, having been principally developed for use with joint PDF methods. Unconditional mean velocities ($< u >$,$< v >$) and mixture fraction ($< \xi >$), as well as variance information is provided along with unconditional mean scalar dissipation ($< \chi >$) data to the CMC solution routine. In return this routine, named QKIN, supplies unconditional mean density information to the tridiagonal solver.

By employing an assumed form mixture fraction probability density function, with mean and variance specified by the unconditional mean data, the required mixing and convection statistics can be determined using Eqns 6.13 and 6.12. After double integration with respect to mixture fraction, the latter equation becomes,

$$\{< \rho\chi \mid \eta > P_\eta\}_R = -2[\int_0^\eta \int_0^\eta \frac{\partial}{\partial x}(\{< \rho u \mid \eta' > P_{\eta'}\}_R) d\eta' d\eta'] \qquad (6.14)$$

The double integration of the streamwise derivative in Eqn 6.14 is carried out between the bounds of 0 and η, and excludes the influence of the possible singularity at the origin. The appropriate boundary conditions on Eqn 6.14 are $\{< \rho\backslash \mid \eta > P_\eta\}_R = 0$ at $\eta = 0.1$ for large values of R[117,135].

The mixture fraction PDFs used in this implementation have clipped Gaussian assumed forms, as was the case in Chapter 4 for ISR modelling. In contrast to ISR applications, the assumed form PDFs of this chapter are supposed to represent the actual uncalculated PDFs, instead of simply being generic examples used in lieu of actual values. Wheras in ISR applications, actual PDFs should be determined and used, it is not currently envisaged that jet flame CMC methods will have actual PDF

information available for use.

Earlier results from CMC jet flame modelling were obtained using Beta function assumed form PDFs[96,102], however in those instances conditional mean scalar dissipation was not calculated via Eqn 6.14, but instead was approximated from unconditional mean values ($< \rho >< \chi >$) in the same way that conditional mass flux is approximated in Eqn 6.13. Beta functions were chosen because of their smooth transition from double-delta-function-like forms near unmixed fluid interfaces to quasi-Gaussian forms in well mixed fluid without their being a requirement to consider end intermittencies. Other researchers have employed Beta function assumed forms in the past (see for example Janicka and Kollmann[18]) with some success, and Girimaji has favourably compared beta function performance against DNS results for passive scalar mixing in statistically stationary (scalar mixing is non-stationary) isotropic turbulence[136].

Initially Beta functions were also used as the assumed form PDFs in attempts to solve Eqn 6.14, however after some effort they were discarded as being unsuitable. Much of the difficulty in their use arose from the non-integrable nature of their derivatives with respect to mean and variance. It has been found that accurate numerical *double* integration, with respect to mixture fraction, of small streamwise differences in PDF form is a difficult task. In contrast to the ISR mixing calculations of Chapter 4, where PDF variance changes were over orders of magnitude, differential streamwise changes in variance are typically of only a few percent.

Clipped Gaussian functions were used because they were found to be more amenable to the solution of Eqn 6.14, and because of the general acceptance of this assumed form as a reasonable representation of true mixture fraction PDFs[15] under general mixing conditions. It should be pointed out that the clipped Gaussian forms employed in this thesis are distinct from those used by Bilger and coworkers[15,137] which made use of empirical estimates of free stream intermittency. Here, the end intermittencies are exactly equal to the clipped areas under the PDF curve to the left of zero and right of unity mixture fractions, with the area under the curve between these points being less than unity.

In the course of developing a robust solution method for Eqn 6.14, two distinct methodologies emerged. These two methods both represent an advance over the

earlier weighted averaging techniques (see above), but neither of the methods is clearly superior to the other. In the following sections, both the 'lumped' and 'local' solution methods for Eqn 6.14 will be described. Section 6.3 contains a comparison of the mixing statistics predicted by these two methods and the earlier weighted averaging technique.

6.2.1 Local Calculation of Scalar Dissipation Rate

Solution of Eqn 6.14, via the 'local' method, proceeds by first substituting in the approximate form of the conditional mass flux (see Eqn 6.13), followed by a re-arrangement of the order of integration and differentiation to give,

$$\{< \rho\chi \mid \eta >\}_R^+ = \frac{-2}{\{P_\eta\}_R}\{< \rho u > \frac{\partial}{\partial x}(\int_0^\eta \int_0^\eta P_{\eta'} d\eta' d\eta')\}_R \qquad (6.15)$$

where streamwise changes in $< \rho u >$ have been neglected.

At each radial point, the unconditional mean mixture fraction, scalar dissipation, streamwise velocity, density and mixture fraction variance are employed to evaluate the term within the $\{\ldots\}_R$ brackets on the right hand side of Eqn 6.15.

The local method is a robust technique that guarantees the non-negativity of the calculated conditional mean scalar dissipation profiles and their consistency with the unconditional mean scalar dissipation field. These desirable properties are ensured by separately treating each point in physical space which contributes to the cross-stream averaged statistic. This is in contrast to the 'lumped' method which treats cross-stream averaged statistics directly.

At each point in physical space, the local method only considers the components of the streamwise change in the mixture fraction PDF which will have an effect upon the cross-stream averaged statistic. Any change in mixture fraction variance that is associated with radial convective transport or diffusion is neglected, since these effects sum to zero when averaged across the flow. Only those streamwise changes in mixture fraction variance that can be attributed to the local unconditional mean scalar dissipation are included in the calculation of the conditional mean scalar dissipation rate profile.

The streamwise change mixture fraction variance, at a radial location r, that

can be attributed to scalar dissipation alone can estimated from the following:

$$\frac{\delta < \xi'^2(r) >^*}{\delta x} \approx \frac{- < \chi(r) >}{< u(r) >} \tag{6.16}$$

At each radial point, the estimate above is used to determine the streamwise change in the double integral of the mixture fraction PDF at the mean mixture fraction of that point. The PDF value itself is also calculated, so that its its cross-stream average can be used in the denomenator coeficient on the right hand side of Eqn 6.15. Since use of Eqn 6.16 guarantees that the inner term of Eqn 6.15 will be non-positive and proportional to the local unconditionally averaged scalar dissipation rate ($< \chi >$), the cross-stream averaged $\{< \rho\chi \mid \eta > P_\eta\}_R$ profile is assured of being non-negative and of having an area equal to the cross-stream averaged unconditional scalar dissipation rate.

$$\int_0^1 \{< \rho\chi \mid \eta > P_\eta\}_R d\eta \approx \{< \rho >< \chi >\}_R \tag{6.17}$$

In effect, the local method can be thought of as a discretization of the jet flow into a large number of radially spaced imperfectly stirred reactors. These conceptual reactors have mean mixture fractions which are determined by the local unconditional mean values and changes variance that are calculated from the local value of unconditional mean scalar dissipation rate.

Apart from its application in jet flame modelling, the 'local' method of scalar dissipation calculation seems well suited for use in more complex elliptic flow calculations. The generalization of the 'lumped' method, described below, to more complex flow geometries is more difficult proposition.

6.2.2 Lumped Calculation of Scalar Dissipation Rate

The 'lumped' solution method for Eqn 6.14 is a more direct technique, than the local method, and makes fewer algebraic approximations. However, it does not guarantee non-negativity of the resulting conditional mean scalar dissipation profiles, nor consistency with the unconditional mean scalar dissipation statistics.

In the lumped approximation, shown below, the influence of streamwise variation in velocity is retained.

$$\{< \rho\chi \mid \eta >\}_R^+ = \frac{-2}{\{P_\eta\}_R} \frac{\partial}{\partial x} \{(< \rho u > \int_0^\eta \int_0^\eta P_{\eta'} d\eta' d\eta')\}_R \tag{6.18}$$

In contrast to the 'local' method, the lumped method sees the PDF second integrals being calculated using the actual mixture fraction unconditional means and variances at each point, followed by the averaging of these integrals across the flow. The difference between the cross-stream averaged PDF second integrals at the current and preceding axial locations provides the cross stream averaged conditional mean scalar dissipation profile.

Some difficulties can arise in applying the lumped method to jet flame modelling. The method is sensitive to errors in the discretization or modelling of mixture fraction mean and variance fields at the boundaries of the computational domain. Any small irregularities in the calculation of the PDF second integrals at these points can corrupt the entire calculation, leading to poor accuracy.

In applying the lumped method, it was found that determining accurate near-field scalar dissipation rate profiles was particularly difficult. In many instances, partially negative scalar dissipation profiles could result from regulated changes in outer boundary entrainment rates. Further, checking calculations such as Eqn 6.17 revealed that the lumped method tends to overpredict the cross-stream averaged unconditional mean scalar dissipation rate. This is perhaps due to either the sources of error mentioned above, or a possible inconsistency between the Reynolds flux calculations for mixture fraction mean and variance (which are used directly by the lumped method) and those for the unconditional mean scalar dissipation rate.

The lumped method should be the natural choice for jet flame calculations of conditional mean scalar dissipation rate. However, care must be taken to ensure that the unconditional mean statistics, upon which it relies, are calculated in a consistent and well behaved manner. It will be shown that the accuracy of the lumped method is questionable in the current implementation.

6.3 Comparison of Mixing Models

At this point, it is appropriate to reconcile the mixing and convection statistics calculated using past methods[96,102] with those used at present (see also [104,105]). Unfortunately, it is not possible to compare either calculation method with experimental or DNS results for the purpose of verification. Some experimental results

Designation	A
Nozzle diameter	3.75 mm
Fuel composition	$100\%H_2$
Jet velocity	300 m/s
Coflow velocity	1.0 m/s
Stoich. Mixture Fraction	0.028
Visible flamelength	$\sim 180D$
Jet Reynolds number	10000

Table 6.1: Characteristics of experimentally measured H_2 jet flame.

should come to hand in the near future (see Stårner *et al*[138,139]), which will give the needed insight upon turbulent diffusion flame structure, but at present there are no such data. Direct Numerical Simulation (DNS) of the mean shearing highly turbulent combustion that is of interest here, is currently not feasible.

In order to compare different conditional mean scalar dissipation calculation methods, excluding chemical kinetic effects, comparisons were made for both pure-hydrogen flames computed with chemical equilibrium conditional mean scalar profiles. Thus in the mixing model comparisons that follow, density feedback effects resulting from mixing interaction with chemical reactions are not considered.

The pure hydrogen flame used for comparison is identical to that studied experimentally by Barlow and Carter[150,151,152]. Both CMC and Joint PDF turbulent combustion model predictions for this flame have been made in the past and have been compared with the available data[102,104]. The macroscopic characteristics of this hydrogen jet flame are summarized in Table 6.1.

The stoichiometric flamelength (L_{st}) is defined as the axial distance from the nozzle to where the unconditional mean mixture fraction at the jet centreline is equal to the stoichiometric mixture fraction. In the case of the flame A, the stoichiometric length is around $L_{st} \approx 133$ nozzle diameters. The predicted stoichiometric flamelength agrees well with experimentally measured mean mixture fraction data[55,104,150,152], and can be seen to be approximately twenty five percent less than the corresponding visible flamelength L_{vs}. Visible flamelength L_{vs} has no precise definition, but rather is simply the apparent end of the luminous contour of the flame and is usually estimated with the naked eye. As the luminous contour is sub-

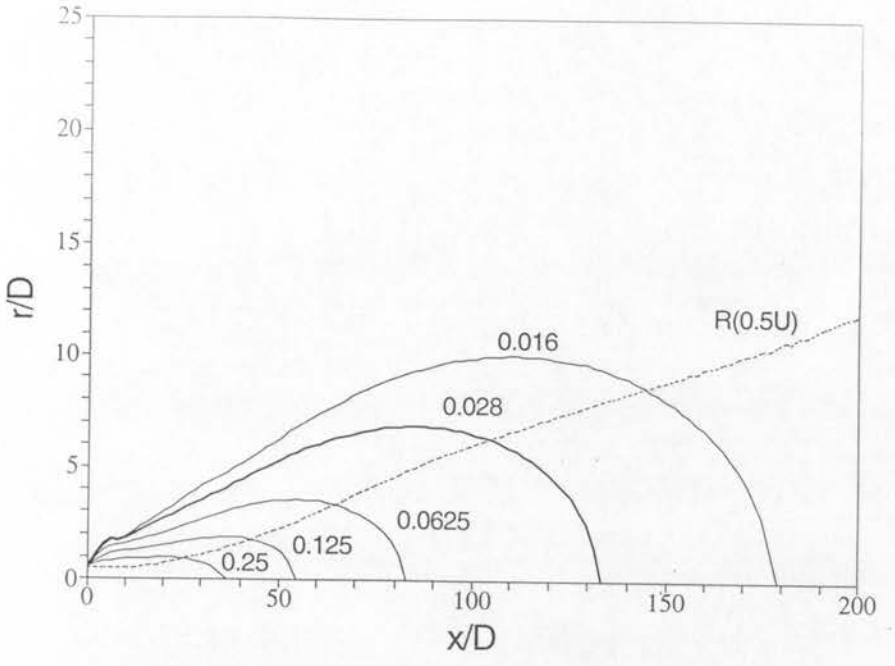

Figure 6.1: Unconditional Mean Mixture Fraction Contours for Jet Flame A The half-velocity radius ($R_{0.5U}$) is plotted using dashed lines.

ject to instantaneous turbulent fluctuations and can vary according to flame colour, luminous intensity, and background lighting, determination of its maximum length is a somewhat subjective measurement.

Calculated mean mixture fraction contours for flame A are plotted in Fig. 6.1 in physical space with an expanded radial ordinate. The half-velocity radius ($R_{0.5U}$) is also plotted to facilitate a comparison of the physical proximity of the mean shear layer to the mean stoichiometric contour in each case. It is evident that the mean stoichiometric mixture fraction contour lies beyond the principal shearing zone of the jet for more than half of the stoichiometric flamelength.

Predicted cross-stream averaged unconditional mean scalar dissipation rate $\{< \chi >\}_R$ is plotted as a function of axial location in Fig. 6.2. The profiles labelled 'local' and 'lumped' have been calculated by convolving cross-stream averaged conditional mean scalar dissipation with the cross-stream averaged PDF according to Eqn 6.17. The 'true' profile has been calculated by averaging unconditional mean scalar dissipation values across the flow width.

There are no discernable differences, between the true $\{< \chi >\}_R$ profile and

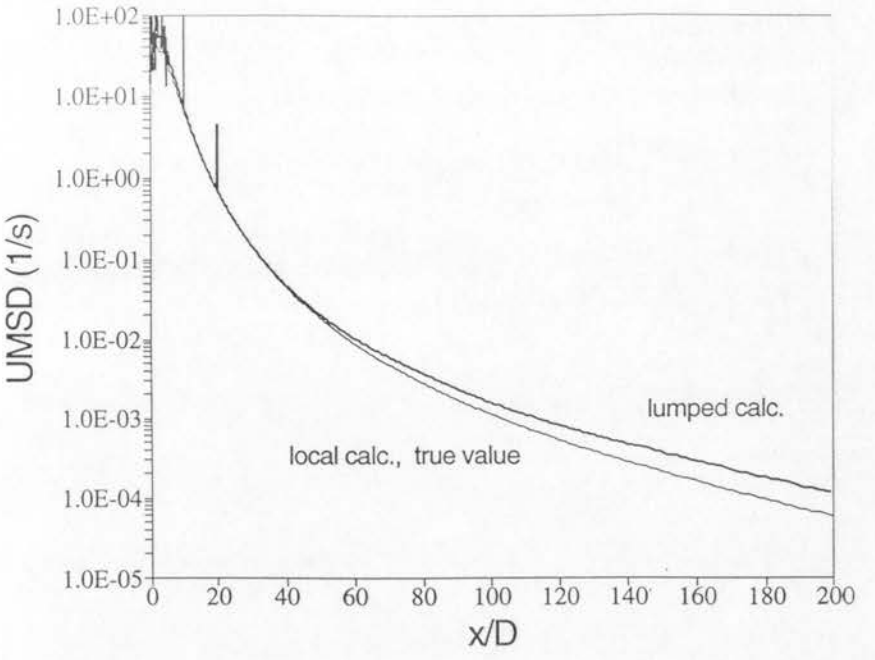

Figure 6.2: Calculated cross-stream averaged unconditional mean scalar dissipation rate as a function of non-dimensional axial distance from the nozzle (x/D).

that calculated by the 'local' method, on the semi-log plot shown in Fig. 6.2. Small differences do exist but they are of the order of five percent. The 'lumped' profile shows reasonable agreement in the upstream zones of the flame, but tends to increasingly overpredict $\{< \chi >\}_R$ with increasing axial distance from the nozzle.

This tendency towards overprediction seems to stem from the susceptibility of this method to numerical error in the determination of $\{< \chi \mid \eta >\}_R^+$. As the lumped method involves finding a small streamwise difference between two large averaged profiles (see Eqn 6.18), deviations from the expected profile are likely to occur downstream where the magnitude of sought after difference becomes small. It is conceivable that there may also be an inconsistency between the unconditional mean calculation of scalar dissipation rate and those for mixture fraction mean and variance. Such an inconsistency would contribute to the observed discrepancy, since the lumped method makes use of the latter two statistics without any reference to the former.

Important differences between the different methods for $\{< \chi \mid \eta >\}_R^+$ calculation can be seen in Fig. 6.3 which compares predictions at four axial locations in

jet flame A. Two important trends in conditional mean scalar dissipation rate profile evolution can be observed from Fig. 6.3. Firstly, the influence of the approximate x^{-4} power dependence of unconditional mean scalar dissipation upon axial distance from the nozzle (see Fig. 6.2) can be seen in the declining levels of the plateaux regions of the scalar dissipation profiles. This decline is evident in the predictions of all three of the scalar dissipation calculation methods, however the relative position of the predicted profiles, with respect to each, other changes somewhat.

In upstream zones ($x/D < 90$), the weighted averaging technique (see Eqn 6.13, and Refs [102,104]) predicts significantly lower value than those predicted by the local and lumped methods described in Sections 6.2.1 & 6.2.2. Further downstream, the weighted averaging technique yields predictions which are in good agreement with those of the local calculation method, whilst the lumped predictions fall below these values.

The second trend of note in Fig. 6.3 is the effect of jet dispersion. At increasing distances from the nozzle, rich mixture fraction fluid becomes increasingly rare due to jet mixing with the zero-mixture fraction surroundings. Correspondingly, the cross-stream averaged mixture fraction PDF ($\{P_\eta\}_R$) peak shifts towards lean mixture fractions, and PDF values decrease at rich mixture fractions. At axial locations where PDF values tend to zero, the weighted averaging method for scalar dissipation prediction cannot be applied, and the scalar dissipation profile at these mixture fractions is statistically indeterminate.

The ability to predict conditional mean scalar dissipation rates in these mixture fraction zones is not considered important since the conditional mean statistics there do not contribute significantly to any unconditional mean statistics. In practice, these rich mixture fraction zones are deemed physically unrealizable and are dropped from CMC calculations.

This treatment is also applied to low probability zones in the local and lumped methods for $\{< \chi \mid \eta >\}_R^+$ calculation. This is done to avoid the small numerical errors present in the $\{P_\eta < \chi \mid \eta >\}_R$ profile predictions, at rich mixture fractions, from being magnified by division by the very low PDF values at these mixture fractions. For the CMC calculations reported here and in the following chapter, an arbitrary minimum PDF threshold was set at 10^{-10} and mixture fraction grid points with cross-

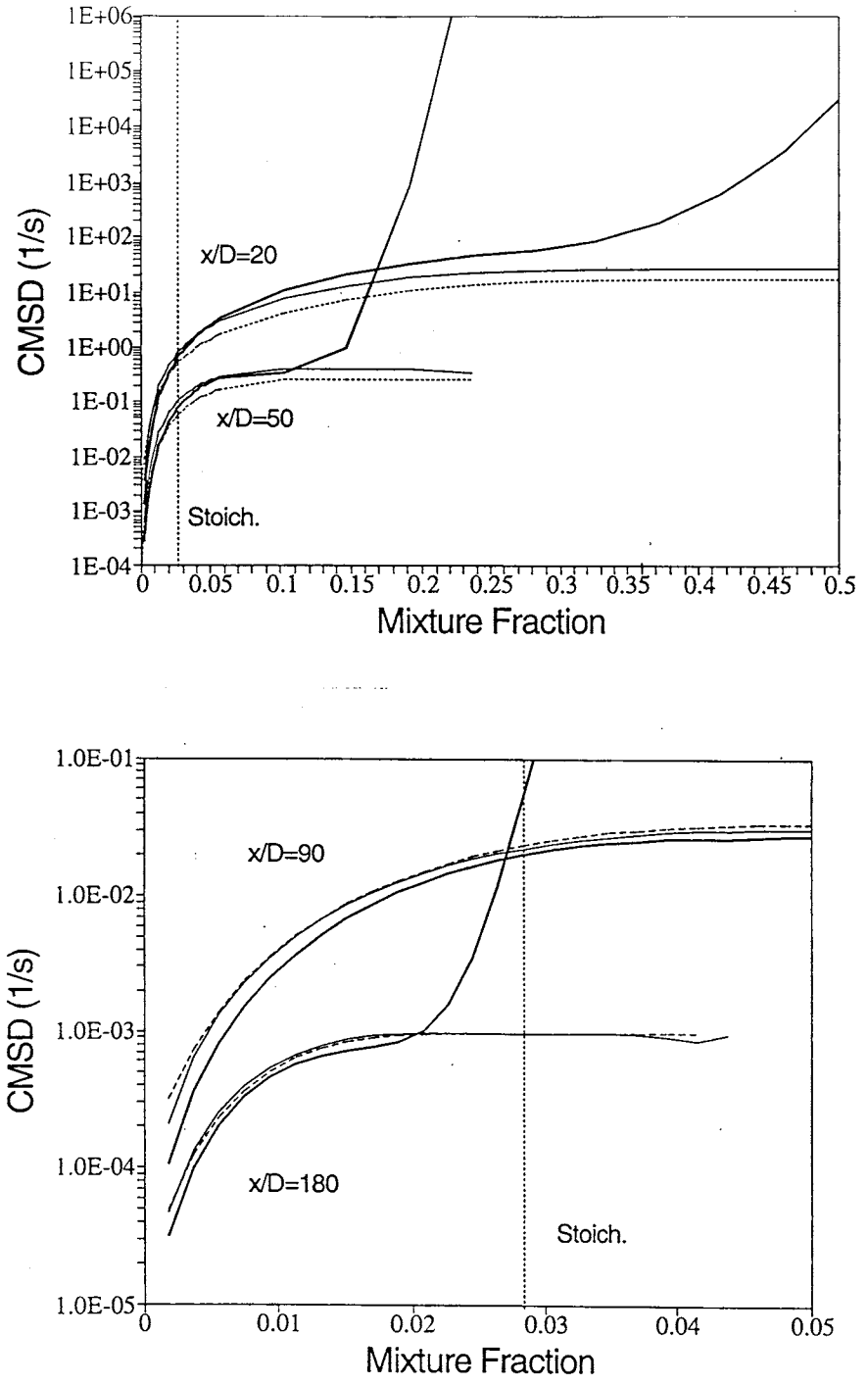

Figure 6.3: Predictions of conditional mean scalar dissipation rate at $x/D = 20, 50, 90, 180$ in jet flame A. Line types denote prediction method : bold - lumped, plain - local dotted - averaged

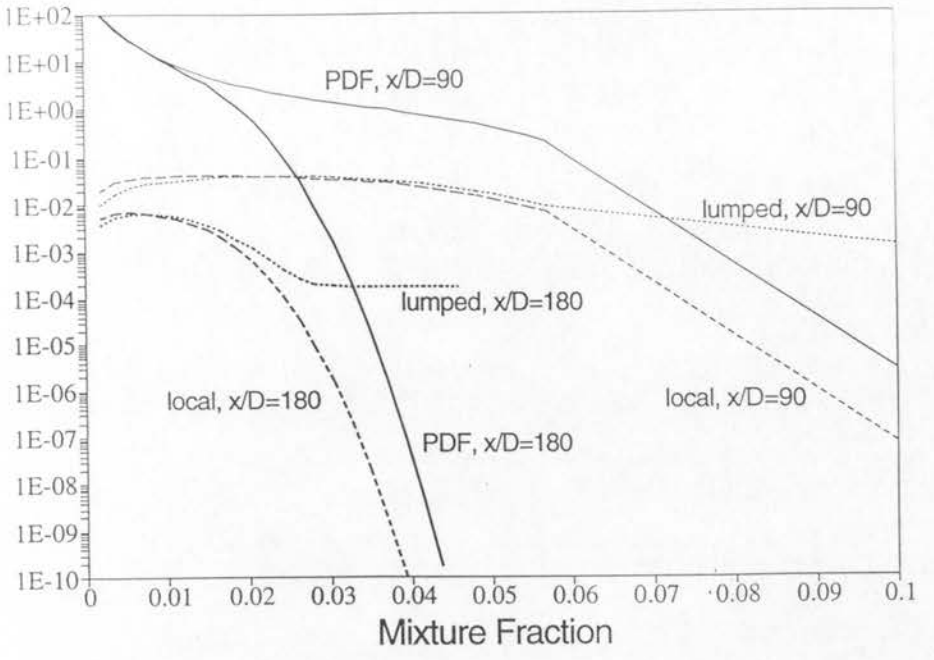

Figure 6.4: Predicted PDF ($\{P_\eta\}_R$) and $\{P_\eta < \chi \mid \eta >\}_R$ at $x/D = 90, 180$.

stream averaged PDF values below this level were excluded from the calculation.

In Fig. 6.3, the location of this PDF lower threshold in mixture fraction space can be inferred from the mixture fraction values where the predicted profiles are terminated. It is apparent that the local and lumped predictions of $\{< \chi \mid \eta >\}_R^+$ differ greatly in low probability zones near the PDF threshold. The poor agreement, at rich mixture fractions, between the lumped method prediction and those of the local and weighted average methods is a result of the larger numerical errors inherent in the method.

In Fig. 6.4, the differences between the rich mixture fraction predictions of $\{P_\eta < \chi \mid \eta >\}_R$ can be readily compared. The minimal decrease in the lumped model prediction of $\{P_\eta < \chi \mid \eta >\}_R$ with decreasing mixture fraction PDF leads to the high $\{< \chi \mid \eta >\}_R^+$ tails observed in Fig. 6.3. These tails are similar to those found in the predicted conditional mean scalar dissipation profiles of low outlet unmixedness imperfectly stirred reactors (see Section 4.2), and similarly are not likely to be physically realizable. The physical measurement of conditional mean scalar dissipation rates in very low probability mixture fraction zones is a difficult task, and so it is not likely that experimental findings in this area will become available in the

near future.

Based on the results of the comparison presented in this section, it appears that the local method of calculation of conditional mean scalar dissipation is best suited for use in CMC axisymmetric jet flame modelling. In the following chapter, this mixing method is used exclusively to analyze the effects of turbulence chemistry interactions in H_2 and $H_2 - CO$ jet flames as predicted by the CMC model.

6.4 Discussion

In this chapter, a conditional moment closure (CMC) model has been described for axisymmetric nonpremixed turbulent jet flames. The main points of this model can be summarized as follows:

1. As with earlier CMC models, the jet flame model makes use of a single conditioning variable, namely mixture fraction. Statistics conditioned upon mixture fraction alone cannot be used to effect a first order chemical closure, as described in Section 3.2.3, when in the presence of high levels of reactant premixing or extinction and ignition phenomena. Thus strictly speaking, the current model is inapplicable in cases such as lifted diffusion flames and bluff body stabilized flames with high mixing rates, since extinction and premixing is known to occur at the base of these flames.

2. One of the key simplifying assumptions made in this jet flame model, is that conditionally averaged statistics show only a very weak radial dependence. This assumption, which is supported by theoretical[6,7] and experimental evidence[8,9], allows the reactive scalar conservation equations (Eqn 6.1) to be reduced to an essentially one dimensional form. It seems optimistic to expect the validity of the radial independence assumption to extend to more complex elliptic flow fields. Intuitively, radial independence would seem to be associated with the existence of a boundary layer like flow pattern. Indeed, recent experimental evidence suggests that some radial dependence exists for conditional mean temperature in the immediate near-field of axisymmetric hydrogen jet flames[152]. These preliminary experimental results show that the radial dependence of conditional mean statistics disappears for locations removed from the near field.

The influence of near-field radial dependence on the overall modelling of these jet flames seems to be insignificant. However, these findings do not bode well for future model development in more complex flow arrangements.

3. A comparison has been made of three contemporary methods for calculating the conditional mean scalar dissipation rate which is required for the closure of Eqn 6.6. In the past, an approximate averaging technique has been employed to calculate conditional mean scalar dissipation[102,104], however this method does not guarantee conservation of mixture fraction as is required by Eqn 6.12. Of the two new proposed calculation methods which obey Eqn 6.12, the 'local' method (see Section 6.2.1) has been found to be the most robust and accurate for the conditions studied here. This method will be adopted in the analyses of the following chapter.

Further discussion of the above points can be found in Chapter 9, where they will be presented in the context of future model development.

Chapter 7

Jet Flame Calculations

The principal focus of past nonpremixed jet flame research has been the examination of the interaction that occurs between chemical reaction, turbulent mixing, radiative heat transfer and other associated processes. The interactions between these basic aerothermochemical processes govern important phenomena such as fuel efficiency, byproduct formation, sooting tendency, extinction and ignition characteristics etc.

One of the foremost areas of current jet flame research is the study of nitrogen oxide (NO_x) formation (see Refs [51,53,65,96,102,104,137] and [140]-[152] inclusive). Although this research has been largely driven by the need to find a means of limiting NO_x formation in practical nonpremixed combustion devices[129], nitric oxide (NO) is interesting from a theoretical point of view because its formation is kinetically limited. In other words, rather than having its formation rate being governed by mixing processes, NO is formed at a rate that is limited by its rate of chemical reaction.

The accurate prediction of NO formation in turbulent jet diffusion flames is a good test for 'coupled' turbulent combustion models such as the joint PDF method[51] and the CMC method[96,102,104]. These coupled models account for turbulence-chemistry interactions whilst globally tracking species concentrations throughout the flame. If a coupled model correctly treats the fundamental aspects of chemical reaction, turbulent mixing and radiative heat transfer, then it should be able to predict NO yield in jet flames with some confidence.

Unfortunately, it is difficult to ensure that all three of these aspects are treated appropriately at the same time, since in many cases simplifying assumptions are nec-

essary in order to make the modelled problem tractable. The modelling assumptions made in connection with turbulent mixing processes within the CMC method have been discussed in the preceding chapter (see Section 6.2). The bulk of these modelling assumptions are inherent in the overall model and are best investigated by independent means such as direct numerical simulation[34,57].

Chemical kinetic assumptions can be investigated with the existing CMC model because of its ability to inexpensively employ detailed chemical mechanisms. The accuracy of the reduced mechanisms similar to those employed by other jet flame models[51] can be readily determined. The usual assumption made in connection with radiative heat transfer is that of optical-thinness, ie: energy radiated from gaseous species at one point is not absorbed by those species at another point within the flame. There has been some suggestion that this assumption may be inappropriate in hydrogen jet flames (see Appendix B), and it is clearly inadequate in flames with radiation losses from solid phase particles.

In this chapter, CMC model predictions are presented for hydrogen (H_2) and hydrogen/carbon monoxide/nitrogen ($CO - H_2 - N_2$) fuelled flames over a range of flow conditions (Sections 7.1,7.2). Comparison of the results presented here (see also Refs. [96,102,104]) with existing experimental measurements, serves as a means of validating the jet flame model described in Chapter 6. Apart from comparing the direct chemical evidence of turbulence-chemistry interaction, such as super-equilibrium radical formation, temperature depression and so on, a comparison of predicted and measured NO_x formation will be presented and discussed (Section 7.5).

The form and behaviour of the conditional mean terms of the CMC reactive scalar equations are examined in Section 7.3. The importance of chemical mechanism detail to overall model performance will be evaluated (Section 7.4). A two step reduced mechanism is compared with a full twenty-three step mechanism in the case of H_2 combustion, and a three step mechanism is compared with a twenty-five step mechanism for the $CO - H_2$ jet flames. Radiation losses are also investigated in an attempt to determine the validity of the optical-thinness assumption (Section 7.6).

The chapter is concluded with a general discussion of the advantages and disadvantages of the CMC jet flame model (Section 7.7) and a brief summary in point form (Section 7.8).

Designation	Flame A
Nozzle diameter (D)	3.75mm
Fuel composition	$100\%H_2$
Jet velocity (U_j)	300m/s
Coflow velocity	1.0 m/s
Stoich. Mixture Fraction ($\xi_{stoic.}$)	0.028
Visible flamelength (L_{vs})	$\sim 180D$
Cold Jet Reynolds number (Re_D)	10000

Table 7.1: Characteristics of experimentally measured H_2 jet flame.

7.1 Hydrogen Flames

A series of calculations were made for turbulent nonpremixed H_2 jet flames similar to that studied by Barlow and Carter[150,151,152]. The characteristics of Barlow and Carter's flame are given in Table 7.1, which has been transposed from Section 6.3.

The CMC calculations were made with fifty grid points unevenly spread across the mixture fraction domain, with the bulk of these points being concentrated around the stoichiometric mixture fraction. A further fifty grid points were employed in stream function space in the solution of the von Mises-transformed boundary layer equations for the unconditional mean turbulent field. These unconditional mean equations were solved using a Reynolds stress/flux closure, which is described extensively by the authors of the code[134]. The relationship between the CMC subroutine (QKIN) and the jet flame program[134] (JFLAME) is described in Appendix C, where a listing of the former code can be found.

The H_2 chemical mechanism employed consisted of twelve chemical species and twenty-three reversible reaction steps, and is listed in Table A.1 of Appendix A as reactions $1-17$ and $30-34$. Thermo-chemical data and reaction rate evaluations were provided by CHEMKIN-II subroutines[121]. Radiation losses were treated using an optically-thin approximation for emission from gaseous H_2O which was proposed by Kuznetzov and Sabelnikov[26] and is described in Appendix B.

The full mechanism H_2 calculations required approximately six CPU hours to reach completion on a DEC Alpha workstation, running at $\sim$ 15 Mflops. The overwhelming majority of this computation time was consumed by the integration of the

numerically stiff CMC equations. The computational cost associated with this integration is demonstrated by the fact that a fast chemistry calculation, which involves no integration of the stiff turbulence-chemistry interaction equations, requires only ~ 5 CPU minutes when using the same jet flame code.

Smaller CMC calculations have been performed in the past[102,104] with the same chemical mechanism but only 24 mixture fraction grid points, and these runs were found to require only around one CPU hour of computation to reach completion.

7.1.1 Predicted H_2 Jet Flame Characteristics

Before comparing specific CMC predictions with corresponding experimental measurements, it is appropriate to describe the general behaviour of the predicted conditional mean statistics in various locations within the jet flame. These statistics show departure from chemical equilibrium that is qualitatively similar to that observed in ISR predictions for H_2 combustion (see Section 5.1). However, the level of departure varies with axial location in accordance with streamwise changes in turbulent mixing intensity.

This trend can be seen from the predicted conditional mean reactive scalar profiles, corresponding to jet flame A, plotted in Fig. 7.1, for various axial fractions of the visible flamelength (L_{vs}) listed in Table 7.1. Note that the reactive scalar profiles of this chapter are given in terms of mole fraction, rather than the mass fraction form in which they appear in the CMC equations. This has been done so as to facilitate comparison with experimental data.

It can be seen that in upstream locations of the flame, the major product species (H_2O) is greatly depressed below the adiabatic equilibrium profile. This depression is indicative of the interference of turbulent mixing processes with the mole consuming reactions that form H_2O. At the same time, the principal radical species (H,O,OH) are present in super-equilibrium concentrations as they adjust, via rapid two-body reactions, to the subequilibrium levels of H_2O. It is evident that turbulent mixing processes transport the conditional mean radical species to lean and rich mixture fractions outside the reaction zone. Increased mixing rates appear to cause the monatomic hydrogen profile peak to shift to richer mixture fractions, but no shifts are evident for the hydroxyl or monatomic oxygen radicals.

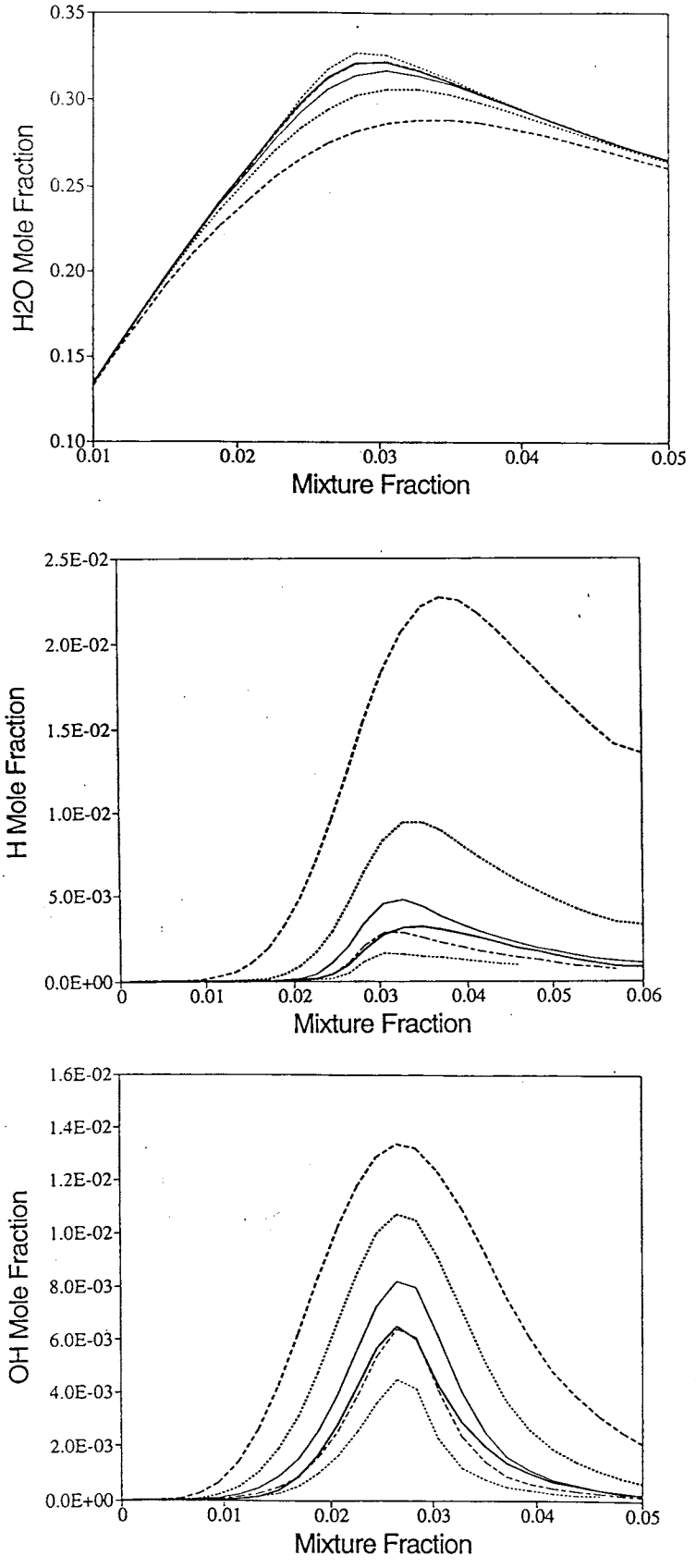

Figure 7.1: Conditional mean H_2O, H and OH mole fraction profiles at various axial locations. Line type denotes location (x/L_v) : 0.125 - bold dash, 0.25 - bold dot. 0.5 - plain solid, 0.75 - plain dash, 1.0 - plain dot, adiabatic equilibrium - bold solid

At axial locations further from the nozzle, the degree of departure from chemical equilibrium declines as a result of the streamwise reduction in turbulent mixing intensity, as described in Section 6.3. In the absence of radiation losses, the chemical system tends towards a state of adiabatic chemical equilibrium[96]. However, in the calculated results shown here radiative losses cause radical levels to fall substantially below adiabatic equilibrium levels towards the end of the flame. The amount of H_2O accordingly exceeds adiabatic equilibrium as the radicals are consumed in the face of declining flame temperatures.

Conditional mean flame temperature and nitric oxide mole fractions are plotted in Fig. 7.2 at various axial locations in jet flame A. It is clear that the predicted peak conditional mean flame temperature remains at least $100K$ below the adiabatic equilibrium profile peak at all axial locations. The temperature depression in the upstream zones is due to turbulence-chemistry interaction, which inhibits the exothermic formation of H_2O whilst the endothermic process of radical formation is comparatively unhindered. This depression, being related to variations in chemical reaction rates, is most evident near stoichiometric. In downstream zones, particularly near the visible flametip the temperature depression is radiation induced, and this is reflected by the fact that the depression is more uniform over a range of mixture fractions.

Nitric oxide levels build up along the length of the flame, with the peak levels occuring at the stoichiometric mixture fraction. As these predictions consider only the thermal formation pathway[128], it is not surprising that the NO profile peaks near the mixture fraction where the conditional mean temperature profile peaks. The almost linear decrease in conditional mean NO mole fraction away from stoichiometric suggests that NO is only formed at stoichiometric and is transported to richer and leaner mixture fractions.

7.1.2 Comparison of H_2 Jet Flame Data

The experimental data provided by Barlow and Carter[150,152] is the first to include conditional mean nitric oxide measurements within a flame, and thus has provided great insight into thermal NO formation in jet diffusion flames. This data has been used as a source for comparison with CMC and joint PDF model predictions on

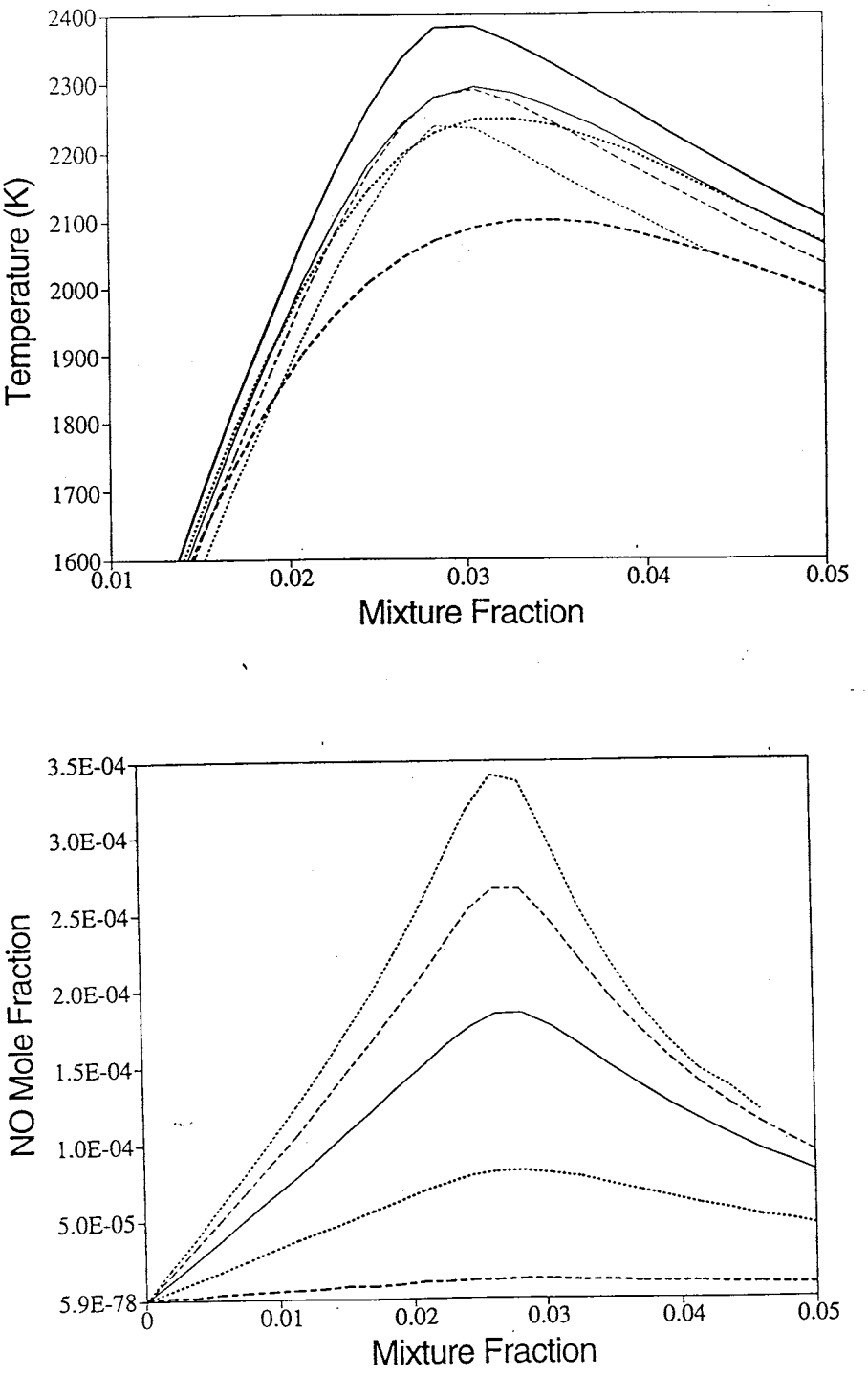

Figure 7.2: Conditional mean temperature and NO mole fraction profiles at various axial locations. Line type denotes location (x/L_v) : 0.125 - bold dash, 0.25 - bold dot, 0.5 - plain solid, 0.75 - plain dash, 1.0 - plain dot, adiabatic equilibrium - bold solid

earlier occasions[102,104].

A comparison of conditional mean temperature profiles from experimental measurement and model prediction can be seen in Fig. 7.3. The near-field temperature profiles show poor quantitative agreement, with the predicted profile peak being some $110K$ below the measured peak temperature of $2212K$. Further downstream, the agreement between measurement and prediction improves to within $30K$, but with a reversal of the order so that the predicted curves exceed the measured curves.

It should be noted that the measured temperature profile at $x/L_{vs} = 0.125$ exceeds the adiabatic chemical equilibrium curve at lean mixture fractions to the left of $\eta = 0.02$. A similar, though weaker, phenomenon can be seen in the temperature profiles of strained laminar flamelets[130]. The lean-side super-equilibrium temperatures are present in the near-field of the jet flame, where the reaction zone most likely falls within the flamelet regime, but is absent at downstream measurement locations where the reaction zone is more distributed. It is thus apparent that the poor agreement between the upstream temperature profiles may be the result of the inability of the CMC model to account for differential diffusion effects.

A comparison of conditional mean H_2O profiles in the near-field would seem to support this assertion. It is evident from Fig. 7.3 that the measured H_2O profile substantially exceeds the profile predicted by the CMC model with its uniform diffusivity assumption. The measured rich side H_2O profile exceeds adiabatic equilibrium in the near field, and the location of the profile peak is rich shifted compared to the model prediction. Super-equilibrium excursions of this type have been noted for $CO - H_2 - N_2$ turbulent diffusion flames[50] and appear to be present in the measurements of Cheng *et al*[153] for lifted H_2 jet flames. The observed super-equilibrium H_2O levels may also be due to experimental error which Barlow and Carter[150] cite as being of the order of $\sim 5\%$ of the peak value.

Far field comparisons of H_2O profiles shows that the predicted profile exceeds measurements at halfway along the visible flamelength, but that at $x = 0.75L_{vs}$ the measured profile exceeds the prediction by a substantial margin. It is not clear why this is the case, but an examination of the scatter of instantaneous measured data points[150] suggests that this elevated mean value may be a spurious result. This type of unexpected deviation is not present in the far-field measurements of Cheng

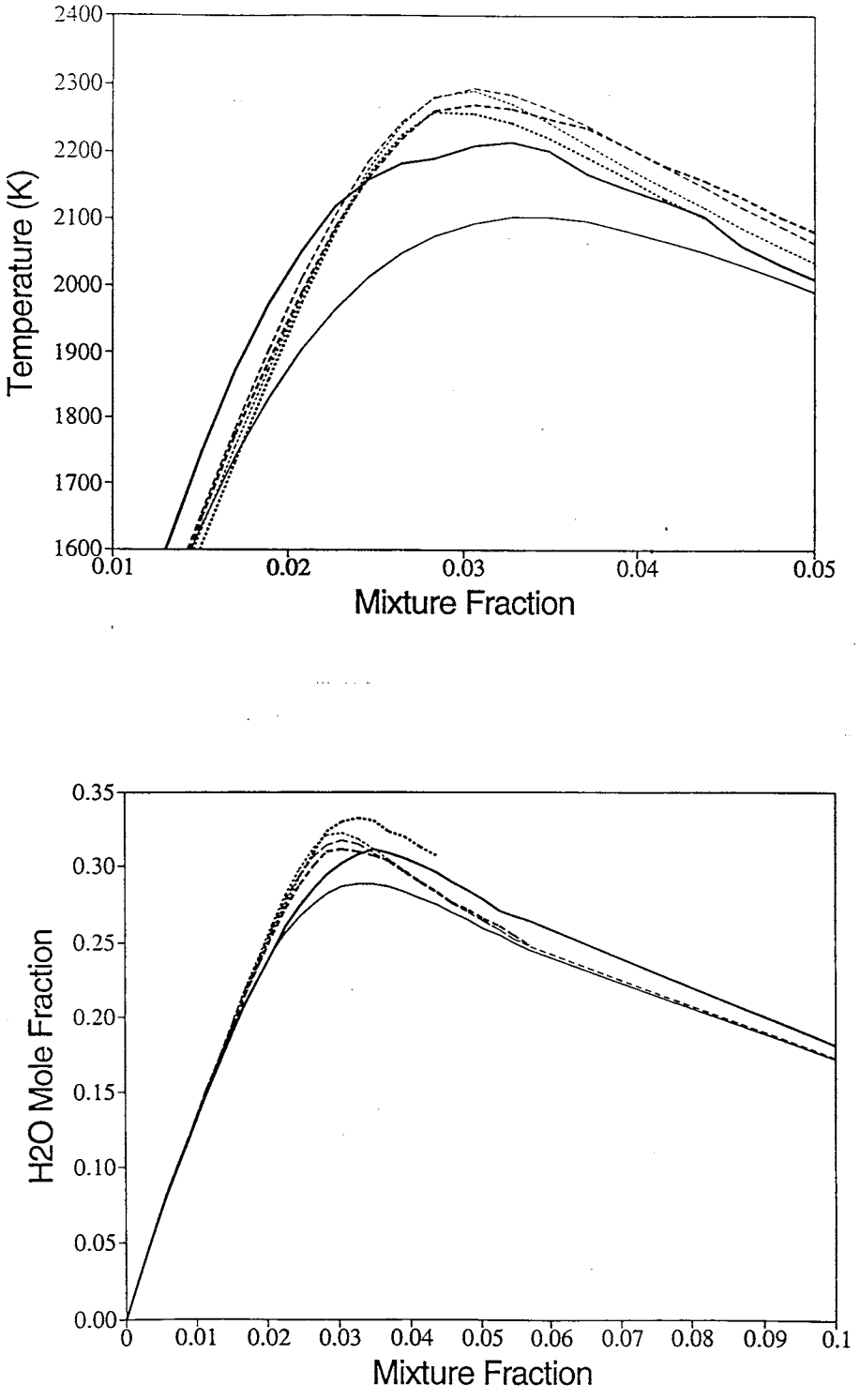

Figure 7.3: Conditional mean temperature and H_2O mole fraction profiles at various axial locations. Line type denotes source (bold lines - Expt, plain lines - CMC) and location (x/L_v): 0.125 - solid, 0.5 - dashed, 0.75 - dotted

et al[153].

A comparison of measured and predicted OH radical profiles (see Fig. 7.4) shows that at all axial locations, the predicted OH peak is approximately $7 - 12\%$ below the corresponding peak measured value. There is no apparent shift in the location of the peak OH mole fraction for different axial distances from the nozzle. The CMC method may be slightly underpredicting the intensity of turbulent mixing processes throughout the flame, or alternatively the reactions in the chemical mechanism responsible for the net formation of OH may be slightly slow. Barlow and Carter[150] cite the measurement uncertainty for OH (OH is measured by laser induced fluorescence) to be around five percent of the peak value.

A comparison of conditional mean NO mole fraction profiles (Fig. 7.4) reveals that the CMC model predictions are $\sim 80\%$ lower than the peak experimental measurement at $x/L_{vs} = 0.125$, but that the predicted NO profiles rapidly overtake the measured profiles by the end of the flame. At the stoichiometric flametip ($L_{st} \approx 0.75L_{vs}$), the predicted peak conditional mean NO mole fraction is $\sim 25\%$ greater than the corresponding experimental measurement. In discussing this trend in NO agreement between the different profiles, it is useful to consider near and far-field effects.

Bearing in mind the thermal sensitivity of the Zeldovich pathway for NO production, it would seem that the near-field underprediction by the CMC model is a result of the $\sim 110K$ underprediction of conditional mean temperature at this location (see Fig. 7.3). As was mentioned above, this underprediction is in turn likely to be the result of differential diffusion effects.

A similar tendency towards underprediction was noted for joint PDF modelling of this flame[102], where the joint PDF model employed the same jet flame code as is employed in this investigation. The possibility of the excessive predicted temperature depression being a result of inappropriately high turbulent mixing rates, must be discarded when it is recognized that the predicted radical (OH) levels are lower than the measured values at $x/L_{vs} = 0.125$. This behaviour in the radicals is indicative of a less perturbed rather than more perturbed chemical system.

In the light of recent evidence presented by Barlow and Carter[152] (see Section 6.4), it is expected that near-field radial dependence of conditionally averaged

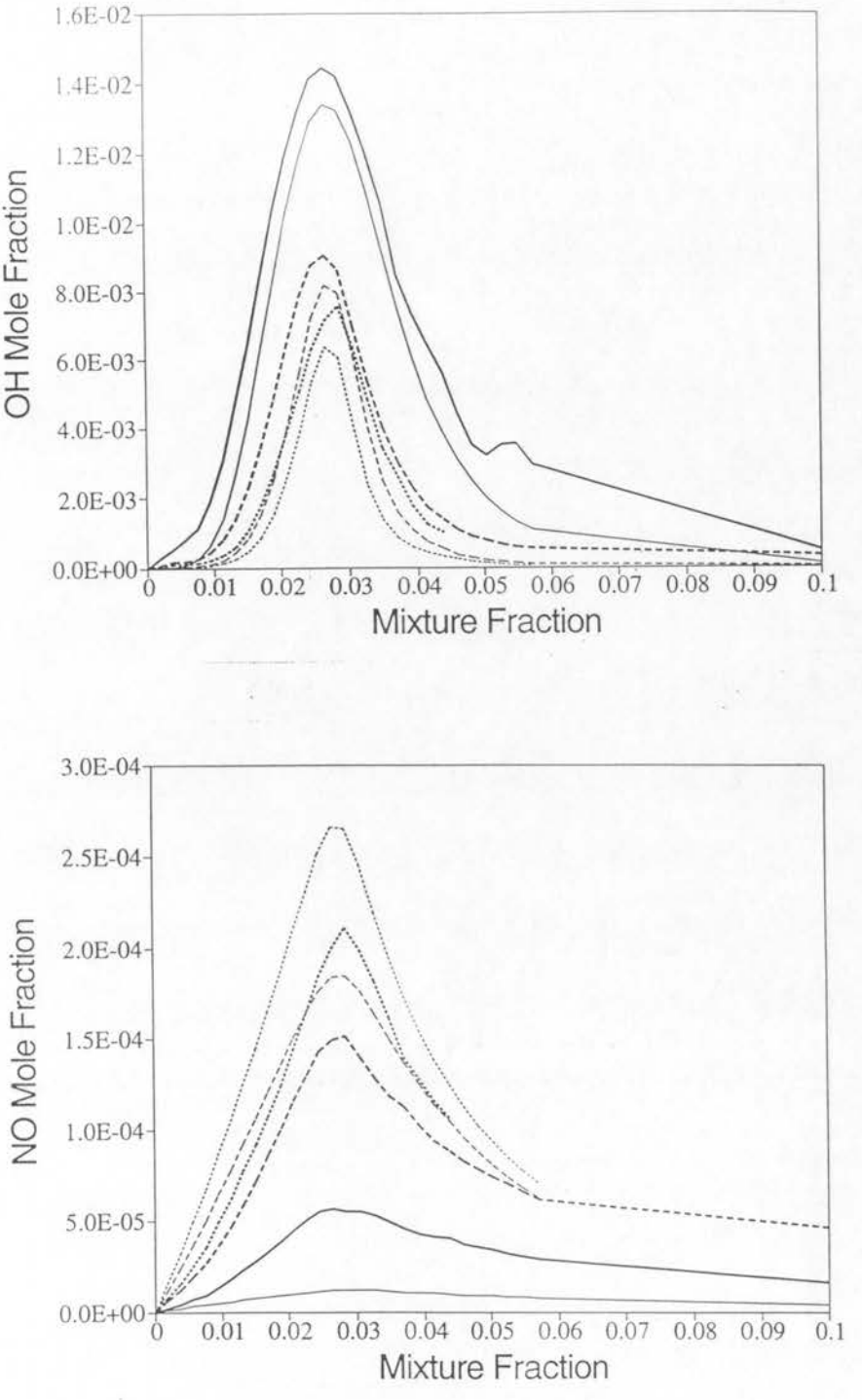

Figure 7.4: Conditional mean OH and NO mole fraction profiles at various axial locations. Line type denotes source (bold lines - Expt, plain lines - CMC) and location (x/L_v): 0.125 - solid, 0.5 - dashed, 0.75 - dotted

statistics may also play a role in the discrepancies in the CMC model's near-field predictive capability. This radial dependence can be seen to contribute to the high levels of scatter in the near-field instantaneous measurements of NO concentration by Barlow and Carter[150,104], when it is remembered that their scatter-plots contained data from many radial stations at each axial location.

The absence of a radially dependent CMC formulation cannot solely account for the degree of discrepancy observed in the near-field predictions, since it must be remembered that the near-field predictions of the fully two-dimensional joint PDF model agreed closely with the CMC estimates[102]. Instead, given that the near-field reaction zones appear to be exhibiting flamelet-like characteristics, it might prove more useful to investigate the importance of local conditional mean scalar dissipation rate *fluctuations* in the CMC methodology. The refinements recently suggested by Klimenko[154] may need to be incorporated to improve CMC model performance under these conditions.

Far-field NO overprediction would appear to be primarily due to the overprediction of conditional mean temperature in these zones. This temperature overprediction may be due to the alleged under-estimation of turbulent mixing rates throughout the flame (see comments on OH) or may be due to inaccuracies arising from the radiation submodel. In an effort to test this last hypothesis, the calculations were repeated using an alternate radiation submodel[155]. This alternate model also employed an optically-thin approximation, and produced the same streamwise trend with only a $\sim 2\%$ decrease in the predicted NO profiles near the flametip.

The comparison of conditional mean NO mole fraction profiles presented here indicates that the near-field discrepancies noted above are not signifcant in the overall formation of NO. The inadequacies in the calculations arising out of poor radiation modelling and/or insufficient turbulent intensity must be considered more important in this application.

7.1.3 Favre Averaged Profiles

In Fig. 7.5, predicted and measured unconditionally (Favre) averaged profiles for mean mixture fraction, temperature and NO mole fraction are compared at various axial locations. It is evident from the figure that the predicted evolution of the mean

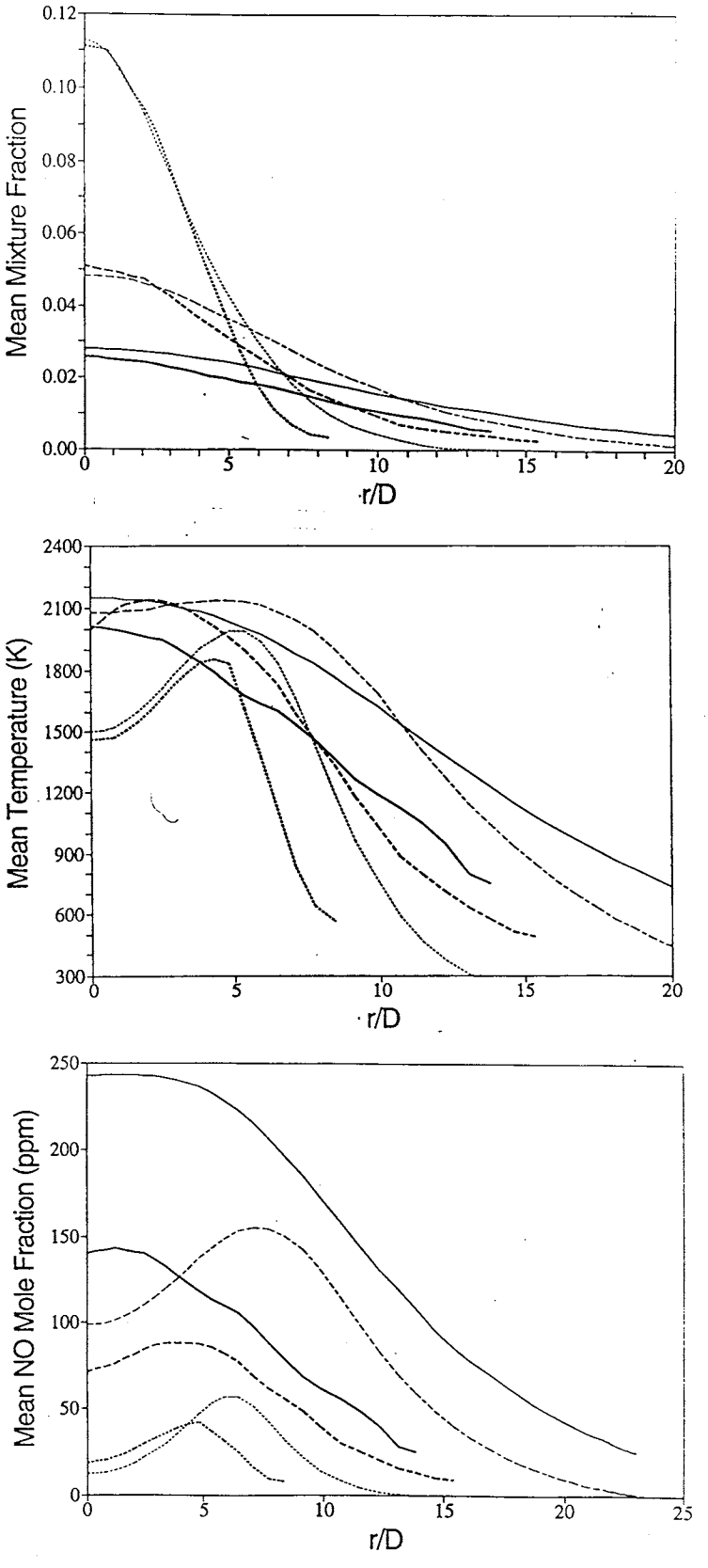

Figure 7.5: Unconditional (Favre) mean mixture fraction, temperature and NO mole fraction profiles at various axial locations. Line type denotes source (bold lines - Expt, plain lines - CMC) and location (x/L_v): 0.75 - solid, 0.5 - dashed, 0.25 - dotted

mixture fraction field agrees well with the measured field, but that the predicted flame is slightly longer and broader than that indicated by experiment. Better agreement between the measured and predicted mixture fraction fields may be achieved by adjusting some of the 'tunable' constants, within the myriad of submodels that compose the Reynolds stress/flux closure model, but the value of this exercise is questionable.

The point values of the predicted mean mixture fraction field, together with those of the mixture fraction variance field (not shown) produce the assumed form mixture fraction PDFs at regular radial intervals. These PDFs are used in convolution integrals with the predicted conditional mean data of the preceding section to produce the temperature and NO mole fraction fields found in Fig. 7.5.

Comparing the mean temperature fields, the slightly greater broadness of the predicted flame is evident from the outward radial shift of the location of the predicted peak mean temperature. The stoichiometric mean flametip ($x/L_{vs} = 0.75$) temperatures reflect the discrepancy between conditional mean flame temperatures at this axial location. Since the unconditional mean temperatures differ by something of the order of $\sim 100K$ rather than the $\sim 30K$ conditional mean difference, it would seem that the level of predicted mixture fraction variance at the flametip is lower than the true value. The predicted mean NO field also shows the influence of the broadened mean mixture fraction field. Further, the predicted mean NO mole fraction at the stoichiometric flametip is around $\sim 70\%$ greater than the measured mean value. This discrepancy is wider than that noted for the conditional mean profiles ($\sim 25\%$), and again is an indicator of possible underprediction of mixture fraction variance levels by the Reynolds stress/flux model.

7.2 Hydrogen-Carbon Monoxide Flames

Hydrogen-CO fuel mixtures are studied because whilst they are relatively simple in terms of chemical kinetics, they involve the CO oxidation reaction which is one of the crucial processes in hydrocarbon combustion. Sometimes called 'syngas', $H_2 - CO$ fuels are coal derivatives that represent an intermediate level in chemical complexity between hydrogen and hydrocarbon combustion.

Designation	Flame B
Nozzle diameter (D)	3.2 mm
Fuel composition (vol.)	$40\%CO/30\%H_2/30\%N_2$
Jet velocity (U_j)	55 m/s
Coflow velocity	2.4 m/s
Stoich. Mixture Fraction ($\xi_{stoic.}$)	0.3
Cold Jet Reynolds number (Re_D)	8500

Table 7.2: Characteristics of a experimentally measured syngas jet flame.

Experiments have been carried out by Drake and coworkers[130,143,156] upon a syngas flame of composition $40\%CO/30\%H_2/30\%N_2$ by volume. The major characteristics of this flame are summarized in Table 7.2, where it is designated as flame B. A number of other syngas jet flame studies have been published[50,157,158], but these were concerned with the extinction characteristics of these flames and thus cannot be treated with the current CMC model. The syngas flame studied here has been characterised as being far from extinction[130] and is thus amenable to singly conditioned CMC modelling.

Model calculations were made over a range of flow conditions for flames similar to flame B, where the computational methods used were identical to those reported for the H_2 calculations of Section 7.1. The syngas calculations were made using a fifteen-species twenty-five step chemical mechanism listed in Table A.1 as reactions $1-20$ and $30-34$. This mechanism consists of the wet CO mechanism of Rogg and Williams[159] with additional thermal NO reactions (see Appendix A).

Calculation times were of the order of ~ 3 CPU hours on a DEC Alpha workstation running at $\sim 15Mflops$. This time is approximately half that of the pure H_2 runs, a reflection of the greatly reduced length of the syngas flame ($L_{st} \approx 43D$). As with the H_2 runs, the bulk of the computation time went into integrating the CMC equations.

7.2.1 Predicted $CO - H_2$ Jet Flame Characteristics

The predicted conditional mean reactive scalar profiles of flame B appear to lack one of the principal features that was found in flame A. There is evidently a great deal

less radiative heat loss in the syngas flame compared to the pure H_2 flame.

In Fig. 7.6, predicted conditional mean profiles of the major product species (H_2O,CO_2) and temperature are plotted versus mixture fraction for various axial locations in flame B. Note that in contast to the method of reporting axial locations used by Barlow and Carter[150] (used in Section 7.1), Drake[130] has nondimensionalized axial length by the nozzle diameter and so that convention is adopted here as well. The visible flamelength should be around $L_{vs} \sim 60D$ based on experimental and predicted values of the stoichiometric flamelength $L_{st} \sim 45D$.

It is evident from Fig. 7.6 that the level of departure from chemical equilibrium decreases monotonically with increasing axial distance from the nozzle. This trend is a result of the decline in turbulence levels as the calculations move further from the nozzle. Flame B's far field temperature profiles increase with increasing axial distance, rather than decreasing under the influence of radiant losses as was the case for flame A.

Similarly, the conditional mean major product mole fractions of flame B do not exceed adiabatic equilibrium levels in the reaction zone. The reason for the reduced radiant losses from flame B as compared to flame A, is that the conditional mean flame temperatures are around $\sim 200K$ cooler in the former which amounts to an approximate 40% decrease in the fourth power temperature difference associated with radiant losses. In addition, the fuel stream is diluted with a significant amount of nitrogen which reduces the partial pressure of the radiation emitting species, H_2O and CO_2. The residence time of flame B is approximately 50% greater than that of flame A, but this effect is insufficient to counter the two points mentioned above.

It is evident that the major product profiles deviate substantially from the adiabatic equilibrium profiles at rich mixture fractions away from the reaction zone. This behaviour is due to the presence of substantial turbulent mixing of reaction zone species to richer fractions, in the case of the jet flame. Turbulent mixing is of course not included in chemical equilibrium calculations.

Figure 7.7 contains plots of predicted conditional mean mole fractions of the radicals H and OH for flame B. It is clear that the radical profiles are elevated far above the adiabatic equilibrium level at all locations, but relax somewhat towards this level near the end of the flame. It is evident that the H profile peaks on the

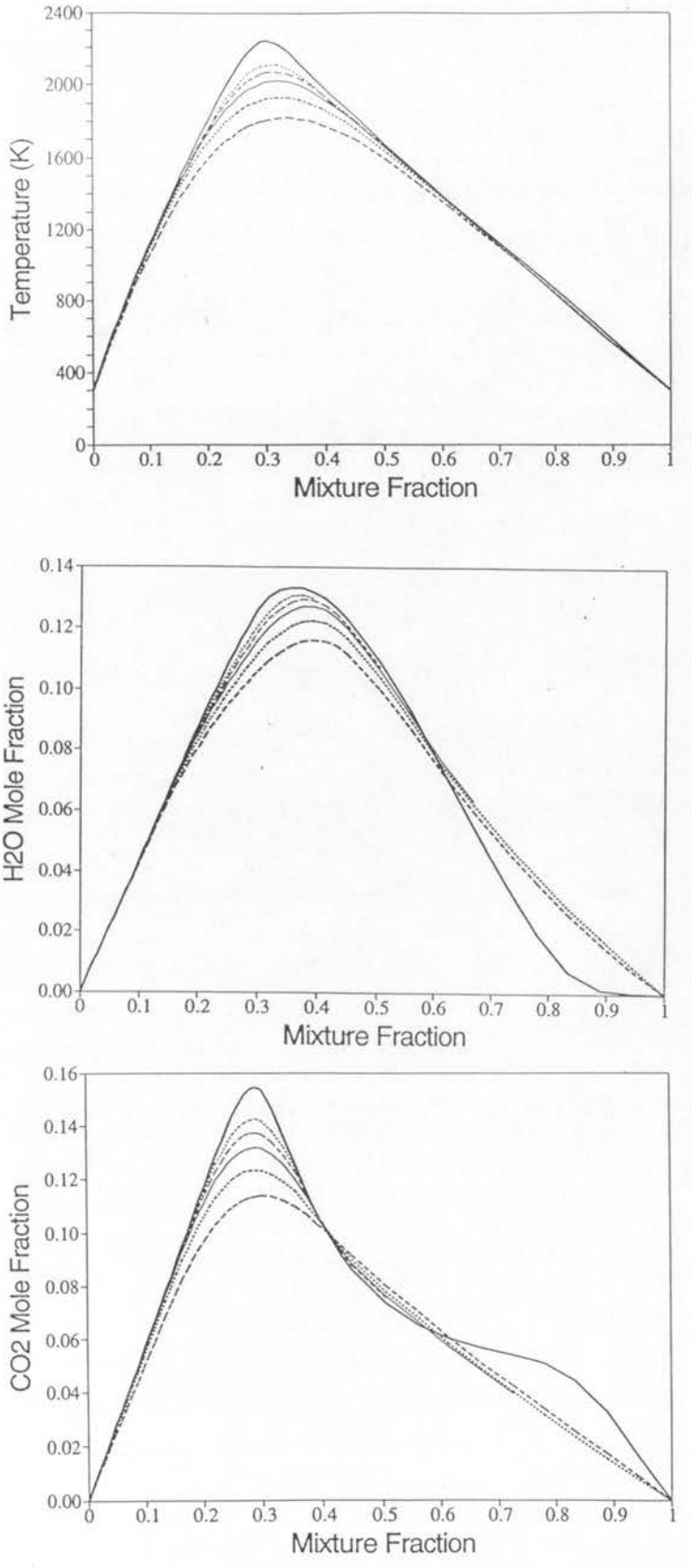

Figure 7.6: Conditional mean temperature, and H_2O and CO_2 mole fraction profiles at various axial locations. Line type denotes location (x/D) : 10 - bold dash, 25 - bold dot, 40 - plain solid, 50 - plain dash, 60 - plain dot, adiabatic equilibrium - bold solid

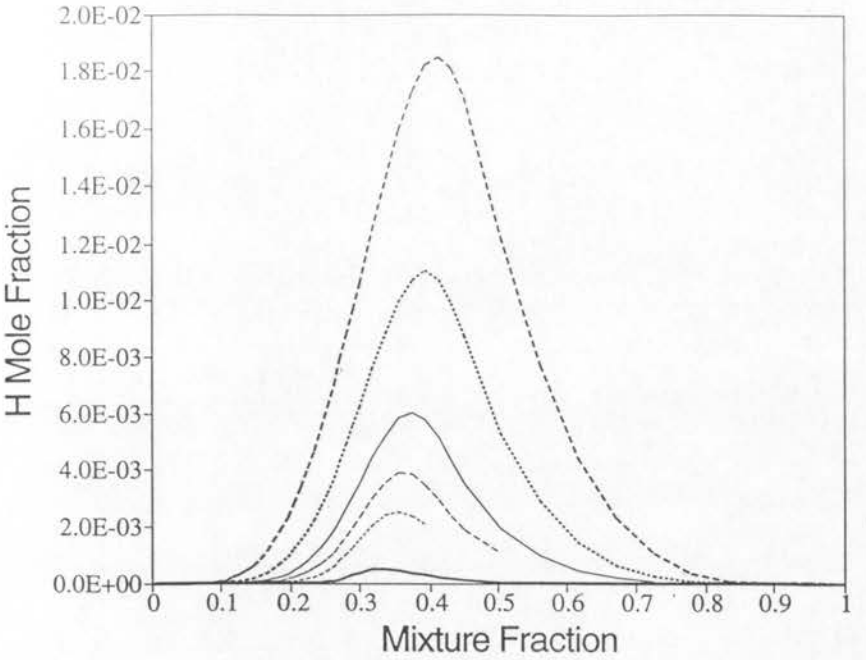

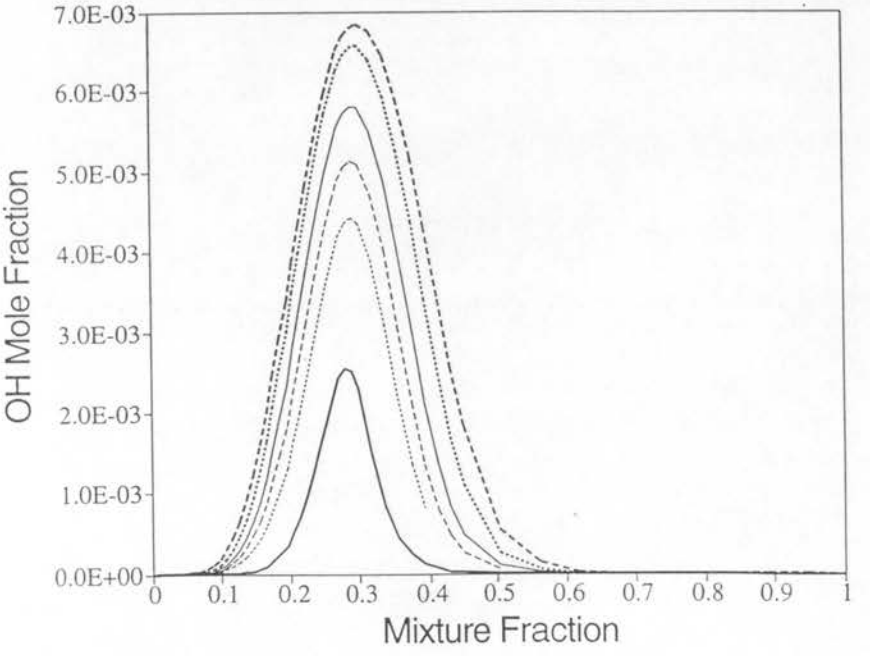

Figure 7.7: Conditional mean H and OH mole fraction profiles at various axial locations. Line type denotes location (x/D) : 10 - bold dash, 25 - bold dot, 40 - plain solid, 50 - plain dash, 60 - plain dot, adiabatic equilibrium - bold solid

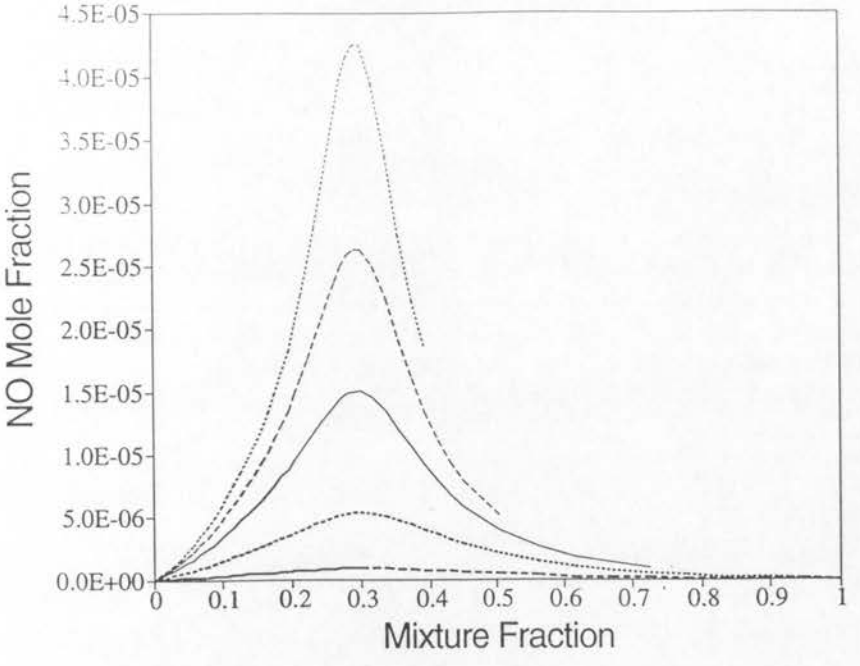

Figure 7.8: Conditional mean NO mole fraction profiles at various axial locations. Line type denotes location (x/D) : 10 - bold dash, 25 - bold dot, 40 - plain solid, 50 - plain dash, 60 - plain dot, adiabatic equilibrium - bold solid

rich side of stoichiometric and is shifted to richer mixture fractions with increased mixing intensity. The OH profile peaks on the lean side, but no shifting of this peak is evident with changes in axial location.

Predicted conditional mean nitric oxide profiles can be seen for various axial locations in Fig. 7.8. As with the pure hydrogen predictions, flame B's conditional mean nitric oxide levels slowly build up with increasing axial distance from the nozzle. The NO is again being formed by the Zeldovich thermal mechanism in the immediate vicinity of the stoichiometric mixture fraction, and is being transported by mixing action to other mixture fractions. In contrast to the pure-hydrogen calculations, flame B shows substantial levels of NO_2 forming at very lean mixture fractions ($0 < \eta < 0.1$). The formation of NO_2 in these zones accounts for the small positive curvature in the predicted NO profiles near the origin. Such curvature is not evident in the almost NO_2-free pure H_2 flames.

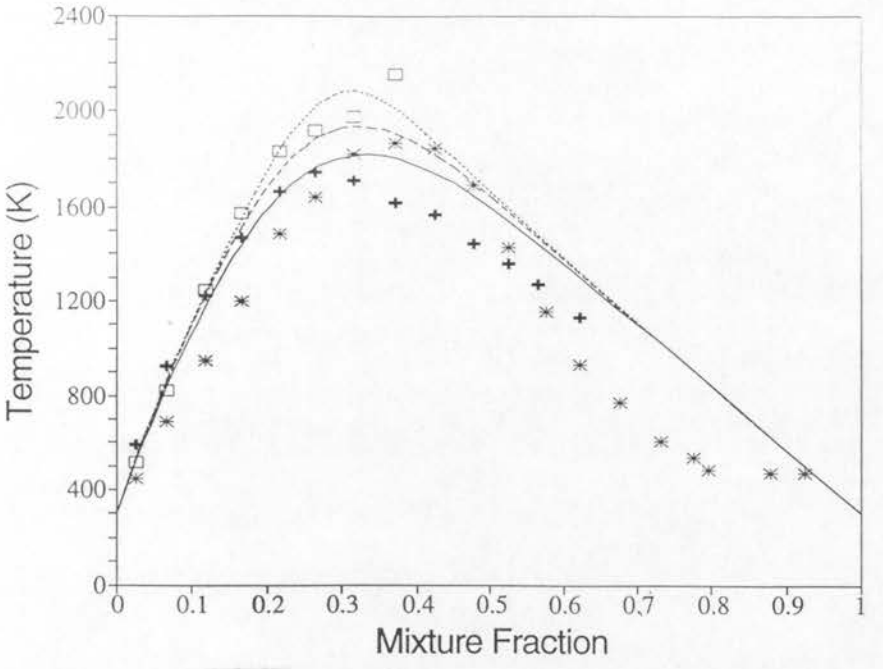

Figure 7.9: Conditional mean temperature profiles at various axial locations. Lines denote predictions, symbols denote experiment. Locations (x/D): 10 - asterisk/solid line, 25 - cross/dashed line, 50 - box/dotted line

7.2.2 Comparison of $CO - H_2$ Data

Drake presents experimentally determined conditional mean data in an early paper[130] which only includes the major species and temperature. Conditional mean hydroxyl (OH) radical levels are quoted but not plotted. Conditional mean nitric oxide measurements were not made in this early paper, they have only recently been achieved in a flame of any kind[150]. Unconditional NO and NO_2 measurements have been made[143], and will be addressed in later sections.

A comparison of measured and predicted conditional mean flame temperatures can be drawn from Fig. 7.9. The agreement between the measured and predicted temperature data is patchy but falls within $100K$ for the most part. As with the pure H_2 data comparison, it is useful to discuss the near and far field behaviour separately.

In the near-field cases $(x/D = 10)$, the CMC predicted temperature profile peaks some $100K$ below the measured profile peak, and is shifted by comparison towards stoichiometric. The measured conditional mean profile deviates hundreds of degrees below adiabatic equilibrium levels even for the leaner mixture fractions

($\eta < 0.2$). At very rich mixture fractions ($\eta > 0.5$) even greater depressions below adiabatic equilibrium are present.

Drake[130] compares this near-field temperature behaviour with strained laminar flamelet results and finds good lean mixture fraction agreement, but the rich side measurements fall between the flamelet results and the adiabatic chemical equilibrium curve. As with the near-field hydrogen comparison (see Section 7.1.2), it is evident that the differential diffusive nature of near field flame structures cannot be ignored. In contrast to flame A, the differential molecular transport processes in flame B lead to lean-side temperature depression, below equilibrium, rather than elevation.

The far-field measured and predicted temperature profiles agree quite well on the lean side of stoichiometric, but the profiles diverge at rich mixture fractions. At the $x/D = 25$ station, the rich side predictions are around $\sim 200K$ greater than the measured values between the mixture fractions of $0.3 < \eta < 0.6$. The discrepancy is more on the order of $100K$ at the downstream location of $x/D = 50$. There appears to be a sharp increase in the measured temperature on the rich side of stoichiometric, which was not explained by Drake[130]. Examining the streamwise trend in rich-side temperature measurements, there appear to be inconsistencies between the three profiles which raise questions about the accuracy of these rich side measurements.

Drake[130] presents conditional mean major species information in a slightly unorthodox format. The degree of progress of H_2 and CO oxidation to H_2O and CO_2 is represented by the following normalized 'oxidation fractions' involving species mole fractions X_i:

$$f_{C-ox} \equiv < \frac{X_{CO2}}{X_{CO2} + X_{CO}} \mid \eta > \tag{7.1}$$

$$f_{H-ox} \equiv < \frac{X_{H2O}}{X_{H2O} + X_{H2}} \mid \eta > \tag{7.2}$$

Oxidation fraction values of zero indicate a complete lack of the oxidized product whilst unity values correspond with total oxidization of the referenced fuel species.

Unfortunately, these oxidation fractions cannot be determined exactly from the predicted conditional mean statistics since the strength of the correlations between CO and CO_2, and H_2 and H_2 is not known. Instead of comparing true predicted oxidation fraction data with the measurements, approximate values are compared

which are determined from the fraction of the conditional means (rather than the conditional mean of the fraction). This approximation is of the same order of accuracy as the first order chemical closure employed in the solution of the CMC equations (see Section 3.2.3). Measured and predicted carbon and hydrogen oxidation fraction profiles are plotted for comparison in Fig. 7.10.

Reasonable agreement between the measured and predicted hydrogen oxidation fractions (f_{H-ox}) can be seen in Fig. 7.10. The predicted profiles show the expected trend of increasing oxidation fraction with increasing axial distance from the nozzle. Both the measured and predicted profiles tend to unity for lean mixture fractions ($\eta < 0.2$) where all of the H_2 fuel species has been consumed.

Both the measured and predicted hydrogen oxidation fraction profiles lie close to the equilibrium curve, but the former behave in an unexpected manner at the different axial measurement locations. Reference to Drake[130] shows that the near-field profile ($x/D = 10$) lies above the equilibrium curve at rich mixture fractions whilst the corresponding laminar flamelet profile lies far below this curve. The measured profile at the next axial station downstream lies substantially below the near field curve, whilst the profile at the furthermost station falls between these two extremes. The reason behind this non-monotonic behaviour is not clear.

Comparing carbon oxidation fraction profiles (Fig. 7.10) shows that there is poor agreement between the prediction and measurement. Whilst both the predicted and measured profiles show substantial departure from equilibrium, the measured profile maxima tend to be typically 0.1 below the predicted profile maxima at corresponding axial locations. As with the hydrogen oxidation fraction profiles, the measured carbon f_{C-ox} profiles do not display a monotonic trend with axial distance. Qualitatively, it would seem that the discrepancy between the measured and predicted f_{C-ox} profiles suggests that the predicted flame is closer to equilibrium than the true flame.

Drake[130] states that the measured conditional mean OH mole fraction profile peaks at a value approximately six times higher than the equilibrium peak value at $x/D = 10$. This value decreases monotonically until the peak measured value is only around four times greater than equilibrium at $x/D = 50$. With these ratios in mind, an examination of Fig. 7.7 shows that the predicted two and threefold OH excess is

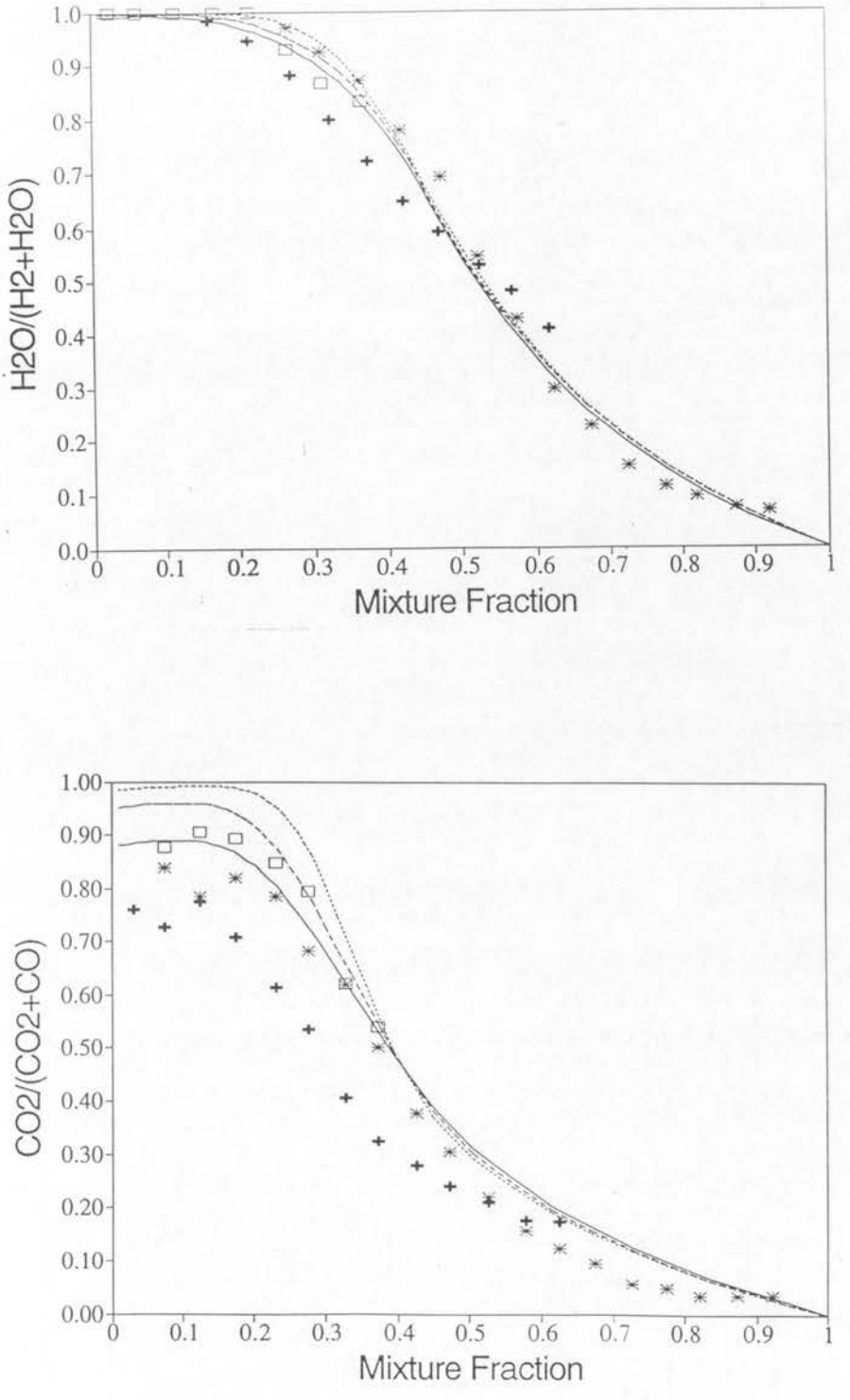

Figure 7.10: Conditional mean hydrogen and carbon oxidation fraction profiles at various axial locations. Lines denote predictions, symbols denote experiment. Locations (x/D): 10 - asterisk/solid line, 25 - cross/dashed line, 50 - box/dotted line

indicative of the predicted flame being closer to chemical equilibrium than the true flame.

7.2.3 Favre Averaged Profiles

Predicted and measured favre averaged radial profiles are plotted for the axial locations $x/D = 10, 25, 50$ in Fig. 7.11. It is evident that the predicted and measured mean mixture fraction profiles agree quite well, particularly in the far field. At $x/D = 10$, the profile agreement is good except near the centreline where the measured profile is $\sim 10\%$ lower than the CMC prediction. The discrepancy at $x/D = 25$ is of the order of $\sim 20\%$ over most of the flow radius, with the measured profile being leaner than the predicted. The differences between the radial profiles at $x/D = 50$ are less than $\sim 5\%$ at all points.

A comparison of favre averaged temperature profiles reveals similar levels of agreement between measurement and prediction. This good agreement must be due at least in part to the good agreement between the lean-side measured and predicted conditional mean temperature profiles. No radial profiles of favre averaged NO are available for comparison[130], however overall emission data are compared and discussed in Section 7.5.

7.3 Chemical Production and Transport

It is instructive to examine not only conditional averages of reactive species, but also their rates of formation and transport in mixture fraction space. The CMC jet flame equation (Eqn 6.6) presented in Section 6.1 consists of a balance of three terms. These terms represent the processes of formation via chemical reaction, turbulent mixing, and mean convection.

In practice, the chemical reaction and turbulent mixing terms act as sources on the right hand side of Eqn 6.6 for the axial convection of conditional mean reactive scalars. In the following, both the turbulent mixing and chemical reaction terms of Eqn 6.6 will be referred to as 'sources' for convenience sake, despite the fact that srictly speaking only the latter of the two is a source term. Further, these 'sources' will be understood to be normalized by the conditional mean density and velocity

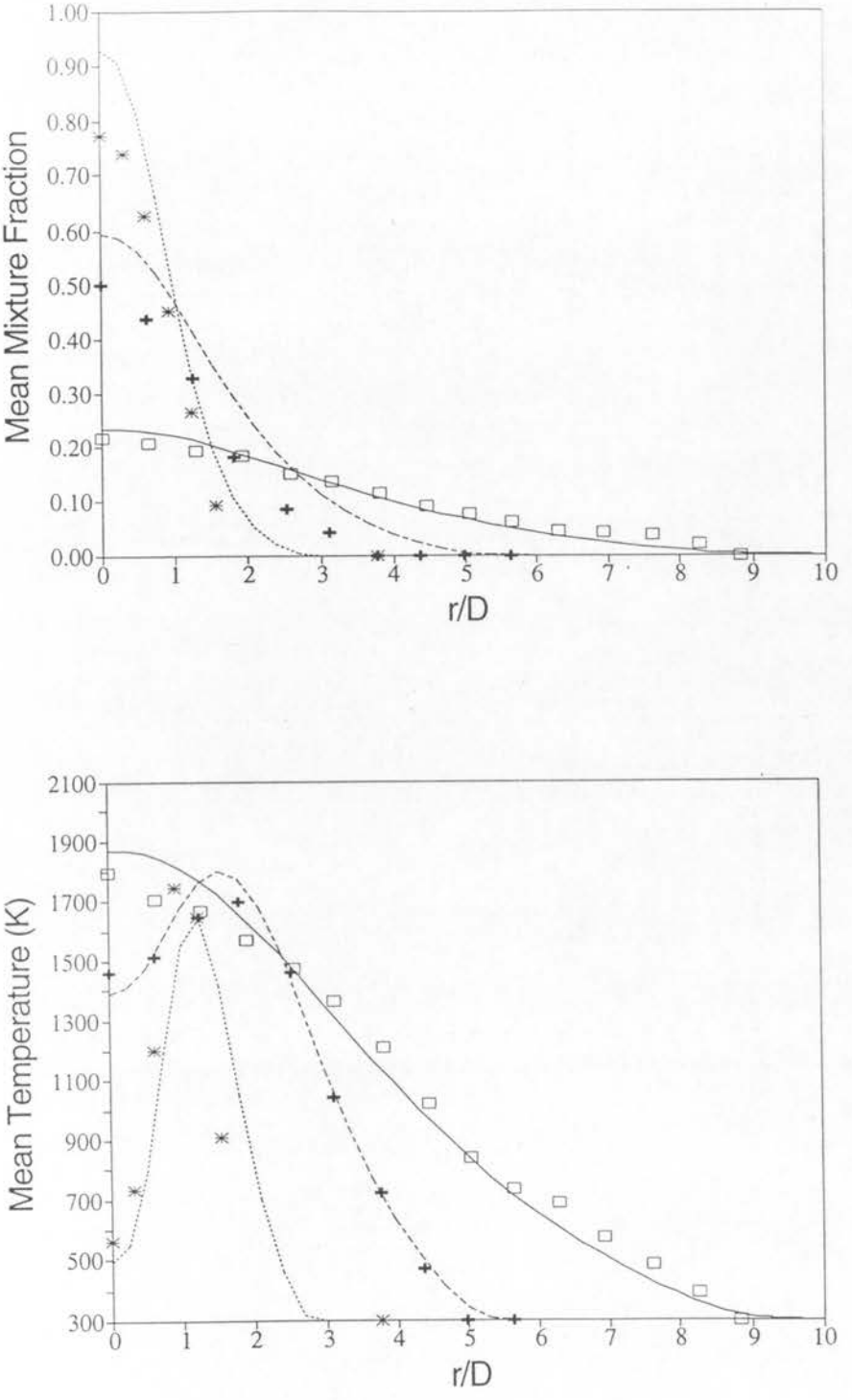

Figure 7.11: Unconditional (Favre) mean mixture fraction and temperature profiles at various axial locations. Lines denote prediction, symbols denote experiment. Locations (x/D): 10 - asterisk/dotted line, 25 - cross/dashed line, 50 - box/solid line

of the left hand side of Eqn 6.6 so that they represent changes with axial location rather than with time.

As the predicted source profiles of both flames A and B have similar characteristics, only the profiles of flame B will be plotted here. General comments made in connection with flame B, apply also to flame A. The magnitude and form of the conditional mean sources for carbon dioxide (CO_2) and monatomic hydrogen (H) mass fraction can be seen in Fig. 7.12. The source profiles of both the major product species CO_2 and principal radical species H appear to be well balanced between chemical reaction and turbulent mixing. It is clear that the chemical formation of CO_2 on the lean side of stoichiometric ($\xi_{stoic} = 0.3$) is closely matched by the rapid mixing of CO_2 away from this mixture fraction location.

It is also apparent from the figure that a small amount of positive curvature must be present in the CO_2 mass fraction profiles at $x/D = 10, 25$ which evidently results from chemical consumption around $\eta \approx 0.5$. Both the processes of chemical production and turbulent mixing diminish in magnitude with increasing axial position.

The formation and mixing sources for H radical also diminish at more distant axial positions. The sign of the sources changes across mixture fraction space, from net chemical production immediately to the rich side of stoichiometric ($0.3 < \eta < 0.45$), to net consumption at still richer fractions. Net consumption features also at lean mixture fractions, where it is likely that radical molecules transported from stoichiometric are undergoing recombination due to the lower temperatures at these mixture fractions. The rich side consumption of H radical also probably results from low temperatures favouring net radical recombination over formation.

The net result of the opposed sources shown in Fig. 7.12, can be seen in Fig. 7.13. As expected from the conditional mean mole fraction profiles, the net change in CO_2 with axial location is positive at all but the inert mixture fractions on the rich side of $\eta \approx 0.5$. The near-field decrease in rich CO_2 levels results from the mixing field 'correcting' the initial equilibrium profile estimate. Note that the flattening of the lean side profile corresponds with the cessation of CO_2 oxidation reactions at lean mixture fractions towards the flametip. Beyond the stoichiometric flametip, the profile is essentially zero across the physically realizable portion of mixture fraction

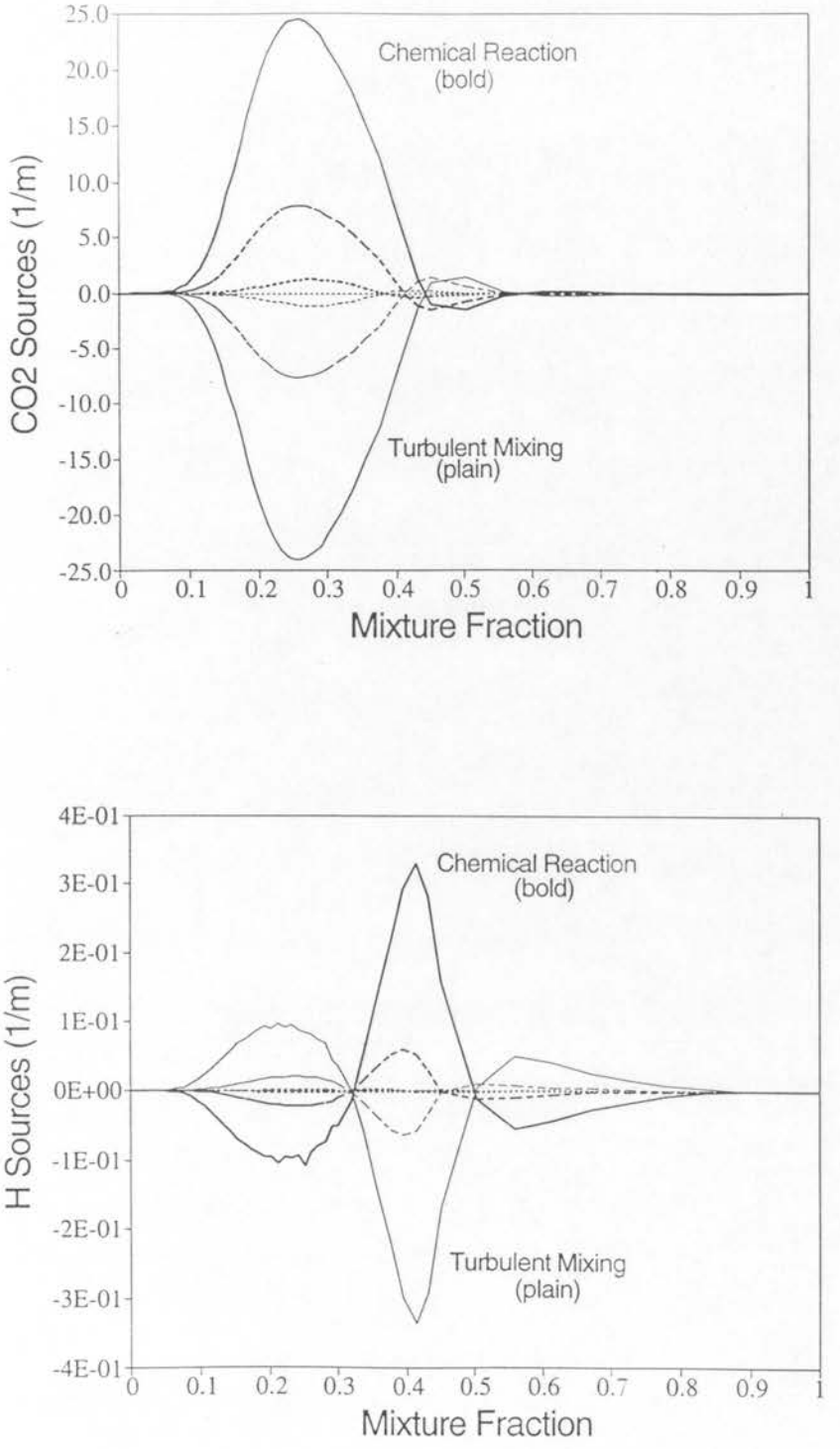

Figure 7.12: Conditional mean chemical production and turbulent mixing profiles at various axial locations in flame B. Line type denotes location: Locations (x/D): 10 - solid, 25 - dashed, 50 - dotted

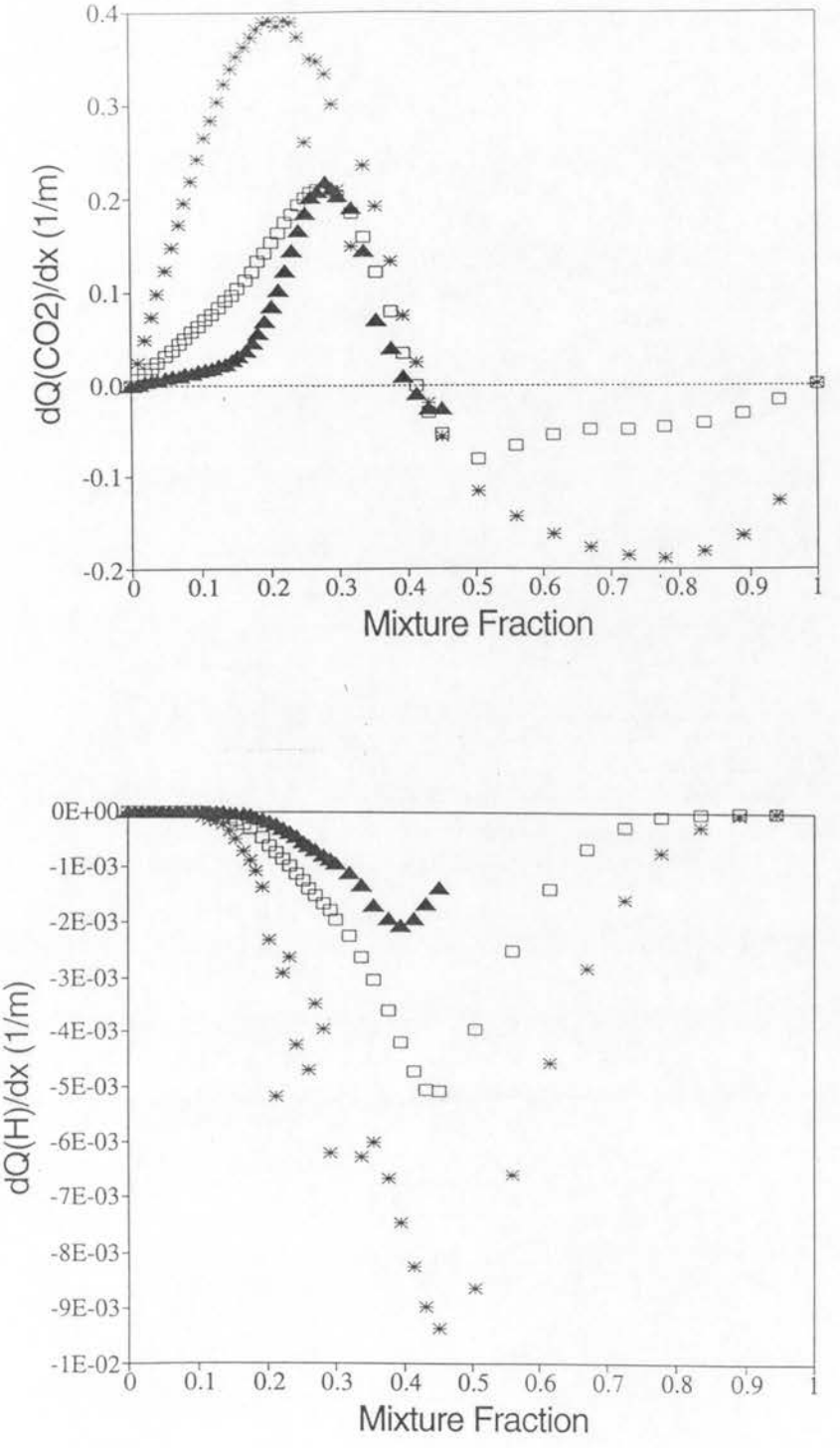

Figure 7.13: Conditional mean reactive scalar rate of change with distance at various axial locations in flame B. Symbol type denotes location: Locations (x/D): 10 - asterisk, 25 - box, 50 - triangle

space and thus CO_2 behaves as a conserved scalar.

The net change in H with increasing axial length is negative at all mixture fractions, except in the inert regions near $\eta = 0, 1$ were there is no change at all. This trend is part of the overall relaxation of the chemical system after having been strongly perturbed by intense mixing at locations further upstream.

The source profiles discussed above (CO_2,H) are essentially mixing limited, in that the chemical reactions are limited by the mixing processes which deliver fresh reactants to the stoichiometric zone from the surrounding inert fuel and oxidizer zones. This is essentially the case for the bulk of the major species and radicals. It is however, definitely not the case for oxides of nitrogen and standardized enthalpy. The conditional mean source profiles for these scalars are plotted in Fig. 7.14 for the locations corresponding to the figures above.

It is evident that in the case of standarized enthalpy, radiative losses overwhelm turbulent mixing processes by orders of magnitude at all mixture fractions except zero and unity. The magnitude of the radiant loss profile increases with increasing axial location. This increase is because of the increase in flame temperatures which in turn result from the diminishing levels of turbulent intensity with axial location. The standardized enthalpy source profiles for flame A, do not exhibit the monotonic increase seen in Fig. 7.14. Rather they increase to a point where the influence of radiant losses causes the flame temperatures to decline, and thereafter the radiant loss profile declines also.

The nitric oxide (NO) source profiles are not like the mirror-image profiles of Fig. 7.12. It is clear that chemical formation significantly dominates turbulent mixing, such that some $\sim 30\%$ of the net formation at $x/D = 50$ carries over into the convective change in NO mass fraction. The magnitude of the source profiles increases with axial location, largely because the increase in flame temperature causes the chemical formation rate to increase. Although the curvature of the NO mass fraction profile correspondingly becomes more and more negative, the turbulent mixing rate cannot keep pace with chemical reaction. This is because of the axial decline in conditional mean scalar dissipation rate.

The source term balances shown in this section demonstrate some important points. Firstly, the levels of some reactive species can be approximated by a reactive-

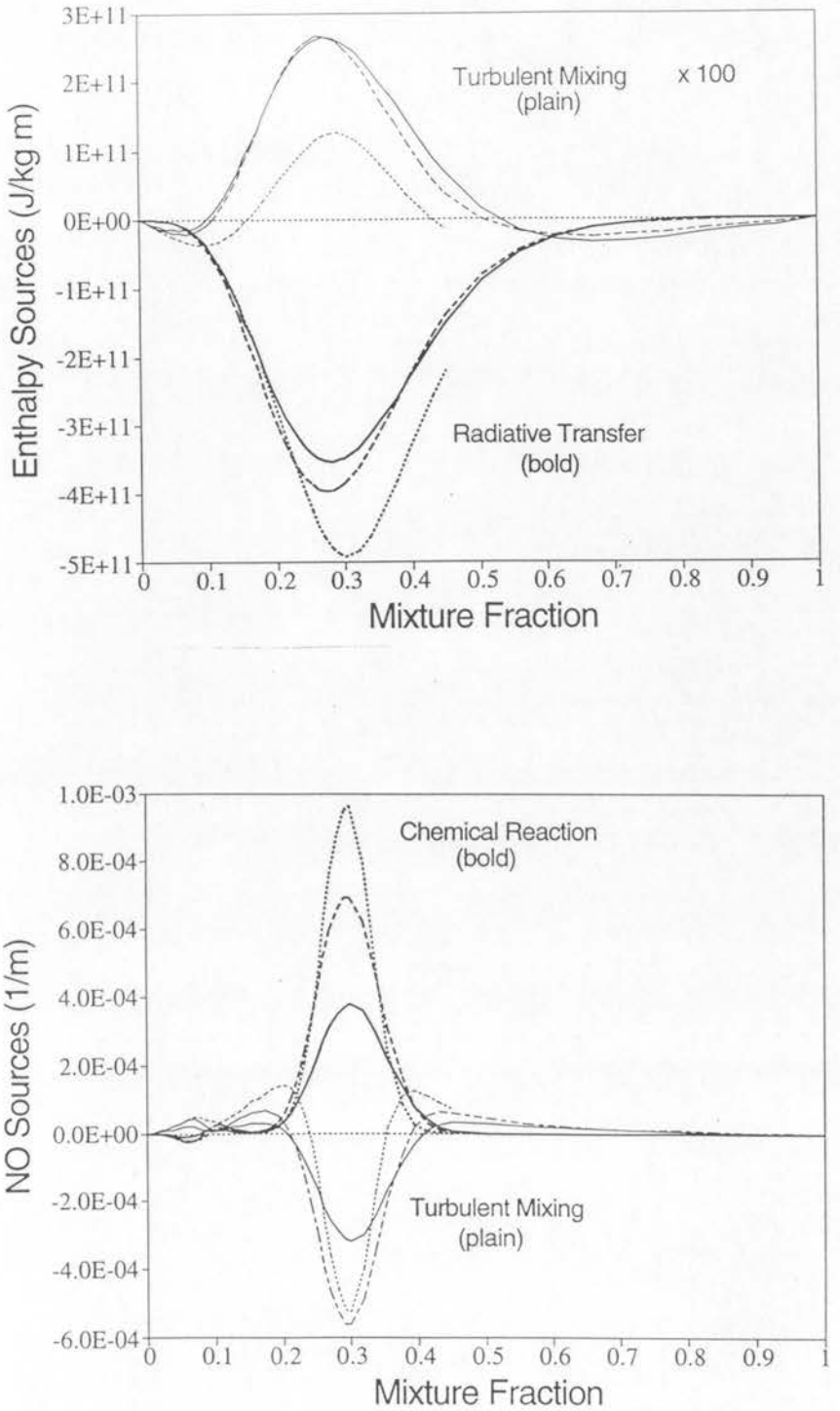

Figure 7.14: Conditional mean chemical production and turbulent mixing profiles at various axial locations in flame B. Line type denotes location: Locations (x/D): 10 - solid, 25 - dashed, 50 - dotted

diffusive balance alone. This is particularly true of mixing limited species in zones where the rate of turbulent mixing is high. However, there are also other species whose formation is not balanced between chemical reaction and diffusive transport, such as NO, and must involve a substantial convective component. The second important point to note, is that increased turbulent mixing rates cause the chemical formation rates of mixing limited species to similarly increase. In zones where turbulent mixing is intense, chemical formation rates are inclined to be similarly rapid. Under these conditions, the partial chemical equilibrium and steady state assumptions used to derive reduced chemical mechanisms may become invalid. The advantages yielded by these assumptions, when valid, and the effect of their disintegration upon model prediction is addressed in the next section.

7.4 Reduced Chemical Mechanisms

There is a considerable advantage to be had in using reduced chemical descriptions of full mechanisms. The derivation of the two and three step abbreviated mechanisms for H_2 and $CO-H_2$ combustion is a relatively straight forward process (see Appendix A). This process results in robust schemes that exhibit reasonable agreement with the larger ($\sim$ 25 step) mechanisms from which they are derived, whilst requiring a great deal less computation time in general application.

In some modelling instances, reduced chemical mechanisms are a mandatory requirement. This is true of virtually all applications of the joint PDF method, where the dimensionality of the reactive scalar composition space must be limited in order for the problem to remain tractable (see Section 2.2.2). Another example is in the application of 'real' chemistry to current DNS schemes, where computational resources are typically stretched in resolving the fluid dynamic aspects of the flow, and cannot bear the added burden of extensive chemical reaction calculations.

It is thus of some interest to gauge the performance and accuracy of reduced chemical mechanisms under turbulent diffusion flame modelling conditions, without introducing the uncertainty of having to use different modelling approaches for each mechanism. To this end, reduced mechanism calculations have been performed for flames A and B using the two and three step reduced mechanisms derived in Appendix

A.

The calculation times for the H_2 and $CO - H_2$ runs were only ~ 20 and ~ 13 CPU minutes respectively on the DEC Alpha workstation employed in Sections 7.1 and 7.2 which ran at a rate of $\sim 15 Mflops$. These run times represent an order of magnitude saving in computational cost, which makes their use seem highly attractive. It remains to be seen whether the loss in chemical accuracy is acceptable when considered in the context of this computational saving.

7.4.1 Two-Step H_2 Mechanism Results

Full and reduced mechanism predictions of conditional mean water (H_2O) and monatomic hydrogen radical (H) mole fraction for flame A are plotted in Fig. 7.15. It is evident that the reduced mechanism overpredicts the peak value of the conditional mean H_2O profile at all of the axial locations shown in the figure. This overprediction does not exceed 5% of the full mechanism predictions peak value at any location.

Coincident with the overprediction of the major product species, the reduced mechanism tends to underpredict monatomic hydrogen radical levels consistently throughout the flame. The magnitude of this underprediction can be as high as $\sim 30\%$ towards the end of the flame, but is up to four times smaller than this in the near-field of the jet.

As a result of the reduced mechanism predictions favouring exothermic product formation over endothermic radical formation, the corresponding conditional mean temperature predictions peak above the full mechanism temperature predictions (see Fig. 7.16). The level of the discrepancy between the different mechanisms can be as high as $\sim 50K$ in the near-field but drops to only a degree or two by the end of the flame.

The discrepancies observed between the full and reduced mechanisms for temperature, and H_2O and H mole fractions qualitatively agree with the results reported by Gutheil *et al*[126] for calculations carried out for laminar counterflow diffusion flames. Although it is not shown here, the present two-step mechanism overpredicts the levels of the steady state radical species (O,OH) in the same way as was reported by Gutheil *et al*[126].

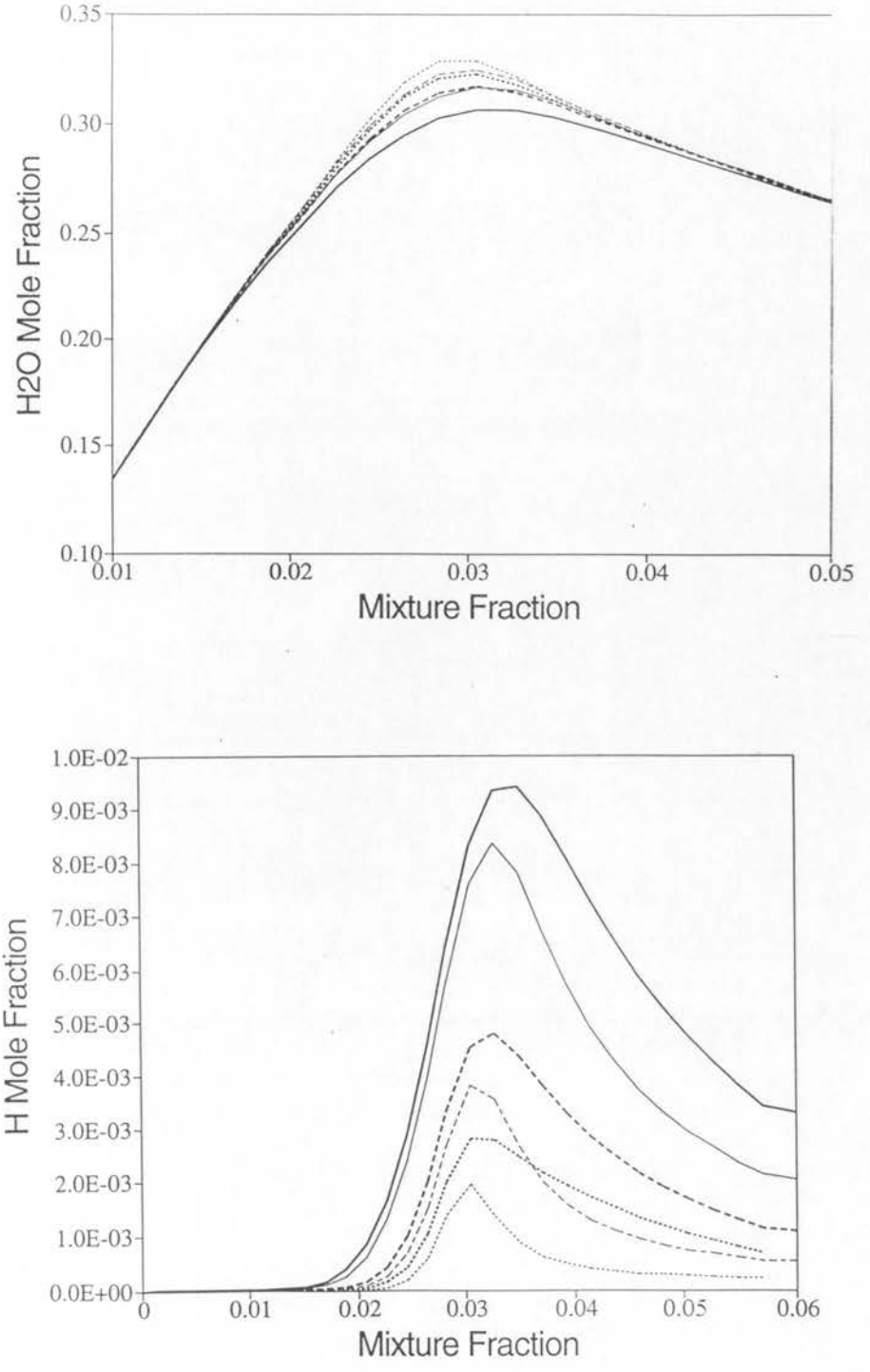

Figure 7.15: Conditional mean H_2O and H mole fraction profiles at various axial locations in flame A. Line type denotes mechanism (bold lines - full, plain lines - 2-stp) and location (x/L_v): 0.25 - solid, 0.5 - dashed, 0.75 - dotted

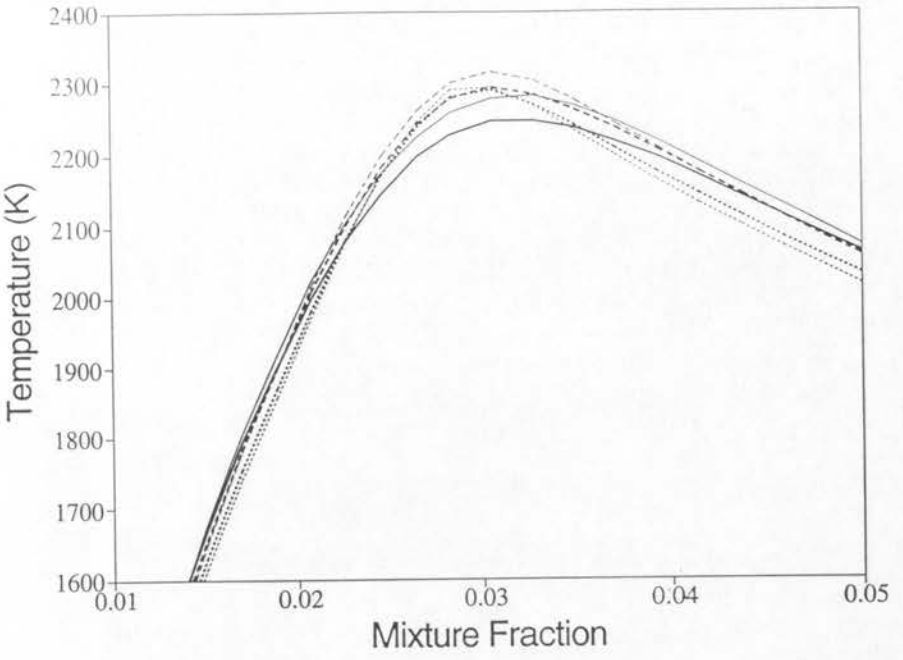

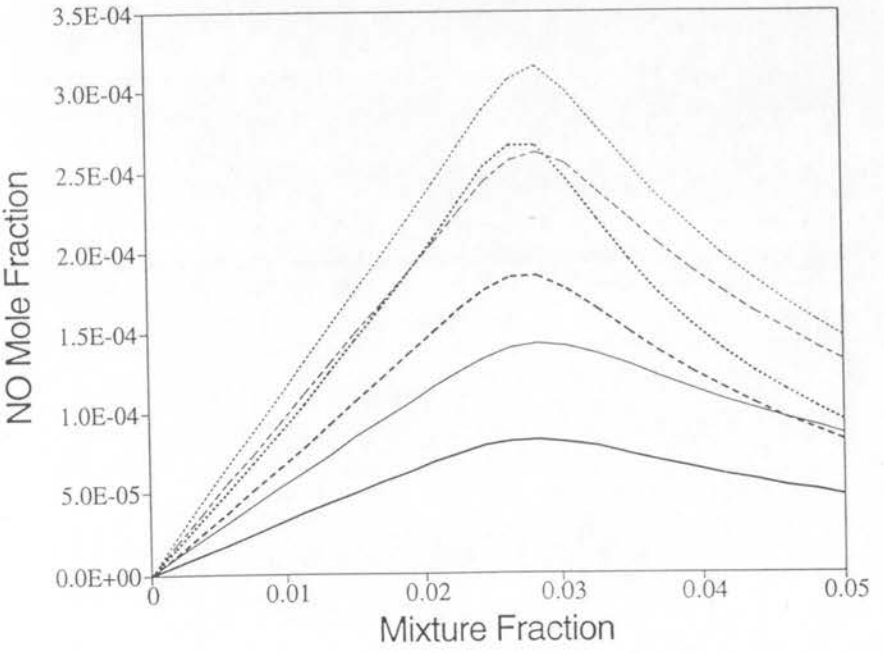

Figure 7.16: Conditional mean temperature and NO mole fraction profiles at various axial locations in flame A. Line type denotes mechanism (bold lines - full, plain lines - 2-stp) and location (x/L_v): 0.25 - solid, 0.5 - dashed, 0.75 - dotted

The influence of overpredicted temperature and monatomic oxygen (O) levels is clearly evident in the reduced mechanism predictions for NO mole fraction, formed via the thermal mechanism[128]. The reduced mechanism overpredicts the peak conditional mean NO mole fraction by around 50% in the near field of the flame, but this discrepancy is reduced to $\sim$ 20% by the end of the flame. The improving agreement between the full and reduced mechanism NO predictions results from the improved agreement in temperature and O radical levels.

The results presented here demonstrate that the reduced mechanism predictions improve in accuracy towards the end of the flame but do quite poorly in the intense mixing of the upstream sections of the flame. This trend is a result of the breakdown of the steady-state and partial equilibrium assumptions used in the derivation of the reduced mechanism (see Appendix A), when the chemical system is strongly perturbed by turbulent interaction.

7.4.2 Three-Step $CO - H_2$ Mechanism Results

It was noted in the derivation of the three-step reduced $CO - H_2$ chemistry (see Appendix A), that this mechanism is in effect equivalent to the preceding two step hydrogen mechanism with an appended step accounting for CO oxidation.

Predicted conditional mean H_2O, CO_2 and H mole fraction profiles are plotted in Fig. 7.17 for various axial locations within flame B. It is evident that in contrast to the H_2 comparison, the reduced $CO - H_2$ mechanism underpredicts H_2O formation at all axial stations when compared to the corresponding full mechanism predictions. The level of underprediction is only around $\sim$ 5% of the full mechanism peak value. Carbon dioxide peak conditional mean mole fractions are overpredicted by around $\sim$ 7% in a comparison of reduced to full mechanism values. Thus, the reduced mechanism overpredicts one of the major products to about the same degree that it underpredicts the other.

Monatomic hydrogen radical (H) mole fractions are overpredicted by the reduced mechanism, a fact which also contrasts with the pure hydrogen comparison. The level of this discrepancy remains approximately equal throughout flame B at around $\sim$ 30%. Despite the underprediction of H formation, the reduced mechanism tends also to slightly underpredict flame temperature (see Fig. 7.18).

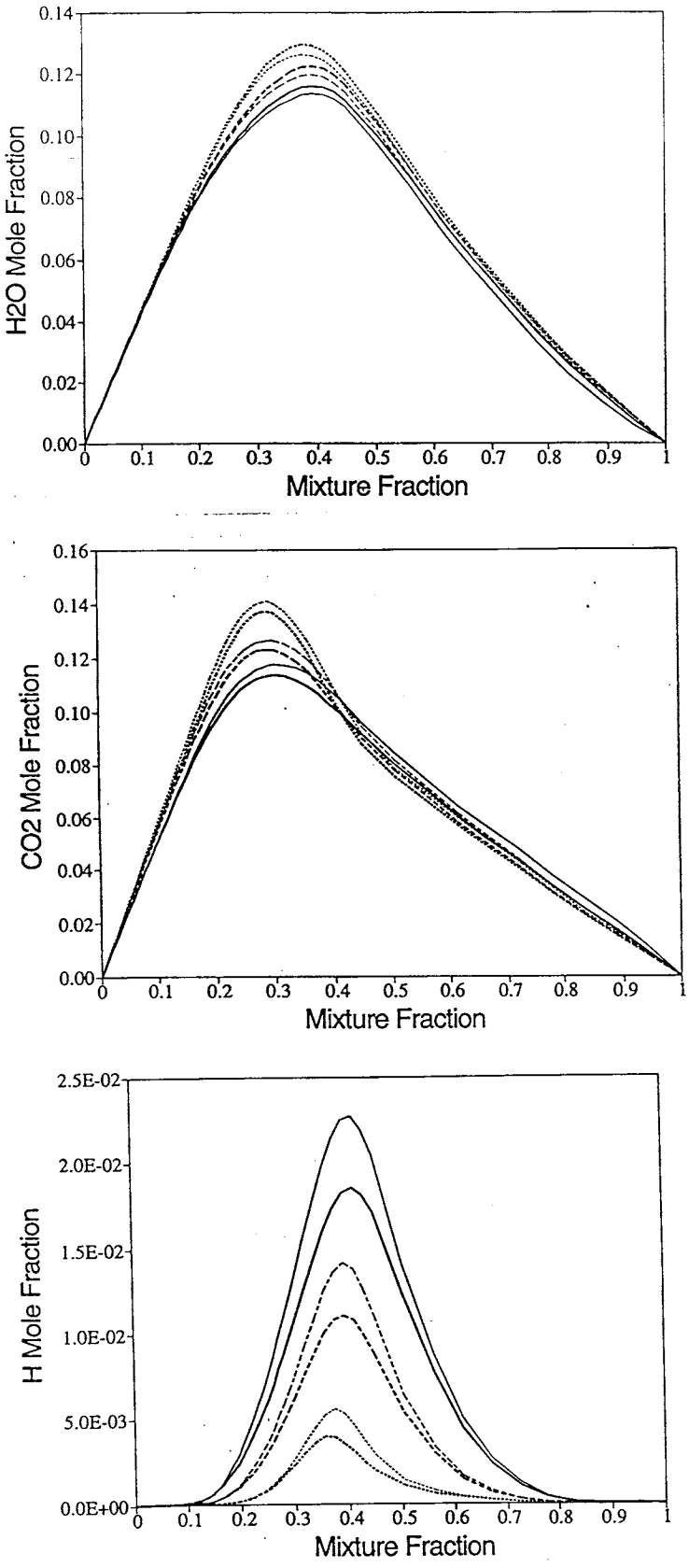

Figure 7.17: Conditional mean H_2O, CO_2 and H mole fraction profiles at various axial locations in flame B. Line type denotes mechanism (bold lines - full, plain lines - 2-stp) and location (x/D): 10 - solid, 25 - dashed, 50 - dotted

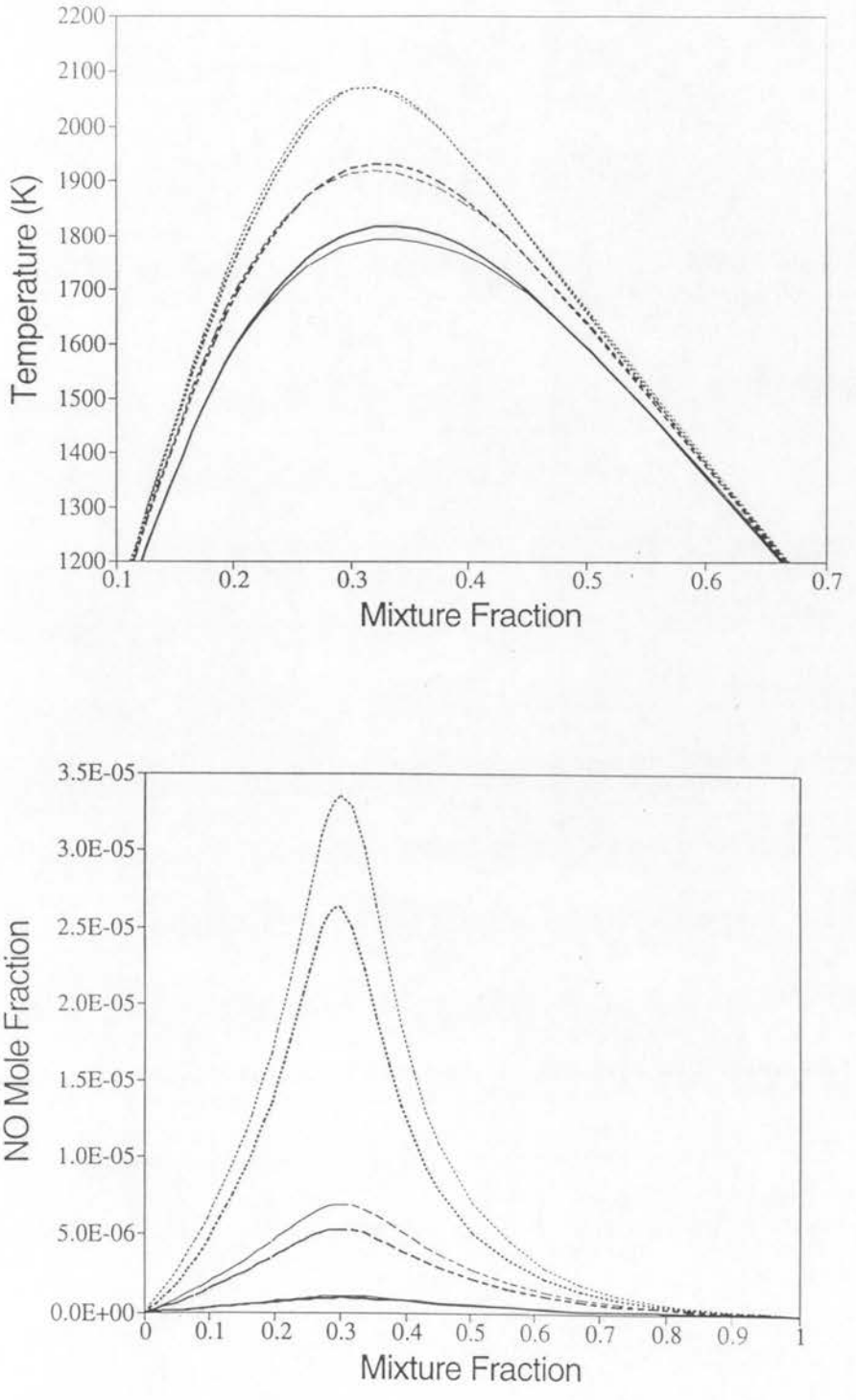

Figure 7.18: Conditional mean temperature and NO mole fraction profiles at various axial locations in flame B. Line type denotes mechanism (bold lines - full, plain lines - 2-stp) and location (x/D): 10 - solid, 25 - dashed, 50 - dotted

The magnitude of the temperature discrepancy between full and reduced mechanism predictions is comparatively modest, only around $40K$ in the near field and less than a degree further downstream. The accuracy of the reduced mechanism predictions for NO formation is slightly better than that found for the pure H_2 comparison. This may be a result of the lower predicted temperatures despite the excess of monatomic oxygen radical (not shown). The reduced mechanism predictions for overall NO_x emissions suffer from not being able to predict NO_2 formation, since this species is not carried in the reduced set for nitrogen chemistry. This problem is not so severe in the pure H_2 case where NO_2 levels are virtually insignifcant.

7.5 Emission of Nitrogen Oxides

Nitrogen oxide (NO_x) emission from laboratory jet flames has typically been expressed in terms of emission indices. Emission index (EI_i) is a dimensionless number which is defined as the total mass flow rate of a selected species (i) normalized by the nozzle mass flow rate (see below).

$$EI_i \equiv \frac{\dot{m}_i}{\dot{m}_{nozz}} \tag{7.3}$$

In defining a NO_x emission index, it is customary to treat moles of nitric oxide (NO) and nitrogen dioxide (NO_2) as though they have the same molecular weight. This is equivalent to taking it as read that all NO produced will be subsequently oxidized to NO_2. Thus the emission index for NO_x is given by,

$$EI_{NOX} \equiv \frac{W_{NO2}}{W_{NO}} EI_{NO} + EI_{NO2} \tag{7.4}$$

where W_{NO} is the molecular weight of NO ($= 30.01 g/mol$) and W_{NO2} is the molecular weight of NO_2 ($= 46.01 g/mol$).

Emission index profiles for flames A and B are plotted in Fig. 7.19 versus non-dimensional axial location. These emission index profiles are typical of all the jet flames modelled to date. The emission indices of fuel species, such as H_2 and CO (in the case of flame B), are progressively consumed along the length of the flame until they are completely depleted. At the same time, the major product species (H_2O,CO_2) build up to plateau levels and remain constant after the stoichiometric flametip.

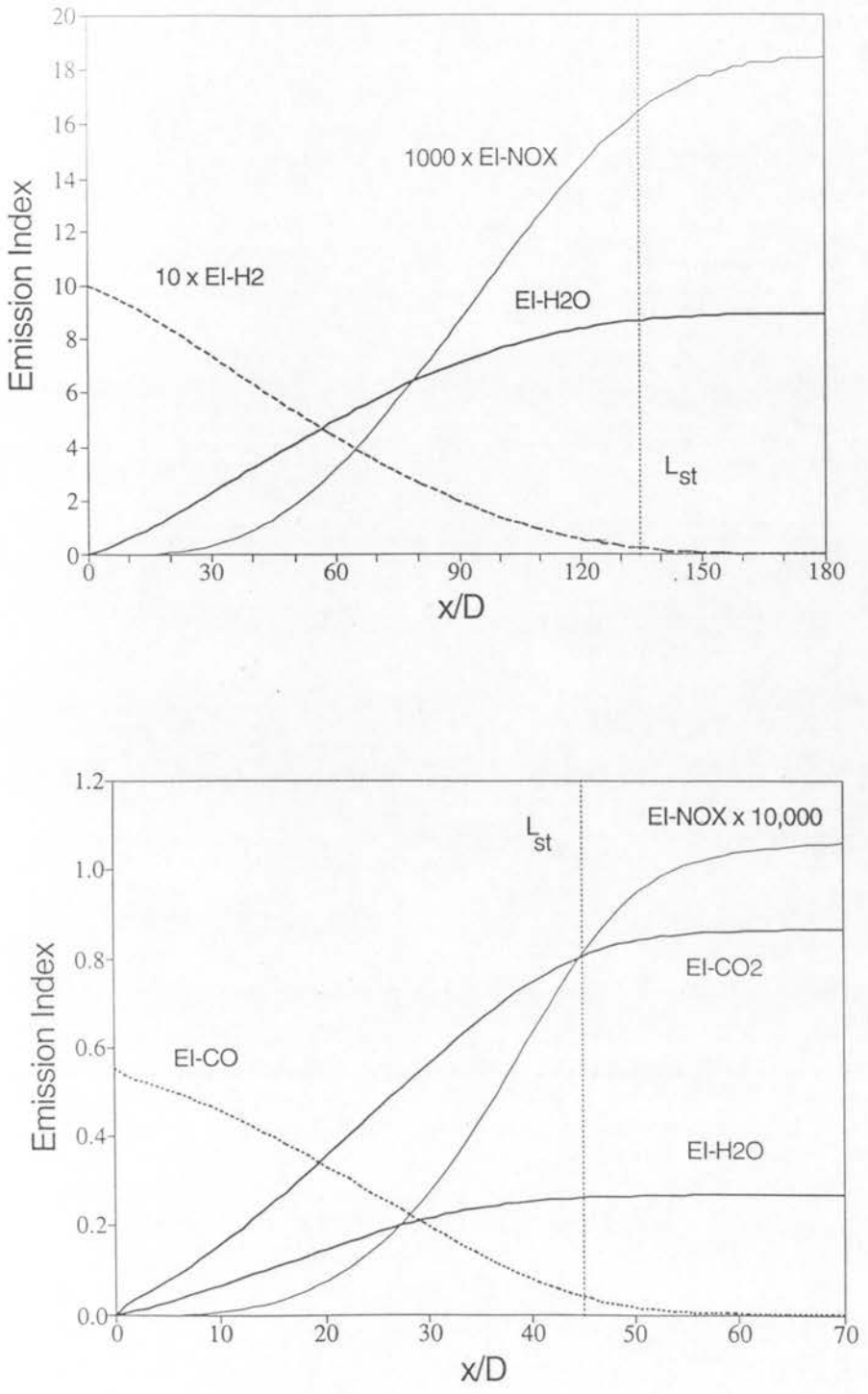

Figure 7.19: Emission indices versus axial location for various species in flames A and B. L_{st} denotes stoichiometric flamelength.

Flame	Source	EI_{NOX}	Additional notes
A	Ref.[150]	1.36e-2	Determined by cross-flow integration of laser point measurements. NO_2 NOT included.
A	Ref.[145]	1.52e-2	Determined by cross-flow integration of sample probe measurements
A	Ref.[104]	2.92e-2	Full chemistry, adiabatic CMC (Used early mixing model, see Section 6.2)
A	Ref.[104]	1.90e-2	Full chemistry, non-adiabatic CMC (Used early mixing model,see Section 6.2)
A	*ibidem*	1.80e-2	Full chemistry, non-adiabatic CMC
A	*ibidem*	2.09e-2	2-step chemistry, non-adiabatic CMC
B	Ref.[143]	7.50e-5	Determined by cross-flow integration of sample probe measurements
B	*ibidem*	1.08e-4	Full chemistry, non-adiabatic CMC
B	*ibidem*	1.33e-4	3-step chemistry, non-adiabatic CMC

Table 7.3: Postflame EI_{NOX} values from modelling and experiment.

The behaviour of NO_x is slightly different however, and plateau values are reached somewhat beyond the stoichiometric flametip, closer to the estimated location of the visible flametip. This behaviour is a result of the kinetically limited nature of NO_x formation. In contrast to the major product species, NO and NO_2 levels are orders of magnitude below the corresponding chemical equilibrium levels. As such, NO_x levels will continue to rise until they reach equilibrium or the formation reactions cease due to dilution of the hot post-flame gases with the colder surrounding air. In nonpremixed turbulent jet flames the latter situation always applies.

Smith *et al*[104] report experimentally determined values of post-flame EI_{NOX} from Barlow and Carter[150] and Driscoll *et al*[145] in comparison with earlier CMC calculated values. These values are presented in Table 7.3, for comparison with the values calculated in this investigation. The experimental values reported by Drake *et al*[143] and predictions for flame B are also included.

An examination of Table 7.3 reveals that the CMC model predictions made in this investigation are somewhat lower than those made by Smith *et al*[104]. These differences can be attributed to the revised mixing model adopted in this investigation (see Section 6.3). It is also apparent that the EI_{NOX} predictions made with the reduced chemical mechanisms described in the previous section, are at least 10% greater than the corresponding full mechanism predictions. It should be remem-

bered that the reduced mechanism calculations do not calculate NO_2 levels, and so the EI_{NOX} statistics quoted in these cases are based upon weighted NO only. The relative amount of NO_2 (EI_{NO2}/EI_{NOX}) predicted in flames A and B, using full mechanisms, was of the order of 1% and 20% respectively. The discrepancies between the measured and predicted EI_{NOX} values are of the order of $\sim 20\%$, and are consistent with the observed differences in conditional mean NO profiles.

Many researchers have studied how EI_{NOX} scales with varied macroscopic flame parameters such as jet velocity, nozzle diameter and fuel composition. In recent years, Driscoll and coworkers[144,145] have experimentally investigated influences such as fuel dilution, flamelength variations due to changes in coflow velocity and swirl etc. Turns and associates[146,147] have investigated the effects or radiation, fuel dilution and global residence time. Chen and Kollmann[51] have modelled NO_x emission scaling with global residence time and provide supporting argument for the observed trends in hydrogen jet flames[144].

It is now quite well known that hydrogen EI_{NOX} statistics from a wide range of jet flame cases can be collapsed onto a single line on a log-log plot[51,96,144]. The NO_x emission index seems to scale with global residence time (τ_g) according to the following expression,

$$\frac{EI_{NOX}}{\tau_g} \propto (\frac{U_j}{D})^a \tag{7.5}$$

where U_j is the centreline jet velocity at the nozzle, D is the nozzle diameter. a is a constant and τ_g is defined by the equation below.

$$\tau_g \equiv \frac{L_f^3}{D^2 U_j} \tag{7.6}$$

The scaling relation given by Eqn 7.5 relates emission index normalized by residence time to an estimate the the mean rate of strain in the jet flame (U_j/D). For a given flame chemistry, a global Damkohler number can be said to be proportional to the inverse of this quantity[144]. The index (a) of Eqn7.5 indicates thus scales NO_x formation with inverse Damkohler number, a measure of the predominance of turbulent mixing over chemical reaction.

The flamelength L_f employed in Eqn 7.6 is the visible flamelength ($L_f \equiv L_{vs}$) in the definition given by the experimentalists Chen and Driscoll[144]. Combustion modellers prefer to use the stoichiometric flamelength as the scaling length ($L_f \equiv L_{st}$)

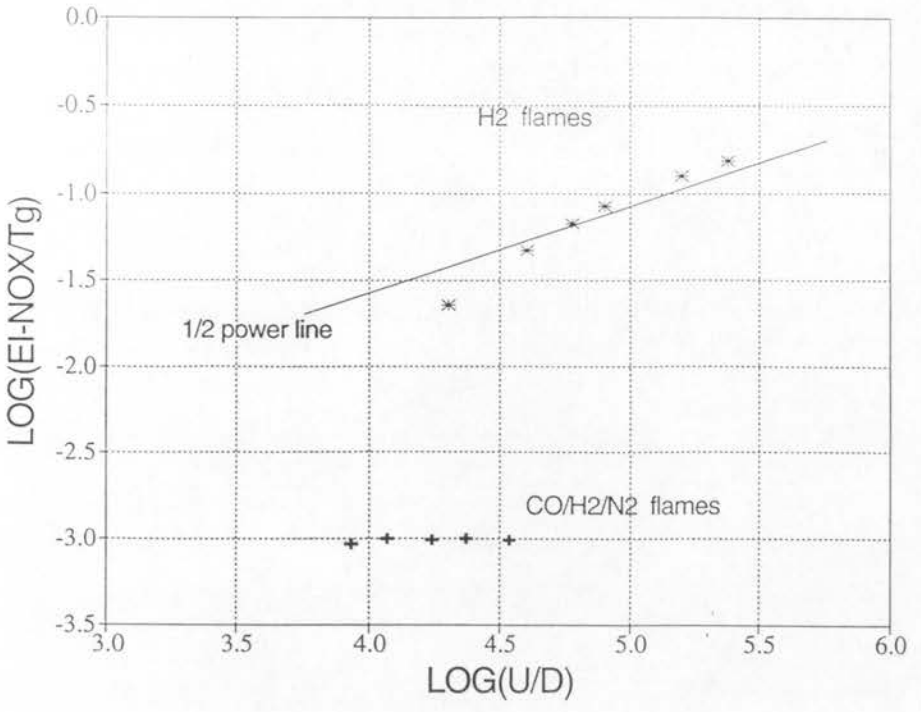

Figure 7.20: Predicted postflame EI_{NOX}/τ_g scaling with U_j/D from calculations for H_2 and $CO/H_2/N_2$ round jet flames.

because it can be determined from computations. Both definitions of flamelength give the same scaling relation (Eqn 7.5) with the scaling index being approximately equal to one half ($a \approx 0.5$) for round hydrogen jet flames[51,96,144].

The CMC calculated postflame EI_{NOX} values for H_2 and $CO - H_2$ flames are scaled and plotted versus U_j/D in Fig. 7.20. It is evident from the figure that the H_2 predictions behave in the expected manner. At high values of U_j/D, EI_{NOX}/τ_g tends to obey the 1/2 power scaling law espoused by Chen and Driscoll[144] and Chen and Kollmann[51]. However, at longer residence times the predicted values scale with a higher slope than that observed experimentally.

Chen and Kollmann[51] noted a similar trend in their calculations for pure H_2 flames with radiation loss. This unexpected behaviour was attributed to the alleged inaccuracy of the optically-thin radiation model under these conditions. Smith *et al*[96] and Chen and Kollmann[51] both report that the drop off in EI_{NOX}/τ_g at small U_j/D is not present in adiabatic H_2 model predictions.

As was mentioned in Section 7.1.2, an alternative optically-thin radiation submodel[155] was trialled against the current model (see Appendix B), but the predicted NO_x for-

mation levels changed by less than 5%. An analysis of radiation losses from the H_2 flames studied here is given in the following section.

The results from $CO - H_2$ calculations suggest that for round syngas jet flames with the composition studied here, EI_{NOX}/τ_g does not scale with U_j/D. Turns and Myhr[146] report that for the syngas flames they studied. EI_{NOX}/τ_g did not scale with jet Reynolds number. This has been found to be the case with the EI_{NOX}/τ_g statistics calculated here, although they are not plotted. The results calculated here suggest that EI_{NOX} scales linearly with τ_g for round syngas jet flames.

The half-power scaling with inverse Damkohler number, that has been noted for round hydrogen jet flames[51,144], does not seem to extend to syngas flames, nor does it appear to extend to the methane flames studied to date[145].

7.6 Radiation Losses

In the absence of accurate measurements of radiation losses from turbulent jet diffusion flames, it is difficult to draw conclusions from studying model predictions alone. Turns and Myhr[146] provide measurements of radiant fraction (f_{rad}) for syngas and hydrocarbon jet flames. However, in this investigation radiation from H_2 jet flames is of primary concern since it has been claimed to cause the deviations from experiment noted earlier[51].

Turns and Myhr[146] measured radiant fraction (f_{rad}) using a heat flux transducer positioned at the flame midlength, at a radius R from the centreline. Radiant fractions were estimated from radiant flux measurements (q_{rad}) from the transducer by the following expression:

$$f_{rad} = \frac{q_{rad} 4\pi R^2}{\dot{m}_{nozz} \Delta H_{comb}} \tag{7.7}$$

The estimated value of total radiation loss, given by the numerator of the expression above, is normalized by the nozzle mass flow rate $\dot{m}_{nozz}$ (assuming the nozzle mass to be undiluted fuel) and the heat of combustion of the fuel (ΔH_{comb}).

As it is not clear what value should be ascribed to the heat of combustion, a slightly different radiant loss indicator is adopted here. This quantity which shall be referred to as the specific heat loss ($\Delta h(x)$), describes the total enthalpy lost to the

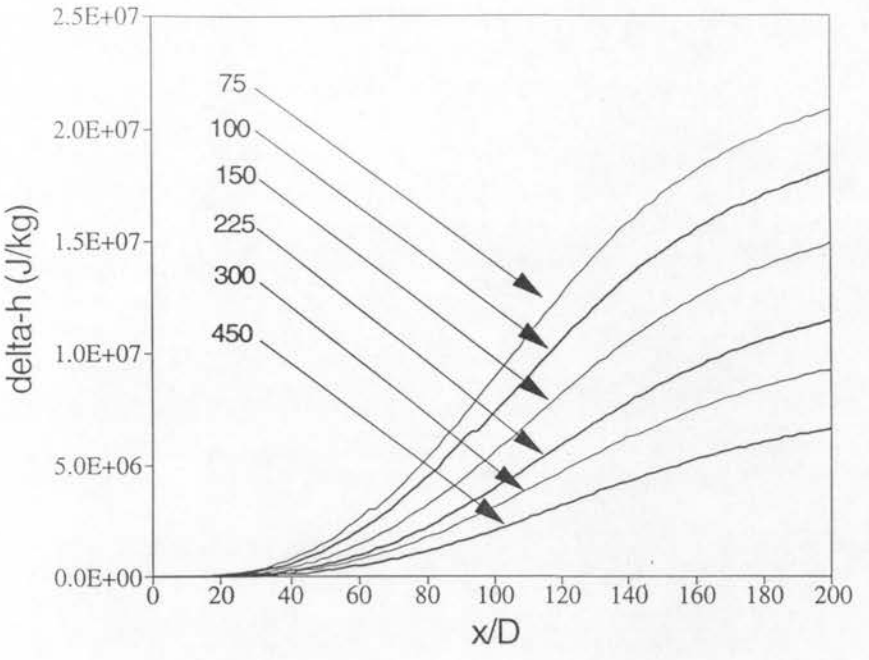

Figure 7.21: Predicted axial variation in specific heat loss $\Delta h(x)$ for pure H_2 jet flames with varying jet velocity but constant nozzle diameter $D = 3.75mm$. Labels denote jet velocity in metres per second.

surroundings between the nozzle exit plane and the measurement location. Specific heat loss ($\Delta h(x)$) is formally defined below,

$$\Delta h(x) \equiv \frac{1}{\dot{m}_{nozz}} \int_0^\infty (\bar{h}_{ad}(x,r) - \bar{h}_{rad}(x,r))\bar{\rho}\bar{u}rdr \tag{7.8}$$

where $h_{ad}(x,r)$ is the standardized enthalpy at a point in physical space that results from the adiabatic mixing of the pure fuel and air streams, and $h_{rad}(x,r)$ is the corresponding value in the presence of radiant losses. These quantities are readily available from the existing CMC jet flame data. It can be seen that the radiant fraction defined above should only differ from specific heat loss in the post-flame region by a constant factor, namely the heat of combustion used by Turns and Myhr[146].

Axial profiles of predicted specific heat loss for a range of different H_2 jet flames is plotted in Fig. 7.21. All of the flames have the same nozzle diameter ($D = 3.75mm$) and vary only in jet velocity which is given in the figure in units of metres per second. It is evident from Fig. 7.21, that the specific heat loss profiles show little sign of levelling off even at locations beyond the stoichiometric and visible flamelengths ($L_{st} \approx 135D.L_{vs} \approx 180D$). The post-flame gases remain sufficiently hot beyond the

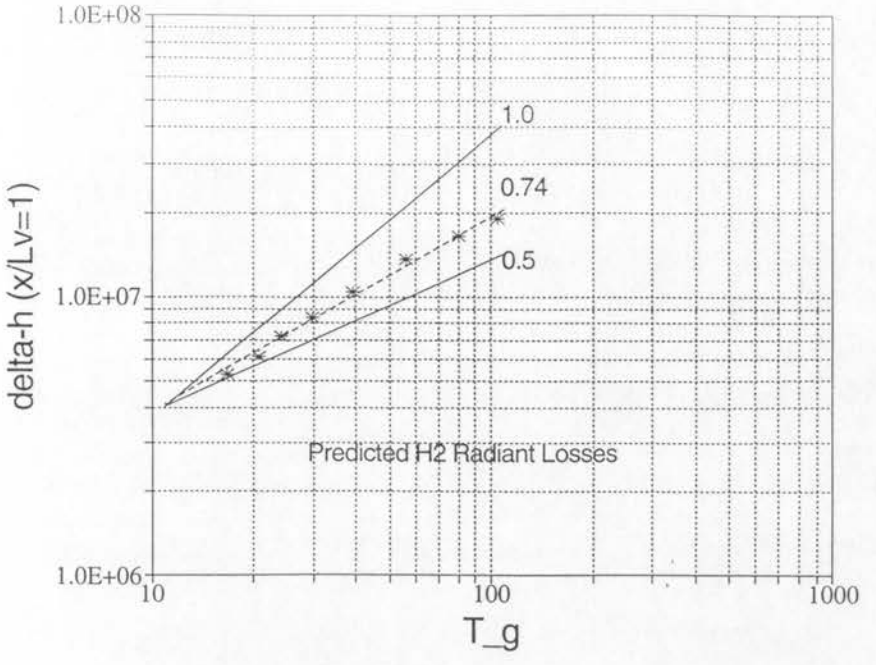

Figure 7.22: Predicted variation in visible flametip specific heat loss $\Delta h(x = L_{vs})$ with global residence time τ_g for pure H_2 jet flames.

end of the flame for radiation heat transfer to continue transferring energy from the system. In theory the specific energy loss profiles will only reach plateau values when the post-flame gas temperatures fall to ambient levels. However the amount of specfic energy lost beyond a few visible flamelengths is small in proportion to the total loss.

In order to investigate the influence of global residence time upon radiation losses from H_2 jet flames, specific energy loss values at the visible flamelength have been arbitrarily chosen to represent the overall radiation loss in each case. This decision is justified by the fact that the different specfic energy loss profiles remain in constant proportion to one another at large distances from the nozzle. Further, radiation effects at locations substantially beyond the visible flametip can have no significant effect upon NO_x formation (see Fig. 7.19).

Predicted specific energy losses at the visible flametip are plotted against global residence time (τ_g) for pure H_2 jet flames in Fig. 7.22. Note that the residence time employed here is that defined in Eqn 7.6, rather than that employed by Turns and Myhr[146]. Although different in magnitude, both residence times are directly proportional to the convective timescale. It is apparent from the figure that $\Delta h(x =$

L_{vs}) exhibits a ~ 0.74 power law dependence upon the global residence time. This power law dependence is somewhat less than the ~ 1 dependence reported by Chen and Kollmann[51]. It is however, higher than the ~ 0.67 and ~ 0.30 dependences of C_2H_2 and CH_4 which can incur additional radiation losses as a result of soot formation[51].

Although it may be purely coincidental, it should be noted the trend in power law dependence with fuel type is in qualitative agreement with the rankings of the adiabatic flame temperatures of the fuel species. It is difficult to judge precisely what power law dependence should be exhibited by H_2 jet flames, and the questions surrounding the accuracy of the optically-thin radiation loss approximation remain unanswered.

7.7 Discussion

Having discussed specific results in the preceeding sections, it is now appropriate to discuss, the advantages and disadvantages of CMC jet model in a more general context. These advantages and disadvantages are discussed in relation to other jet flame models in the following.

7.7.1 Advantages of CMC Jet Flame Modelling

It has been shown that the CMC jet flame model is capable of producing detailed chemical predictions in turbulent jet flames without stretching the computational capacity of a workstation-sized computer. This ability is evidently not shared by other contemporary turbulent jet flame models.

The CMC method can be used to model turbulent jet flames of non-hydrocarbon and simple hydrocarbon fuels (H_2,$CO - H_2$,CH_4,CH_3OH) using chemical mechanisms with ~ 20 reactive species and around ~ 10 CPU hours of workstation computation time. Alternatively, reduced chemical mechanisms can be employed for the same fuels mentioned above, and computation times become so low as to be trivial.

Joint PDF methods require substantially more computational resources to implement. Sion and Chen[52] report that methanol (CH_3OH) jet flame calculations using a four-step reduced mechanism require approximately 1200 CPU seconds per

calculated diameter of axial length. Given that flames of the type reported require calculations out to axial lengths of $\sim 100D$, the full computation time must have been of the order of ~ 30 CPU hours on the CRAY XMP-48 supercomputer used in the study.

It has been seen in Section 7.4, that reduced chemical mechanisms introduce errors into calculated predictions for non-hydrocarbon turbulent jet flames. These errors are at their greatest for radical species and temperature in intensely mixed zones such as the near-nozzle mixing field. Breakdown of the assumptions made in reduced mechanism derivation occurs under these conditions, and lead to the observed discrepancies with full predictions. Whilst the discrepancies in temperature and major species levels typically become small in quiescent downstream zones, the effect of these small differences is substantial for important species such as NO and NO_2.

The discrepancies between full and reduced chemical mechanisms in hydrocarbon flames is likely to be more serious, particularly when important rich side chemistry is neglected. The ISR analysis of full and skeletal methane mechanisms (see Section 5.2) provides a rough guide to the level of error that might be incurred in modelling hydrocarbon flames with reduced mechanisms. Chen and Kollmann[48] have reported difficulties in modelling CO and CO_2 levels with a four-scalar constrained-equilibrium chemical model, in a propane (C_3H_8) jet flame. These kinds of problems seem to be inherent in reduced mechanism modelling.

To date hydrocarbon flames have not been modelled using the CMC method. However, there are no impediments to employing a comprehensive C_1 mechanism such as a skeletal methane mechanism[1] in the jet flame model, and predictions will be compared against suitable experimental measurements in the immediate future. Beyond this objective, the modelling of complex fuels (eg: octane, decane etc.) in turbulent nonpremixed jet flames, with short mechanisms seems to be amenable to CMC methods. It is difficult to envisage these types of calculations being performed with any other contemporary turbulent jet flame model.

It could be argued that steady laminar flamelet methods (SLFM), as described in Chapter Two, can model similarly complex chemistry with the same if not less

[1] see Appendix A for an example

computational cost. However, as was mentioned in Section 2.2.1, SLFM is only valid where the smallest scales of turbulence are larger than the the reaction zone. Whilst this may be the case in the near-field of the jet, it is frequently not so in the far-field.

7.7.2 Disadvantages of CMC Jet Flame Modelling

A number of significant disadvantages of the CMC jet flame method have become apparent through the course of this investiagtion. The bulk of these disadvantages are associated with the near-field behaviour of turbulent jet flames.

As with all conditional moment closure methods which make use of mixture fraction as a single conditioning variable, the jet flame model cannot be employed in the presence of extinction and ignition phenomena. As has been mentioned earlier, the reason for this is that the first order closure approximation for the chemical reaction terms is inaccurate under these conditions. This exclusion prevents lifted diffusion flames and blow-out conditions from being studied with the jet flame model.

This is evidently not the case for the joint PDF method which in theory is capable of predicting flame blow-off conditions. Some difficulties are associated with deriving the required reduced mechanisms that are valid under extinction conditions, but nevertheless useful studies have been made of near extinction behaviour[160].

In order to be applicable under extinction and ignition conditions, the CMC closure should employ an additional conditioning variable to account for reaction progress. This has not been done to date, but the future development plans in this direction are discussed in Chapter Nine.

Aside from the issue of first order chemical closure validity, the current CMC jet flame model appears to have further problems in the jet near-field. The recent results of Barlow and Carter[152] show that conditional mean temperature and nitric oxide display a radial dependence near the nozzle of pure hydrogen flames. This evidence invalidates the assumption of radial independence, suggested by Bilger[8,9] and Klimenko[6,7], and used in the simplification of the jet flame model to a quasi one dimensional problem. The observed radial dependence quickly weakens as the mean two dimensional boundary layer structure of the jet becomes established away from the near-field, and so is of no consequence over the majority of the flamelength.

The impact of the findings of Barlow and Carter[152] will be further discussed in Chapter Nine.

There is now a substantial body of evidence that suggests that differential diffusion effects are important in the near field of H_2 and $CO - H_2$ jet diffusion flames[102,130,150]. Further specific differential diffusion studies have been conducted for $H_2 - CO_2$ jet flames where the 'fuel' stream contains species with vastly different molecular transport properties [161,162]. Differential molecular diffusion is not accounted for in the current CMC formulation. The means of treating the high wave number effects associated with differential diffusion are not immediately apparent in the current methodology, and will require substantial theoretical development to produce a modified closure scheme. The inability to treat differential diffusion is shared by the joint PDF method[5], but is treated by laminar flamelet methods.

It is apparent that the near field of jet flames studied here display flamelet like qualities[130]. This is a reasonable conclusion since the mean scalar gradients are at their highest in the near field, and turbulent fluctuation levels are comparatively low. Problems can arise for the current CMC method when modelling conditions include very thin flamelet zones. Conditional mean correlations with fluctuations in scalar dissipation rate should be accounted for[154], but in doing so the global nature of the current CMC method is lost. The modified theory, recently proposed by Klimenko[154], is a local one that is similar in application to flamelet methods.

The application of Joint PDF methods in thin flamelet regimes is also potentially problematic. Under these conditions, difficulties arise in predicting localized extinction due to the sensitivity of these predictions to the arbitrary maximum distances in composition space over which particles are allowed to interact. If this distance is too great, then predictions of localized extinction can result where none actually occurs.

7.8 Summary

The main points raised in this chapter are summarized here in point form. The comparison of predicted and measured H_2 and $CO - H_2$ flame data has revealed that:

- the jet flame model gives generally good agreement for conditional mean reactive scalar profiles.

- in the near-field of jet flames, significant flamelet-like behaviour causes differential diffusion to be important and these effects cannot be accounted for by the jet flame model.

- the far-field agreement is good although there are indications that the level of departure from chemical equilibrium is slightly underestimated by the jet flame model. Favre averaged data suggest that this underprediction may be due to the underprediction of mixture fraction variance levels throughout the jet flame.

Reduced chemical mechanisms have been tested against full mechanism predictions in H_2 and $CO - H_2$ flames and it has been found that:

- two and three step H_2 and $CO - H_2$ mechanisms require around twenty times less computation time than the full twenty-three and twenty-five step mechanisms.

- the reduced mechanisms provide better major species agreement with the full mechanisms under the more quiescent mixing conditions present near the end of the flames studied. The intense mixing which occurs at upstream locations leads to poorer agreement.

- the kinetically limited species, NO, tends to be overpredicted by around $\sim$ 20% towards the end of the flames studied. This results from poor agreement between predictions of the rate controlling reactive scalars such as temperature and monatomic oxygen.

The overall emission of oxides of nitrogen (NO_x) from the flames studied tends to exceed the measured levels by around $\sim 20 - 30\%$. The predicted trends in NO_x emission index with changing flow conditions were found to conform to the following:

- Good agreement was found with existing modelled and measured EI_{NOX} trend data. A half power dependence of EI_{NOX}/τ_g upon inverse Damkohler number was found for H_2 flames, as has been reported elsewhere[51,144].

- The predicted higher dependence of EI_{NOX}/τ_g upon inverse Damkohler number at low values of U_j/D has also been observed by others for radiating H_2 jet flames[51]. This discrepancy with experiment does not occur if adiabatic calculations are made[51,96], however the quantitative agreement between individual flame comparisons worsens.

Radiation losses from pure H_2 jet flames were analysed and the following conclusions were drawn:

- The trend in radiant loss from H_2 jet flames with global residence time seems to be higher than that of any of the hydrocarbon flames studied by experiment[146].
- The ~ 1 power dependence of radiant fraction upon global residence time reported elsewhere was not found in this investigation. A more modest value of ~ 0.74 is reported here, but this dependence is still inexplicably higher than the dependence for sooting hydrocarbon flames.
- An alternative optically-thin radiation model was tested but was not found to provide significantly different NO_x predictions. The questions raised by Chen and Kollmann[51] regarding the validity of the optically-thin radiation approximation remain open.

A general discussion of CMC model performance in comparison with other contemporary jet flame models has been presented.

- The principal advantage of the CMC model over other jet flame methods is its ability to make predictions using full chemical mechanisms at a comparatively low computational cost.
- The main disadvantage of the method is its inability to treat ignition and extinction phenomena, and various problems associated with near-field jet flame structure. These near-field problems like inability to handle differential diffusion and very thin flamelet-like structures are shared by the joint PDF method. These problems are not significant in jet flame predictions away from the near-field.

Chapter 8

Steady Premixed Reactors

In this chapter, conditional moment closure methods are proposed for a special class of turbulent premixed combustion problems. As was noted earlier (see Sections 2.3 and 3.3), premixed turbulent combustion is generally very difficult to model because thermochemical and fluid dynamic characteristics at any point in the flammable mixture can depend strongly upon the proximity and topology of the local flame front.

Conditional moment closure (CMC) methods can no more solve these general cases than other current methods. However, for a special class of problems in the intermediate regime of turbulent premixed combustion, CMC methods can provide chemically detailed solutions without requiring knowledge of flame front dynamics.

The model proposed in this chapter is intended to be applicable to steady state turbulent premixed reactors with spatially uniform conditional mean reactive scalar fields. Although this class of problems may seem somewhat restricted, it is important to note that the operating conditions of lean-premixed gas turbine combustors, which are currently used in low-NO_x utility-class power plants, fall within this domain. Aero-propulsion gas turbines may also be routinely operated in lean-premixed configurations in future, in order to comply with future tightening of aircraft emission regulations[129]. Gas turbine combustors are characterised by high mass flow rates, intense turbulent mixing and very short overall residence times. Under these types of conditions, the CMC methods of this chapter could be of use in predicting thermo-chemical yields, particularly in the recirculation zones associated with flame holders. It does not seem however, that spark ignition internal combustion processes

have the appropriate flame width to turbulent length scale ratio, nor the required steadiness, to be treated with the model presented here.

In some ways, the combustion model of this chapter can be viewed as a turbulent premixed generalisation of a perfectly stirred reactor (PSR). In this model there is a continous influx of unburnt mixture into the reactor core where vigorous mixing with the burning core fluid occurs, and yields outlet fluid that is neither fully burnt nor fully unburnt. By contrast, PSRs are not subject to core mixing and as a result the reactedness of the outlet fluid is only dependent on the residence time within the reactor.

This modelling concept has been employed by Correa and coworkers[92,93], as well as Roekaerts[94], in the development of the premixed PaSR (Partially Stirred Reactor) which makes use of joint PDF methods for modelling turbulence-chemistry interaction. Although similar in concept, the CMC model for steady premixed reactors uses a specially tailored reaction progress variable (RPV) which includes the effects of radiation losses upon the system (see Section 3.3). Accordingly, the model presented here is henceforth referred to by the acronym PTURCEL which stands for *P*remixed *Tur*bulent *R*eactor *C*alculation with *E*nergy *L*oss.

In the following section, PTURCEL-specific model equations are derived from the general equations presented in Chapter Three. The closure problems associated with PTURCEL modelling are addressed in Section 8.2. Lastly, a short discussion of the current state of premixed conditional moment closure methods can be found in Section 8.3.

8.1 PTURCEL Model Derivation

For the purposes of model derivation, a PTURCEL is defined as a volume of intense turbulent mixing where premixed chemical reactions are occuring such that the conditional mean reactive scalar statistics are not functions of position or time. It is envisaged that some kind of chemical 'forcing' is present, ie: a steady influx of unburnt fluid, so that trivial solutions to this steady problem are avoided. Whilst the conditional mean reactive scalars within the PTURCEL are not functions of space or time, the values at the inlet area may have different values. It is not expected

that conditional mean mixing statistics will be spatially independent. however they should be sufficiently uniform so that volume averages are representative of the mixing processes.

The conditional averaging employed in PTURCEL model derivation makes use of the reaction progress variable (RPV) c, defined in Section 3.3, as the conditioning variable. The definition of c is reproduced below.

$$c(\underline{x},t) \equiv \frac{\Omega(\underline{x},t) - \Omega_{unburnt}}{\Delta h^s_{ad-u}} \tag{8.1}$$

The variable Ω is defined by,

$$\Omega \equiv h^s - 2h \tag{8.2}$$

where h denotes instantaneous standardized enthalpy and Δh^s_{ad-u} is the sensible enthalpy difference between adiabatic equilibrium (h^s_{ad}) and unburnt (h^s_u) conditions.

The equations relevant to PTURCEL modelling can be derived from Eqn 3.64 which is reproduced below.

$$\begin{aligned} <\rho \mid \zeta> \frac{\partial}{\partial t}(Q_i P_\zeta) + \nabla\cdot(<\rho\underline{u}Y_i \mid \zeta> P_\zeta) = \\ \nabla\cdot(<\rho D \mid \zeta> \nabla Q_i P_\zeta) + <\rho w_i \mid \zeta> P_\zeta + \tfrac{\partial G_\zeta}{\partial \zeta} \end{aligned} \tag{8.3}$$

The same closure for the conditional mean flux G_ζ is applied here as was mentioned in Section 3.3 (see Eqns 3.66 and 3.67), and the approximate expression is substituted into Eqn 8.3. The resulting equation (see below) differs from 3.68 in that the simplification afforded by the RPV PDF conservation equation (Eqn 3.60) is not applied immediately.

$$\begin{aligned} <\rho \mid \zeta> \frac{\partial}{\partial t}(Q_i P_\zeta) + \nabla\cdot(<\rho\underline{u} \mid \zeta> Q_i P_\zeta) = \\ P_\zeta[<\rho w_i \mid \zeta> + <e_y \mid \zeta> + <e_Q \mid \zeta>] + \\ \tfrac{\partial}{\partial\zeta}(<\rho D(\nabla c)^2 \mid \zeta> Q_i P_\zeta - <\rho \mathcal{S}_c \mid \zeta> Q_i P_\zeta) \end{aligned} \tag{8.4}$$

The deviational terms in Eqn 8.4 are identical to those given by Eqns 3.69 and 3.70. The derivation is now at the point of averaging these general CMC equations over the PTURCEL reaction volume. Some clarifying comments are appropriate at this stage.

To simplify the final PTURCEL equations, it is necessary to assume that the conditional mean reactive scalar statistics ($Q_i(\zeta), i = 1,\ldots,N$) at the outlet from

the reaction zone are identical to those within the core of the reaction zone. This assumption is similar to that applied in the case of the ISR model derivation of Chapter 4. The basis for this assumption stems from the underlying definition of a PTURCEL, which does not allow for spatial variations in conditional mean reactive scalar values. Inlet values of the conditional mean reactive scalars can vary from those in the reactor core, and are distinguished from core values by the additional subscript 0 (eg: $Q_{i,0}$).

The error terms ($< e_y \mid \zeta >$,$< e_Q \mid \zeta >$) are neglected in the following analysis. This assumption is made as a simplifying step based on experience in nonpremixed systems[107], and may well require revision if development of this model proceeds further.

Averaging Eqn 8.4 over the reactor core volume (V), whilst applying the divergence theorem for inlet/outlet areas (A), and the steady state assumption inherent in the PTURCEL definition, yields Eqn 8.5.

$$\int_A [(< \rho \underline{u} \mid \zeta > Q_i P_\zeta)_{out} - (< \rho \underline{u} \mid \zeta > Q_{i,0} P_\zeta)_{in}] \cdot d\underline{A} = \int_V P_\zeta < \rho w_i \mid \zeta > + \frac{\partial}{\partial \zeta}(\frac{\partial}{\partial \zeta}(< \rho D(\nabla c)^2 \mid \zeta > Q_i P_\zeta) - < \rho \mathcal{S}_c \mid \zeta > Q_i P_\zeta) dV \quad (8.5)$$

A similar treatment of the RPV PDF equation (Eqn 3.60) yields the following,

$$\int_A [(< \rho \underline{u} \mid \zeta > P_\zeta)_{out} - (< \rho \underline{u} \mid \zeta > P_\zeta)_{in}] \cdot d\underline{A} = - \int_V \frac{\partial}{\partial \zeta}(\frac{\partial}{\partial \zeta}(< \rho D(\nabla c)^2 \mid \zeta > P_\zeta) + < \rho \mathcal{S}_c \mid \zeta > P_\zeta) dV \quad (8.6)$$

which can be employed to simplify Eqn 8.5 to give:

$$\int_A (Q_i - Q_{i,0})(< \rho \underline{u} \mid \zeta > P_\zeta)_{in} \cdot d\underline{A} = \int_V P_\zeta [< \rho w_i \mid \zeta > + < \rho D(\nabla c)^2 \mid \zeta > \frac{\partial^2 Q_i}{\partial \zeta^2} - < \rho \mathcal{S}_c \mid \zeta > \frac{\partial Q_i}{\partial \zeta}] dV \quad (8.7)$$

By adopting the averaging nomenclature of Section 4.1. then Eqn 8.7 can be rewritten as:

$$\{\{\rho\}\}(Q_i - Q_{i,0}) \frac{\{P_\zeta^*\}_{in}}{\tau_r} = \{\{P_\zeta < \rho w_i \mid \zeta >\}\} + \{\{P_\zeta < \rho D(\nabla c)^2 \mid \zeta >\}\} \frac{\partial^2 Q_i}{\partial \zeta^2} - \{\{P_\zeta < \rho \mathcal{S}_c \mid \zeta >\}\} \frac{\partial Q_i}{\partial \zeta} \quad (8.8)$$

The definition of the mass flow rate weighted RPV PDF $\{P_\zeta^*\}$ given by,

$$\{P_\zeta^*\} \equiv \frac{A}{\dot{m}} \{P_\zeta < \rho \underline{u} \mid \zeta >\} \quad (8.9)$$

where $\dot{m}$ is the total mass flow rate through the reactor, and the reactor residence time τ_r is given by,

$$\tau_r \equiv \frac{\{\{\rho\}\}V}{\dot{m}} \tag{8.10}$$

The RPV PDF conservation equation can be rewritten in the manner of Eqn 8.8 as follows:

$$\frac{\{\{\rho\}\}}{\tau_r}(\{P_\zeta^*\}_{out} - \{P_\zeta^*\}_{in}) = -\frac{\partial}{\partial\zeta}(\frac{\partial}{\partial\zeta}(\{\{< \rho D(\nabla c)^2 \mid \zeta > P_\zeta\}\}) + \{\{< \rho\mathcal{S}_c \mid \zeta > P_\zeta\}\}) \tag{8.11}$$

Together, Eqns 8.8 and 8.11 describe the conservation of reaction progress variable PDF and of reactive scalars conditionally averaged upon this reaction progress variable. All of the elements present in the nonpremixed analogue of the PTURCEL, the ISR, are present in the equations above.

In the conditional mean reactive scalar equation, a three-way balance of terms is possible between chemical reaction, turbulent mixing and inflow-outflow convective transfer. Further, there is an additional contribution that results from the non-conserved nature of the conditioning variable. This added term considerably increases the difficulty involved in solving the PTURCEL equations as compared to the ISR equations. The principal difficulties encountered in attempting solve the PTURCEL system are described in the next section.

8.2 Proposed Closure Strategy

Similar to the ISR model, a special case of the PTURCEL model applies when the inlet PDF ($\{P_\zeta^*\}_{in}$) is a delta function at the unburnt state. In this unburnt-inlet case ($\{c^*\}_{in} = 0$), the inflow-outflow convective transfer term on the left hand side of Eqn 8.8 is identically zero for all RPV values other than zero (see below).

$$0 = \{\{< \rho w_i \mid \zeta >\}\} + \{\{< \rho D(\nabla c)^2 \mid \zeta >\}\}\frac{\partial^2 Q_i}{\partial\zeta^2} - \{\{< \rho\mathcal{S}_c \mid \zeta >\}\}\frac{\partial Q_i}{\partial\zeta} \tag{8.12}$$

In this case, no information regarding the inlet conditional mean reactive scalar values at non-zero ζ is physically obtainable. In more general cases, ζ zones where the inlet PDF is non-zero will have associated conditional mean reactive scalar information which must be incorporated into the left hand side term of Eqn 8.8.

For the purposes of discussing a closure strategy for the PTURCEL system, attention will be confined to the special unburnt-inlet case. The RPV PDF conservation equation (Eqn 8.11) can be manipulated to yield an estimate of the core averaged conditional mean reactive scalar dissipation rate ($\{\{< \rho D(\nabla c)^2 \mid \zeta >\}\}$), by double integrating both sides of the equation with respect to ζ.

$$\{\{< \rho D(\nabla c)^2 \mid \zeta\}\} = \frac{1}{\{\{P_\zeta\}\}}[\frac{\{\{\rho\}\}}{\tau_r}(\zeta - \int_0^\zeta \int_0^{\zeta'} \{P^*_{\zeta''}\}_{out} d\zeta'' d\zeta') - \int_0^\zeta \{\{< \rho \mathcal{S}_c \mid \zeta' > P_{\zeta'}\}\} d\zeta'] \tag{8.13}$$

The boundary conditions upon this equation are $\{\{< \rho D(\nabla c)^2 \mid \zeta\}\} = 0$ for $\zeta = 0, \hat{\zeta}$ where $\hat{\zeta}$ is the upper bounding value of the RPV which depends upon the concentrations and enthalpies of formation of the species involved in the PTURCEL calculation.

The most appropriate boundary conditions upon Eqn 8.12 are $Q_i(\zeta = 0) = Y_{i,unburnt}$ and $\frac{\partial Q_i}{\partial \zeta}(\zeta = \hat{\zeta}) = 0$, since to be capable of specifying burnt conditional mean reactive scalar values negates the purpose of solving the PTURCEL equations. It is reasonable to expect the slope of the conditional mean reactive scalar profiles to tend to zero at $\zeta = \hat{\zeta}$ since this upper bound represents a highly radiatively cooled state that is far from where the principal reactions will be taking place ($\zeta \sim 1$). The influence of the upper boundary conditions upon the reaction zone statistics should ideally be small.

Equation 8.13 provides the means of determining conditional mean reactive scalar dissipation, which is needed to close Eqn 8.12, if the residence time and the core and outlet averaged RPV PDFs are known. These data values could possibly be determined from flow rate, and temperature and major species information alone, if this information has been measured or calculated for the target reactor.

With this information, $\{\{< \rho D(\nabla c)^2 \mid \zeta\}\}$ can be determined iteratively by solving Eqn 8.12 and 8.13 simultaneously. A first order closure approximation for $\{\{< \rho \mathcal{S}_c \mid \zeta >\}\}$ can be determined by evaluating the instantaneous expression (Eqn 3.55) with the appropriate conditional mean reactive scalar values at each solution step. The determination of the steady state solution profiles of $\{\{< \rho D(\nabla c)^2 \mid \zeta\}\}$ and $\{\{< \rho \mathcal{S}_c \mid \zeta >\}\}$ would likely be a time consuming process, and one that is prone to diverge rapidly if the starting estimates are poorly chosen. On the other hand, if the initial estimates are PTURCEL solutions for a case with similar run conditions,

convergence could occur very quickly.

8.2.1 Application of Closure Strategy

In many cases, although estimates of reactor residence time may exist for a target reactor it is quite possible that no measurements of the required PDF information will be available.

It might seem that if the PDF information were available then there would be little need to engage in a PTURCEL calculation. This is not necessarily true, since if the purpose of carrying out the calculation is to determine the levels of minor species such as NO, NO_2 and CO within a reaction zone for a case where these cannot be directly measured, PTURCEL methods could be used to estimate these values. Temperature and major species information would be used to determine the PDF forms.

Practical combustors and reactors are typically difficult environments in which to make accurate quantitative measurements. Limited optical access, high background interference, 'dirty' flame conditions and so forth, restrict the means of measurement to methods such as CARS (Coherent Anti-Stokes Raman Spectroscopy) where only temperature and major species information is available[163].

However, in the event that the required PDF information is not at hand, then a means of predicting the PDF data must be devised. One effective method might be to employ an existing turbulent premixed flame model, such as the Bray-Moss-Libby model (see Section 2.3) using simplified chemistry to determine the core and outlet RPV means and variances. This information would allow appropriate presumed form RPV PDFs to be adopted, and the PTURCEL calculation could proceed from that point to 'chemically refine' the BML model prediction.

In an effort to carry out a parametric study of PTURCEL predictions for a simple hydrogen system in the absence of any real data, a crude 'k-epsilon' approach was devised for predicting RPV mean and variance information.

K-epsilon approach for predicting RPV PDFs

The objective of the following 'order-of-magnitude' method is to roughly estimate RPV PDF information solely from specifications of chemical mechanism, reactor residence time (τ_r) and turbulent mixing frequency (ω_t).

Further simplifications of the unburnt-inlet PTURCEL equations were made in order to reduce the required modelling effort. Firstly, the core averaged and outlet averaged RPV PDFs were assumed to be identical. This assumption implies that the conditional mean mass flow rate that weights the latter PDF is uniform across ζ-space. There is some support for this assumption in the conditional mean velocity information presented by Mantel and Bilger from a DNS study of thickened wrinkled premixed flames[107], provided it is assumed that changes in flux area correspond with changes in specific volume.

The instantaneous RPV equation (Eqn 3.54) yields the following expression for outlet/core mean RPV when averaged over time and the reactor volume under unburnt-inlet PTURCEL conditions.

$$\{\{\bar{c}^*\}\} = \{\bar{c}^*\}_{out} = \{\{\bar{\mathcal{S}}_c\}\}\tau_r \tag{8.14}$$

Note that the influence of velocity-RPV correlations at the inlet and outlet have been neglected. The equation governing core averaged RPV variance ($\{\{\bar{c'^2}\}\}$) is given below for unburnt-inlet PTURCEL conditions:

$$\{\{\bar{c'^2}\}\} = 2\tau_r[\{\{c'\bar{\mathcal{S}'}_c\}\} - \{\{D(\bar{\nabla c})^2\}\}] \tag{8.15}$$

As with Eqn 8.14, the influence of RPV-variance-velocity correlations at the inlet and outlet areas is neglected in Eqn 8.15. In order to close the set of equations, $\{\{\bar{\mathcal{S}}_c\}\}$ is calculated at each solution step by taking the convolution of the core averaged PDF with the $\{\{< \mathcal{S}_c \mid \zeta' >\}\}$ profile in ζ-space. The unconditional mean scalar dissipation rate is modelled using a $k-\epsilon$ expression.

$$\{\{D(\bar{\nabla c})^2\}\} \approx \omega_t\{\{\bar{c'^2}\}\} \tag{8.16}$$

where ω_t is the turbulent mixing frequency obtained by normalizing the core averaged turbulent kinetic energy dissipation rate ($\{\{\epsilon\}\}$) by the core averaged turbulent kinetic energy ($\{\{k\}\}$). The core averaged correlation between RPV fluctuations and

fluctuations in the RPV source term ($\{\{c'\bar{\mathcal{S}}'_c\}\}$), is modelled as the convolution of the core averaged PDF with the product of ζ and the conditional mean source term minus the mean.

$$\{\{c'\bar{\mathcal{S}}'_c\}\} \approx \int_0^{\hat{\zeta}} \zeta\{\{P_\zeta\}\}\{\{< \mathcal{S}_c \mid \zeta >\}\}d\zeta - \{\{\bar{c}\}\}\{\{\bar{\mathcal{S}}_c\}\} \tag{8.17}$$

Core and outlet averaged RPV means and variances were estimated using the submodels described above. These means and variances were then used to construct RPV PDFs with clipped Gaussian assumed forms. Initial solution estimates were calculated using adiabatic conditions at $\zeta = 1$, with values between $\zeta = 0$ and $\zeta = 1$ being estimated by linear interpolation. Initial estimates for $Q_i(\zeta)$ values at $\zeta > 1$ were set equal to the unity ζ values.

The preliminary PTURCEL calculations made with these starting estimates failed to converge, even after prolonged run times. Laminar flamelet values were also employed as starting estimates, having been determined from the laminar premixed code of Kee *et al*[122], but no additional progress was made. Difficulty was encountered in ensuring the positivity of the conditional mean reactive scalar dissipation rate profiles. Aerothermochemical inconsistencies arising from poor starting estimates seemed to be the cause of these difficulties.

The results of these preliminary calculations suggest that further PTURCEL development should only be undertaken with better estimates of the RPV PDF and conditional mean RPV source term profiles. It is clear that PTURCEL model development remains at a preliminary stage.

8.3 Discussion

The principal motive behind formulating the PTURCEL model, was to develop the simplest possible premixed CMC methodology in order to determine what issues are of concern in this relatively undeveloped area. It is hoped that eventually, PTURCEL methods will have a practical application in the areas mentioned at the beginning of this chapter.

The demonstrated capacity of nonpremixed CMC methods to predict the effects of turbulent mixing upon detailed chemical systems would be of great use if

carried over to premixed CMC modelling. Currently, premixed PaSR calculations (joint PDF method) for steady premixed reactors with 43-step $CO - H_2$ chemical mechanisms require around $\sim$ 15 CPU hours to converge on an 8 Mflop computer[92]. Based on comparison with ISR performance, an operational PTURCEL model could potentially reduce the required computation time for this calculation by two orders of magnitude.

Aside from PTURCEL modelling, Mantel and Bilger[107,164] are investigating the possibility of applying premixed CMC models to a class of turbulent premixed flame brushes, where the conditional mean velocity and conditional mean reactive scalar dissipation rate statistics appear to be independent of location. The possibility of this type of premixed CMC application was first suggested by Bilger[97] some time ago, but as yet no modelling attempt has been made for these flames.

Chapter 9

Concluding Discussion

The primary objective of this investigation has been to develop conditional moment closure (CMC) methods from the theories, presented by Bilger[8,9] and Klimenko[6,7], into a series of fully functional models for turbulent combustion.

This objective has been attained to a satisfactory degree. The nonpremixed CMC models for imperfectly stirred reactors (ISRs) and axisymmetric jet flames are at an advanced stage of development. The latter model has been demonstrated to give very good agreement with experimental measurements in non-hydrocarbon jet diffusion flames, both here (Chapter 7) and in earlier publications[96,102]. The ISR model has not yet been compared directly with experiment, but the parametric studies conducted here (Chapter 5) and elsewhere[103] have produced results which are self-consistent and reasonable.

The development of a premixed CMC model of any type remains at a preliminary stage. This state of affairs reflects the inherent complexity associated with premixed combustion in comparison with nonpremixed combustion. A steady premixed reactor model has been proposed to predict the influence of turbulent fluctuations in reactive species concentrations upon chemical reactions. This model, known as PTURCEL (*P*remixed *Tur*bulent *R*eactor *C*alculation with *E*nergy *L*oss) applies in situations which are already treated by other methods such as the Joint PDF (JPDF) method. These situations include the flame stabilization zones of lean-premixed gas turbine combustors[92].

A functional PTURCEL model would reduce the computational cost of predicting the behaviour of steady premixed reactors by orders of magnitude compared

to JPDF methods. It is evident that further investigations into the nature of conditional mean reactive scalar dissipation rates and reaction progress variable (RPV) probability density functions (PDFs), under PTURCEL conditions, is required at this stage.

9.1 Major Findings

The major findings that have resulted from the development of the nonpremixed CMC combustion models are summarized as follows.

ISR Model

The Imperfectly Stirred Reactor (ISR) model can be viewed as a nonpremixed generalisation of the well known Perfectly Stirred Reactor (PSR) model. Applications of the ISR model are limited to nonpremixed turbulent combustion where conditional mean reactive scalar statistics are not dependent upon location or time. Some spatial dependence can be tolerated, in which case the use of ISR modelling must be recognized as an approximate method and the modeller must satisfy him or herself that it is a valid approximation.

The imperfectly stirred model takes into account the effects of chemical interactions with turbulent mixing processes, in addition to interactions with the inlet-outlet convective processes found in PSR models. By varying the relative strengths of the terms responsible for turbulent mixing, mean convection and chemical reaction, ISR predictions can be made to vary in a continuous fashion from a flamelet-like approximation to a PSR-ensemble approximation. The former approximation is dominated by a reactive-diffusive balance of terms, whilst the latter is essentially a reactive-convective balance without significant mixing.

In the application of ISR modelling to practical applications such as nonpremixed gas turbine combustors, it is expected that the predicted results will lie in the hybrid regime between these two limiting approximations.

In general it can be concluded that ISR predictions tend to be perturbed further from chemical equilibrium levels through decreasing the reactor residence time, or increasing the change in conserved scalar variance across the reactor. In actual

practice, these quantities will need to be determined from the target reactor, as will the form and magnitude of mixture fraction PDFs averaged at the inlet area, outlet area and across the reactor core.

The ISR model easily handles large ($\sim$ 50 species, $\sim$ 250 steps) chemical mechanisms whilst computation times remain less than one CPU hour on a fast workstation. This capacity for chemical detail at low computational cost far outstrips the ability of JPDF methods under similar conditions. It appears that no other method is capable of making calculations of turbulence-chemistry-convection interactions at this level of chemical detail.

Jet Flame Model

The CMC jet flame model has the advantage of requiring a great deal less computation time than other contemporary jet flame models. In comparable run cases, the CMC jet flame method takes around two orders of magnitude less time to reach completion than the JPDF method. Further, given the same computation time the CMC method can handle detailed chemical mechanisms whilst other methods must employ reduced chemical approximations.

Some part of this time saving is due to the simplifications, to the two-dimensional CMC reactive scalar equations, that are afforded by the simple boundary-layer approximation of jet flame dynamics. This approximation allows the turbulent flow field to be treated with a parabolic marching routine instead of requiring a fully elliptic solution. It should be noted that in the comparison of run times given above, both methods employed the same parabolic solver.

The boundary-layer structure of nonpremixed jet flames indirectly gives rise to a further important simplification. It has been shown elsewhere that the cross-flow dependence of conditional mean statistics is weak in the presence of a boundary-layer structure. With this assumption, it is possible to reduce the fully two-dimensional conditional mean reactive scalar equation to a quasi one-dimensional problem. In this case, cross-flow averaging accounts for any weak cross-flow dependence.

The predicted results for H_2 and $CO - H_2$ jet flames show good agreement with experimental measurements. In all cases however, there is evidence of processes in the

near-field zones of jet flames that are not accounted for in the current implementation. It has been suggested that these processes are associated with the existence of thin flamelet reaction zones, and near-field flow structures that do not conform to the boundary layer approximation.

The former near-field process gives rise to differential diffusion effects observable in measured temperature and some major species conditional mean profiles. Differential diffusion is not treated in the current model implementation. The possibility also exists that nonpremixed combustion in the thin flamelet regime may require the existing CMC model to account for local fluctuations in conditional mean scalar dissipation rates[154].

The latter near-field process leads to inaccurate predictions from boundary layer approximations of the full Navier-Stokes equations. Further, evidence of radially dependent conditional mean statistics have been found in the near field of hydrogen jet flames[152]. This evidence would appear to invalidate the simplifying assumption mentioned above, for the near-field of jet diffusion flames.

These near-field discrepancies do not have a large impact on the overall predicted structure of turbulent jet diffusion flames, since this is governed principally by far field effects. The accuracy of the streamwise decay of turbulent kinetic energy, the method for calculating conditional mean scalar dissipation rate, and the radiative transfer of heat are of prime importance. All of these areas are subject to continuing research. The accuracy of the radiation submodel has been questioned elsewhere[51], and has been tested here for H_2 jet flames. The results seem to indicate that the optically-thin estimate of radiative transfer may be overpredicting heat loss.

9.2 Future Directions

Much can be done to further develop the models presented in this investigation. In this section, the possible future avenues of CMC model development are speculated upon, and suggestions are made to assist this future development.

Differential Diffusion Modelling

In the early stages of CMC jet flame development, it was thought that differential diffusion could be treated by simply relating the transport of molecular species to the transport of enthalpy via constant inverse Lewis numbers[96]. This was however a false assumption, as it was found that such a treatment greatly overestimated the statistical rate of decorrelation of different species in decaying homogeneous turbulence.

It is apparent that differential diffusion effects are confined to high wave numbers, such that the process operates over very short distances only. Simply using constant Lewis number relationships, determined from laminar diffusion flame calculations, incorrectly imposes differential diffusion behaviour on the large scale mixing motions.

A semi-empirical approach might yield results if the 'effective' Lewis numbers applying to each species are made a function of local Reynolds number. In this way, if the local turbulence Reynolds number is large then differential diffusion effects should be small, with virtually uniform effective Lewis numbers for all species. Conversely, if the local Reynolds number is small, then the Lewis numbers should more closely reflect the individual molecular transport properties of each species.

In the presence of differential diffusion, the concept of a unique mixture fraction is invalid. Thus, if differential diffusion effects are to be treated then whatever selection of mixture fraction is made (say normalised hydrogen or oxygen atomic mass etc.) will lead to source terms in the mixture fraction conservation equation. The presence of these source terms requires modifications to be made to the standard unconditional mean conserved scalar closure schemes.

In the context of the CMC reactive scalar equations, a conditional mean mixture fraction source term will appear in a similar form to the RPV source term in the premixed CMC equations. In contrast to the RPV source term in premixed CMC methods, the evaluation of the mixture fraction source term should not present any special difficulties.

Complex Flow Cases

The task of extending CMC modelling to the direct calculation of more complex flow cases, such as flows with strong recirculation and non-boundary-layer structures, seems quite difficult at this stage. It is possible that immediate practical applications can be found for the existing models without having to take this step. An example of this is discussed in the next section.

Based on the experimental evidence of near-field measurements in H_2 jet flames[152], it seems unlikely that statistics conditioned upon mixture fraction alone will exhibit the same degree of cross-stream independence found in the far-field of jet flames. In this case, it would seem that the elliptical calculation of the CMC equations would be a more time consuming exercise since it could potentially involve as many *sets* of reactive scalar equations as there are physical grid points in the computation domain. It is more likely that judicious domain decomposition would reduce this workload, with each set of conditional mean reactive scalar equations covering a zone of related physical locations.

The determination of conditional mean velocity and scalar dissipation rate profiles from the unconditional mixing field is more problematic. The methods employed for simple jet flames, particularly in the estimation of conditional mean velocity will have to be modified and no obvious substitute is apparent to the author. However, the 'local' method for the calculation of conditional mean scalar dissipation rate (see Section 6.2) should be adaptable to more complex flow geometries.

In applying singly conditioned CMC methods to complex flow geometries, care must be taken in treating the zones of inert premixing that can occur. If partial premixing is a dominant feature of the flame being studied, then a doubly conditioned CMC method is required. The future development of these closures is discussed at the end of this chapter.

Practical Applications

Notwithstanding the above complications, there are promises of immediate applications for the CMC models developed in this investigation. The most useful application of the existing models can be found in the prediction of pollutant formation in

nonpremixed gas turbine combustors.

It is envisaged that the combination of the ISR model and a variant of the existing jet flame model, known as a Dilution Flow Reactor (DFR), could be used to 'post-process' solutions of combustor flow patterns. In this application, detailed solutions of combustor flow patterns would be derived using commercially available CFD software. This software would typically use fast chemistry or eddy-breakup methods to determine densities and pressures to effect a solution.

Taking the combustor flow pattern as input data, and using ISR predictions of primary recirculation zone chemical yields, the DFR code would then compute the evolution of conditional mean reactive scalar profiles throughout the dilution zone of the combustor.

Representative conditional mean scalar dissipation rates and velocities could be determined approximately by averaging the unconditional mean flow field over the cross-sectional area of the combustor. The DFR code would calculate an unconditional mean temperature and density field in the course of computation. These calculated fields could be compared with the input flow field solution. In the event that the DFR-predicted density field is substantially different from the initially computed field, action would have to be taken to correct the discrepancy.

Zone modelling of gas turbine combustors has been attempted in the past, using ensembles of PSRs and plug flow reactors, with moderate success. The increased sophistication of the ISR and DFR models over these earlier models, in itself warrants the trial of this phenomenological approach.

Another application of of the ISR/DFR models could be the prediction of hazardous waste incinerator performance. The ability of CMC methods to employ detailed chemical mechanisms in predictions of turbulent combustion, would seem to lend itself to this application.

The zone model applications described above in no way allow for substantial localized premixing of reactants such as can occur in intense nonpremixed combustion. Under these conditions, a CMC method is required which conditions upon both mixture fraction and a suitable reaction progress variable.

Doubly-Conditioned Closure

By employing conditional mean reactive scalar statistics which are conditioned upon both mixture fraction and some measure of overall reaction progress, a first order chemical closure should be possible for nonpremixed turbulent combustion with extinction and ignition events.

Double conditioning would add a further dimension to the computations already required in single conditioned CMC methods, and would correspondingly require more computational resources.

The development of doubly conditional methods should logically start with the combining of the simplest possible mixture fraction and RPV singly conditional methods. The first doubly conditional CMC model developed should be a steady reactor like the ISR and PTURCEL models. In addition to the scalar dissipation terms appearing in the ISR and PTURCEL equations, a doubly conditioned steady reactor model would have cross-dissipation effects between mixture fraction and RPV to consider. Bilger[8] has derived the general doubly conditional CMC reactive scalar equations and has speculated on the importance of the various resulting terms.

The immediate way forward towards the eventual goal of doubly conditional CMC methods requires the successful development and testing of simple premixed CMC methods. By DNS and experimental investigation of premixed flame structure, CMC models such as PTURCEL can be further developed. The experience gained with premixed CMC will then complement the existing body of knowledge accumulated in the development of nonpremixed CMC methods.

Bibliography

[1] World Energy Outlook to the Year 2010. OECD, Paris. 1993.

[2] Garrett C. W., *Prog. Energy Combust. Sci.* 18:369-407 (1992).

[3] Dahl D. A., Zimmerman D., Ryan R., "An overview of combustion emissions in the United States". in *Emissions from Combustion Processes: Origin, Measurement and Control*, Clement R., Kugel R. (eds.), Lewis Publishers, Boston. (1990)

[4] Mellor A. M., Ferguson C. R., "Practical Problems in Turbulent Reacting Flows". in *Turbulent Reacting Flows*, Libby P. A., Williams F. A. (eds.), Springer-Verlag, Berlin. (1980)

[5] Pope S. B., *Twenty-Third Symposium International) on Combustion*, the Combustion Institute, Pittsburgh, 1990, pp591-612.

[6] Klimenko A. Yu., *Fluid Dynamics*, 1990, v25, pp327-334.

[7] Klimenko A. Yu., "Conditional Moment Closure and Diffusion in Conserved Scalar Phase Space", Ecolen Scientific Research Laboratory Paper, Moscow.

[8] Bilger R. W., "Conditional Moment Methods for Turbulent Reacting Flow using Crocco Variable Conditions", *Charles Kolling Laboratory Report*, TNF-99, University of Sydney. (1991)

[9] Bilger R. W., *Physics of Fluids A*, 1993, v5, pp436-444.

[10] Burke S. P., Schumann T. E. W., *Proceedings of the First Symposium on Combustion*, the Combustion Institute, Pittsburgh, 1965. Reprinted from *Industrial and Engineering Chemistry*, American Chemical Society. 1928.

[11] Hawthorne W. R., Weddell D. S., Hottel H. C., *Third Symposium on Combustion, Flames and Explosion Phenomena*, (Williams and Wilkins, Baltimore 1949), pp266-288.

[12] Toor H. L., *Journal of the American Institute Chemical Engineering*, 1962, v8, pp70-78.

[13] Lin C. H., O'Brien E. E., *Journal of Fluid Mechanics*, 1974, v64, pp195-206.

[14] Kent J. H., "Turbulent Jet Diffusion Flames", PhD Thesis, University of Sydney. (1972)

[15] Bilger R. W., "Turbulent Flows with Nonpremixed Reactants", in *Turbulent Reacting Flows*, Libby P. A., Williams F. A. (eds.), Springer-Verlag, New York. (1980). pp65-113.

[16] Bilger R. W., *Annual Review of Fluid Mechanics*, 1989, v21, pp101-135.

[17] Dixon-Lewis G., Goldsworthy F. A., Greenberg J. B., *Proceedings of the Royal Society*, 1975, v346, p261.

[18] Janicka J., Kollmann W., *Seventeenth Symposium (International) on Combustion*. the Combustion Institute, Pittsburgh, 1978. p421.

[19] Magnussen B. F., Hjertager B. H., *Sixteenth Symposium (International) on Combustion*, the Combustion Institute, Pittsburgh, 1976, p719.

[20] Spalding D. B., *Thirteenth Symposium (International) on Combustion*. the Combustion Institute, Pittsburgh, 1970, p649.

[21] Spalding D. B., *Sixteenth Symposium (International) on Combustion*, the Combustion Institute, Pittsburgh. 1976, p1657.

[22] Ahmadi-Befrui B., Brandstatter W., Kratchowill H., "Calculation of Inhomogeneous Charge Combustion in a Swirl-Assisted Lean-Burn Engine", SAE Paper 910266, SAE International Congress and Exposition, Detroit, 1991.

[23] Ahmadi-Befrui B., Kratchowill H., "Multidimensional Calculation of Combustion in a Loop-Scavenged Two-Stroke Cycle Engine", *International Symposium on Diagnostics and Modelling of Combustion Engines*. Kyoto, Japan. 1990.

[24] Correa S. M., Shyy W., *Progress in Energy and Combustion Science*, 1987. v13, pp249-292.

[25] Bilger R. W., *Combustion Science and Technology*, v22, pp251-261. (1980)

[26] Kuznetzov V. R., Sabelnikov V. A., *Turbulence and Combustion*, Hemisphere Publishing Corporation, New York. (1986)

[27] Williams F. A., "Recent advances in theoretical descriptions of turbulent diffusion flames", in *Turbulent Mixing in Non-Reactive and Reactive Flows*, Murthy S. N. B., ed., Plenum Press, pp189-208. (1974)

[28] Peters N., *Progress in Energy and Combustion Science*, 1984, v10, pp319-339.

[29] Peters N., *Twenty-First Symposium (International) on Combustion*, the Combustion Institute, Pittsburgh, 1986, pp1231-1250.

[30] Peters N., *Combustion Science and Technology*, 1983. v30, pp1-17.

[31] Williams F. A., *Combustion Theory* (2nd Edition), Addison-Wesley Publishing Company. (1985)

[32] Bilger R. W., *Twenty-Second Symposium (International) on Combustion*, the Combustion Institute, Pittsburgh, 1988, p475.

[33] Mell W. E., Kosaly G., Riley J. J., "Investigation of the Laminar Flamelet Model for Nonpremixed Turbulent Reacting Flows", WSS/CI Paper No. 93-074. Presented at the 1993 Fall Western States Meeting of the Combustion Institute, Menlo Park, California. 1993.

[34] Mell W. E., Nilsen V., Kosaly G., Riley J. J., *Physics of Fluids*, 1994. v6, pp1331-1356.

[35] Buch K. A., Dahm W. J. A., "Fine scale structure of conserved scalar mixing in turbulent shear flows: $Sc > 1$, $Sc = 1$ and implications fro reacting flows", University of Michigan Report No 026779-5, The University of Michigan. Ann Arbor, Michigan. 1992.

[36] Dahm W. J. A., Bish E. S., "High resolution measurements of molecular transport and reaction processes in turbulent combustion", in *Turbulence and Molecular Processes in Combustion*, pp287-302, (T. Takeno, ed.), Elsevier Science Publishers, Amsterdam. 1993.

[37] Buch K. A., Dahm W. J. A., Dibble R. W., Barlow R. S., *Twenty-Fourth Symposium (International) on Combustion*, the Combustion Institute, Pittsburgh, 1992, pp295-301.

[38] Bish E. S., Dahm W. J. A., "Nonequilibrium Structure of H_2 Air Combustion in Turbulent Jets", AIAA Paper No. 94-0100, Presented at the Thirty-Second Aerospace Sciences Meeting and Exhibit, Reno, Nevada. (1994)

[39] Bilger R. W., Dibble R. W., *Combustion Science and Technology*, 1982, v28, pp161-172.

[40] Mauss F., Keller D., Peters N., *Twenty-Third Symposium (International) on Combustion*, the Combustion Institute, Pittsburgh, 1990, p693.

[41] Barlow R. S., Chen J.-Y., *Twenty-Fourth Symposium (International) on Combustion*, the Combustion Institute, Pittsburgh, 1992, pp231-237.

[42] Pope S. B., *Combustion Science and Technology*, 1981, v25, pp159-174.

[43] Pope S. B., *Progress in Energy and Combustion Science*, 1985, v11, pp119-192.

[44] Pope S. B., "PDF/Monte Carlo Methods for Turbulent Combustion and their implementation on Parallel Computers", in *Turbulence and Molecular Processes in Combustion*, Takeno T. (ed.), Elsevier Science Publishers B. V. (1993)

[45] Correa S. M., Gulati A., *Combustion and Flame*, 1992, v89, pp195-213.

[46] Correa S. M., Pope S. B., *Twenty-Fourth Symposium (International) on Combustion*, the Combustion Institute, Pittsburgh, 1992, pp279-285.

[47] Masri A. R., Pope S. B., *Combustion and Flame*, 1990, v81, pp13-29.

[48] Chen J.-Y., Kollmann W., *Twenty-Second Symposium (International) on Combustion*, the Combustion Institute, Pittsburgh, 1988, pp645-653.

[49] Chen J.-Y., Kollmann W., *Combustion and Flame*, 1990, v79, pp75-99.

[50] Chen J.-Y., Dibble R. W., Bilger R. W., *Twenty-Third Symposium (International) on Combustion*, the Combustion Institute, Pittsburgh, 1990, pp775-780.

[51] Chen J.-Y., Kollmann W., *Combustion and Flame*, 1992, v88, pp397-412.

[52] Sion M., Chen J.-Y., *Combustion Science and Technology*, 1993, v88, pp89-114.

[53] Koszykowski M. L., Armstrong R. C., Chen J.-Y., Dai F., Brown N. J., "Turbulent Jet Flame Modeling with Comprehensive Chemical Kinetics for NO_x Prediction", submitted to the *Twenty-Fifth Symposium (International) on Combustion*, the Combustion Institute, Pittsburgh, 1994.

[54] Chen J.-Y., Kollmann W., *Twenty-Third Symposium (International) on Combustion*, the Combustion Institute, Pittsburgh, 1992, pp751-757.

[55] Barlow R. S., Dibble R. W., Chen J.-Y., Lucht R. P., *Combustion and Flame*, 1990, v82, pp235-251.

[56] Chen J.-Y., Kollmann W., Dibble R. W., *Combustion Science and Technology*, 1989, v64, pp315-346.

[57] Pope S. B., *Theoretical and Computational Fluid Dynamics*, 1991, v2, pp255-270.

[58] Kerstein A. R., *Combustion Science and Technology*, 1988, v60, p391.

[59] Kerstein A. R., *Combustion and Flame*, 1989, v75, p397.

[60] Kerstein A. R., *Journal of Fluid Mechanics*, 1990, v216, p411.

[61] Kerstein A. R., *Journal of Fluid Mechanics*, 1991, v231, p361.

[62] Kerstein A. R., *Combustion Science and Technology*, 1992, v81, pp75-96.

[63] McMurtry P. A., Menon S., Kerstein A. R., *Twenty-Fourth Symposium (International) on Combustion*, the Combustion Institute, Pittsburgh, 1992, pp271-278.

[64] Frankel S. H., Madnia C. K., McMurtry P. A., Givi P., "Binary Scalar Mixing and Reaction in Homogeneous Turbulence: Some Linear Eddy Model Results", Presented at the Seventh Annual Conference of the Advanced Combustion Engineering Research Center, Park City, Utah, 1993.

[65] Calhoon W. H., Menon S., Goldin G., "Comparison of Reduced and Full Chemical Mechanisms for NO_x Prediction in Nonpremixed Turbulent H_2-Air Jet Flames", AIAA Paper No. 94-0676, Presented at the Thirty Second Aerospace Sciences Meeting and Exhibit, Reno, Nevada, 1994.

[66] Givi P., *Progress in Energy and Combustion Science*, 1989, v15, pp1-107.

[67] McMurtry P. A., Givi P., "Spectral Simulations of Turbulent Reacting Flows", in *Numerical Approaches to Combustion Modeling*, (E. S. Oran, J. P. Boris eds), Progress in Astronautics and Aeronautics, 1990, v135, American Institute of Astronautics and Aeronautics, Washington DC.

[68] Bray K. N. C., "Turbulent Flows with Premixed Reactants", in *Turbulent Reacting Flows*, Libby P. A., Williams F. A. (eds.), Springer-Verlag, Berlin. (1980)

[69] Pope S. B., *Annual Review of Fluid Mechanics*, 1987, v19, pp237-270.

[70] Bray K. N. C., Moss J. B., *Acta Astronautica*, 1977, v4, pp291-320.

[71] Libby P. A., Bray K. N. C., *Combustion and Flame*, 1980, v39, pp33-41.

[72] Bray K. N. C., Libby P. A., Masuya G., Moss J. B., *Combustion Science and Technology*, 1981, v25, pp127-140.

[73] Bray K. N. C., Libby P. A., Moss J. B., *Combustion and Flame*, 1985, v61, pp87-102.

[74] Cant R. S., Bray K. N. C., *Twenty-Second Symposium (International) on Combustion*, the Combustion Institute, Pittsburgh, 1988, pp791-799.

[75] Howe N. M., Shipman C. W., Vranos A., *Ninth Symposium (International) on Combustion*, the Combustion Institute, Pittsburgh, 1963, pp36-48.

[76] Moss J. B., *Combustion Science and Technology*, 1980, v22, pp119-129.

[77] Cant R. S., Rogg B., Bray K. N. C., *Combustion Science and Technology*, 1990. v69, pp53-61.

[78] Bray K. N. C., Champion M., Libby P. A., *Twenty-Second Symposium (International) on Combustion*, the Combustion Institute, Pittsburgh, 1988, pp763-769.

[79] Pope S. B., Anand M. S., *Twentieth Symposium (International) on Combustion*, the Combustion Institute, Pittsburgh, 1984, pp403-410.

[80] Anand M. S., Pope S. B., *Combustion and Flame*, 1987, v67, pp127-142.

[81] Pope S. B., Cheng W. K., *Twenty-First Symposium (International) on Combustion*, the Combustion Institute, Pittsburgh, 1986, pp1473-1481.

[82] Pope S. B., Cheng W. K., *Twenty-Second Symposium (International) on Combustion*, the Combustion Institute, Pittsburgh, 1988, pp781-789.

[83] Marble F. E., Candel S. M., *Seventeenth Symposium (International) on Combustion*, the Combustion Institute, Pittsburgh, 1979, pp761-769.

[84] Cant R. S., Pope S. B., Bray K. N. C., *Twenty-Third Symposium (International) on Combustion*, the Combustion Institute, Pittsburgh, 1990, pp809-815.

[85] Clavin P., Williams F. A., *Journal of Fluid Mechanics*, 1979, v90, pp589-604.

[86] Mantel T., Borghi R., *Combustion and Flame*, 1993, v96, pp443-457.

[87] Ashurst W. T., "The Eddy Structure Model of Turbulent Flame Propagation : Expanding Spherical and Steady Planar Cases", Paper presented at the 1993 Fall Meeting of the Western States Section, the Combustion Institute, SRI International, Menlo Park, California.

[88] Ashurst W. T., *Combustion Science and Technology*, 1993, v92, pp87-103.

[89] Kerstein A. R., *Twenty-First Symposium (International) on Combustion*, the Combustion Institute, Pittsburgh, 1986, pp1329-1340.

[90] Peters N., *Journal of Fluid Mechanics*, 1992, v242, pp611-629.

[91] Trouve A., "The Production of Premixed Flame Surface Area in Turbulent Shear Flow", presented at the Twenty-Fifth Symposium (International) on Combustion, University of California at Irvine, August 1994. To appear in *Combustion and Flame.*

[92] Correa S. M., *Combustion and Flame*, 1993, v93, pp41-60.

[93] Correa S. M., Braaten M. E., *Combustion and Flame*, 1993, v94, pp469-486.

[94] Roekaerts D., *Computers Fluids*, 1992, v21, pp97-108.

[95] Bilger R. W., *Combustion Science and Technology*, 1976, v13, pp155-170.

[96] Smith N. S. A., Bilger R. W., Chen J.-Y., *Twenty-Fourth Symposium (International) on Combustion*, the Combustion Institute, Pittsburgh, 1992, pp263-269.

[97] Bilger R. W., "Conditional Moment Closure Modelling and Advance Laser Measurements", in *Turbulence and Molecular Processes in Combustion*, Takeno T. (ed.), Elsevier Science Publishers BV. (1993)

[98] Kolmogorov A. N., "The local structure of turbulence in incompressible viscous fluid for very large Reynolds numbers", *Journal of the Russian Academy of Sciences*, 1941, v30, pp301-305.

[99] Taylor G. I., "Diffusion by continuous movements", *Proceedings of the London Mathematical Society*, 1921, v20, pp196-212.

[100] Launder B. E., *International Journal of Numerical Methods in Fluids*, 1989, v9, p963.

[101] Bilger R. W., "Combustion Theory and Conditional Moment Closure Modelling", Invited Paper for the Zeldovich Memorial International Conference on Combustion, the Russian Academy of Science, Moscow. September 1994.

[102] Smith N. S. A., Bilger R. W., Carter C. D., Barlow R. S., Chen J.-Y., " A Comparison of CMC and PDF Modelling Predictions with Experimental Nitric Oxide LIF/Raman Measurements in a Turbulent H_2 Jet Flame". to appear in *Combustion Science and Technology.* (1993)

[103] Smith N. S. A., Bilger R. W., "Conditional Moment Closure for Turbulent Nonpremixed Combustion Modelled as an Imperfectly Stirred Reactor", submitted to *Combustion and Flame.* (1994)

[104] Smith N. S. A., Bilger R. W., Barlow R. S., Carter C. D., Chen J.-Y., "Radiation Effects on Nitric Oxide Formation in Turbulent Hydrogen Jet Flames Diluted with Helium", to be submitted to *Combustion Science and Technology.* (1994)

[105] Smith N. S. A., Bilger R. W., "Conditional Moment Closure for Turbulent Nonpremixed Jet Flames: Mixing and Chemical Reaction", in preparation (1994)

[106] Li J. D., Bilger R. W., *Physics of Fluids*, 1993, v5, pp3255-3264.

[107] Mantel T., Bilger R. W., "Some Conditional Statistics in a Turbulent Premixed Flame Derived from Direct Numerical Simulation", in preparation.

[108] Glarborg P., Kee R. J., Grcar J. F., Miller J. A., "PSR : A FORTRAN Program for Modeling Well Stirred Reactors", Sandia Report SAND86-8209, Sandia National Laboratories, Livermore, California. (1986)

[109] Chen J.-Y., Dibble R. W., *Combustion Science and Technology*, 1991. v84, pp45-50.

[110] Broadwell J. E., Breidenthal R. E., *Journal of Fluid Mechanics*, 1982, v125, p397.

[111] Broadwell J. E., Mungal M. G., *Twenty-Second Symposium (International) on Combustion*, the Combustion Institute, Pittsburgh, 1988, pp579-587.

[112] Lutz A. E., Dibble R. W., Kee R. J., Broadwell J. E., " A Model for Detailed Chemical Kinetics in Turbulent Nonpremixed Jet Flames", Presented at the *AIAA 29th Aerospace Sciences Meeting*, Reno, January 1991. Paper No. 91-0478.

[113] Andreatta D., Chen J.-Y., Dibble R. W., " An Engine Combustion Model with Detailed Chemical Kinetics and Simplified Mixing". Presented at the 1993 Fall Meeting of the Western States Section of the Combustion Institute, Menlo Park, California. Paper No. WSCI 93-070.

[114] Flagan R. C., Appleton J., *Combustion and Flame*, 1974, v23, p249.

[115] Swithenbank J., Turan A., Felton P. G., "Three-dimensional two-phase mathematical modelling of gas turbine combustors", in *Gas Turbine Combustor Design Problems*, Lefebvre A. H. (ed.), Hemisphere Publishing, 1980, pp249-314.

[116] Chen J.-Y., "Stochastic Modeling of Partially Stirred Reactors", WSS/CI Paper 93-071. Presented at the 1993 Fall Meeting of the Western States Section of the Combustion Institute, Menlo Park, California.

[117] Klimenko A. Yu., Bilger R. W., "Relationship between conserved scalar pdfs and scalar dissipation in turbulent flows", *Charles Kolling Laboratory Report TNF-101*, University of Sydney, 1993.

[118] Bilger R. W., "Incompletely Stirred Reactors", Private Communication, May 1994.

[119] Smooke M. D., Giovangigli V., in *Reduced Kinetic Mechanisms and Asymptotic Approximations for Methane-Air Flames*, Smooke M. D., ed., Springer Verlag, New York, 1990. p23.

[120] Warnatz J., "Detailed Chemistry of Hydrocarbon Combustion and its Coupling with Flow Processes", in *Turbulence and Molecular Processes in Combustion*, Takeno T. (ed.), Elsevier Science Publishers BV, 1993.

[121] Kee R. J., Rupley F. M., Miller J. A., "Chemkin-II: A FORTRAN Chemical Kinetics Package for the Analysis of Gas-Phase Chemical Kinetics". *Sandia Report* SAND 89-8009, Sandia National Laboratories, (1989).

[122] Kee R. J., Grcar J. F., Smooke M. D., Miller J. A., "A FORTRAN Program for Modeling Steady Laminar One-Dimensional Premixed Flames". *Sandia Report* SAND 85-8240, Sandia National Laboratories, (1985).

[123] Dixon-Lewis G., David T., Gaskell P. H., *Archivum Combustionis*, 1986, v6, p1.

[124] Dixon-Lewis G., MIssaghi M., *Twenty-Second Symposium (International) on Combustion*, the Combustion Institute, Pittsburgh, 1988, pp1461-1470.

[125] David T., Gaskell P. H., Dixon-Lewis G., "Structure and Properties of Methane-Air and Hydrogen-Air Counterflow Diffusion Flames", Private communication, 1986.

[126] Gutheil E., Balakrishnan G., Williams F. A., "Structure and Extinction of Hydrogen-Air Diffusion Flames", in *Reduced Kinetic Mechanisms for Applications in Combustion Systems*, Peters N., Rogg B., (eds), Springer-Verlag, Heidelberg. (1993)

[127] Gutheil E., Williams F. A., *Twenty-Third Symposium (International) on Combustion*, the Combustion Institute, Pittsburgh, 1990, pp513-521.

[128] Zeldovich Ya. B., Sadovnikov P. Ya., Frank-Kamenetskii D. A., "Oxidation of nitrogen in combustion", translated by M. Shelef, Academy of Sciences of the USSR, Moscow (1947).

[129] Correa S. M., *Combustion Science and Technology*, 1993, v87, pp329-362.

[130] Drake M. C., *Twenty-First Symposium (International) on Combustion*, the Combustion Institute, Pittsburgh, 1986, pp1579-1589.

[131] Miller J. A., Bowman C. T., *Progress in Energy and Combustion Science*. 1989, v15, pp287-338.

[132] Cameron C. D., Brouwer J., Samuelson G. S., *Twenty-Second Symposium (International) on Combustion*, the Combustion Institute, Pittsburgh. 1988, pp465-474.

[133] Richards C. D., Samuelson G. S., *Twenty-Third Symposium (International) on Combustion*, the Combustion Institute, Pittsburgh, 1990, pp1071-1077.

[134] Chen J.-Y., Kollmann W., Dibble R. W., "Numerical computation of turbulent free shear flows using a block tridiagonal solver for a staggered grid system". Presented at the 18th Annual Pittsburgh Conference on Modelling and Simulation. Pittsburgh, USA. 1987.

[135] Girimaji S. S., *Physics of Fluids A*, 1992, v4, pp2529-2537.

[136] Girimaji S. S., *Combustion Science and Technology*, 1991, v78, pp177-196.

[137] Kent J. H., Bilger R. W., *Sixteenth Symposium (International) on Combustion*, the Combustion Institute, Pittsburgh. 1977, p1643.

[138] Stårner S. H., Bilger R. W., Lyons K. M., Frank J. H., Long M. B.. "Conserved Scalar Measurements in Turbulent Diffusion Flames by a Raman and Rayleigh Ribbon Imaging Method". Presented at the 1993 Fall Meeting of the Western States Section of the Combustion Institute. October 18-19th 1993. SRI International, Menlo Park, California.

[139] Stårner S. H., Bilger R. W., Lyons K. M., Frank J. H., Long M. B., "Conserved Scalar Measurements in Turbulent Diffusion Flames by a Raman and Rayleigh Ribbon Imaging Method". *Twenty-Fifth Symposium (International) on Combustion*, the Combustion Institute, Pittsburgh. (to appear)

[140] Lavoie G. A., Schlader A. F., *Combustion Science and Technology*, 1974. v8, pp215-224.

[141] Bilger R. W., Beck R. E., *Fifteenth Symposium (International) on Combustion*, the Combustion Institute, Pittsburgh. 1974. pp541-551.

[142] Bilger R. W., *Combustion and Flame*. 1976, v26, pp115-123.

[143] Drake M. C., Pitz R. W., Correa S. M.. Lapp M., *Twentieth Symposium (International) on Combustion*, the Combustion Institute, Pittsburgh. 1984. pp1983-1990.

[144] Chen R.-H., Driscoll J. F., *Twenty-Third Symposium (International) on Combustion*, the Combustion Institute, Pittsburgh. 1990. pp281-288.

[145] Driscoll J. F., Chen R.-H., Yoon Y., *Combustion and Flame*, 1992, v88. pp37-49.

[146] Turns S. R., Myhr F. H., *Combustion and Flame*, 1991, v87, pp319-335.

[147] Turns S. R., Myhr F. H., Bandaru R. V.. Maund E. R., *Combustion and Flame*, 1993, v93, pp255-269.

[148] Vranos A., Knight B. A., Proscia W. M., Chiapetta L., Smooke M. D., *Twenty-Fourth Symposium (International) on Combustion*, the Combustion Institute, Pittsburgh. 1992. pp377-384.

[149] Rokke N. A., Hustad J. E., Sonju O. K., Williams F. A., *Twenty-Fourth Symposium (International) on Combustion*, the Combustion Institute, Pittsburgh. 1992. pp385-393.

[150] Barlow R. S., Carter C. D., *Combustion and Flame*, 1994, v97, pp261-280.

[151] Carter C. D., Barlow R. S., *Optics Letters*, 1994, v19, pp299-301.

[152] Barlow R. S., Carter C. D., "Relationships among nitric oxide, temperature and mixture fraction in hydrogen jet flames". Submitted to *Combustion and Flame*.

[153] Cheng T. S., Wehrmeyer J. A., Pitz R. W., *Combustion and Flame*, 1992, v91, pp323-345.

[154] Klimenko A. Yu., *Fluid Dynamics*, 1993, v28, pp630-637. (Translated from *Izvestiya Rossiiskoi Akademii Nauk, Mehkanika Zhidkosti i Gaza*, 1992, no5, pp50-59.)

[155] Hubbard G. L., Tien C. L., *American Society of Mechanical Engineers Journal of Heat Transfer*, 1978, v100, p236.

[156] Correa S. M., Drake M. C., Pitz R. W., Shyy W., *Twentieth Symposium (International) on Combustion*, the Combustion Institute. Pittsburgh. 1984. pp337-343.

[157] Correa S. M., Gulati A., *Twenty-Second Symposium (International) on Combustion*, the Combustion Institute, Pittsburgh, 1988. pp599-606.

[158] Masri A. R., Dibble R. W., *Twenty-Second Symposium (International) on Combustion*, the Combustion Institute, Pittsburgh, 1988. pp607-618.

[159] Rogg B., Williams F. A., *Twenty-Second Symposium (International) on Combustion*, the Combustion Institute, Pittsburgh, 1988. pp1441-1451.

[160] Lee Y. Y., Pope S. B., "Nonpremixed Turbulent Reacting Flow Near Extinction". submitted to *Combustion and Flame* (1994).

[161] Smith L. L., Dibble R. W., Talbot L., Barlow R. S., Carter C. D., "Laser Raman Scattering Measurements of Differential Molecular Diffusion in Turbulent Nonpremixed Jet Flames of H_2/CO_2 Fuel", presented at the Twenty-Fifth Symposium (International) on Combustion, University of California at Irvine, August 1994. To appear in *Combustion and Flame.*

[162] Smith L. L., Dibble R. W., Talbot L., Barlow R. S., Carter C. D., "Laser Raman Scattering Measurements of Differential Molecular Diffusion in Nonreacting and Reacting Laminar and Turbulent Jet Flows". AIAA Paper AIAA-93-0804, presented at the Thirty-First Aerospace Sciences Meeting and Exhibit, Reno, Nevada, January 1993.

[163] Anderson T. J., Eckbreth A. C., *Twenty-Third Symposium (International) on Combustion*, the Combustion Institute, Pittsburgh, 1990. pp1885-1891.

[164] Mantel T., Bilger R. W., "The Effects of Damkohler Number on Conditional Statistics in a Turbulent Premixed Flame". in preparation.

[165] Peters N., "Flame Calculations with Reduced Mechanisms - An Outline", in *Reduced Kinetic Mechanisms for Application in Combustion Systems*, Peters N. , Rogg B., (eds), Springer-Verlag, Heidelberg. (1993)

[166] Chen J.-Y., Liu Y., Rogg B., "CO-H_2-N_2/Air Diffusion Flames: Thermal Radiation and Transient Effects", in *Reduced Kinetic Mechanisms for Application in Combustion Systems*, Peters N., Rogg B., (eds), Springer-Verlag, Heidelberg. (1993)

[167] Peters N., Kee R. J., *Combustion and Flame*, 1987, v68, pp17-29.

[168] Peters N., in *Reduced Kinetic Mechanisms and Asymptotic Approximations for Methane-Air Flames* (M. D. Smooke Eds.). Lecture Notes in Physics 384, Springer-Verlag, 1991, pp48-67.

[169] Chen J.-Y., *Combustion Science and Technology*, 1988. v57, pp89-94.

[170] Lam S. H., *Combustion Science and Technolog*, 1993. v89, pp375-404.

[171] Mikheev A. A., *Principles of Heat Transfer*, Gosenergoizdat, Moscow, 1949.

[172] Becker H. A., *Fifteenth Symposium (International) on Combustion*, the Cobustion Institute, Pittsburgh, 1974. pp601-615.

[173] Brown P. N., Byrne G. D., Hindmarsh A. C., *SIAM Journal of Scientific and Statistical Computation*, 1989, v10, pp1038-1051.

Appendix A

Reduced Chemical Mechanisms

In this Appendix, the two and three step reduced mechanisms used for H_2 and CO-H_2 combustion modelling, in Chapter 7, are derived from the starting mechanism given in Table A.1. This starting mechanism consists of all of the wet-CO steps of the short mechanism derived by Rogg and Williams[159]. These reactions are in turn contained in the more general mechanism tabulated by Peters[165] which is valid for hydrocarbons up to propane (C_3H_8).

A.1 Notes on Table A.1

Apart from a starting mechanism for $CO - H_2$ reduced mechanism derivation, Table A.1 also serves as a reference for the skeletal methane mechanism employed in Chapter 5. The hydrocarbon-specific steps (reactions 21-29) are not required in the analysis presented here however. These hydrocarbon steps are the main C_1 reactions identified in the Smooke[119] skeletal mechanism, but the rate constants are chosen to be consistent with the hydrocarbon mechanism of Peters[165]. The small number of nitrogen chemistry steps included in the table (reactions 30-34) are also non-essential in the overall chemical scheme, but are obviously important in the context of predicting the formation of nitrogen oxides (NO_x). The well known Zeldovich reduction of these steps will be given at the end of this appendix.

Entries in Table A.1 have units of cal, mol, K, cm and s. The symbols E_a, α and A represent the activation energy, temperature exponent and multiplying coefficient of Arrhenius reaction rate expressions such as that given below for a reaction rate

No.	Reaction Description	A	α	E_a
1f.	$O_2 + H \rightarrow OH + O$	2.00E14	0.00	16800.
1b.	$OH + O \rightarrow H + O_2$	1.57E13	0.00	841.3
2f.	$H_2 + O \rightarrow OH + H$	5.06E04	2.67	6286.
2b.	$H + OH \rightarrow O + H_2$	2.22E04	2.67	4371.
3f.	$H_2 + OH \rightarrow H_2O + H$	1.00E08	1.60	3298.
3b.	$H_2O + H \rightarrow H_2 + OH$	4.31E08	1.60	18274.
4f.	$O + H_2O \rightarrow OH + OH$	1.47E10	1.14	16991.
4b.	$OH + OH \rightarrow H_2O + O$	1.59E09	1.14	100.4
5.	$H + O_2 + M \rightarrow HO_2 + M$	2.30E18	-0.80	0.00
6.	$H + HO_2 \rightarrow OH + OH$	1.50E14	0.00	1004.
7.	$H + HO_2 \rightarrow H_2 + O_2$	2.50E13	0.00	693.1
8.	$H + HO_2 \rightarrow H_2O + O$	3.00E13	0.00	1721.
9.	$OH + HO_2 \rightarrow H_2O + O_2$	6.00E13	0.00	0.00
10.	$O + HO_2 \rightarrow OH + O_2$	1.80E13	0.00	-406.3
11.	$HO_2 + HO_2 \rightarrow H_2O_2 + O_2$	2.00E12	0.00	0.00
12f.	$HO_2 + H_2O \rightarrow H_2O_2 + OH$	2.86E13	0.00	32790.
12b.	$H_2O_2 + OH \rightarrow HO_2 + H_2O$	1.00E13	0.00	1800.
13f.	$H_2O_2 + M \rightarrow OH + OH + M$	1.30E17	0.00	45500.
13b.	$OH + OH + M \rightarrow H_2O_2 + M$	9.86E14	0.00	-5070.
14.	$H_2O_2 + H \rightarrow HO_2 + H_2$	1.60E14	0.00	3800.0
15.	$OH + H + M \rightarrow H_2O + M$	2.20E22	-2.00	0.00
16.	$H + H + M \rightarrow H_2 + M$	1.80E18	-1.00	0.00
17.	$O + O + M \rightarrow O_2 + M$	1.89E15	0.00	-1788.0
18.	$CO + OH \rightleftharpoons CO_2 + H$	4.400E06	1.50	-740.4
19.	$HCO + H \rightarrow CO + H_2$	2.000E14	0.00	0.00
20.	$CO + H + M \rightleftharpoons HCO + M$	1.136E15	0.00	2381.
21.	$CH_4 \rightleftharpoons CH_3 + H$	6.300E14	0.00	104000.
21L	$CH_4 + M \rightleftharpoons CH_3 + H + M$	1.000E17	0.00	86000.
22.	$CH_4 + H \rightleftharpoons CH_3 + H_2$	2.200E04	3.00	8750.
23.	$CH_4 + OH \rightleftharpoons CH_3 + H_2O$	1.600E06	2.10	2460.
24.	$CH_3 + O \rightarrow CH_2O + H$	6.800E13	0.00	0.00
25.	$CH_2O + H \rightarrow HCO + H_2$	2.500E13	0.00	3991.
26.	$CH_2O + OH \rightarrow HCO + H_2O$	3.000E13	0.00	1195.
27.	$CH_3 + O_2 \rightarrow CH_3O + O$	7.000E12	0.00	25652.
28.	$CH_3O + H \rightarrow CH_2O + H_2$	2.000E13	0.00	0.00
29.	$CH_3O + M \rightarrow CH_2O + H + M$	2.400E13	0.00	28812.
30.	$O + N_2 \rightarrow NO + N$	1.40E14	0.00	75800.
31.	$N + O_2 \rightarrow NO + O$	6.40E09	1.00	6280.
32.	$OH + N \rightarrow NO + H$	4.00E13	0.00	0.00
33.	$NO + HO_2 \rightarrow NO_2 + OH$	2.11E12	0.00	-480.
34.	$NO_2 + H \rightarrow NO + OH$	3.50E14	0.00	1500.

Table A.1: Skeletal Chemical Mechanism for Fuels up to Methane

constant k_j corresponding to the jth reaction in the table.

$$k_j = A_j T^{\alpha_j} \exp \frac{-E_{a,j}}{\bar{R}T} \tag{A.1}$$

The Universal Gas Constant is denoted here by the symbol $\bar{R}$. Third body efficiencies M_i for three-body reactions given in Table A.1, taken from Peters[165] (also see Warnatz[120]), are $M_{H2O} = 6.5$, $M_{CO2} = 1.5$, $M_{CO} = 0.75$, $M_{O2} = 0.4$, $M_{N2} = 0.4$ and $M_{other} = 1.0$.

The reader should note that reaction expressions listed in the table with two-way arrows between reactants and products, are treated as being reversible. The corresponding reverse reaction rates are calculated from the forward rate and the value of the equilibrium constant in these cases. In some instances, both the forward and reverse reactions are explicitly listed with the reference number for the forward reaction being denoted by the suffix 'f' and the back reaction by the suffix 'b'. Reactions 21 and 21L represent the high and low pressure limits of the same reaction (methane pyrolysis), and a Lindemann[119] formulation is adopted for treating the pressure fall-off between these two rates.

A.2 Reduction Procedure

The simplified mechanisms that result from the following reduction scheme are identical to those developed by Chen *et al*[50,166] and have often been used in the past for making joint PDF model predictions of H_2 and $CO-H_2$ combustion[48,49,50,51,96,102].

In order to derive a reduced mechanism from a comprehensive set of chemical reactions it is neccesary to assume that some minor species abundances are in steady state and that some selected reactions are in partial equilibrium [167]. Steady state species assumptions are applicable in cases where the rate at which a species is produced is much slower than the rate at which it is consumed[168]. Equilibration of chemical reactions is valid where the characteristic time scales of those reactions are much smaller than the characteristic time scale of the global reaction step to which they are related. Chen[169] gives a useful description of a general procedure for deriving reduced chemical mechanisms, and Lam[170] describes the process in a comprehensive systematic method applicable to automatic reduction.

Two step reduced mechanisms for H_2 combustion assume that O, OH and HO_2 are steady whilst the major species H_2, O_2 and H_2O and the radical species H are non-steady. Reduction of the set of the first 17 reactions, given in Table A.1, using the method described by Peters et al[167] leads to the following expressions for the combined diffusion-convection transport terms $L(\gamma_i)$ for each reactive species specific molar abundance γ_i, in terms of the chemical reaction rates w_j.

$$L(\gamma_H)+[L(\gamma_{OH})+2L(\gamma_O)-L(\gamma_{HO_2})] = 2w_{1f}-2w_{1b}+2w_6+2w_8+2w_{13f}-2w_{13b}-2w_5-2w_{15}-2w_{16} \quad (A.2)$$

$$L(\gamma_{H_2O})+[L(\gamma_{OH})+L(\gamma_O)-L(\gamma_{HO_2})] = 2w_{1f}-2w_{1b}+2w_6+2w_8+2w_{13f}-2w_{13b} \quad (A.3)$$

$$L(\gamma_{H_2})+[L(\gamma_{HO_2})-L(\gamma_{OH})-2L(\gamma_O)] = -3w_{1f}+3w_{1b}-3w_6-3w_8-3w_{13f}+3w_{13b}+w_5+w_{15}+w_{16} \quad (A.4)$$

$$L(\gamma_{O_2}) + [L(\gamma_{HO_2}) + L(\gamma_{H_2O_2})] = -w_{1f} + w_{1b} - w_6 - w_8 - w_{13f} + w_{13b} \quad (A.5)$$

In the expressions above, the transport terms enclosed in square brackets correspond to transport of minor species and thus have negligible magnitude in comparison to the remaining terms. Neglect of the bracketed terms results in expressions describing the transport and chemical production of the non-steady species H_2, O_2, H_2O and H.

Examination of the stoichiometry of the reaction rate groupings given above leads to the following global reaction mechanism.

$$w_I : \qquad 3H_2 + O_2 \rightleftharpoons 2H + 2H_2O$$

$$w_{II} : \qquad 2H + M \rightarrow H_2 + M$$

Where $w_I = w_{1f} - w_{1b} + w_6 + w_8 + w_{13f} - w_{13b}$, and thereby contains the major chain branching and chain carrying reactions of the hydrogen-air chemical system, and $w_{II} = w_5 + w_{15} + w_{16}$ which describes chain termination and three body recombination reactions.

Radical OH concentration is determined from the partial equilibrium expression for reactions 3f and 3b, as given in Table A.1, which are assumed to be fast compared to other reactions involving OH[50].

$$C_{OH} = \frac{C_H C_{H_2O}}{K_3 C_{H_2}} \quad (A.6)$$

Where K_3 is the equilibrium constant relating the rate of reaction 3f to the rate of its back reaction, ie: $K_3 = k_{3f}/k_{3b}$.

The remaining species are well approximated by steady state expressions involving the appropriate consumption and production reactions for each species. O radical concentration is given by,

$$C_O = \frac{k_{1f}C_{O_2}C_H + k_{2b}C_{OH}C_H + k_{4b}C_{OH}C_{OH}}{k_{4f}C_{H_2O} + k_{1b}C_{OH} + k_{2f}C_{H_2}} \tag{A.7}$$

HO_2 concentration is calculated from a quadratic formula,

$$C_{HO_2} = \frac{\sqrt{b^2 + 4ac} - b}{2a} \tag{A.8}$$

where the quadratic coeficients are given by:

$$a = 2k_{11}C_{HO_2}C_{HO_2}$$

$$b = (k_6 + k_7 + k_8)C_H + k_{12f}C_{H_2O} + k_9C_{OH} + k_{10}C_O$$

$$c = k_5C_HC_{O_2}C_M + k_{12b}C_{H_2O_2}C_{OH}$$

H_2O_2 concentration is found from,

$$C_{H_2O_2} = \frac{k_{12f}C_{HO_2}C_{H_2O} + k_{11}C_{HO_2}C_{HO_2} + k_{13b}C_{OH}C_{OH}}{k_{12b}C_{OH} + k_{13f}C_M} \tag{A.9}$$

The three step CO/H_2 reaction mechanism can be thought of as comprising the the hydrogen two step mechanism, with one further step accounting for the oxidation of CO to CO_2. The non-steady species of interest in these flames are as for pure hydrogen with the addition of CO and CO_2. The steady species HCO must be considered in addition to those mentioned above. A similar reduction process to that outlined above for pure hydrogen is applicable to the CO/H_2 chemical system and yields the following global reactions:

$$w_{IC}: \qquad 3H_2 + O_2 \rightleftharpoons 2H + 2H_2O$$

$$w_{IIC}: \qquad 2H + M \rightarrow H_2 + M$$

$$w_{IIIC}: \qquad H_2O + CO \rightleftharpoons H_2 + CO_2$$

The global reaction rates are given by:

$$w_{IC} = w_I \tag{A.10}$$

$$w_{IIC} = w_{II} + w_{20} \tag{A.11}$$

$$w_{IIIC} = w_{18} \tag{A.12}$$

where the additional reaction rate terms result from the H radical consuming formation of HCO in the case of w_{IIC}, and the chain carrying oxidation of CO to CO_2 in the case of w_{IIIC}. The addition of CO to the H_2-air chemical system has no effect on the expressions for the steady state species as given for the case of pure hydrogen. All that remains is to determine the concentration of the steady state species HCO:

$$C_{HCO} = \frac{k_{20f} C_{CO} C_H C_M}{k_{19} C_H + k_{20b} C_M} \tag{A.13}$$

A.3 Nitric Oxide Thermal Pathway

In reducing the already abridged nitrogen chemistry reaction steps given in Table A.1, the first step taken is that of neglecting nitrogen dioxide (NO_2) formation. Although, practically all of the nitric oxide (NO) produced in combustion systems is eventually converted to NO_2 under atmospheric conditions, it typically represents only a small fraction of the immediate NO_x output from non-hydrocarbon combustion.

Of the remaining reactions (30-32), the rate limiting step was identified as reaction 30 by Zeldovich[128]. With the assumption of steady state monatomic nitrogen (N) levels, the overall nitric oxide formation reaction is given by the following,

$$w_{NO}: \qquad N_2 + O_2 \rightarrow 2NO \tag{A.14}$$

where the rate (w_{NO}) is equal to,

$$w_{NO} = k_{30} C_O C_{N2} \tag{A.15}$$

Due to the high activation energy required for reaction 30 to proceed to an appreciable extent, nitric oxide formation is highly sensitive to temperature variation and is thus known as the Zeldovich thermal mechanism. As can be inferred from Eqn A.15, that nitric oxide formation via the thermal mechanism is also sensitive to variations in monatomic oxygen radical (O) levels. Although this sensitivity is

substantially weaker than the sensitivity to temperature variation. accurate prediction of NO formation using partial equilibrium estimates of O (see above) is potentially problematic. Some useful comments on nitrogen chemistry approximations in hydrogen-air laminar diffusion flames have been made by Gutheil *et al*[126].

Appendix B

Radiation Submodel

Throughout this investigation, radiation losses have been calculated using a simple gas-phase emissivity model described by Kuznetzov and Sabelnikov[26]. Apart from being used by Kuznetzov and coworkers (see Ref. [26] for a listing), this model has also been used by Chen and Kollmann[51] and may well have been employed elsewhere. Radiative losses from solid phase particles such as soot and other byproducts have not been included in any of the analyses presented in this thesis.

Kuznetzov and Sabelnikov[26] report that their model is based upon experimental observations of Mikheev[171], who studied radiative heat transfer between a heating element and small enclosing hemispheres of water vapour.

For optically thin conditions, where effectively no heat is absorbed by vapour between the emission source and the surroundings, the radiative flux from water vapour (I_{H2O}) can be approximated by the following expression:

$$I_{H2O}(T) = 4\beta_{H2O}(T)p_{H2O}\sigma_0(T^4 - T_{bk}^4) \tag{B.1}$$

It can be seen that the instantaneous radiative flux from water vapour (I_{H2O}), is a function of instantaneous temperature T, the partial pressure of the water vapour p_{H2O}, and a data fitting function of temperature $\beta_{H2O}(T)$, where σ_0 is the Stefan-Boltzmann constant and T_{bk} is the effective background temperature. The product of the partial pressure of water, and the data fitting function can be seen to represent the Planck mean absorption coefficient for H_2O.

Kuznetzov and Sabelnikov propose a similar expression, for non-luminous radiative flux from gaseous carbon dioxide (I_{CO_2}), which is also based upon experimental

observation[171]. Together, these two radiative losses represent the bulk of the total radiative flux ($I \approx I_{H2O} + I_{CO2}$) from all gaseous species in hydrogen/carbon combustion.

$$I = 4\sigma_0[\beta_{H2O}p_{H2O} + \beta_{CO2}p_{CO2}](T^4 - T_{bk}^4) \tag{B.2}$$

The data fitting functions (β_{H2O}, β_{CO2}) are linear functions of temperature and for the constants given below, have units of $m^{-1}Pa^{-1}$[26]:

$$\beta_{H2O} = 2.0 \times 10^{-5} - 6.4 \times 10^{-9}T \tag{B.3}$$

$$\beta_{CO2} = 4.6 \times 10^{-5} - 1.3 \times 10^{-8}T \tag{B.4}$$

In applying this radiation submodel in conditional moment closure methods, conditionally averaged radiative fluxes have been approximated by evaluating Eqn B.2 in terms of conditional mean temperatures and partial pressures. Thus it has been assumed that the optically-thin conditional mean radiation loss term $< \mathcal{S}_h \mid \eta >$ can be approximated by:

$$\begin{aligned} < \mathcal{S}_h \mid \eta > = -4\sigma_0[\beta_{H2O}(< T \mid \eta >) < p_{H2O} \mid \eta > \\ +\beta_{CO2}(< T \mid \eta >) < p_{CO2} \mid \eta >]((< T \mid \eta >)^4 - T_{bk}^4) \end{aligned} \tag{B.5}$$

Other CO_2 and H_2O gaseous emission models exist, notably that of Becker[172] and Hubbard and Tien[155]. The latter model produces similar predictions of radiative flux, with small differences which may be due to errors in the experimental data upon which they are based. The model of Becker[172] tends to predict much higher radiant fluxes than either the current model of that of Hubbard and Tien[155] All of these models are applicable for optically-thin heat transfer only.

Chen and Kollmann[50] have suggested that optically-thin radiation models may substantially overpredict radiation losses from turbulent jet flames of hydrogen. Their suggestion is based upon a comparison of predictions of radiant fraction (f_{rad}), by the Kuznetzov and Sabelnikov[26] submodel within a joint PDF turbulent combustion model, with the experimental results of Turns and Myhr[146]. Radiant fraction (f_{rad}) is an approximate global measure of the ratio of heat transfer from a flame by radiation to the amount of heat produced by chemical reaction. For a non-luminous flame that is free of soot, the radiant fraction should monotonically decrease with decreasing global residence time[146].

Based on experimental observation, Turns and Myhr claimed that a similar power law dependence existed between radiant fraction and global residence time for all soot-free hydrocarbon and carbon monoxide flames. Chen and Kollmann[50] compared this power law dependence with their radiant fraction calculations for pure hydrogen jet flames and found that their predictions showed a significantly stronger dependence than what was expected.

Appendix C

Computer Codes

This appendix contains the principal FORTRAN coded elements of the two non-premixed conditional moment closure (CMC) models presented in Chapters 4-7. It is not intended for this to be a complete listing, as many of the called subroutines and functions are publicly available (such as CHEMKIN II, SVODE, TWOPNT, PEQUIL etc.), are of no special interest (eg: gaussian PDF subroutines), or do not represent original work (eg: JFLAME, written in the main by J.-Y. Chen[134]).

However, all of the FORTRAN codes written by the author and used throughout the course of this investigation can be made available, upon request to the author. The codes belonging to QKIN and FIREBALL are listed at the end of this appendix in double column format and are not page numbered.

C.1 FIREBALL : ISR Program

The FORTRAN code for the implementation of Imperfectly Stirred Reactors (ISRs) described in Chapters 4 and 5 is known as FIREBALL. This code employs the public domain two-point boundary value problem solver (TWOPNT) that is used in the laminar premixed flame code (PREMIX) written by R. J. Kee, J. F. Grcar, M. D. Smooke and J. A. Miller of Sandia National Laboratories[122].

However, where PREMIX has grid points in one-dimensional physical space, FIREBALL discretizes mixture fraction space. FIREBALL supplies TWOPNT with steady state and transient solution residuals via the subroutines RHSFN0, RHSFN1 and RHSFN2 (nonreactive, adiabatic and radiative versions), and computes finite

difference Jacobian approximations using RHSJAC. The right-hand-side functions (RHSFN0,RHSFN1) contain the actual implementation of the CMC equations given in Chapter 4.

Conditional mean scalar dissipation rate data is calculated by the subroutine CHIISR, which in turn employs a Gaussian pdf routine GAUDI which computes gaussian PDFs and second integrals.

Chemical kinetic data is provided by the CHEMKIN II Gas Phase Subroutine Library[121], with the input chemical mechanism having been interpreted by the CHEMKIN II Interpreter beforehand.

FIREBALL can be paused (and later restarted) at any point since it reads its remaining CPU time allowance from an external file after each step. This restart capacity is a useful function since it allows solutions from existing calculated cases to be used as starting estimates for new runs.

Table C.1 contains the subroutines called by FIREBALL in call order, as well as a description of their function, and whether they are included in the code listing or not.

C.2 QKIN : Jet Flame Subroutine

The CMC 2-dimensional code, QKIN (Version 3.3), is designed for use with any 2-dimensional fluid dynamic solver. Throughout the course of this investigation, QKIN has been used in conjunction with the boundary layer equation solver written by J.-Y. Chen and coworkers[134]. The solver, referred to as JFLAME in this thesis, has been slightly modified to accommodate the 'workspace' and parameter passing arrangements required by QKIN. The solution mechanics of JFLAME are identical to that of the unmodified original.

The workspace allocation of QKIN is explained in the code listing itself, whilst the subroutines called by QKIN are described in Table C.2.

The relationship between QKIN and its calling program can be described as follows. After each axial step taken by the calling program, it passes unconditional mean information such as density, velocity, mean mixture fraction, mixture fraction variance, radial position and scalar dissipation rate to QKIN.

Name	*Listed Y/N ?*	*Description*
CK ...	N	Chemkin II Subroutines (see Ref [121])
CHEMINI	N	Inputs initial ISR data
RESUMEI	N	Inputs restart ISR data
FDETA	N	Calculates mixture fraction grid finite differences
CHIISR	Y	Calculates conditional mean scalar dissipation rates
GAUDI	N	Calculates gaussian profiles and their second integrals
TREMAIN	N	Checks available CPU time and returns this value in seconds
TWOPNT	N	Two point boundary value problem solver (see Ref [122])
RHSFN0	Y	Residual solution function for non-reactive CMC cases
RHSFN1	Y	Residual solution function for reactive adiabatic CMC cases
RHSFN2	Y	Residual solution function for reactive non-adiabatic CMC cases
SCOPY	N	BLAS routine. copies one vector to another
RHSJAC	Y	Calculates Jacobian via finite difference approximation
SGBCO	N	BLAS routine. factors band real matrices
SGBSL	N	BLAS routine. solves banded matrix equations
CHECK0	N	Checks for negative species mass fractions and corrects
QINCON	N	Driver for STANJAN equilibrium chemistry code
ZARRAY	N	Resets an array so that it contains only zero values

Table C.1: Subroutines called by FIREBALL

Name	*Listed Y/N ?*	*Description*
CK ...	N	Chemkin II Subroutines (see Ref [121])
CHEMIN	N	Inputs conditional mean initialization data
RESUME	N	Inputs restart data
GXTREM	N	Determines threshold upon conditional mean scalar dissipation rate from chemical rate data. CMSD values above this level prevent CMC calculation
UCHIGAU	Y	Determines conditional mean scalar dissipation rate and velocity from unconditional mean data using local method
GAUDIM	N	Calculates gaussian profiles and their second integrals
AVERUX2	Y	Determines conditional mean scalar dissipation rate and velocity from unconditional mean data using PDF weighting method
TWZONE	Y	Handles statistically indeterminate zones of mixture fraction space
RHSFN0	Y	Residual solution function for non-reactive CMC cases
RHSFN1	Y	Residual solution function for reactive adiabatic CMC cases
RHSFN2	Y	Residual solution function for reactive non-adiabatic CMC cases
SVODE	N	Stiff ODE Solver used to solve CMC equations contained within RHSFNs see Ref [173]
TREMAIN	N	Checks available CPU time and returns this value in seconds
CHECK0	N	Checks for negative species mass fractions and corrects
QINCON	N	Driver for STANJAN equilibrium chemistry code
Q2UCV	N	Determines unconditional mean statistics by convolving conditional mean values with mixture fraction PDFs at each radial point
WSTAT	N	Reports output status when an error or scheduled output is required

Table C.2: Subroutines called by QKIN

QKIN employs this data to determine mixture fraction PDFs and conditional mean velocity and scalar dissipation rate data. QKIN then completes the same axial step as was just completed by the calling program. At the completion of that step, QKIN passes updated unconditional mean density information back to the calling program. The cycle is then repeated as many times as necessary until the end of the calculation is reached.

```
C#############################################################C
C
      PROGRAM FIREBALL      ! Version 2.0
C
C     This code is a zero-dimensional CMC method closure
C     for an idealized turbulent nonpremixed ISR
C     (Imperfectly Stirred Reactor).
C
C     Nigel S. A. Smith  (v1.0 9/1993, v2.0 7/1994)
C
C#############################################################C
C
C     Description of Primary Variables
C
C-------------------------------------------------------------C
C
C     Real Variables:
C
C     ABOVE(*)      Array of upper boundary conditions upon the
C                   solution.
C
C     BELOW(*)      Array of lower boundary conditions upon the
C                   solution.
C
C     BOUNDQ(*)     Rich and lean boundary values for reactive scalars
C
C     CHI(*)        Array of conditional mean scalar dissipation rate*density
C
C     D2C(*)        Finite difference coefficient based on ETA(*) spacing
C
C     D2M(*)        Finite difference coefficient based on ETA(*) spacing
C
C     D2P(*)        Finite difference coefficient based on ETA(*) spacing
C
C     DETA(*)       Differences between ETA(*) grid points
C
C     EPDF(*)       Core volume averaged mixture fraction PDF
C
C     ETA(*)        Mixture fraction grid
C
C     OPDF(*)       Outlet area averaged (mass flow rate weighted) mixture
C                   fraction PDF.
C
C     Q(*)          Array of current conditional mean reactive scalars at
C                   all points in mixture fraction space.  Q(*) is
C                   partitioned as follows:
C
C          Q(1) ... Q(NUMSCA)      values of reactive scalars 1...,numsca
C                                  at mixture fraction grid point # 1.
C          Q((I-1)*NUMSCA) .... Q(I*NUMSCA)   values of reactive scalars at
C                                             Ith mixture fraction grid point
C          etc....
C
C     Q0(*)           Array of inlet-value conditional mean reactive scalars at
C                     all points in mixture fraction space.  Q0(*) is
C                     partitioned identically to Q(*).
C
C     QCOEF(*)        Inlet-outlet difference term coefficient array
C
C     QJAC(*)         Finite difference approximation to Jacobian matrix.
C                     Location of entries correspond to the solution vector
C                     contained in Q(*).
C
C     QRES(*)         Residual vector calculated by RHSFN's.  Residual
C                     entries correspond to Q(*) partitioning.
C
C     QRESPT(*)       Perturbed residual vector calculated by RHSFN's and used
C                     by RHSJAC.  Residual entries correspond to Q(*)
C                     partitioning.
C
C     QU(*)           Array of conditional mean reactive scalars at
C                     all points in mixture fraction space at the last
C                     time step.  QU(*) is partitioned identically to Q(*).
C
C     RKFH            Communication of standardized enthalpy with hidden
C                     reduced mechanism codes.  These codes are transparent
C                     and QKIN is unchanged if they are used.  They link in
C                     place of selected CHEMKIN II routines.
C
C     RHO(*)          Conditional mean density
C
C     RTRES           Reciprocal of residence time (1/s)
C
C     T(*)            Conditional mean temperature array
C
C     TPBFFR(*)     TWOPNT's I/O buffer array.  Used to pass solutions
C                   residuals, and other info to and fro.
C
C     UCM(*)          Unconditional mean area averaged outlet reactive scalars
C
C     VRWORK(*)       TWOPNT's real workspace
C
C     WORK(*)         Chemkin II Real workspace
C
C     WT(*)           Array of molecular weights in units of (g/mol).
C
C-------------------------------------------------------------C
C
C     Integer Variables:
C
C
C     IOCONT          I/O Counter
C
C     IPIVOT(*)       Pivot array required by TWOPNT
C
C     IPT             Communication of grid point index with hidden
C                     reduced chemistry codes.
C
C     IRAD            Radiation flag
C
C     IREPRT          TWOPNT diagnostic output flag
C
C     IRMODE           Flow-of-control flag, describes state of the run
C
C     ISCONT          Timestep counter
C
C     ISOPT           Initialize/Restart flag
C
C     IVWORK(*)       TWOPNT's integer workspace
C
C     IWORK(*)        Integer workspace for Chemkin II
C
C     IXMODE          Status flag for CHIISR
C
C     LTPLVL(*)       Output level control flags for TWOPNT
C
C     NETAPT          Number of mixture fraction grid points
C
C     NUMSCA          Number of reactive scalars
C
C
C-------------------------------------------------------------C
C
C     Logical Variables:
C
C     YADAPT        TWOPNT adaptive grid enable/disable flag
C
C     YETAMK(*)     TWOPNT marker array for new grid point placement
C
C     YFUNCT        TWOPNT residual function flag
C
C     YGNITE        Ignition flag (true - reactive CMC, false - non-reactive)
C
C     YJACOB        TWOPNT Jacobian flag
C
C     YQACTV(*)     TWOPNT array indicating actively solved scalars
```

```
C
C     YREENT      TWOPNT re-entry flag
C
C     YSAVE       TWOPNT save solution flag
C
C     YSCCES      TWOPNT success flag
C
C     YSHOW       TWOPNT display solution flag
C
C     YSOLVE      TWOPNT solve using inverted Jacobian flag
C
C     YSTORE      TWOPNT store solution for time-stepping
C
C     YTIME       TWOPNT time-stepping flag
C
C     YTPERR      TWOPNT error flag
C
C     YUPDAT      TWOPNT grid-change flag
C
C
C#############################################################C
C
      IMPLICIT REAL (A-H,O-X,Z), INTEGER (I-N), LOGICAL (Y)
C
      PARAMETER(NETAMX=96,NSPCMX=60,NELMX=8,NSCAMX=NSPCMX+1,
     1 LENWK=5000,LENIWK=5000,LENCWK=5000,NMAXQ=NSCAMX*NETAMX,
     2 LIMVIW=3*NETAMX,LIMVRW=7*NMAXQ+2*NETAMX,NBNDMX=6*NSCAMX-2,
     3 UNITY=1.0,ZERO=0.0,VBIG=1.E20,VSML=1.E-20)
C
      CHARACTER*24 CSTATUS
      CHARACTER*78 CTITLE
      CHARACTER*16 CWORK(LENCWK)
      CHARACTER*10 FILENM
C
      REAL VRWORK(LIMVRW),ABOVE(NMAXQ),BELOW(NMAXQ),
     1 TPBFFR(NMAXQ),WT(NSPCMX),WORK(LENWK),
     2 Q(NMAXQ),QU(NMAXQ),Q0(NMAXQ),QJAC(NMAXQ*NBNDMX),
     3 QRES(NMAXQ),QRESPT(NMAXQ),CHI(NETAMX),BOUNDQ(2*NSCAMX),
     4 ETA(NETAMX),D2M(NETAMX),D2C(NETAMX),D2P(NETAMX),
     5 T(NETAMX),DETA(NETAMX),OPDF(NETAMX),EPDF(NETAMX),
     6 UCM(NSCAMX),RHO(NETAMX),QCOEF(NETAMX)
C
      INTEGER LTPLVL(2),IVWORK(LIMVIW),IPIVOT(NMAXQ),
     1 IWORK(LENIWK),IRAD
C
      LOGICAL YTPERR,YQACTV(NSCAMX),YADAPT,YFUNCT,YJACOB,
     1 YREENT,YSAVE,YSHOW,YSOLVE,YSTORE,YSCCES,YTIME,YUPDAT,
     2 YGNITE,YETAMX(NETAMX)
C
      COMMON/COMLNE/REFH,IPT    ! for communication with SUBCHM
      SAVE /COMLNE/
C
      EXTERNAL RHSFN0,RHSFN1,RHSFN2
C
C+++++++++++++++++++++++++++++++++++++++++++++++++++++++++++++
C////////////////// PROGRAM INITIALIZATION ////////////////////
C
C     Set I/O Unit Numbers
      LSTINP=5
      LQOUT=40
      LCHDAT=41
      LREST=42
      LMWT=43
      LSCOUT=35
      LINK=65
      LEROUT=37
      LDIAGN=39
      LUCDAT=44
      LTPOUT=46
      LTPBIN=47
      LQZERO=48
C
C     Open I/O files
      OPEN(UNIT=LINK,FILE='linkfile.d',FORM='UNFORMATTED')
      OPEN(UNIT=LEROUT,FILE='ckerr.d',FORM='FORMATTED')
      OPEN(UNIT=LCHDAT,FILE='isrchem.d',FORM='FORMATTED')
      OPEN(UNIT=LSCOUT,FILE='isrlog.d',FORM='FORMATTED')
      OPEN(UNIT=LMWT,FILE='mwtfil.d',FORM='FORMATTED')
      OPEN(UNIT=LDIAGN,FILE='israux.d',FORM='FORMATTED')
      OPEN(UNIT=LTPOUT,FILE='tpout.d',FORM='FORMATTED')
      OPEN(UNIT=LTPBIN,FILE='tpbin.d',FORM='UNFORMATTED')
C
C     Initialize CHEMKIN II
      CALL CKINIT(LENIWK,LENWK,LENCWK,LINK,LEROUT,IWORK,WORK,CWORK)
      CALL CKINDX(IWORK,WORK,NUMEL,NUMSPC,NUMRCN,NFIT)
      CALL CKRP(IWORK,WORK,R1,R2,PATM)
      CALL CKWT(IWORK,WORK,WT)
C
C     Set number of reactive scalars and determine size of Jacobian
C     bands resulting from the number of scalars
      NUMSCA=NUMSPC+1
      NBANDS=6*NUMSCA-2
C
C     Output Molecular Weights for Postprocessing Conversion of Y --> X
      DO 2000 IWT=1,NUMSCA-1
      WRITE(LMWT,*) WT(IWT)
2000  CONTINUE
      CLOSE(LMWT)
C
C     Calculate  machine precision to size Jacobian perturbations
      PERT=SQRT(R1MACH(1))
      ABPERT=PERT
      RLPERT=PERT
C
C     Input and process raw data ready for calculations
C     where CHEMINI initializes and RESUMEI restarts
      READ(LSTINP,*) ISOPT
      IF(ISOPT.EQ.0) THEN
      NETAPT=NETAMX   !/3
      CALL CHEMINI(NETAPT,NUMSCA,ETA,Q,Q0,TRES,PRESSQ,BOUNDQ,
     1  FOXRAT,XMFRC,CORMRF,XMFRCV,CORMFV,OMFRCV,YGNITE,IRAD,
     2  IPH2O,IPCO2,T,CTITLE,WORK,IWORK,PATM,SSABS,SSREL,TDABS,
     3  TDREL,TOLER0,TOLER1,TOLER2,ISTEP0,ISTEP1,ISTEP2,NUMEL,
     4  TINIT,TMAX,TMIN,PERT,TOLTMP,LEVEL,LCHDAT,LSCOUT,LQZERO,
     5  LDIAGN)
      TELPSE=ZERO
      ELSE
      CALL RESUMEI(NETAPT,NUMSCA,ETA,Q,Q0,T,TMIN,TMAX,BOUNDQ,
     1 TINIT,TELPSE,YGNITE,IRAD,IPH2O,IPCO2,SSABS,SSREL,TDABS,TDREL,
     2 TOLER0,TOLER1,TOLER2,ISTEP0,ISTEP1,ISTEP2,FOXRAT,XMFRC,CORMRF,
     3 XMFRCV,CORMFV,OMFRCV,CHI,TRES,PATM,PRESSQ,TOLTMP,CTITLE,LEVEL,
     4 LREST,LSCOUT,LQZERO,LDIAGN)
      ENDIF
C
      RTRES=1./TRES
C
C     Set up TWOPNT flags and initializing inputs
      LTPLVL(1)=LEVEL ! full output of info messages from TWOPNT
      LTPLVL(2)=LEVEL ! only output solution at highest level of TWOPNT
      YREENT=.FALSE.
      IPASES=1
      MXETAD=NETAMX/4
      ISSAGE=2
      ITDAGE=2
      TDECR=2.2
      TINCR=2.0
      TSTEP=TINIT
      YADAPT=.TRUE.
      DO 2600 J=1,NUMSCA-1
      YQACTV(J)=.TRUE.
      YUPDAT=.FALSE.
2600  CONTINUE
      DO 2700 I=1,NETAPT
       YETAMK(I)=.FALSE.
       ABOVE(I*NUMSCA)=VBIG
       BELOW(I*NUMSCA)=-1.*VBIG
```

```
293           DO 2700 J=1,NUMSCA-1
294            ABOVE(J+(I-1)*NUMSCA)=UNITY+PERT
295            BELOW(J+(I-1)*NUMSCA)=ZERO-PERT
296   2700    CONTINUE
297   C
298   C       Set I/O Counter and Step Counter
299           IOCONT=0
300           ISCONT=1
301   C
302   C////////////////// MAIN EXECUTION SECTION ////////////////////
303   C
304   2900    CONTINUE
305   C       Calculate Delta Eta arrays for F.D equations
306   C       if grid changes have occured
307           YOUTPT,YUPDAT  OR  ISCONT .EQ. 1
308           CALL FDETA(NETAPT,ETA,D2M,D2C,D2P,Q0,QCOEF,
309          1 YOUTPT,YETAMK,NUMSCA,LSCOUT,LDIAGN)
310   C
311   C       If the ETA grid has changed or been initialized
312   C       then CHI will need to be re/calculated.
313   C
314   C       Calculate Conditional Mean Scalar Dissipation in the Reactor
315   C       as a function of operating mixture fraction mean, variance
316   C       and residence time.
317   C
318           IXMODE=0
319   2950    CONTINUE
320            CALL CHIISR(NETAPT,ETA,XMFRC,CORMRF,XMFRCV,CORMFV,
321          1  OMFRCV,CHI,RHO,QCOEF,RTRES,OPDF,PDF0,PDF1,EPDF,
322          2  TOLTMP,PRESSQ,Q,T,WORK,IWORK,NUMSCA,IXMODE,
323          3  ISCONT-1,LSCOUT,LDIAGN)
324   C
325   3000    CONTINUE
326   C
327   C       Check elapsed CPU time and exit if limit is exceeded
328           CALL TREMAIN(CPUTIM)
329           WRITE(LSCOUT,*) ISCONT,CPUTIM,NETAPT
330           IF(CPUTIM.LT.1.) THEN
331           WRITE(LSCOUT,*) 'FIREBALL HAS OVERRUN THE CPU LIMIT TIME'
332           WRITE(LSCOUT,*) 'A HALT HAS BEEN CALLED.'
333           IRMODE=3  ! Flags unsuccessful convergence and halt
334           GOTO 4000
335           ENDIF
336   C
337   C       Call Two point boundary value problem solver
338           CALL TWOPNT
339          1 (YTPERR,LTPOUT,LTPLVL,LIMVIW,IVWORK,LIMVRW,VRWORK,ABOVE,YQACTV,
340          2 YADAPT,BELOW,LTPBIN,TPBFFR,NUMSCA,CONDIT,YFUNCT,YJACOB,YETAMK,
341          3 ETA,IPASS,IPASES,MXETAD,NETAMX,NETAPT,YREENT,IREPRT,YSAVE,0,
342          4 YSHOW,YSOLVE,SSABS,ISSAGE,SSREL,ISTEP0,ISTEP1,ISTEP2,YSTORE,
343          5 YSCCES,TDABS,ITDAGE,TDECR,TDREL,YTIME,TINCR,TMAX,TMIN,TOLER0,
344          6 TOLER1,TOLER2,TINIT,TSTEP,YUPDAT,Q)
345   C
346           NQ=NETAPT*NUMSCA
347   C
348           IF(YTPERR) THEN
349            WRITE(LSCOUT,*) 'TWOPNT ERROR EXCEPTION, SEE  tpout.d'
350            IRMODE=3  ! flag failure induced exit
351           ELSE
352            IF(.NOT.YSCCES .AND. .NOT.YREENT) THEN
353             IF(IREPRT.EQ.2) THEN
354              WRITE(LSCOUT,*) 'ERROR IN SOLVING, REPORT= ',IREPRT
355              WRITE(LSCOUT,*) 'NEED MORE THAN ',NETAMX
356              WRITE(LSCOUT,*) 'GRID POINTS TO CARRY ON'
357              IRMODE=3 ! flag failure induced exit
358             ELSE
359              IF(IREPRT.EQ.1) THEN
360               WRITE(LSCOUT,*) 'ERROR IN SOLVING, REPORT= ',IREPRT
361               YREENT=.FALSE.
362               IRMODE=3
363              ELSE
364               IF(IREPRT.EQ.3) THEN
365                WRITE(LSCOUT,*) 'ERROR IN SOLVING, REPORT= ',IREPRT
366               YREENT=.FALSE.
367               IRMODE=3
368              ENDIF
369             ENDIF
370            ENDIF
371           ELSE
372            IF(YREENT) THEN    ! TWOPNT is requesting a job done
373             IF(YFUNCT) THEN  ! TWOPNT wants a residual evaluation
374              WRITE(LDIAGN,*) 'RESIDUAL EVALUATION'
375              IF(.NOT. YGNITE) THEN
376               CALL RHSFN0(NETAPT,NUMSCA,TPBFFR,QU,Q0,BOUNDQ,QCOEF,
377          1     YTIME,TSTEP,D2M,D2C,D2P,CHI,QRES,LDIAGN)
378              ELSE
379               IF(IRAD.EQ.0) THEN
380                CALL RHSFN1(NETAPT,NUMSCA,TPBFFR,QU,Q0,BOUNDQ,QCOEF,
381          1      YTIME,TSTEP,D2M,D2C,D2P,CHI,PRESSQ,WT,
382          2      WORK,IWORK,T,TOLTMP,QRES,LDIAGN)
383               ELSE
384                CALL RHSFN2(NETAPT,NUMSCA,TPBFFR,QU,Q0,BOUNDQ,QCOEF,
385          1      YTIME,TSTEP,D2M,D2C,D2P,CHI,PRESSQ,WT,
386          2      WORK,IWORK,IRAD,IPH2O,IPCO2,T,TOLTMP,QRES,
387          3      LDIAGN)
388               ENDIF
389              ENDIF
390              CALL SCOPY(NQ,QRES,1,TPBFFR,1) ! Copy residual -> buffer
391              IXMODE=1
392              GOTO 2950
393             ELSE
394              IF(YJACOB) THEN
395              WRITE(LDIAGN,*) 'JACOB ENTRY'
396   C           Calculate Jacobian given the solution in the buffer
397               CALL RHSJAC(NUMSCA,NETAPT,NBANDS,YTIME,YGNITE,IRAD,ABPERT,
398          1     RLPERT,TSTEP,T,TOLTMP,PRESSQ,WT,IPH2O,IPCO2,
399          2     D2M,D2C,D2P,CHI,IWORK,WORK,TPBFFR,QU,Q0,QRES,QRESPT,
400          3     BOUNDQ,QCOEF,QJAC,LDIAGN)
401   C
402   C           Calculate LU decomposition of BTD Jacobian and return in QJAC
403   C           (Note QRESPT is only being used as workspace, since it has
404   C            no use outside of RHSJAC)
405               CALL SGBCO(QJAC,NBANDS,NQ,2*NUMSCA-1,2*NUMSCA-1,
406          1     IPIVOT,RCOND,QRESPT)
407               IF(RCOND.LE.ZERO) THEN
408                WRITE(LSCOUT,*) 'SINGULAR JACOBIAN ENCOUNTERED'
409                IRMODE=3 ! flag failure induced exit
410               ELSE
411                CONDIT=UNITY/RCOND
412                GOTO 3000
413               ENDIF
414              ELSE
415               IF(YSOLVE) THEN
416               WRITE(LDIAGN,*) 'SOLVE'
417   C            Calculate Solution vector given residual in buffer, and LU
418   C            decomposed Jacobian.  Result is returned in buffer. 0 input
419   C            flags solution of residual rather than transpose of residual
420                CALL SGBSL(QJAC,NBANDS,NQ,2*NUMSCA-1,2*NUMSCA-1,
421          1     IPIVOT,TPBFFR,0)
422               DO 3200 I=1,NQ
423   3200        IF(ABS(TPBFFR(I)).LT.1.E-60) TPBFFR(I)=0.
424               GOTO 3000
425              ELSE
426               IF(YSTORE) THEN  ! TWOPNT wants to save an upstream solution
427                WRITE(LDIAGN,*) 'STORE after ',ISCONT
428                ISCONT=ISCONT+1
429                TELPSE=TELPSE+TSTEP
430                CALL SCOPY(NQ,TPBFFR,1,QU,1)
431                CALL CHECK0(NETAPT,NUMSCA,NUMSCA-1,QU)
432                IXMODE=1
433                GOTO 2950
434               ELSE
435                IF(YSHOW) THEN  ! TWOPNT is passing out an intermediate solution
436                 GOTO 3000
437                ELSE
438                 IF(YSAVE) THEN  ! TWOPNT is passing out a restart solution
```

```
                IRMODE 2 ! flag print and return, no exit
               ELSE
                IF(YUPDAT) THEN  ! TWOPNT has has found a
C                                  solution and adapted the eta grid
                 CALL CHECK0(NETAPT,NUMSCA,NUMSCA-1,TPBFFR)
                 GOTO 2900 ! re-enter with recalculated grid differences
                ENDIF
               ENDIF
              ENDIF
             ENDIF
            ENDIF
           ENDIF
          ENDIF
          WRITE(LSCOUT,*) 'SUCCESSFUL CONVERGENCE !!'
          IRMODE=1 ! flags successful converegence
         ENDIF
        ENDIF
       ENDIF
C
C/////////////// DATA OUTPUT SECTION //////////////////////
C
4000  CONTINUE
C
      CALL CHECK0(NETAPT,NUMSCA,NUMSCA-1,Q)
C
      DO 1731 I=1,NETAPT
      TI=MAX(300.,T(I))
      DELTAT=0.E0
      IPT=I
      REFH=Q(I*NUMSCA)
1740  CONTINUE
      TI=TI-DELTAT
      CALL CKHBMS(TI,Q(1+(I-1)*NUMSCA),IWORK,WORK,HBML)
      CALL CKCPBS(TI,Q(1+(I-1)*NUMSCA),IWORK,WORK,CP)
      DELTAT=(HBML-Q(I*NUMSCA))/CP
      IF(ABS(DELTAT).GT.TOLTMP) GOTO 1740
      T(I)=TI
1731  CONTINUE
C
C     Output Q and T data to file
      IOCONT=IOCONT+1
      ICT1=IOCONT/10
      ICT2=MOD(IOCONT,10)
      FILENM='isrout'//CHAR(ICT1+48)//CHAR(ICT2+48)//'.d'
      OPEN(UNIT=LQOUT,FILE=FILENM,FORM='FORMATTED')
      WRITE(LQOUT,*) 'FIREBALL OUTPUT FILE'
      WRITE(LQOUT,*) '===================='
      WRITE(LQOUT,7800) CTITLE
      WRITE(LQOUT,*)
      IF(IRMODE.EQ.1) THEN
      CSTATUS='Run Status : CONVERGED !'
      ELSE
      CSTATUS='Run Status : INCOMPLETE '
      ENDIF
      WRITE(LQOUT,2400) CSTATUS
      WRITE(LQOUT,*)
      WRITE(LQOUT,*) 'Step No./ Elapsed time (s)/ Step size (s):'
      WRITE(LQOUT,*) ISCONT,TELPSE,TSTEP
      WRITE(LQOUT,*) 'Limits on time step (s):'
      WRITE(LQOUT,*) TMIN,TMAX
      WRITE(LQOUT,*) 'Solution tolerances (absolute,relative):'
      WRITE(LQOUT,*) SSABS,SSREL
      WRITE(LQOUT,*) 'Grid refinement tolerances:'
      WRITE(LQOUT,*) TOLER0,TOLER1,TOLER2
      WRITE(LQOUT,*) 'No. timesteps initially, smoothing and retiring:'
      WRITE(LQOUT,*) ISTEP0,ISTEP1,ISTEP2
      WRITE(LQOUT,*) 'Output Level from TWOPNT:'
      WRITE(LQOUT,*) LEVEL
      WRITE(LQOUT,*)
      WRITE(LQOUT,*) 'Residence Time (sec) / Operating Pressure (atm):'
      WRITE(LQOUT,*) TRES, PRESSQ/PATM
      WRITE(LQOUT,*)
      WRITE(LQOUT,*) 'Fuel-Oxid. Mass Flow Ratio / Operating Mix Frac:'
      WRITE(LQOUT,*) FOXRAT,XMFRC
      WRITE(LQOUT,*)
      WRITE(LQOUT,*) 'Conserved Scalar Variances (Outlet, Core, Inlet):'
      WRITE(LQOUT,*) XMFRCV,CORMFV,OMFRCV
      WRITE(LQOUT,*)
      WRITE(LQOUT,*) 'Ignition/Radiation Flags:'
      IF(YGNITE) THEN
       WRITE(LQOUT,*) 1,IRAD
      ELSE
       WRITE(LQOUT,*) 0,IRAD
      ENDIF
      WRITE(LQOUT,*)
      WRITE(LQOUT,*) 'H2O Species Index/ CO2 Species Index:'
      WRITE(LQOUT,*) IPH2O,IPCO2
      WRITE(LQOUT,*)
      WRITE(LQOUT,*) 'Number of ETA grid points:'
      WRITE(LQOUT,*) NETAPT
      WRITE(LQOUT,*)
      WRITE(LQOUT,*) 'Tabulated ETA, ENTHALPY and CHI data:'
      DO 4010 I=1,NETAPT
4010  WRITE(LQOUT,*) ETA(I),Q(NUMSCA*I),CHI(I)
      DO 4020 I=1,NETAPT
      DO 4025 J=1,NUMSCA-1
      WRITE(LQOUT,*) Q(J+(I-1)*NUMSCA)
4025  CONTINUE
      WRITE(LQOUT,*) T(I)
4020  CONTINUE
      CLOSE(LQOUT)
C
C     Calculate Unconditional Mean Statistics using an assumed form
C     pdf supplied in OPDF by CHIISR.
C
C      Recalculate Beta-fn difference grids
       DETA(1)=0.5*(ETA(2)-ETA(1))
       DETA(NETAPT)=0.5*(ETA(NETAPT)-ETA(NETAPT-1))
       DO 4100 IETA=2,NETAPT-1
        DETA(IETA)=0.5*(ETA(IETA+1)-ETA(IETA-1))
4100   CONTINUE
C
      DO 4200 J=1,NUMSCA-1
      SUM=PDF0*Q(J)
      DO 4300 I=1,NETAPT
      SUM=SUM+DETA(I)*OPDF(I)*Q(J+(I-1)*NUMSCA)
4300  CONTINUE
      UCM(J)=SUM+PDF1*Q(J+(NETAPT-1)*NUMSCA)
4200  CONTINUE
C
      HSUM=PDF0*Q(NUMSCA)
      TSUM=PDF0*T(1)
      RSUM=0.
      PDFSUM=PDF0
      DO 4400 I=1,NETAPT
       CALL CKRHOY(PRESSQ,T(I),
     1 Q((I-1)*NUMSCA+1),IWORK,WORK,RHO(I))
       TSUM=TSUM+OPDF(I)*DETA(I)*T(I)
       HSUM=HSUM+OPDF(I)*DETA(I)*Q(NUMSCA*I)
       RSUM=RSUM+OPDF(I)*DETA(I)*RHO(I)
       PDFSUM=PDFSUM+OPDF(I)*DETA(I)
4400  CONTINUE
      PDFSUM=PDFSUM+PDF1
      TSUM=(TSUM+PDF1*T(NETAPT))/PDFSUM
      HSUM=(HSUM+PDF1*Q(NUMSCA*NETAPT))/PDFSUM
      RSUM=(RSUM+PDF1*RHO(NETAPT)+PDF0*RHO(1))/PDFSUM
      CHISUM=(OMFRCV-XMFRCV)*RTRES
C
C     Open file and output unconditional data
      FILENM='isrucm'//CHAR(ICT1+48)//CHAR(ICT2+48)//'.d'
      OPEN(UNIT=LUCDAT,FILE=FILENM,FORM='FORMATTED')
      WRITE(LUCDAT,*)
      WRITE(LUCDAT,*) 'FIREBALL UNCONDITIONALLY AVERAGED DATA OUTPUT'
      WRITE(LUCDAT,*)
      WRITE(LUCDAT,7800) CTITLE
```

```
      WRITE(LUCDAT,2400) CSTATUS
      WRITE(LUCDAT,*)
      WRITE(LUCDAT,*) 'Residence Time (sec) / Operating Pressure (atm):'
      WRITE(LUCDAT,*) TRES, PRESSQ/PATM
      WRITE(LUCDAT,*)
      WRITE(LUCDAT,*) 'Fuel-Oxid. Mass Flow Ratio / Operating Mix Frac'
      WRITE(LUCDAT,*) FOXRAT,XMFRC
      WRITE(LUCDAT,*)
      XMFSQ=XMFRC*(1.-XMFRC)
      WRITE(LUCDAT,*) 'CS Variances: Outlet / Core / Inlet'
      WRITE(LUCDAT,*) XMFRCV,CORMFV,OMFRCV
      WRITE(LUCDAT,*)
      WRITE(LUCDAT,*) 'Unmixedness: Outlet / Core / Inlet'
      WRITE(LUCDAT,*) XMFRCV/XMFSQ,CORMFV/XMFSQ,OMFRCV/XMFSQ
      WRITE(LUCDAT,*)
      WRITE(LUCDAT,*) 'Scalar Dissipation (1/s) / Mixing Freq. (1/s)'
      WRITE(LUCDAT,*) CHISUM,3.*CHISUM/CORMFV
      WRITE(LUCDAT,*)
      WRITE(LUCDAT,*) 'MEAN TEMPERATURE (K):',TSUM
      WRITE(LUCDAT,*) 'MEAN DENSITY (kg/m**3):',RSUM*1.E3
      WRITE(LUCDAT,*) 'MEAN ST. ENTHALPY (J/kg):',HSUM*1.E-4
      WRITE(LUCDAT,*)
      WRITE(LUCDAT,*) 'MEAN SPECIES MASS FRACTIONS:'
      DO 4500 J=1,NUMSCA-1
      WRITE(LUCDAT,*) J,UCM(J)/PDFSUM
4500  CONTINUE
      CLOSE(LUCDAT)
C
C     If a continuation has been requested, then go back to start
      IF(IRMODE.EQ.2) GOTO 3000
C
2400  FORMAT(1X,A24)
7800  FORMAT(A78)
      STOP
      END
C=============================================================
C
C+++++++++++++++++++++++++++++++++++++++++++++++++++++++++++++
      SUBROUTINE RHSFN0(NETAPT,NUMSCA,Q,QU,Q0,BOUNDQ,QCOEF,
     1  YTIME,TSTEP,D2M,D2C,D2P,CHI,QRES,LDIAGN)
C
      IMPLICIT REAL (A-H,O-X,Z), INTEGER (I-N), LOGICAL (Y)
C
      REAL TSTEP
      INTEGER NETAPT,NUMSCA,LDIAGN
      LOGICAL YTIME
      DIMENSION Q(*),QU(*),D2M(*),D2C(*),D2P(*),
     1 CHI(*),QRES(*),BOUNDQ(*),QCOEF(*),Q0(*)
C
C     CALCULATE SOURCE TERMS AT
C     THE BOUNDARIES, IMPOSING A
C     ZERO CURVATURE RULE TO GET
C     A VIRTUAL GRID POINT = -ETA(2)
C
      IBOUND=1
      CRET=1.
1500  CONTINUE
      IADD=(IBOUND/NETAPT)*NUMSCA
      DO 1510 J=1,NUMSCA
      QRES(J+(IBOUND-1)*NUMSCA)=(BOUNDQ(J+IADD)-
     1  Q(J+(IBOUND-1)*NUMSCA))*CRET
1510  CONTINUE
      IF(IBOUND.EQ.1) THEN
      IBOUND=NETAPT
      GOTO 1500
      ENDIF
C
C     CALCULATE SOURCE TERMS
C     AWAY FROM THE BOUNDARIES
C
       DO 1602 I=2,NETAPT-1
       DO 1602 J=1,NUMSCA
       IJ=J+(I-1)*NUMSCA
       QRES(IJ)=0.5*CHI(I)*(D2C(I)
     1 *Q(IJ)+D2M(I)*Q(IJ-NUMSCA)+D2P(I)
     2 *Q(IJ+NUMSCA))-(Q(IJ)-Q0(IJ))*QCOEF(I)
1602  CONTINUE
C
      IF(YTIME) THEN    ! add transient to residual for timesteps
       DO 1603 I=1,NETAPT*NUMSCA
       DQDT=(Q(I)-QU(I))/TSTEP
       QRES(I)=QRES(I)-DQDT
1603   CONTINUE
      ENDIF
C
      RETURN
      END
C=============================================================
C
C+++++++++++++++++++++++++++++++++++++++++++++++++++++++++++++
      SUBROUTINE RHSFN1(NETAPT,NUMSCA,Q,QU,Q0,BOUNDQ,QCOEF,
     1  YTIME,TSTEP,D2M,D2C,D2P,CHI,PRESSQ,WT,
     2  WORK,IWORK,T,TOLTMP,QRES,LDIAGN)
C
      PARAMETER(NSPCMX=60)
C
      IMPLICIT REAL (A-H,O-X,Z), INTEGER(I-N), LOGICAL (Y)
C
      REAL WDOT(NSPCMX)
      REAL TSTEP,PRESSQ,TOLTMP
      INTEGER IWORK(*),NUMSCA,NETAPT,LDIAGN
      LOGICAL YTIME
      COMMON/COMLNE/REFH,IPT   ! for communication with SUBCHM
      SAVE /COMLNE/
      DIMENSION Q(*),QU(*),D2M(*),D2C(*),D2P(*),WT(*),
     1 WORK(*),T(*),QRES(*),CHI(*),QCOEF(*),Q0(*),
     2 BOUNDQ(*)
C
      DO 1595 I=1,NETAPT
      TI=MAX(T(I),300.)
      DELTAT=0.0
      REFH=Q(I*NUMSCA)
      IPT=I
1594  CONTINUE
      TI=TI-DELTAT
      CALL CKHBMS(TI,Q(1+(I-1)*NUMSCA),IWORK,WORK,HBML)
      CALL CKCPBS(TI,Q(1+(I-1)*NUMSCA),IWORK,WORK,CP)
      DELTAT=(HBML-Q(NUMSCA*I))/CP
      IF(ABS(DELTAT).GT.TOLTMP) GOTO 1594
      T(I)=TI
1595  CONTINUE
C
C     CALCULATE SOURCE TERMS
C     AT THE BOUNDARIES
C
      CRET=1.
      IBOUND=1
1597  CONTINUE
      IPT=IBOUND
      IADD=(IBOUND/NETAPT)*NUMSCA
c      CALL CKWYP(PRESSQ,T(IBOUND),
c     1 Q((IBOUND-1)*NUMSCA+1),IWORK,WORK,WDOT)
      DO 1599 J=1,NUMSCA-1
      WDOT(J)=0.
      QRES(J+(IBOUND-1)*NUMSCA)=WDOT(J)*WT(J)-
     1  (BOUNDQ(J+IADD)-Q(J+(IBOUND-1)*NUMSCA))*CRET
1599  CONTINUE
      QRES(IBOUND*NUMSCA)=(BOUNDQ(IADD+NUMSCA)-
     1  Q(IBOUND*NUMSCA))*CRET
      IF(IBOUND.EQ.1) THEN
       IBOUND=NETAPT
       GOTO 1597
      ENDIF
C
C     CALCULATE SOURCE TERMS
C     AWAY FROM THE BOUNDARIES
```

```
731   C
732           DO 1602 I=2,NETAPT-1
733           IPT=I
734           CALL CKWYP(PRESSQ,T(I),
735         1 Q(1+(I-1)*NUMSCA),IWORK,WORK,WDOT)
736           DO 1603 J=1,NUMSCA-1
737           IJ=J+(I-1)*NUMSCA
738           WDOTJ=WDOT(J)*WT(J)
739           QRES(IJ)=WDOTJ+0.5*CHI(I)*(D2C(I)
740         1 *Q(IJ)+D2M(I)*Q(IJ-NUMSCA)+D2P(I)
741         2 *Q(IJ+NUMSCA))-QCOEF(I)*(Q(IJ)-Q0(IJ))
742   1603    CONTINUE
743           QRES(I*NUMSCA)=(D2M(I)*Q((I-1)*NUMSCA)+D2P(I)*Q((I+1)*NUMSCA)
744         1  +D2C(I)*Q(I*NUMSCA))*0.5*CHI(I)-QCOEF(I)*(Q(I*NUMSCA)
745         2  -Q0(I*NUMSCA))
746   1602    CONTINUE
747   C
748           IF(YTIME) THEN  ! add transient to residual for timestepping
749           DO 1604 I=1,NETAPT*NUMSCA
750           DQDT=(Q(I)-QU(I))/TSTEP
751           QRES(I)=QRES(I)-DQDT
752   1604    CONTINUE
753           ENDIF
754   C
755           RETURN
756           END
757   C=============================================================
758   C
759   C+++++++++++++++++++++++++++++++++++++++++++++++++++++++++++++
760         SUBROUTINE RHSFN2(NETAPT,NUMSCA,Q,QU,Q0,BOUNDQ,QCOEF,
761         1  YTIME,TSTEP,D2M,D2C,D2P,CHI,PRESSQ,WT,
762         2  WORK,IWORK,IRAD,IPH2O,IPCO2,T,TOLTMP,QRES,
763         3  LDIAGN)
764   C
765           PARAMETER(NSPCMX=60)
766           PARAMETER(SIGMA=5.6697E-5,B1=2.E-8,B2=6.4E-12,B3=4.6E-8,
767         1 B4=1.3E-11,XEMIS=4.*SIGMA) ! B CONSTANTS ADJUSTED FOR PRESSURE
768   C                                    IN dynes/cm**2, RATHER THAN Pa
769   C
770           IMPLICIT REAL (A-H,O-X,Z), INTEGER(I-N), LOGICAL (Y)
771   C
772           REAL WDOT(NSPCMX),XMOLFR(NSPCMX)
773           REAL TSTEP,PRESSQ,TOLTMP
774           INTEGER IWORK(*),NUMSCA,NETAPT,IRAD,IPH2O,IPCO2,LDIAGN
775           LOGICAL YTIME
776           COMMON/COMLNE/REFH,IPT    ! for communication with SUBCHM
777           SAVE /COMLNE/
778           DIMENSION Q(*),QU(*),D2M(*),D2C(*),D2P(*),WT(*),
779         1 WORK(*),T(*),QRES(*),CHI(*),QCOEF(*),Q0(*),
780         2 BOUNDQ(*)
781   C
782   C     CALCULATE TEMPERATURES CORRESPONDING TO STANDARDIZED
783   C     ENTHALPY AND SPECIES MASS FRACTIONS
784   C
785           DO 1595 I=1,NETAPT
786           TI=T(I)
787           DELTAT=0.0
788           IPT=I
789           REFH=Q(I*NUMSCA)
790   1596    CONTINUE
791           TI=TI-DELTAT
792           CALL CKHBMS(TI,Q(1+(I-1)*NUMSCA),IWORK,WORK,HBML)
793           CALL CKCPBS(TI,Q(1+(I-1)*NUMSCA),IWORK,WORK,CP)
794           DELTAT=(HBML-Q(NUMSCA+(I-1)*NUMSCA))/CP
795           IF(ABS(DELTAT).GT.TOLTMP) GOTO 1596
796           T(I)=TI
797   1595    CONTINUE
798   C
799   C     CALCULATE SOURCE TERMS
800   C     AT THE BOUNDARIES
801   C
802           CRET=1.
803           IBOUND=1
804   1597    CONTINUE
805           IPT=I
806           IADD=(IBOUND/NETAPT)*NUMSCA
807           CALL CKWYP(PRESSQ,T(IBOUND),
808         1 Q((IBOUND-1)*NUMSCA+1),IWORK,WORK,WDOT)
809           DO 1599 J=1,NUMSCA-1
810           QRES(J+(IBOUND-1)*NUMSCA)=WDOT(J)*WT(J)-
811         1  (BOUNDQ(IADD+J)-Q((IBOUND-1)*NUMSCA+J))*CRET
812   1599    CONTINUE
813   C
814   C       CALCULATE EMISSIVITY AND THEN RADIATION LOSS
815           CALL CKYTX(Q(1+(IBOUND-1)*NUMSCA),IWORK,WORK,XMOLFR)
816           EM=XMOLFR(IPH2O)*(B1-B2*T(IBOUND))*PRESSQ
817         1 +(IRAD-1)*XMOLFR(IPCO2)*(B3-B4*T(IBOUND))*PRESSQ
818           THNRAD=XEMIS*EM*(T(IBOUND)**4-T(1)**4)
819   C
820           QRES(NUMSCA+(IBOUND-1)*NUMSCA)=-1.*THNRAD-
821         1  (BOUNDQ(IADD+NUMSCA)-Q(IBOUND*NUMSCA))*CRET
822           IF(IBOUND.EQ.1) THEN
823            IBOUND=NETAPT
824            GOTO 1597
825           ENDIF
826   C
827   C     CALCULATE SOURCE TERMS
828   C     AWAY FROM THE BOUNDARIES
829   C
830           DO 1602 I=2,NETAPT-1
831           IPT=I
832           CALL CKWYP(PRESSQ,T(I),
833         1 Q(1+(I-1)*NUMSCA),IWORK,WORK,WDOT)
834           DO 1602 J=1,NUMSCA-1
835           IJ=J+(I-1)*NUMSCA
836           WDOTJ=WDOT(J)*WT(J)
837           QRES(IJ)=WDOTJ+0.5*CHI(I)*(D2C(I)
838         1 *Q(IJ)+D2M(I)*Q(IJ-NUMSCA)+D2P(I)
839         2 *Q(IJ+NUMSCA))-QCOEF(I)*(Q(IJ)-Q0(IJ))
840   1602    CONTINUE
841   C
842           DO 1600 I=2,NETAPT-1        ! 2 LOOPS AIDS VECTORIZATION
843   C       CALCULATE EMISSIVITY AND THEN RADIATION LOSS
844           CALL CKYTX(Q(1+(I-1)*NUMSCA),IWORK,WORK,XMOLFR)
845           EM=XMOLFR(IPH2O)*(B1-B2*T(I))*PRESSQ
846         1 +(IRAD-1)*XMOLFR(IPCO2)*(B3-B4*T(I))*PRESSQ
847           THNRAD=XEMIS*EM*(T(I)**4-T(1)**4)
848   C
849           QRES(NUMSCA+(I-1)*NUMSCA)=(D2C(I)*Q(I*NUMSCA)+
850         1 D2M(I)*Q((I-2)*NUMSCA+NUMSCA)+D2P(I)
851         2 *Q(I*NUMSCA+NUMSCA))*0.5*CHI(I)-THNRAD
852         3 -QCOEF(I)*(Q(I*NUMSCA)-Q0(I*NUMSCA))
853   1600    CONTINUE
854   C
855           IF(YTIME) THEN  ! add transient to residual for timestepping
856           DO 1605 I=1,NUMSCA*NETAPT
857           DQDT=(Q(I)-QU(I))/TSTEP
858           QRES(I)=QRES(I)-DQDT
859   1605    CONTINUE
860           ENDIF
861   C
862           RETURN
863           END
864
865   C+++++++++++++++++++++++++++++++++++++++++++++++++++++++++++++++++++++++++++++++++++++++++++++++++++++++++++++++++++++++++++++++C
866   C
867   C=====================================================================C
868   C
869           SUBROUTINE RHSJAC(NUMSCA,NETAPT,NBANDS,YTIME,YGNITE,IRAD,ABPERT,
870         1  RLPERT,TSTEP,T,TOLTMP,PRESSQ,WT,IPH2O,IPCO2,
871         2  D2M,D2C,D2P,CHI,IWORK,WORK,Q,QU,Q0,QRES,QRESPT,BOUNDQ,QCOEF,
872         3  QJAC,LDIAGN)
873   C
874   C       This subroutine forms the block tridiagonal Jacobian matrix (see note)
875   C       for the system of equations by taking a finite difference
876   C       approximation of the RHS residuals QRES over perturbations
```

```
C       in the solution vector Q of the order of the machine roundoff.
C
C       The BTD form of the Jacobian arises from the fact that the
C       residual at a given mixture fraction point and species is
C       only a function of the species at the mixture fraction
C       point in question and those adjacent to it, rather than
C       being a function of all species at all points.
C
C       Since forming a Jacobian matrix is computationally
C       expensive, it is important that this subroutine be efficiently
C       designed.  An important timesaver is the fact that Jacobian
C       columns which have no common non-zero rows can be computed from
C       a single perturbation of the solution vector for a given
C       species over all mixture fraction points.  The criteria for
C       this uncommonality is that the columns be separated by at least
C       2 mixture fraction points (ie: 2*NUMSCA columns).
C
C       Rather than conditionally select RHS functions within
C       the Jacobian loops, the same loop structure is repeated for
C       each of the three types of RHS function.  The subroutine
C       selects which loop structure to call before commencing.
C
C       NOTE:  Although this subroutine calculates a BTD Jacobian,
C       the output of this matrix is in 'BAND STORAGE' form to
C       economize on required memory space and to conform with
C       LINPACK decomposition and solution routine requirements.
C       Band Storage involves storing the non-zero column portions
C       of the BTD matrix in the bottom of the columns of the BSM,
C       where the diagonal submatrices lie NUMSCA from the bottom.
C
        IMPLICIT REAL (A-H,O-X,Z), INTEGER (I-N), LOGICAL (Y)
        PARAMETER(NETAMX=96,ITRIDG=3,NTHIRD=NETAMX/ITRIDG+1)
        REAL SAVEQ(NTHIRD),PERTBN(NTHIRD)
C
        REAL ABPERT,RLPERT,TSTEP,T(*),PRESSQ,WT(*),WORK(*),
     1  Q(*),QU(*),Q0(*),QRES(*),QRESPT(*),QJAC(*),QCOEF(*),
     2  D2M(*),D2C(*),D2P(*),CHI(*),TOLTMP,
     3  BOUNDQ(*)
        INTEGER NUMSCA,NETAPT,IPH2O,IPCO2,IWORK(*),IRAD,LDIAGN,
     1  NBANDS
        LOGICAL YTIME,YGNITE
C
C       Set BTD to BSM conversion column offset
        IBTBFF=4*NUMSCA-1
C
C       Zero Jacobian storage space
        CALL ZARRAY(NBANDS*NUMSCA*NETAPT,QJAC)
C
C       Select which RHS function is to be called and call the appropriate
C       Jacobian Loop
        IF (.NOT. YGNITE) THEN
C
C*********************QJAC for unreactive mixing**********************C
C       Evaluate Unperturbed Residual
         CALL RHSFN0(NETAPT,NUMSCA,Q,QU,Q0,BOUNDQ,QCOEF,
     1   YTIME,TSTEP,D2M,D2C,D2P,CHI,QRES,LDIAGN)
C
C        Individually perturb solution Q at the three sets of separated mixture
C        fraction points for each reactive scalar, then evaluate the residual
C        and fill the columns of the Jacobian corresponding to each sepcies
C        in the selected separated set.
C
         DO 100 INDEP=1,ITRIDG  ! loops over the separated MF sets
          DO 100 J=1,NUMSCA  ! loops over species in each set
C
           IDX=0
           DO 101 I=INDEP,NETAPT,ITRIDG
            IJN=J+(I-1)*NUMSCA
            IDX=IDX+1
            SAVEQ(IDX)=Q(IJN)
            PERTBN(IDX)=ABS(Q(IJN))*RLPERT+ABPERT
            Q(IJN)=Q(IJN)+PERTBN(IDX)
101        CONTINUE
C
C          Evaluate the residual corresponding to the perturbation of
C          species J at all mixture fraction points in a
C          separated set.
           CALL RHSFN0(NETAPT,NUMSCA,Q,QU,Q0,BOUNDQ,QCOEF,
     1      YTIME,TSTEP,D2M,D2C,D2P,CHI,QRESPT,LDIAGN)
C
C          Restore the solution Q to its unperturbed state
           IDX=0
           DO 102 I=INDEP,NETAPT,ITRIDG
            IDX=IDX+1
            Q(J+(I-1)*NUMSCA)=SAVEQ(IDX)
102        CONTINUE
C
C          Fill the Jacobian columns corresponding to the particular
C          separated set INDEP and perturbed species J
C
           IDX=0
           DO 103 I=INDEP,NETAPT,ITRIDG
            IDX=IDX+1
            ICOLUM=(I-1)*NUMSCA+J    ! Calculate Jacobian column index
            ICOLNQ=(ICOLUM-1)*NBANDS  ! Convert to 1-D array index
            ITOP=MAX(I-1,1)
            IBOT=MIN(I+1,NETAPT)
            IRFFST=IBTBFF-ICOLUM  ! Add BTD to BSM offset
            DO 104 II=ITOP,IBOT
             IIN1=(II-1)*NUMSCA
             DO 105 JJ=1,NUMSCA
              IIJJ=JJ+IIN1
              QJAC(IRFFST+IIJJ+ICOLNQ)=(QRESPT(IIJJ)-QRES(IIJJ))
     1         /PERTBN(IDX)
105          CONTINUE
104         CONTINUE
103        CONTINUE
100       CONTINUE
C*********************QJAC for unreactive mixing**********************C
C
         ELSE
          IF(IRAD.EQ.0) THEN
C
C**************QJAC for reactive adiabatic mixing*********************C
C       Evaluate Unperturbed Residual
          CALL RHSFN1(NETAPT,NUMSCA,Q,QU,Q0,BOUNDQ,QCOEF,
     1    YTIME,TSTEP,D2M,D2C,D2P,CHI,PRESSQ,WT,
     2    WORK,IWORK,T,TOLTMP,QRES,LDIAGN)
C
C        Individually perturb solution Q at the three sets of separated mixture
C        fraction points for each reactive scalar, then evaluate the residual
C        and fill the columns of the Jacobian corresponding to each sepcies
C        in the selected separated set.
C
         DO 110 INDEP=1,ITRIDG  ! loops over the separated MF sets
          DO 110 J=1,NUMSCA  ! loops over species in each set
C
           IDX=0
           DO 111 I=INDEP,NETAPT,ITRIDG
            IJN=J+(I-1)*NUMSCA
            IDX=IDX+1
            SAVEQ(IDX)=Q(IJN)
            PERTBN(IDX)=ABS(Q(IJN))*RLPERT+ABPERT
            Q(IJN)=Q(IJN)+PERTBN(IDX)
111        CONTINUE
C
C          Evaluate the residual corresponding to the perturbation of
C          species J at all mixture fraction points in a
C          separated set.
           CALL RHSFN1(NETAPT,NUMSCA,Q,QU,Q0,BOUNDQ,QCOEF,
     1    YTIME,TSTEP,D2M,D2C,D2P,CHI,PRESSQ,WT,
     2    WORK,IWORK,T,TOLTMP,QRESPT,LDIAGN)
C
C          Restore the solution Q to its unperturbed state
           IDX=0
           DO 112 I=INDEP,NETAPT,ITRIDG
```

```
1023              IDX=IDX+1
1024              Q(J+(I-1)*NUMSCA)=SAVEQ(IDX)
1025  113       CONTINUE
1026  C
1027  C         Fill the Jacobian columns corresponding to the particular
1028  C         separated set INDEP and perturbed species J
1029  C
1030              IDX=0
1031              DO 113 I=INDEP,NETAPT,ITRIDG
1032               IDX=IDX+1
1033               ICOLUM=(I-1)*NUMSCA+J    ! Calculate Jacobian column index
1034               ICOLNQ=(ICOLUM-1)*NBANDS     ! Translate to 1-D array position
1035               ITOP=MAX(I-1,1)
1036               IBOT=MIN(I+1,NETAPT)
1037               IRFFST=IBTBFF-ICOLUM   ! Add BTD to BSM offset
1038               DO 114 II=ITOP,IBOT
1039                IIN1=(II-1)*NUMSCA
1040                DO 115 JJ=1,NUMSCA
1041                 IIJJ=JJ+IIN1
1042                 QJAC(IRFFST+IIJJ+ICOLNQ)=(QRESPT(IIJJ)-QRES(IIJJ))
1043       1          /PERTBN(IDX)
1044  115           CONTINUE
1045  114          CONTINUE
1046  113         CONTINUE
1047  110       CONTINUE
1048  C**************QJAC for reactive adiabatic mixing*******************C
1049  C
1050          ELSE
1051  C
1052  C**************QJAC for reactive non-adiabatic mixing****************C
1053  C       Evaluate Unperturbed Residual
1054            CALL RHSFN2(NETAPT,NUMSCA,Q,QU,Q0,BOUNDQ,QCOEF,
1055       1     YTIME,TSTEP,D2M,D2C,D2P,CHI,PRESSQ,WT,
1056       2     WORK,IWORK,IRAD,IPH2O,IPCO2,T,TOLTMP,QRES,LDIAGN)
1057  C
1058  C         Individually perturb solution Q at the three sets of separated mixture
1059  C         fraction points for each reactive scalar, then evaluate the residual
1060  C         and fill the columns of the Jacobian corresponding to each sepcies
1061  C         in the selected separated set.
1062  C
1063            DO 120 INDEP=1,ITRIDG  ! loops over the separated MF sets
1064             DO 120 J=1,NUMSCA  ! loops over species in each set
1065  C
1066              IDX=0
1067              DO 121 I=INDEP,NETAPT,ITRIDG
1068               IJN=J+(I-1)*NUMSCA
1069               IDX=IDX+1
1070               SAVEQ(IDX)=Q(IJN)
1071               PERTBN(IDX)=ABS(Q(IJN))*RLPERT+ABPERT
1072               Q(IJN)=Q(IJN)+PERTBN(IDX)
1073  121          CONTINUE
1074  C
1075  C           Evaluate the residual corresponding to the perturbation of
1076  C           species J at all mixture fraction points in a
1077  C           separated set.
1078              CALL RHSFN2(NETAPT,NUMSCA,Q,QU,Q0,BOUNDQ,QCOEF,
1079       1     YTIME,TSTEP,D2M,D2C,D2P,CHI,PRESSQ,WT,
1080       2     WORK,IWORK,IRAD,IPH2O,IPCO2,T,TOLTMP,QRESPT,LDIAGN)
1081  C
1082  C           Restore the solution Q to its unperturbed state
1083              IDX=0
1084              DO 122 I=INDEP,NETAPT,ITRIDG
1085               IDX=IDX+1
1086               Q(J+(I-1)*NUMSCA)=SAVEQ(IDX)
1087  122          CONTINUE
1088  C
1089  C           Fill the Jacobian columns corresponding to the particular
1090  C           separated set INDEP and perturbed species J
1091  C
1092              IDX=0
1093              DO 123 I=INDEP,NETAPT,ITRIDG
1094               IDX=IDX+1
1095               ICOLUM=(I-1)*NUMSCA+J    ! Calculate Jacobian column index
```

```
1096              ICOLNQ=(ICOLUM-1)*NBANDS     ! Translate to 1-D array position
1097              ITOP=MAX(I-1,1)
1098              IBOT=MIN(I+1,NETAPT)
1099              DO 124 II=ITOP,IBOT
1100               IRFFST=IBTBFF-ICOLUM   ! Add BTD to BSM offset
1101               IIN1=(II-1)*NUMSCA
1102               DO 125 JJ=1,NUMSCA
1103                IIJJ=JJ+IIN1
1104                QJAC(IRFFST+IIJJ+ICOLNQ)=(QRESPT(IIJJ)-QRES(IIJJ))
1105       1          /PERTBN(IDX)
1106  125           CONTINUE
1107  124          CONTINUE
1108  123         CONTINUE
1109  120       CONTINUE
1110  C**************QJAC for reactive non-adiabatic mixing****************C
1111  C
1112            ENDIF
1113           ENDIF
1114          RETURN
1115          END
1116  C+++++++++++++++++++++++++++++++++++++++++++++++++++++++++++++++++++++C
1117  C
1118  C=====================================================================C
1119  C
1120         SUBROUTINE CHIISR(NETAPT,ETA,XMFRC,CORMRF,XMFRCV,CORMFV,
1121       1 OMFRCV,CHI,RHO,QCOEF,RTRES,OPDF,OPDF0,OPDF1,EPDF,
1122       2 TOLTMP,PRESSQ,Q,T,WORK,IWORK,NUMSCA,IMODE,INIT,LSCOUT,LDIAGN)
1123  C
1124         IMPLICIT REAL (A-H,O-X,Z), INTEGER (I-N), LOGICAL (Y)
1125         PARAMETER(NETAMX=96,VSML=1.E-20,IUNITY=1,IZERO=0)
1126         REAL ETA(*),CHI(*),Q(*),T(*),QCOEF(*),
1127       1 OPDF(*),EPDF(*),RHO(*),WORK(*),PRESSQ,RTRES,
1128       2 SCR1(NETAMX),SCR2(NETAMX)
1129         INTEGER NETAPT,LSCOUT,LDIAGN,NUMSCA,IWORK(*)
1130         COMMON /SAVCOR2/ PDF(NETAMX),BCHI(NETAMX),PDF0,PDF1
1131         COMMON/COMLNE/REFH,IPT    ! for communication with SUBCHM
1132         SAVE /SAVCOR2/,/COMLNE/
1133  C
1134         IF(INIT.EQ.0) THEN
1135  C       Initialize Gaudi, inputs are immaterial at this stage
1136          CVAL=0.
1137          CALL GAUDI(XMFRC,OMFRCV,XMFRC,OMFRCV,NETAPT,ETA,EPDF,
1138       1    EPDF0,EPDF1,BCHI,SCR1,SCR2,CVAL,INIT,LDIAGN)
1139         ENDIF
1140  C
1141         IF(IMODE.EQ.0) THEN
1142          INIT=1
1143          CVAL=0.
1144  C       Call Gaudi to get Core averaged Pdf, other outputs are
1145  C       not wanted and will be overwritten in the following call.
1146          CALL GAUDI(CORMRF,CORMFV,XMFRC,OMFRCV,NETAPT,ETA,PDF,
1147       1  PDF0,PDF1,BCHI,SCR1,SCR2,CVAL,INIT,LDIAGN)
1148  C       Call Gaudi to get inlet averaged Pdf.
1149          CALL GAUDI(XMFRC,OMFRCV,XMFRC,OMFRCV,NETAPT,ETA,EPDF,
1150       1    EPDF0,EPDF1,BCHI,SCR1,SCR2,CVAL,INIT,LDIAGN)
1151  C       Call Gaudi to get outlet Pdf and CHI (needs to be divided
1152  C       by core PDF and residence time and multiplied by RHOM)
1153          CVAL=OMFRCV-XMFRCV
1154          CALL GAUDI(XMFRC,XMFRCV,XMFRC,OMFRCV,NETAPT,ETA,OPDF,
1155       1  OPDF0,OPDF1,BCHI,SCR1,SCR2,CVAL,INIT,LDIAGN)
1156         ENDIF
1157  C
1158  C      Determine temperature and density
1159         DO 2950 I=1,NETAPT
1160          TI=MAX(300.,T(I))
1161          DELTAT=0.E0
1162          IPT=I
1163          REFH=Q(I*NUMSCA)
1164  1740    CONTINUE
1165          TI=TI-DELTAT
1166          CALL CKHBMS(TI,Q(1+(I-1)*NUMSCA),IWORK,WORK,HBML)
1167          CALL CKCPBS(TI,Q(1+(I-1)*NUMSCA),IWORK,WORK,CP)
1168          DELTAT=(HBML-Q(I*NUMSCA))/CP
```

```
1169          IF(ABS(DELTAT).GT.TOLTMP) GOTO 1740
1170          T(I)=TI
1171          CALL CKRHOY(PRESSQ,TI,
1172         1  Q((I-1)*NUMSCA+1),IWORK,WORK,RHO(I))
1173   2950   CONTINUE
1174   C
1175   C      Get unconditional mean density and normalize CHI*PDF product
1176   C      by PDF
1177          PDFACC=PDF0
1178          RHOM=RHO(1)*PDF0
1179          DO 1250 I=2,NETAPT
1180           DETA=0.5*(ETA(I)-ETA(I-1))
1181           PDFI=MAX(PDF(I),VSML)
1182           RHOM=RHOM+(RHO(I)*PDF(I)+RHO(I-1)*PDF(I-1))*DETA
1183           CHI(I)=BCHI(I)/PDFI
1184           PDFACC=PDFACC+(PDF(I)+PDF(I-1))*DETA
1185   1250   CONTINUE
1186          PDFACC=PDFACC+PDF1
1187          RHOM=RHOM+RHO(NETAPT)*PDF1
1188          RHOM=RHOM/PDFACC
1189   C
1190   C      Get CHI and inlet-outlet difference coefficient for CMC eqn use.
1191          DO 1300 I=1,NETAPT
1192           CHI(I)=-2.*CHI(I)*RHOM*RTRES
1193           PDFI=MAX(PDF(I),VSML)
1194           QCOEF(I)=EPDF(I)/PDFI*RTRES*RHOM
1195   1300   CONTINUE
1196   C
1197          RETURN
1198          END
```

```
C                    VERSION 3_3 ============================C
C
C*****************************************************************C
      SUBROUTINE QKIN1(STX,ENDX,XMFRC,XMFRCV,YPOSN,VEL,VELY,
     1 CHI,RHO,PRESS,NPTMX,NPTS,IMODE,UCTEMP,UCENTH,DRHODF,
     2 SPEC1,SPEC2,SPEC3,SPEC4,SPEC5,SPEC6,SPEC7,
     3 NRMX,RSPACE,NIMX,ISPACE,NCMX,CSPACE)
C
C  This subroutine package that includes QKIN, CHEMIN, AVERUX, UCHIGAU,
C  RESUME, and RHSFN0,1,2 etc. (collectively referred to as QKIN)
C  solves a parabolic set of partial differential equations in
C  mixture fraction space to find species mass fractions resulting
C  from turbulent mixing and chemical reaction.  The local species
C  mass fractions are approximated by a conditional mean value
C  (conditional on mixture fraction) and the method is therefore
C  appropriate for flames where the deviations in species mass fractions
C  at a given value of mixture fraction are small.  Thus this method
C  is inappropriate for flames near extinction, and it is suggested
C  that a doubly conditional mean be employed rather than the singly
C  conditional mean of this method.
C
C  In VERSION 2, optically thin radiation losses were included in
C  calculations to allow for variation in standardized enthalpy.
C  The interpolation approximation for conditional mean scalar
C  dissipation and conditional mean velocity (as proposed by Bilger 1991,
C  and implemented in the subroutine INTERUX) was upgraded to a
C  cross-stream mixture fraction PDF weighted approach (proposed
C  by Klimenko 1991, and implemented in the subroutine AVERUX).
C
C  In VERSION 2_1, first attempts at modelling differential diffusion (DD)
C  effects have been made by introducing the DD specific right hand side
C  functions RHSFN3, RHSFN4 and RHSFN5 for non-reactive, reactive-adiabatic
C  and reactive non-adiabatic flows respectively.  Further, the subroutine
C  REJIG is required to correct DD-induced drift of the grid points in
C  mixture fraction space.
C
C  In VERSION 2_4, a rigorous means for determining conditional mean
C  scalar dissipation has been introduced as an option via the
C  subroutine UCHIGAU.  This subroutine calculates c.m.s.d. by
C  double integrating the convective change in the mixture
C  fraction PDF across mixture fraction space.
C
C  In VERSION 3_0, the common block philosophy has been abandoned in
C  favour of a workspace arrangement.  Differential diffusion sections have
C  also been eliminated.  The banded nature of the Jacobian matrix has
C  been exploited.  In output structure, QTER and QOUT have been
C  combined, with the RCQ and RUQ outputs that were in QTER being added to
C  the ETA and ENTHALPY columns in QOUT.  Some rationalization of variable
C  names has occured.
C
C  In VERSION 3_1, unconditional mean data is produced for the calling code
C  and as an additional output.  This is necessary since the calling code
C  typically doesn't take the same care with PDF convolution as is taken
C  here.  The subroutine Q2UCV handles the convolution in QKIN3_1 using
C  PDF information from UCHIGAU.
C
C  In VERSION 3_2, CHI calculation via UCHIGAU is perfected leading to
C  slightly different handling (from 3_1) of statistically indeterminate
C  mixture fraction zones.
C
C  In VERSION 3_3, CHI is redefined as CHI = D grad(f)**2, and RCQ and RUQ
C  are redefined as conditional mean CHI and velocity without density.
C  Appropriate modifications are made to relevant subroutines.
C
C  by Nigel S.A. Smith,  Version 1.0 (4/1991) - Version 3.3 (8/1994)
C
C-----------------------------------------------------------------C
C  QKIN inputs are described below:
C
C  STX  Start point of streamwise step in length units measured from
C       the initial point of the streamwise march
C       (Real scalar, Units: metres)
C
C  ENDX  End point of the streamwise step in length units measured
C        from the initial point of the streamwise march
C        (Real scalar, Units: metres)
C
C  XMFRC  An array containing values of mixture fraction at the grid points
C         defined in the turbulent field by the calling program
C         (Real array, Units: Dimensionless)
C
C  XMFRCV An array containing values of mixture fraction variance at the grid
C         points defined in the turbulent field by the calling program
C         (Real array, Units: Dimensionless)
C
C  YPOSN  An array containing values of crossflow position of for each grid
C         point defined in the turbulent field by the calling program as
C         measured from the mean-flow centreline.
C         (Real array, Units: metres)
C
C  VEL    An array containing values of streamwise velocity at the same grid
C         points as those defined for XMFRC
C         (Real array, Units: metres per second)
C
C  VELY   An array containing values of cross-stream velocity at the same grid
C         points as those defined for XMFRC
C         (Real array, Units: metres per second)
C
C  CHI    An array containing values of mean scalar dissipation at the same
C         grid points as those defined for VEL and XMFRC
C         (Real array, Units: per second)
C
C  RHO    An array containing values of mean density at the same grid points
C         as those defined for VEL and XMFRC
C         (Real array, Units: kilograms per cubic metre)
C
C  PRESS  A scalar representing the local pressure assumed uniform across
C         mixture fraction space
C         (Real scalar, Units: atmospheres *** NOTE NON-SI UNIT)
C
C  NPTMX   An integer representing the maximum number of entries in XMFRC
C          VEL, and RHO etc.
C
C  NPTS    An integer representing the actual number of occupied entries in each
C          of the above mentioned arrays.
C
C  IMODE  An integer that controls the function of QKIN.  Input values of IMODE
C         are interpreted as follows:
C
C        IMODE=0      Initialization of mixture fraction space
C                     based on initial data read in from a file
C                     named QCHEM.D
C
C        IMODE=1      Restart of the program from a designated
C                     restart file.  The name of the restart
C                     file is QREST.D
C
C        IMODE=2      Solution of partial differential equations
C                     in mixture fraction space and subsequent
C                     ancilliary calculations
C
C        IMODE=3      Output of calculated mass fraction
C                     profiles after streamwise march has been
C                     voluntarily halted.  On output, IMODE=3
C                     signals the calling program to halt
C
C        IMODE=4      Output new unconditional mean data based
C                     on old conditional mean data after a change
C                     in PDF parameters has been made by the calling
C                     code.  Do not recalculate conditional mean data.
C
C-----------------------------------------------------------------C
C  QKIN outputs are described below:
C
C  RHO    An array containing values of unconditional mean density at
C         the same grid points as those upon input.  Calculated from
```

```
C          convolution with conditional mean data from CMC equations.
C          (Real array, Units: kilograms per cubic metre)
C
C  UCTEMP  Unconditional mean temperature determined from results of
C          conditional moment closure equations for current step, by
C          convolution with assumed form mixture fraction pdfs.
C          (Real array, Units: Kelvins)
C
C  UCENTH  Unconditional mean standardized enthalpy determined from
C          results of conditional moment closure equations for current
C          step, by convolution with assumed form mixture fraction pdfs.
C          (Real array, Units: Joules per kilogram)
C
C  DRHODF  Unconditional mean of conditional mean density-reciprocal derivative
C          with respect to mixture fraction multiplied by mean density.
C          Specialist output required by JFLAME calling code for mean
C          scalar dissipation evolution equation.
C          (Real array, Units: dimensionless)
C
C  SPEC1-7 Arrays each containing a given unconditional mean species mass
C          fraction at the radial points defined upon input.
C          (Units: Dimensionless)
C
C-----------------------------------------------------------------------C
C
C  QKIN Workspaces (RSPACE,ISPACE, and CSPACE) must be provided by the
C  calling code as real, integer and character*16 arrays of minimum
C  lengths I_END, J_END, K_END (defined below).  These workspaces must not
C  be modified or overwritten in any way between calls to QKIN.
C  Description of Internally Defined Workspace structure:
C
C  NRMX, NIMX, and NCMX are the calling code limits on RSPACE, ISPACE and
C  CSPACE respectively. These are checked at run time to ensure that they
C  are not less than I_END, J_END and K_END.
C
C  Parameter Constants: (in order of definition)
C
C  NETAMX  Maximum number of grid points in mixture fraction space
C
C  NELMX   Maximum number of chemical elements.
C
C  NSPCMX  Maximum number of chemical species.
C
C  NSCAMX  Maximum number of reactive scalars.
C
C  NMAXQ   Maximum size of conditional mean species mass fraction and enthalpy
C          sub-workspace beginning at RSPACE address I_Q
C
C  LENIWK  Required CHEMKIN II Integer Work Space Array Length
C
C  LENWK   Required CHEMKIN II Real Work Space Array Length
C
C  LENCWK  Required CHEMKIN II Character Work Space Array Length
C
C  NOUTMX  Maximum number of output files.
C
C  NSPOUT  Number of unconditional mean species output channels (7).
C
C  NEXMX   Maximum number of grid points in unconditional mean data I/O.
C
C  LIMRSC  Required floating point scratchspace size
C
C  LIMISC  Required integer scratchspace size
C
C  GASCON  Universal Gas Constant adjusted to account for CGS units
C          employed in CHEMKIN II
C
C  MFCON   Integer type flag (constant) required by SVODE.  Value depends
C          upon whether QKIN is compiled for Full or Banded Jacobian
C          solving.
C
C  LIMIWK  Array length for integer work space required by SVODE.  Varies
C          at compilation-time according to whether Full or Banded
C          Jacobian solution is required.
C
C  LIMRWK  Array length for real work space required by SVODE.   Varies
C          at compilation-time according to whether Full or Banded
C          Jacobian solution is required.
C
C-----------------------------------------------------------------------
C  I/O Unit number constants:
C
C  LCHDAT  The integer that defines the Fortran Unit Number for the Chemistry
C          Input file to QKIN.  By default, LCHDAT=41
C
C  LDIAGN  The integer that defines the Fortran Unit Number for the Diagnostic
C          output file from QKIN.  By default, LDIAGN=39
C
C  LINK    The integer that defines the Fortran Unit Number for the CHEMKIN II
C          Linking File that is output from INTERP and input by QKIN.
C          By default, LINK=65.
C
C  LMWT    The integer that defined the Fortran Unit Number for the output
C          of species molecular weights to a file MWTFIL.D for subsequent
C          post-processor use.  By default, LMWT=43.
C
C  LQOUT   The integer that defines the Fortran Unit Number for the Species
C          Mass Fraction output file from QKIN.  By default, LQOUT=40
C
C  LREST   The integer that defines the Fortran Unit Number for the Restart
C          File input to QKIN.   By default, LREST=42
C
C  LSCOUT  The integer that defines the Fortran Unit Number for the log output
C          from QKIN.  By default, LSCOUT=35
C
C-----------------------------------------------------------------------
C
C  Contents of ISPACE (Integer Workspace) Partitions are as follows:
C  (All starting addresses conform to J_* where '*' describes the type
C   of variable beginning at that address)
C
C  J_NETA  The number of mixture fraction grid points being used for
C          calculations at the current step.
C
C  J_NMSCA  This integer describes the number of scalars under consideration
C           and is equal to the number of species plus one.  The additional
C           scalar being standardized enthalpy.
C
C  J_COUNT  An integer variable used to count the number of times that
C           output files have been produced by QKIN.  ISPACE(J_COUNT) serves
C           to avoid overwriting existing output files by incrementing
C           output file names
C
C  J_FINDEX An integer variable which describes the output index of the last
C           output file. eg: qout07.d -----> 7
C
C  J_IGN   An integer variable that controls whether or not the mixture
C          is allowed to chemically react or not.  If ISPACE(J_IGN)=0 then
C          chemical source terms are not included in the species PDFs.
C          If ISPACE(J_IGN)=1, chemical reaction is taken into consideration.
C          A value of -1 means that a fast chemistry solution will be
C          applied (this results by avoiding CMC calculation and carrying
C          an adiabatic equilibrium profile downstream untouched).
C
C  J_RAD  An integer variable that controls whether or not radiation
C         emission is included in the CMC calculation. If ISPACE(J_RAD)=0
C         then no radiation losses are included, =1 then H2O emission is
C         considered, =2 then CO2 and H2O emission is considered.
C
C  J_CHI  An integer variable that controls which method for determining
C         conditional mean scalar dissipation is employed.  ISPACE(J_CHI)=0
C         causes the PDF weighted averaging technique to be used, else
C         if ISPACE(J_CHI)=1 then the mixture fraction double integration
C         technique is used.
C
C  J_DELAY  An integer variable which controls whether or not CMC calculations
```

```
C           will be attempted on the current step.  For ISPACE(J_DELAY)=0,
C           calculations will go ahead, else for ISPACE(J_DELAY)=-1 or 1
C           then no calculations will be made.  A value of 1 indicates that
C           excessive scalar dissipation levels have been encountered,
C           -1 indicates that negative values have been encountered.
C
C  J_STOIC  An integer which records the location of the stoichiometric
C           mixture fraction in the mixture fraction grid array.
C
C  J_NMOUT  This integer describes the number of species mass fraction output
C           stations.  This integer is set in CHEMIN by the user input file
C           and must be less than or equal to NOUTMX, the corresponding array
C           limit.
C
C  J_CO2    An integer describing the position of the species CO2 in the
C           species input string of the chemistry input file QCHEM.D and
C           the CHEMKIN II interpreter input file.
C
C  J_H2O    An integer describing the position of the species H2O in the
C           species input string of the chemistry input file QCHEM.D and
C           the CHEMKIN II interpreter input file.
C
C  J_SPC    An array of integers that identify the species mass
C           fractions that are to be output via the arrays
C           SPEC1 thru SPEC7.  (array length NSPOUT)
C     ** for example:  if ISPACE(J_SPC)=8
C     and the CHEMKIN II Interpreter input file has the following line:
C     SPECIES H2 O2 N2 H2O H O OH HO2 H2O2 N NO NO2 END
C     then QKIN will output the eigth species profile (ie: HO2) via
C     the array SPEC1.
C     If ISPACE(J_SPC+3)=5 with the same species number designation,
C     then QKIN will output the fifth species profile (ie: H) via
C     the array SPEC4.
C
C  J_CK     The starting address for CHEMKIN II related information
C
C  J_NMEL   An integer describing the number of chemical elements being used.
C
C  J_NMSPC  An integer describing the number of chemical species being used.
C
C  J_NMRC   An integer describing the number of chemical reactions being used.
C
C  J_NCF    An array of integers describing the number of atoms of each element
C           in each species.  (array length NELMX*NSPCMX)
C
C  J_CKWK    The starting address for the CHEMKIN II integer workspace
C           which is a subspace of ISPACE. (length LENIWK)
C
C  J_SV     The starting address for SVODE related information
C
C  J_STATE  The condition flag for SVODE at input and output.  See
C           SVODE documentation under 'ISTATE' for details.
C
C  J_TASK   Tasking flag for SVODE.  See SVODE documentation under ITASK
C           for details.
C
C  J_OPT    Optional input flag for SVODE.  See SVODE documentation under IOPT
C           for details.
C
C  J_ITOL   Solution tolerance input flag for SVODE.  See SVODE documentation
C           under ITOL for details.
C
C  J_MF     Solution method flag for SVODE.  See SVODE documentation
C           under MF for details.
C
C  J_LIMRWK  Required size of SVODE Real workspace, varies according to
C           type of Jacobian being used.
C
C  J_SVWK   An integer array that provides workspace for the
C           PDE solving subroutine SVODE.  (array length LIMIWK)
C
C  J_SCR    Starting address for general integer scratchspace. (length LIMISC)
C
```

```
C  J_END     End of ISPACE
C
C
C
C  Contents of RSPACE (Real Workspace) Partitions are as follows:
C  (All starting addresses conform to I_* where '*' describes the type
C   of variable beginning at that address)
C
C
C  I_PRESS   A real number that describes the pressure in dynes/cm**2
C
C  I_XNDF    A real number that describes the non-dimensionalizing factor
C           used to calculate non-dimensional axial locations.  For jets
C           this term should be equal to the nozzle diameter.
C
C  I_XON     A real number describing the length from the nozzle in which
C           super-threshold scalar dissipation values completely exclude
C           CMC calculation.
C
C  I_XTRX    A real number describing the upper threshold value for
C           conditional mean scalar dissipation, above which no CMC
C           calculations are performed.
C
C  I_BACKT   A real number describing the background temperature for determining
C           radiation losses.
C
C  I_QPRNT   A real number describing the next axial output location
C           downstream from the current calling point.
C
C  I_QPRAY   A real array containing the non-dimensional axial
C           axial locations where mass fraction and temperature
C           profiles are to be output to files. (array length NOUTMX)
C
C  I_ETA     Real array containing mixture fraction grid points.
C           (array length NETAMX)
C
C  I_CETA1    A real array containing mixture fraction grid difference
C           terms.  These 1st derivative terms are generated from
C           the mixture fraction grid.  (array length NETAMX)
C
C  I_FETA1    A real array containing mixture fraction grid difference
C           terms.  These 1st derivative terms are generated from
C           the mixture fraction grid.  (array length NETAMX)
C
C  I_BETA1    A real array containing mixture fraction grid difference
C           terms.  These 1st derivative terms are generated from
C           the mixture fraction grid.  (array length NETAMX)
C
C  I_CETA2    A real array containing mixture fraction grid difference
C           terms.  These 2nd derivative terms are generated from the
C           mixture fraction grid. (array length NETAMX)
C
C  I_FETA2    A real array containing mixture fraction grid difference
C           terms.  These 2nd derivative terms are generated from the
C           mixture fraction grid. (array length NETAMX)
C
C  I_BETA2    A real array containing mixture fraction grid difference
C           terms.  These 2nd derivative terms are generated from the
C           mixture fraction grid. (array length NETAMX)
C
C  I_RUQ     A real array containing conditional mean velocity.
C           (array length NETAMX)
C
C  I_RCQ     A real array containing conditional mean scalar dissipation.
C            (length NETAMX)
C
C  I_T       A real array containing the conditional mean temperatures
C           for all the grid points in mixture fraction space at the
C           current streamwise location. (array length NETAMX)
C
C  I_CMRHO   A real array containing the reciprocal of conditional mean
C           density. (array length NETAMX)
C
```

```
C  I_Q       A real array that contains stdd. enthalpies and species
C           mass fractions for all points defined in mixture fraction
C           space.  RSPACE(I_Q) to RSPACE(I_Q+NMAXQ-1) is partitioned
C           as follows:
C
C       I_Q..I_Q+NUMSCA-1     - st. enthalpy and species mass fractions at ETA(1)
C     I_Q+NUMSCA..I_Q+2*NUMSCA-1  -  "      "      "     "      "      "  ETA(2)
C   I_Q+2*NUMSCA..I_Q+3*NUMSCA-1  -  "      "      "     "      "      "  ETA(3)
C             "
C             "
C   I_Q+(NETAMX-1)*NUMSCA..I_Q+NMAXQ-1  - st. enthalpy and mass fractions
C                                          at ETA(NETAMX)
C
C                          (where species are given numbers according to
C                           their position in the CHEMKIN II Interpreter
C                           Input File Species List)
C
C  I_PDFS     A real array of mixture fraction PDF values at all mixture
C             fraction and physical location grid points.
C             (length NEXMX*NETAMX)
C
C  I_PDF0     A real array of mixture fraction PDF intermittency values at
C             zero mixture fraction for all physical location grid points.
C             (length NEXMX)
C
C  I_PDF1     A real array of mixture fraction PDF intermittency values at
C             unity mixture fraction for all physical location grid points.
C             (length NEXMX)
C
C  I_UCLM     A real array of unclipped means for the PDFs at each physical
C             grid point. (length NEXMX)
C
C  I_UCLV     A real array of unclipped variances for the PDFs at each physical
C             grid point. (length NEXMX)
C
C  I_CK       The starting address for CHEMKIN II related information
C
C  I_PATM     A real number that gives the value of 1 atm pressure in
C             dynes/cm**2.
C
C  I_WT       A real array of species molecular weights in kilograms/kilomole
C             (length NSPCMX)
C
C  I_CKWK     A real array that provides workspace for the chemistry
C             subroutines of CHEMKIN II.  (length LENWK)
C
C  I_SV       The starting address for SVODE related information
C
C  I_RTOL     A real number describing the relative solution convergence
C             tolerance for SVODE.
C
C  I_ATOL     A real number describing the absolute solution convergence
C             tolerance for SVODE.
C
C  I_SVWK     A real array that provides workspace for the PDE solving
C             subroutine SVODE. (length LIMRWK)
C
C  I_SCR      Starting address of general real scratchspace. (length LIMRSC)
C
C  I_END      End of RSPACE.
C
C-----------------------------------------------------------------------
C
C  Contents of CSPACE (Character*16 Workspace) Partitions are as follows:
C  (All starting addresses conform to K_* where '*' describes the type
C   of variable beginning at that address)
C
C  K_TITLE  An array of character*16 strings that contains the title
C           line found in both in the Chemistry Input File and
C           Restart Files. (length 5)
C
C  K_CKWK     A character*16 array that provides workspace for the chemistry
C             subroutines of CHEMKIN II.  (length LENCWK)
C
C  K_SCR      A character*16 scratchspace. (length 5)
C
C  K_END      End of CSPACE.
C
C-----------------------------------------------------------------------
C
C  Subroutines included in QKIN3_3 source code:
C
C  QKIN3  -  main code
C  CHEMIN -  initial data input
C  RESUME -  restart input
C  RHSFN0, RHSFN1, RHSFN2  -  right hand side residuals for CMC eqns
C  CHECK0 -  negative mass fraction check
C  WSTAT - write output status report
C  QINCON - adiabatic equilibrium code driver
C  UCHIGAU, FIXRUQ - RCQ, RUQ calculation  (ISPACE(J_CHI)=1)
C  AVERUX2 - RCQ,RUC calculation  (ISPACE(J_CHI)=0)
C  GAUDIM, DELTAB, GETDET, GETPDF, QDERF, QREF, GOODI, FGTRAN4, TERP2 - clipped
C           Gaussian PDF codes
C  Q2UCV - unconditional mean calculation
C  TWZONE - statistical indeterminacy handler
C  GXTREM - calculates threshold value of RCQ
C
C######################################################################
C
      IMPLICIT REAL (A-H,O-Z), INTEGER (I-N)
C
      PARAMETER(NETAMX=50,NSPCMX=15,NSCAMX=NSPCMX+1,NMAXQ=NSCAMX*NETAMX,
     1  LENIWK=600,LENWK=600,LENCWK=20,NOUTMX=99,NSPOUT=7,NELMX=6,
     2  NEXMX=50,LIMRSC=MAX(6*NSCAMX,(NEXMX+3)*NETAMX),LIMISC=2*NETAMX,
     3  GASCON=8.314E4)
C
C     The computed Jacobian array can either be treated as
C     being banded or full.  Before compiling, comment out
C     the inappropriate parameter set.  Changes need not be
C     made in the external function parameter listings since
C     the size of the SVODE real workspace is passed to them
C     as a variable.
C
C     Banded Jacobian Parameters
C      PARAMETER(MFCON=25,LIMIWK=30+NMAXQ,
C     1  LIMRWK=22+11*NMAXQ+10*NMAXQ*NSCAMX)
C     Full Jacobian Parameters
      PARAMETER(MFCON=22,LIMIWK=30+NMAXQ,
     1  LIMRWK=22+9*NMAXQ+2*NMAXQ**2)
C
C     Assign RSPACE Real Workspace starting addresses
      PARAMETER( I_PRESS=1, I_XNDF=I_PRESS+1, I_XON=I_XNDF+1,
     1  I_XTRX=I_XON+1, I_BACKT=I_XTRX+1, I_QPRNT=I_BACKT+1,
     2  I_QPRAY=I_QPRNT+1, I_ETA=I_QPRAY+NOUTMX,
     3  I_CETA1=I_ETA+NETAMX, I_FETA1=I_CETA1+NETAMX,
     4  I_BETA1=I_FETA1+NETAMX, I_CETA2=I_BETA1+NETAMX,
     5  I_FETA2=I_CETA2+NETAMX, I_BETA2=I_FETA2+NETAMX,
     6  I_RUQ=I_BETA2+NETAMX, I_RCQ=I_RUQ+NETAMX, I_T=I_RCQ+NETAMX,
     7  I_CMRHO=I_T+NETAMX, I_Q=I_CMRHO+NETAMX, I_PDFS=I_Q+NMAXQ,
     8  I_PDF0=I_PDFS+NEXMX*NETAMX, I_PDF1=I_PDF0+NEXMX,
     9  I_UCLM=I_PDF1+NEXMX,I_UCLV=I_UCLM+NEXMX,
     X  I_CK=I_UCLV+NEXMX, I_PATM=I_CK, I_WT=I_PATM+1,
     1  I_CKWK=I_WT+NSPCMX, I_SV=I_CKWK+LENWK, I_RTOL=I_SV,
     2  I_ATOL=I_RTOL+1, I_SVWK=I_ATOL+1, I_SCR=I_SVWK+LIMRWK,
     3  I_END=I_SCR+LIMRSC )
C
C     Assign ISPACE Integer Workspace starting addresses
      PARAMETER( J_NETA=1, J_NMSCA=J_NETA+1, J_COUNT=J_NMSCA+1,
     1  J_FINDEX=J_COUNT+1, J_IGN=J_FINDEX+1, J_RAD=J_IGN+1,
     2  J_CHI=J_RAD+1, J_DELAY=J_CHI+1, J_STOIC=J_DELAY+1,
     3  J_NMOUT=J_STOIC+1, J_H2O=J_NMOUT+1, J_CO2=J_H2O+1,
     4  J_SPC=J_CO2+1, J_CK=J_SPC+NSPOUT, J_NMEL=J_CK,
     5  J_NMSPC=J_NMEL+1, J_NMRC=J_NMSPC+1, J_NCF=J_NMRC+1,
     6  J_CKWK=J_NCF+NELMX*NSPCMX, J_SV=J_CKWK+LENIWK,
     7  J_STATE=J_SV, J_TASK=J_STATE+1, J_OPT=J_TASK+1,
     8  J_ITOL=J_OPT+1, J_MF=J_ITOL+1, J_LIMRWK=J_MF+1,
```

```
585         9  J_SVWK=J_LIMRWK+1, J_SCR=J_SVWK+LIMIWK,
586         1  J_END=J_SCR+LIMISC )
587   C
588   C     Assign CSPACE Character Workspace starting addresses
589         PARAMETER( K_TITLE=1, K_CKWK=K_TITLE+5,
590         1  K_SCR=K_CKWK+LENCWK, K_END=K_SCR+5 )
591   C
592   C     Assign I/O Unit Numbers
593         PARAMETER( LSCOUT=35, LDIAGN=39, LQOUT=40,
594         1   LCHDAT=41, LREST=42, LMWT=43, LDERF=36, LINK=65 )
595   C
596         CHARACTER*16 CSPACE(*)
597         CHARACTER*20 FILENM
598         REAL RSPACE(*),XMFRC(*),XMFRCV(*),YPOSN(*),VEL(*),VELY(*),
599         1  RHO(*),CHI(*),DRHODF(*),UCTEMP(*),SPEC1(*),SPEC2(*),
600         2  SPEC3(*),SPEC4(*),SPEC5(*),SPEC6(*),SPEC7(*),
601         3  STX,ENDX,PRESS,UCENTH(*)
602         INTEGER ISPACE(*),IMODE,NPTMX,NPTS,NRMX,NIMX,NCMX
603   C
604         COMMON/COMLNE/REPH,IPT    ! Contact with SUBCHM routines (if used)
605         SAVE /COMLNE/
606   C
607         EXTERNAL RHSFN0,RHSFN1,RHSFN2,REX
608   C
609   C#############################################################
610   C
611   C     Record value of input mode flag
612         INMODE=IMODE
613   C
614   C/////////////////VARIABLE INITIALIZATION SECTION//////////////
615   C
616         IF(IMODE.LE.1) THEN
617   C
618          ISPACE(J_DELAY)=0    ! Enable CMC routines
619   C
620   C     Open Log and Diagnostic Outputs
621          OPEN(UNIT=LSCOUT,FILE='qlog.d',FORM='FORMATTED')
622          OPEN(UNIT=LDIAGN,FILE='qaux.d',FORM='FORMATTED')
623   C
624   C     Check workspace limits to see if they are sufficient for
625   C     QKIN3 to use.  Also check if the number of physical points can be
626   C     accommodated.
627          WRITE(LSCOUT,*)
628          WRITE(LSCOUT,*) '** QKIN Version 3.3 ***************'
629          WRITE(LSCOUT,*) '    (nsa smith 8/94)'
630          WRITE(LSCOUT,*)
631          WRITE(LSCOUT,*) 'Workspace bounds must be at least :'
632          WRITE(LSCOUT,*) 'Real        -   ',I_END
633          WRITE(LSCOUT,*) 'Integer     -   ',J_END
634          WRITE(LSCOUT,*) 'Character*16 -  ',K_END
635          WRITE(LSCOUT,*)
636          IF(NRMX.LT.I_END.OR.NIMX.LT.J_END.OR.NCMX.LT.K_END) THEN
637           WRITE(LSCOUT,*)
638           WRITE(LSCOUT,*) 'Insufficient workspace provided !'
639           WRITE(LSCOUT,*) 'Enlarge workspace bounds in calling code.'
640           WRITE(LSCOUT,*)
641           IMODE=3  ! signal halt
642           RETURN
643          ENDIF
644          IF(NPTMX.GT.NEXMX) THEN
645           WRITE(LSCOUT,*)
646           WRITE(LSCOUT,*) 'The number of physical data points exceeds'
647           WRITE(LSCOUT,*) 'the currently defined array limit !'
648           WRITE(LSCOUT,*) 'Recompile QKIN3 with an expanded NEXMX value.'
649           WRITE(LSCOUT,*)
650           IMODE=3
651           RETURN
652          ENDIF
653          LIM=MAX(6*NSCAMX,(NEXMX+3)*NETAMX,4*NETAMX)
654          IF(LIMRSC.LT.LIM) THEN
655           WRITE(LSCOUT,*)
656           WRITE(LSCOUT,*) 'The current size of the real scratchspace'
657           WRITE(LSCOUT,*) 'is less than the required level.  The limit'
```

```
658           WRITE(LSCOUT,*) 'LIMRSC must acommodate all of the following'
659           WRITE(LSCOUT,*) 'requirements:'
660           WRITE(LSCOUT,*) 'NSCAMX*6 =          ',6*NSCAMX
661           WRITE(LSCOUT,*) 'NETAMX*4 =          ',4*NETAMX
662           WRITE(LSCOUT,*) '(NEXMX+3)*NETAMX = ',(NEXMX+3)*NETAMX
663           WRITE(LSCOUT,*)
664           WRITE(LSCOUT,*) 'LIMRSC is currently set at ',LIMRSC
665           WRITE(LSCOUT,*) 'Recompile QKIN3 with an expanded LIMRSC value.'
666           WRITE(LSCOUT,*)
667           IMODE=3
668           RETURN
669          ENDIF
670   C
671   C     Initialize Real and Integer Workspaces
672          DO 1000 I=1,NRMX
673   1000   RSPACE(I)=0.
674          DO 1010 J=1,NIMX
675   1010   ISPACE(J)=0
676   C
677   C     Open Chemkin II I/O Channels
678          OPEN(UNIT=LINK,FILE='linkfile.d',FORM='UNFORMATTED')
679   C
680   C*****CHEMKIN II  Initialization
681          WRITE(LSCOUT,*)
682          WRITE(LSCOUT,*) 'Initializing CHEMKIN II Subroutines:'
683          CALL CKINIT(LENIWK,LENWK,LENCWK,LINK,LSCOUT,ISPACE(J_CKWK),
684         1   RSPACE(I_CKWK),CSPACE(K_CKWK))
685          CALL CKINDX(ISPACE(J_CKWK),RSPACE(I_CKWK),ISPACE(J_NMEL),
686         1   ISPACE(J_NMSPC),ISPACE(J_NMRC),NFIT)
687          CALL CKNCF(NELMX,ISPACE(J_CKWK),RSPACE(I_CKWK),ISPACE(J_NCF))
688          CALL CKRP(ISPACE(J_CKWK),RSPACE(I_CKWK),R1,R2,RSPACE(I_PATM))
689          CALL CKWT(ISPACE(J_CKWK),RSPACE(I_CKWK),RSPACE(I_WT))
690          WRITE(LSCOUT,*)
691          WRITE(LSCOUT,*) 'Initialization completed'
692          WRITE(LSCOUT,*)
693   C
694   C     Close Chemkin II I/O Channels
695          CLOSE(LINK)
696   C
697   C     Output Species Molecular Weights for Postprocessing Usage
698          OPEN(UNIT=LMWT,FILE='mwtfil.d',FORM='FORMATTED')
699          DO 2200 IWT=1,ISPACE(J_NMSPC)
700   2200   WRITE(LMWT,*) RSPACE(I_WT+IWT-1)
701          CLOSE(LMWT)
702   C
703   C     Convert Pressure in atmospheres to CGS units for CHEMKIN II usage
704          RSPACE(I_PRESS)=PRESS*RSPACE(I_PATM)
705   C
706   C     Check for Species overflow and define number of reactive scalars
707          IF(ISPACE(J_NMSPC).GT.NSPCMX) THEN
708           WRITE(LSCOUT,*)
709           WRITE(LSCOUT,*) ISPACE(J_NMSPC)
710           WRITE(LSCOUT,*)' NUMBER OF SPECIES FOUND > INTERNALLY'
711           WRITE(LSCOUT,*)' DEFINED MAXIMUM VALUE.'
712           IMODE=3
713           CALL WSTAT(INMODE,IMODE,ISPACE(J_DELAY),LSCOUT,CSPACE(K_SCR))
714           RETURN
715          ELSE
716           ISPACE(J_NMSCA)=ISPACE(J_NMSPC)+1
717          ENDIF
718   C
719   C*****Initialize Mixture Fraction Grid if so signalled by IMODE
720          IF(IMODE.EQ.0) THEN
721           CALL CHEMIN(NETAMX,ISPACE(J_NMSCA),RSPACE(I_ETA),
722         1   RSPACE(I_Q),RSPACE(I_T),RSPACE(I_CKWK),
723         2   ISPACE(J_CKWK),RSPACE(I_QPRAY),RSPACE(I_SCR),
724         3   RSPACE(I_SCR+3*NSCAMX),RSPACE(I_SCR+4*NSCAMX),RSPACE(I_XON),
725         4   RSPACE(I_XNDF),ISPACE(J_STOIC),ISPACE(J_RAD),ISPACE(J_H2O),
726         5   ISPACE(J_CO2),ISPACE(J_CHI),ISPACE(J_IGN),ISPACE(J_NMOUT),
727         6   NSPOUT,ISPACE(J_SPC),CSPACE(K_TITLE),IMODE,ISPACE(J_NCF),
728         7   NELMX,ISPACE(J_NMEL),ISPACE(J_NMSPC),RSPACE(I_SCR+5*NSCAMX),
729         8   RSPACE(I_PRESS),RSPACE(I_BACKT),LCHDAT,LSCOUT,LDIAGN)
730           ISPACE(J_NETA)=NETAMX
```

```
          ISPACE(J_FINDEX)=1
          IF(IMODE.EQ.3) THEN
           CALL WSTAT(INMODE,IMODE,ISPACE(J_DELAY),LSCOUT,CSPACE(K_SCR))
           RETURN
          ENDIF
         ENDIF
C
C*****Determine mixture fraction grid from restart file if signalled by IMODE
         IF(IMODE.EQ.1) THEN
          CALL RESUME(NETAMX,ISPACE(J_NETA),ISPACE(J_NMSCA),
     1      RSPACE(I_ETA),RSPACE(I_Q),RSPACE(I_T),RSPACE(I_BACKT),
     2      RSPACE(I_QPRAY),RSPACE(I_XON),RSPACE(I_XNDF),
     3      RSPACE(I_RUQ),RSPACE(I_RCQ),ISPACE(J_STOIC),ISPACE(J_RAD),
     4      ISPACE(J_H2O),ISPACE(J_CO2),ISPACE(J_CHI),ISPACE(J_IGN),
     5      ISPACE(J_NMOUT),NSPOUT,ISPACE(J_SPC),CSPACE(K_TITLE),
     6      ISPACE(J_FINDEX),IMODE,LREST,LSCOUT,LDIAGN)
          ISPACE(J_FINDEX)=ISPACE(J_FINDEX)+1
          IF(IMODE.EQ.3) THEN
           CALL WSTAT(INMODE,IMODE,ISPACE(J_DELAY),LSCOUT,CSPACE(K_SCR))
           RETURN
          ENDIF
         ENDIF
C
C*****Determine threshold value of conditional mean scalar dissipation
C     at stoichiometric above which calculations are suspended.  This
C     only applies for ICHI >= 1.
         IF(ISPACE(J_CHI).GE.1) THEN
          CALL GXTREM(ISPACE(J_STOIC),ISPACE(J_NMSCA),RSPACE(I_Q),
     1      RSPACE(I_T),RSPACE(I_PRESS),RSPACE(I_SCR),
     2      RSPACE(I_SCR+NSCAMX),RSPACE(I_CKWK),ISPACE(J_CKWK),
     3      RSPACE(I_XTRX),ISPACE(J_IGN),LDIAGN)
         ENDIF
C
C*****Calculate Grid-Difference Arrays
         RSPACE(I_CETA2)=0.
         RSPACE(I_FETA2)=0.
         RSPACE(I_BETA2)=0.
         RSPACE(I_FETA1)=1./(RSPACE(I_ETA+1)-RSPACE(I_ETA))
         RSPACE(I_CETA1)=-1.*RSPACE(I_FETA1)
         RSPACE(I_BETA1)=0.
         DO 1320 I=2,NETAMX-1
          ETAI=RSPACE(I_ETA+I-1)
          ETAM1=RSPACE(I_ETA+I-2)
          ETAP1=RSPACE(I_ETA+I)
          TOT=1./(ETAP1-ETAM1)
          RSPACE(I_FETA2+I-1)=2.*TOT/(ETAP1-ETAI)
          RSPACE(I_FETA1+I-1)=0.5*RSPACE(I_FETA2+I-1)*(ETAI-ETAM1)
          RSPACE(I_BETA2+I-1)=2.*TOT/(ETAI-ETAM1)
          RSPACE(I_BETA1+I-1)=-0.5*RSPACE(I_BETA2+I-1)*(ETAP1-ETAI)
          RSPACE(I_CETA2+I-1)=-(RSPACE(I_FETA2+I-1)+RSPACE(I_BETA2+I-1))
          RSPACE(I_CETA1+I-1)=-(RSPACE(I_BETA1+I-1)+RSPACE(I_FETA1+I-1))
1320     CONTINUE
         RSPACE(I_CETA2+NETAMX-1)=0.
         RSPACE(I_FETA2+NETAMX-1)=0.
         RSPACE(I_BETA2+NETAMX-1)=0.
         RSPACE(I_BETA1+NETAMX-1)=-1./(RSPACE(I_ETA+NETAMX-1)-
     1     RSPACE(I_ETA+NETAMX-2))
         RSPACE(I_CETA1+NETAMX-1)=-1.*RSPACE(I_BETA1+NETAMX-1)
C
C*****SVODE Initialization
C     Specify desired solution accuracies, solution mode
C     and related parameters
         RSPACE(I_RTOL)=1.0E-5
         RSPACE(I_ATOL)=1.0E-8
         ISPACE(J_ITOL)=1
         ISPACE(J_TASK)=1
         ISPACE(J_OPT)=0
         ISPACE(J_STATE) =
         ISPACE(J_MF) MFCON
         ISPACE(J_SVWK)=2*ISPACE(J_NMSCA)     ! Load 1/2 Bandwidths....
         ISPACE(J_SVWK+1)=2*ISPACE(J_NMSCA)   ! ...NOT USED IN MF=22 CASE
         ISPACE(J_LIMRWK)=LIMRWK     !  Load size of SVODE real workspace
C
```

```
C
C*****Make initializing call to UCHIGAU
         IF(ISPACE(J_CHI).EQ.1) THEN
          ZEROX=0.
          CALL UCHIGAU(NPTMX,NPTS,XMFRC,XMFRCV,YPOSN,VEL,VELY,
     1      CHI,RHO,ZEROX,ZEROX,NETAMX,RSPACE(I_ETA),
     2      RSPACE(I_PDFS),RSPACE(I_PDF0),RSPACE(I_PDF1),
     3      RSPACE(I_UCLM),RSPACE(I_UCLV),RSPACE(I_SCR),
     4      RSPACE(I_SCR+NETAMX),RSPACE(I_SCR+2*NETAMX),
     5      RSPACE(I_SCR+3*NETAMX),RSPACE(I_RUQ),RSPACE(I_RCQ),
     6      RSPACE(I_XTRX),ISPACE(J_SCR),ISPACE(J_DELAY),
     7      ISPACE(J_STOIC),ISPACE(J_NETA),IMODE,LDERF,LDIAGN)
         ELSE
          CALL AVERUX2(NPTMX,NPTS,XMFRC,XMFRCV,YPOSN,VEL,CHI,
     1      RHO,NETAMX,RSPACE(I_ETA),RSPACE(I_PDFS),
     2      RSPACE(I_PDF0),RSPACE(I_PDF1),RSPACE(I_UCLM),RSPACE(I_UCLV),
     3      RSPACE(I_SCR),RSPACE(I_SCR+NETAMX),RSPACE(I_SCR+2*NETAMX),
     4      RSPACE(I_SCR+3*NETAMX),RSPACE(I_RUQ),RSPACE(I_RCQ),
     5      ISPACE(J_SCR),ISPACE(J_NETA),IMODE,LDERF,LDIAGN)
         ENDIF
         IF(IMODE.EQ.3) THEN
          CALL WSTAT(INMODE,IMODE,ISPACE(J_DELAY),LSCOUT,CSPACE(K_SCR))
          RETURN
         ENDIF
C
C******Initialize program output progress variables
         ISPACE(J_COUNT)=1
         RSPACE(I_QPRNT)=RSPACE(I_QPRAY)
C
C******Comment to Log File, header for following progress info
         WRITE(LSCOUT,*)
         WRITE(LSCOUT,598)
         WRITE(LSCOUT,599)      ! Header for log data
C
        ELSE
C
C//////////EQUATION SOLVING SECTION//////////////////////////
C
        IF(IMODE.EQ.2) THEN
C
C*****The turbulent field has marched since last call
C     so must get new velocity and scalar dissipation values
C     and number of active grid points.  UCHIGAU will vary
C     the number of points, and can call a delay.  AVERUX can
C     also vary the number of points.
C
          OLDNPT=ISPACE(J_NETA)
          ISPACE(J_DELAY)=0
          IF(ISPACE(J_CHI).EQ.0) THEN
           CALL AVERUX2(NPTMX,NPTS,XMFRC,XMFRCV,YPOSN,VEL,CHI,
     1      RHO,NETAMX,RSPACE(I_ETA),RSPACE(I_PDFS),
     2      RSPACE(I_PDF0),RSPACE(I_PDF1),RSPACE(I_UCLM),RSPACE(I_UCLV),
     3      RSPACE(I_SCR),RSPACE(I_SCR+NETAMX),RSPACE(I_SCR+2*NETAMX),
     4      RSPACE(I_SCR+3*NETAMX),RSPACE(I_RUQ),RSPACE(I_RCQ),
     5      ISPACE(J_SCR),ISPACE(J_NETA),IMODE,LDERF,LDIAGN)
          ELSE
           CALL UCHIGAU(NPTMX,NPTS,XMFRC,XMFRCV,YPOSN,VEL,VELY,
     1      CHI,RHO,ENDX,STX,NETAMX,RSPACE(I_ETA),
     2      RSPACE(I_PDFS),RSPACE(I_PDF0),RSPACE(I_PDF1),
     3      RSPACE(I_UCLM),RSPACE(I_UCLV),RSPACE(I_SCR),
     4      RSPACE(I_SCR+NETAMX),RSPACE(I_SCR+2*NETAMX),
     5      RSPACE(I_SCR+3*NETAMX),RSPACE(I_RUQ),RSPACE(I_RCQ),
     6      RSPACE(I_XTRX),ISPACE(J_SCR),ISPACE(J_DELAY),
     7      ISPACE(J_STOIC),ISPACE(J_NETA),IMODE,LDERF,LDIAGN)
          ENDIF
          IF(IMODE.EQ.3) THEN
           CALL WSTAT(INMODE,IMODE,ISPACE(J_DELAY),LSCOUT,CSPACE(K_SCR))
           RETURN
          ENDIF
C
1800     CONTINUE
C*****If ISPACE(J_DELAY) has been set to 1 or -1 by
C     UCHIGAU then no CMC calculations are to be done.
```

```
C     TWZONE handles statistical indeterminacy.
        CALL TWZONE(RSPACE(I_ETA),NETAMX,ISPACE(J_NETA),
     1       RSPACE(I_ETA2),RSPACE(I_FETA2),RSPACE(I_BETA2),
     2       IMODE,LSCOUT,LDIAGN)
        IF(IMODE.EQ.1) THEN
         CALL WSTAT(INMODE,IMODE,ISPACE(J_DELAY),LSCOUT,CSPACE(K_SCR))
         RETURN
        ENDIF
C
        IF(ISPACE(J_DELAY).NE.0..OR.ENDX.LE.RSPACE(I_XON)) THEN
C
         CALL TREMAIN(CPUTIM)
         WRITE(LSCOUT,600)ENDX,(ENDX-STX),CPUTIM,ISPACE(J_NETA),
     1     ISPACE(J_DELAY)
C
        ELSE     ! For non-delayed cases
C
C        Check to see if SVODE needs to use a different number of grid
C        points, and set disposable STX.
         TSTX=STX
         NQ=ISPACE(J_NMSCA)*ISPACE(J_NETA)
         IF(OLDNPT.LT.ISPACE(J_NETA)) THEN
          WRITE(LSCOUT,*) 'Number of active mixture fraction'
          WRITE(LSCOUT,*) 'grid points increasing.....'
         ENDIF
         IF(ISPACE(J_STATE).NE.1.AND.OLDNPT.NE.ISPACE(J_NETA)) THEN
          IF(ISPACE(J_NETA).LT.OLDNPT) THEN
           ISPACE(J_STATE)=3
          ELSE
           ISPACE(J_STATE)=1
          ENDIF
         ENDIF
C
2000     CONTINUE
C
C        Find Elapsed CPU time and output status
         CALL TREMAIN(CPUTIM)
         WRITE(LSCOUT,600)ENDX,(ENDX-STX),CPUTIM,ISPACE(J_NETA),
     1     ISPACE(J_DELAY)
C
C*******Solve PDEs using SVODE.  Pass appropriate RHS functions
C        according to run conditions (radiative-adiabatic,
C        reactive-nonreactive etc.)
C
         IF(CPUTIM.GT.0.) THEN
          IF(ISPACE(J_IGN).EQ.1) THEN
           IF(ISPACE(J_RAD).EQ.0) THEN
            CALL SVODE(RHSFN1,NQ,RSPACE(I_Q),TSTX,ENDX,ISPACE(J_ITOL),
     1       RSPACE(I_RTOL),RSPACE(I_ATOL),ISPACE(J_TASK),
     2       ISPACE(J_STATE),ISPACE(J_OPT),RSPACE(I_SVWK),LIMRWK,
     3       ISPACE(J_SVWK),LIMIWK,REX,ISPACE(J_MF),RSPACE,ISPACE)
           ELSE
            CALL SVODE(RHSFN2,NQ,RSPACE(I_Q),TSTX,ENDX,ISPACE(J_ITOL),
     1       RSPACE(I_RTOL),RSPACE(I_ATOL),ISPACE(J_TASK),
     2       ISPACE(J_STATE),ISPACE(J_OPT),RSPACE(I_SVWK),LIMRWK,
     3       ISPACE(J_SVWK),LIMIWK,REX,ISPACE(J_MF),RSPACE,ISPACE)
           ENDIF
          ELSE
           IF(ISPACE(J_IGN).EQ.0) THEN
            CALL SVODE(RHSFN0,NQ,RSPACE(I_Q),TSTX,ENDX,ISPACE(J_ITOL),
     1       RSPACE(I_RTOL),RSPACE(I_ATOL),ISPACE(J_TASK),
     2       ISPACE(J_STATE),ISPACE(J_OPT),RSPACE(I_SVWK),LIMRWK,
     3       ISPACE(J_SVWK),LIMIWK,REX,ISPACE(J_MF),RSPACE,ISPACE)
           ENDIF
          ENDIF
         ELSE
          IMODE=3     ! TIME-LIMIT EXCEEDED
          CALL WSTAT(INMODE,IMODE,ISPACE(J_DELAY),LSCOUT,CSPACE(K_SCR))
          WRITE(LSCOUT,*) 'CPU time limit exceeded'
         ENDIF
C
C        Check for SVODE flagged errors and for negative species
C        mass fractions and correct any where found
```

```
          IF(ISPACE(J_STATE).LT.0) THEN
           WRITE(LSCOUT,*)
           WRITE(LSCOUT,*)' SVODE ERROR # ',ISPACE(J_STATE)
           IF(ISPACE(J_STATE).EQ.-1) THEN
            IF(MFCON.EQ.25) THEN
             WRITE(LSCOUT,*)' Try recompiling with Full Jacobian'
             WRITE(LSCOUT,*)' parameters and restart calculations'
             WRITE(LSCOUT,*)' from last output solution.....'
            ELSE
             WRITE(LSCOUT,*)' attempting to continue....'
             ISPACE(J_STATE)=1
             GOTO 1800
            ENDIF
           ENDIF
           IF(ISPACE(J_STATE).EQ.-4) THEN
            IF(ISPACE(J_CHI).EQ.1) THEN
             CALL GXTREM(ISPACE(J_STOIC),ISPACE(J_NMSCA),RSPACE(I_Q),
     1        RSPACE(I_T),RSPACE(I_PRESS),RSPACE(I_SCR),
     2        RSPACE(I_SCR+NSCAMX),RSPACE(I_CKWK),ISPACE(J_CKWK),
     3        RSPACE(I_XTRX),ISPACE(J_IGN),LDIAGN)
             ISPACE(J_STATE)=1
             GOTO 1800
            ENDIF
           ENDIF
           IMODE=3     ! Signal a halt to the calling code
           CALL WSTAT(INMODE,IMODE,ISPACE(J_DELAY),LSCOUT,CSPACE(K_SCR))
          ENDIF
          CALL CHECK0(NETAMX,ISPACE(J_NMSCA),ISPACE(J_NMSCA)-1,
     1     RSPACE(I_Q))
C
         ENDIF     ! End of DELAY condition
C
        ENDIF
       ENDIF
C
C/////////////////DATA OUTPUT SECTION//////////////////////
C
4000  CONTINUE     ! Error exception escape
C
C*****Calculate temperature from enthalpy and species mass fractions
C     Unpack some integer and real variables
       NUMSCA=ISPACE(J_NMSCA)
       NETAPT=ISPACE(J_NETA)
       PRESSQ=RSPACE(I_PRESS)
C
       DO 1595 I=1,NETAMX
       TI=RSPACE(I_T+I-1)
       DELTAT=0.0
       IPT=I
       REFH=RSPACE(I_Q+I*NUMSCA-1)
1594   CONTINUE
       TI=TI-DELTAT
       CALL CKHBMS(TI,RSPACE(I_Q+(I-1)*NUMSCA),ISPACE(J_CKWK),
     1  RSPACE(I_CKWK),HBML)
       CALL CKCPBS(TI,RSPACE(I_Q+(I-1)*NUMSCA),ISPACE(J_CKWK),
     2  RSPACE(I_CKWK),CP)
       DELTAT=(HBML-RSPACE(I_Q+I*NUMSCA-1))/CP
       IF(ABS(DELTAT).GT.1.) GOTO 1594
       RSPACE(I_T+I-1)=TI
1595   CONTINUE
C
       WRITE(LDIAGN,44) 'CHIC',ENDX,CHI(1),XMFRCV(1),XMFRC(1)
44     FORMAT(A4,4(1X,E15.8))
C
C*****Determine unconditional mean reactive scalar values
       CALL Q2UCV(NETAMX,ISPACE(J_NMSCA),RSPACE(I_ETA),
     1  RSPACE(I_Q),RSPACE(I_T),NPTS,NPTMX,RSPACE(I_PDFS),
     2  RSPACE(I_PDF0),RSPACE(I_PDF1),GASCON,RSPACE(I_PRESS),RHO,
     3  DRHODF,UCTEMP,UCENTH,SPEC1,SPEC2,SPEC3,SPEC4,SPEC5,SPEC6,
     4  SPEC7,RSPACE(I_WT),RSPACE(I_CMRHO),RSPACE(I_SCR),
     5  RSPACE(I_CETA1),RSPACE(I_FETA1),RSPACE(I_BETA1),
     6  XMFRC,XMFRCV,RSPACE(I_SCR+NETAMX),RSPACE(I_SCR+2*NETAMX),
     7  RSPACE(I_SCR+3*NETAMX),RSPACE(I_UCLM),RSPACE(I_UCLV),
```

```
1023        8  ISPACE(J_SPC),IMODE,LDERF,LSCOUT,
1024        9  LDIAGN)
1025  C
1026  C*****Output Q Profiles
1027         XOD=ENDX/RSPACE(I_XNDF)
1028         IF(IMODE.EQ.3.OR.XOD.GE.RSPACE(I_QPRNT).AND.
1029        1   ISPACE(J_COUNT).LE.ISPACE(J_NMOUT)) THEN
1030          INDEXF=ISPACE(J_FINDEX)+ISPACE(J_COUNT)-1
1031          ICT1=INDEXF/10
1032          ICT2=MOD(INDEXF,10)
1033          FILENM='qout'//CHAR(ICT1+48)//CHAR(ICT2+48)//'.d'
1034          WRITE(LSCOUT,*)
1035          WRITE(LSCOUT,700) FILENM,XOD
1036          WRITE(LSCOUT,*)
1037          IF(IMODE.NE.3) WRITE(LSCOUT,599)      ! Next header for log data
1038          OPEN(UNIT=LQOUT,FILE=FILENM,STATUS='NEW')
1039          CALL WSTAT(INMODE,IMODE,ISPACE(J_DELAY),LQOUT,CSPACE(K_SCR))
1040          WRITE(LQOUT,800)' Index: ',INDEXF
1041          WRITE(LQOUT,*)
1042          WRITE(LQOUT,516) CSPACE(K_TITLE),CSPACE(K_TITLE+1),
1043        1  CSPACE(K_TITLE+2),CSPACE(K_TITLE+3),CSPACE(K_TITLE+4)
1044          WRITE(LQOUT,*)' Current Axial Position (metres, nondim):'
1045          WRITE(LQOUT,*) ENDX,XOD
1046          WRITE(LQOUT,*)' Non-dimensionalizing axial length (metres):'
1047          WRITE(LQOUT,*) RSPACE(I_XNDF)
1048          WRITE(LQOUT,*)' Ignition variable (1=flame on, 0=flame off)'
1049          WRITE(LQOUT,*) ISPACE(J_IGN)
1050          WRITE(LQOUT,*)' Radiation variable (2=HCarb flame, 1=H2 flame)'
1051          WRITE(LQOUT,*) ISPACE(J_RAD)
1052          WRITE(LQOUT,*)' H2O and CO2 species numbers for radiation model:'
1053          IF(ISPACE(J_RAD).EQ.0) WRITE(LQOUT,*)
1054          IF(ISPACE(J_RAD).EQ.1) WRITE(LQOUT,*) ISPACE(J_H2O)
1055          IF(ISPACE(J_RAD).EQ.2) WRITE(LQOUT,*) ISPACE(J_H2O),ISPACE(J_CO2)
1056          WRITE(LQOUT,*)' Background Temperature (K):'
1057          IF(ISPACE(J_RAD).NE.0) THEN
1058           WRITE(LQOUT,*) RSPACE(I_BACKT)
1059          ELSE
1060           WRITE(LQOUT,*)
1061          ENDIF
1062          WRITE(LQOUT,*)' Dissipation variable (1=integrated, 0=averaged)'
1063          WRITE(LQOUT,*) ISPACE(J_CHI)
1064          WRITE(LQOUT,*)' Pilot length (diameters):'
1065          WRITE(LQOUT,*) RSPACE(I_XON)/RSPACE(I_XNDF)
1066          WRITE(LQOUT,*)' Stoichiometric Mixture Fraction:'
1067          WRITE(LQOUT,*) RSPACE(I_ETA+ISPACE(J_STOIC)-1)
1068          WRITE(LQOUT,*)' Number of output stations:'
1069          WRITE(LQOUT,*) (ISPACE(J_NMOUT)-ISPACE(J_COUNT)+1)
1070          WRITE(LQOUT,*)' Axial location of output stations (non-dim):'
1071          WRITE(LQOUT,*)(RSPACE(I_QPRAY+J-1),J=ISPACE(J_COUNT),
1072        1                ISPACE(J_NMOUT))
1073          WRITE(LQOUT,*)' Species passed to flow code (spec. #s):'
1074          WRITE(LQOUT,*)(ISPACE(J_SPC+J-1),J=1,NSPOUT)
1075          WRITE(LQOUT,*)' Number of Active Grid Points:'
1076          WRITE(LQOUT,*) ISPACE(J_NETA)
1077          WRITE(LQOUT,*)' ETA, RUQ, RCQ & Q array data:'
1078          DO 3010 I=1,NETAMX
1079           WRITE(LQOUT,400) RSPACE(I_ETA+I-1),RSPACE(I_Q+I*NUMSCA-1),
1080        1    RSPACE(I_RUQ+I-1),RSPACE(I_RCQ+I-1)
1081  3010    CONTINUE
1082          NUMSCA=ISPACE(J_NMSCA)
1083          DO 3020 I=1,NETAMX
1084           DO 3030 J=1,NUMSCA-1
1085            WRITE(LQOUT,*) RSPACE(I_Q+J+(I-1)*NUMSCA-1)
1086  3030     CONTINUE
1087           WRITE(LQOUT,*) RSPACE(I_T+I-1)
1088  3020    CONTINUE
1089          ISPACE(J_COUNT)=ISPACE(J_COUNT)+1
1090          IF(ISPACE(J_COUNT).LE.ISPACE(J_NMOUT))
1091        1    RSPACE(I_QPRNT)=RSPACE(I_QPRAY+ISPACE(J_COUNT)-1)
1092          CLOSE(LQOUT)
1093         ENDIF
1094  C
1095  C     If this is the last call, close Log and Diagnostic output files
```

```
1096          IF(IMODE.EQ.3) THEN
1097           WRITE(LSCOUT,*)
1098           WRITE(LSCOUT,*)'** QKIN Execution terminated **********'
1099           CLOSE(LSCOUT)
1100           CLOSE(LDIAGN)
1101          ENDIF
1102  C
1103  C*****Format statements
1104  400    FORMAT(4(1X,E17.10))
1105  516    FORMAT(5(A16))
1106  598    FORMAT(' Progress Statistics :')
1107  599    FORMAT(5X,'X (m)',11X,'dX (m)',9X,
1108        1  't_cpu (s)',6X,'Np',4X,'Id')
1109  600    FORMAT(3(E15.8,1X),3X,I2,4X,I2)
1110  700    FORMAT('Outputting',1X,A20,1X,'at X/D =',1X,E10.3)
1111  800    FORMAT(A8,2X,I2)
1112  C
1113          RETURN
1114          END
1115  C=============================================================
1116  C
1117  C+++++++++++++++++++++++++++++++++++++++++++++++++++++++++++++
1118          SUBROUTINE RHSFN0(NMXQ,XSTEP,Q,QSORCE,RSPACE,ISPACE)
1119  C
1120  C     This subroutine is passed as an external to the PDE solver
1121  C     SVODE.  RHSFN0 is distinct from RHSFN1,2 in that it calculates
1122  C     the right hand side term of each o.d.e. for non-reactive
1123  C     non-radiative mixing cases.
1124  C
1125  C     INPUT:
1126  C
1127  C     NMXQ   An integer which describes the size of the arrays
1128  C             Q and QSORCE
1129  C     XSTEP   A real variable which describes the value of X
1130  C
1131  C     Q(NMXQ) An array of reals that contains the value of
1132  C              species mass fractions and st. enthalpy at each
1133  C              point in mixture fraction space
1134  C
1135  C              (Units: dimensionless or ergs per gram    )
1136  C              (depending on whether the entry is a mass )
1137  C              (fraction or a standardized enthalpy      )
1138  C
1139  C     OUTPUT:
1140  C
1141  C     QSORCE(NMXQ)  An array of reals that contains the value
1142  C                    of the finite change in Q that will occur
1143  C                    (Units: per metre or ergs per gram metre     )
1144  C                    (depending whether the entry corresponds to a)
1145  C                    (change of species mass fraction or enthalpy )
1146  C
1147  C
1148          IMPLICIT REAL (A-H,O-Z), INTEGER(I-N)
1149  C
1150          PARAMETER(NETAMX=50,NSPCMX=15,NSCAMX=NSPCMX+1,NMAXQ=NSCAMX*NETAMX,
1151        1  LENIWK=600,LENWK=600,LENCWK=20,NOUTMX=99,NSPOUT=7,NELMX=6,
1152        2  NEXMX=50,LIMRSC=MAX(6*NSCAMX,(NEXMX+3)*NETAMX),LIMISC=2*NETAMX,
1153        3  GASCON=8.314E4)
1154          PARAMETER(LIMIWK=30+NMAXQ,LIMRWK=22+11*NMAXQ+10*NMAXQ*NSCAMX)
1155  C
1156          PARAMETER( I_PRESS=1, I_XNDF=I_PRESS+1, I_XON=I_XNDF+1,
1157        1  I_XTRX=I_XON+1, I_BACKT=I_XTRX+1, I_QPRNT=I_BACKT+1,
1158        2  I_QPRAY=I_QPRNT+1, I_ETA=I_QPRAY+NOUTMX,
1159        3  I_CETA1=I_ETA+NETAMX, I_FETA1=I_CETA1+NETAMX,
1160        4  I_BETA1=I_FETA1+NETAMX, I_CETA2=I_BETA1+NETAMX,
1161        5  I_FETA2=I_CETA2+NETAMX, I_BETA2=I_FETA2+NETAMX,
1162        6  I_RUQ=I_BETA2+NETAMX, I_RCQ=I_RUQ+NETAMX, I_T=I_RCQ+NETAMX,
1163        7  I_CMRHO=I_T+NETAMX, I_Q=I_CMRHO+NETAMX, I_PDFS=I_Q+NMAXQ,
1164        8  I_PDF0=I_PDFS+NEXMX*NETAMX, I_PDF1=I_PDF0+NEXMX,
1165        9  I_UCLM=I_PDF1+NEXMX,I_UCLV=I_UCLM+NEXMX,
1166        X  I_CK=I_UCLV+NEXMX, I_PATM=I_CK, I_WT=I_PATM+1,
1167        1  I_CKWK=I_WT+NSPCMX, I_SV=I_CKWK+LENWK, I_RTOL=I_SV,
1168        2  I_ATOL=I_RTOL+1, I_SVWK=I_ATOL+1, I_SCR=I_SVWK+LIMRWK,
```

```
1169        3  I_END=I_SCR+LIMRSC )
1170  C
1171         PARAMETER( J_NETA 1, J_NMSCA=J_NETA+1, J_COUNT=J_NMSCA+1,
1172        1  J_FINDEX=J_COUNT+1, J_IGN=J_FINDEX+1, J_RAD=J_IGN+1,
1173        2  J_CHI=J_RAD+1, J_DELAY=J_CHI+1, J_STOIC=J_DELAY+1,
1174        3  J_NMOUT=J_STOIC+1, J_H2O=J_NMOUT+1, J_CO2=J_H2O+1,
1175        4  J_SPC=J_CO2+1, J_CK=J_SPC+NSPOUT, J_NMEL=J_CK,
1176        5  J_NMSPC=J_NMEL+1, J_NMRC=J_NMSPC+1, J_NCF=J_NMRC+1,
1177        6  J_CKWK=J_NCF+NELMX*NSPCMX, J_SV=J_CKWK+LENIWK,
1178        7  J_STATE=J_SV, J_TASK=J_STATE+1, J_OPT=J_TASK+1,
1179        8  J_ITOL=J_OPT+1, J_MF=J_ITOL+1, J_LIMRWK=J_MF+1,
1180        9  J_SVWK=J_LIMRWK+1, J_SCR=J_SVWK+LIMIWK,
1181        1  J_END=J_SCR+LIMISC )
1182  C
1183         INTEGER ISPACE(*)
1184         REAL RSPACE(*),Q(*),QSORCE(*)
1185  C
1186  C       Unpack some integer variables and realign Real Scratchsapce
1187          NUMSCA=ISPACE(J_NMSCA)
1188          NETAPT=ISPACE(J_NETA)
1189          II_SCR=I_SVWK+ISPACE(J_LIMRWK) ! Variable starting address
1190  C
1191  C       Calculate source terms at lean and rich mixture fraction bounds.
1192  C       Rich bounding point always mixes with ETA=1, no matter what
1193  C       ETA(NETAPT+1) may be.
1194          DO 1600 J=1,NUMSCA
1195           QSORCE(J)=0.0
1196           QSORCE(J+(NETAPT-1)*NUMSCA)=RSPACE(I_RCQ+I-1)*
1197        1     (RSPACE(I_CETA2+I-1)*Q(J+(NETAPT-1)*NUMSCA)+
1198        2     RSPACE(I_BETA2+I-1)*Q(J+(NETAPT-2)*NUMSCA)+
1199        3     RSPACE(I_FETA2+I-1)*Q(J+(NETAMX-1)*NUMSCA))/
1200        4     RSPACE(I_RUQ+NETAPT-1)
1201  1600  CONTINUE
1202  C
1203  C       Calculate source terms away from the bounding mixture
1204  C       fractions.
1205          DO 1700 I=2,NETAPT-1
1206           IP=I+1
1207           IM=I-1
1208           DO 1700 J=1,NUMSCA
1209            QSORCE(J+(I-1)*NUMSCA)=(RSPACE(I_RCQ+I-1)*
1210        1    (RSPACE(I_CETA2+I-1)*Q(J+(I-1)*NUMSCA)+RSPACE(I_BETA2+I-1)*
1211        2    Q(J+(IM-1)*NUMSCA)+RSPACE(I_FETA2+I-1)*Q(J+(IP-1)*NUMSCA)))/
1212        3    RSPACE(I_RUQ+I-1)
1213  1700   CONTINUE
1214  C
1215         RETURN
1216         END
1217  C=============================================================
1218  C
1219  C+++++++++++++++++++++++++++++++++++++++++++++++++++++++++++++
1220         SUBROUTINE RHSFN1(NMXQ,XSTEP,Q,QSORCE,RSPACE,ISPACE)
1221  C
1222  C      This subroutine is passed as an external to the PDE solver
1223  C      SVODE.  RHSFN1 is distinct from RHSFN0,2 in that it calculates
1224  C      the right hand side term of each o.d.e. for reactive
1225  C      non-radiative mixing cases.
1226  C
1227  C      INPUT:
1228  C
1229  C      NMXQ   An integer which describes the size of the arrays
1230  C               Q and QSORCE
1231  C      XSTEP  A real variable which describes the size of the
1232  C               current step
1233  C      Q(NMXQ) An array of reals that contains the value of
1234  C               species mass fractions and temperature at each
1235  C               point in mixture fraction space
1236  C               (Units: dimensionless or ergs per gram     )
1237  C               (depending on whether the entry is a mass  )
1238  C               (fraction or a standardized enthalpy       )
1239  C
1240  C      OUTPUT:
1241  C
```

```
1242  C      QSORCE(NMXQ)  An array of reals that contains the value
1243  C                     of the finite change in Q that will occur
1244  C                     over the step of size XSTEP
1245  C                     (Units: per metre or ergs per gram metre )
1246  C                     (depending whether the entry corresponds to a)
1247  C                     (change of species mass fraction or enthalpy)
1248  C
1249  C
1250         IMPLICIT REAL (A-H,O-Z), INTEGER(I-N)
1251  C
1252         PARAMETER(NETAMX=50,NSPCMX=15,NSCAMX=NSPCMX+1,NMAXQ=NSCAMX*NETAMX,
1253        1  LENIWK=600,LENWK=600,LENCWK=20,NOUTMX=99,NSPOUT=7,NELMX=6,
1254        2  NEXMX=50,LIMRSC=MAX(6*NSCAMX,(NEXMX+3)*NETAMX),LIMISC=2*NETAMX,
1255        3  GASCON=8.314E4)
1256         PARAMETER(LIMIWK=30+NMAXQ,LIMRWK=22+11*NMAXQ+10*NMAXQ*NSCAMX)
1257  C
1258         PARAMETER( I_PRESS=1, I_XNDF=I_PRESS+1, I_XON=I_XNDF+1,
1259        1  I_XTRX=I_XON+1, I_BACKT=I_XTRX+1, I_QPRNT=I_BACKT+1,
1260        2  I_QPRAY=I_QPRNT+1, I_ETA=I_QPRAY+NOUTMX,
1261        3  I_CETA1=I_ETA+NETAMX, I_FETA1=I_CETA1+NETAMX,
1262        4  I_BETA1=I_FETA1+NETAMX, I_CETA2=I_BETA1+NETAMX,
1263        5  I_FETA2=I_CETA2+NETAMX, I_BETA2=I_FETA2+NETAMX,
1264        6  I_RUQ=I_BETA2+NETAMX, I_RCQ=I_RUQ+NETAMX, I_T=I_RCQ+NETAMX,
1265        7  I_CMRHO=I_T+NETAMX, I_Q=I_CMRHO+NETAMX, I_PDFS=I_Q+NMAXQ,
1266        8  I_PDF0=I_PDFS+NEXMX*NETAMX, I_PDF1=I_PDF0+NEXMX,
1267        9  I_UCLM=I_PDF1+NEXMX,I_UCLV=I_UCLM+NEXMX,
1268        X  I_CK=I_UCLV+NEXMX, I_PATM=I_CK, I_WT=I_PATM+1,
1269        1  I_CKWK=I_WT+NSPCMX, I_SV=I_CKWK+LENWK, I_RTOL=I_SV,
1270        2  I_ATOL=I_RTOL+1, I_SVWK=I_ATOL+1, I_SCR=I_SVWK+LIMRWK,
1271        3  I_END=I_SCR+LIMRSC )
1272  C
1273         PARAMETER( J_NETA=1, J_NMSCA=J_NETA+1, J_COUNT=J_NMSCA+1,
1274        1  J_FINDEX=J_COUNT+1, J_IGN=J_FINDEX+1, J_RAD=J_IGN+1,
1275        2  J_CHI=J_RAD+1, J_DELAY=J_CHI+1, J_STOIC=J_DELAY+1,
1276        3  J_NMOUT=J_STOIC+1, J_H2O=J_NMOUT+1, J_CO2=J_H2O+1,
1277        4  J_SPC=J_CO2+1, J_CK=J_SPC+NSPOUT, J_NMEL=J_CK,
1278        5  J_NMSPC=J_NMEL+1, J_NMRC=J_NMSPC+1, J_NCF=J_NMRC+1,
1279        6  J_CKWK=J_NCF+NELMX*NSPCMX, J_SV=J_CKWK+LENIWK,
1280        7  J_STATE=J_SV, J_TASK=J_STATE+1, J_OPT=J_TASK+1,
1281        8  J_ITOL=J_OPT+1, J_MF=J_ITOL+1, J_LIMRWK=J_MF+1,
1282        9  J_SVWK=J_LIMRWK+1, J_SCR=J_SVWK+LIMIWK,
1283        1  J_END=J_SCR+LIMISC )
1284  C
1285         INTEGER ISPACE(*)
1286         REAL RSPACE(*),Q(*),QSORCE(*)
1287  C
1288         COMMON/COMLNE/REFH,IPT
1289         SAVE /COMLNE/
1290  C
1291  C      Unpack some integer and real variables, and realign real scatchspace
1292         NUMSCA=ISPACE(J_NMSCA)
1293         NETAPT=ISPACE(J_NETA)
1294         PRESSQ=RSPACE(I_PRESS)
1295         II_SCR=I_SVWK+ISPACE(J_LIMRWK)  ! variable starting address
1296  C
1297         DO 1595 I=1,NETAPT
1298         TI=RSPACE(I_T+I-1)
1299         DELTAT=0.0
1300         IPT=I
1301         REFH=Q(I*NUMSCA)
1302  1594   CONTINUE
1303         TI=TI-DELTAT
1304         CALL CKHBMS(TI,Q(1+(I-1)*NUMSCA),ISPACE(J_CKWK),
1305        1  RSPACE(I_CKWK),HBML)
1306         CALL CKCPBS(TI,Q(1+(I-1)*NUMSCA),ISPACE(J_CKWK),
1307        2  RSPACE(I_CKWK),CP)
1308         DELTAT=(HBML-Q(I*NUMSCA))/CP
1309         IF(ABS(DELTAT).GT.1.) GOTO 1594
1310         RSPACE(I_T+I-1)=TI
1311  1595   CONTINUE
1312  C
1313  C      Calculate source terms for SVODE at lean and rich boundaries.
1314           IPT=1
```

```
1315            CALL CKWYP(PRESSQ,RSPACE(I_T),Q(1),ISPACE(J_CKWK),
1316         1    RSPACE(I_CKWK),RSPACE(II_SCR))
1317            CALL CKRHOY(PRESSQ,RSPACE(I_T),Q(1),ISPACE(J_CKWK),
1318         1    RSPACE(I_CKWK),RHOI)
1319            RRHOI=1./RHOI
1320            DO 1700 J=1,NUMSCA-1
1321             WDOTJ=RSPACE(II_SCR+J-1)*RSPACE(I_WT+J-1)*RRHOI
1322             QSORCE(J)=WDOTJ/RSPACE(I_RUQ)
1323   1700     CONTINUE
1324            QSORCE(NUMSCA)=0.
1325   C
1326            IPT NETAPT
1327            CALL CKWYP(PRESSQ,RSPACE(I_T+NETAPT-1),
1328         1    Q(1+(NETAPT-1)*NUMSCA),ISPACE(J_CKWK),RSPACE(I_CKWK),
1329         2    RSPACE(II_SCR))
1330            CALL CKRHOY(PRESSQ,RSPACE(I_T+NETAPT-1),Q(1+(NETAPT-1)*NUMSCA),
1331         1    ISPACE(J_CKWK),RSPACE(I_CKWK),RHOI)
1332            RRHOI=1./RHOI
1333            DO 1750 J=1,NUMSCA-1
1334             WDOTJ=RSPACE(II_SCR+J-1)*RSPACE(I_WT+J-1)*RRHOI
1335             QSORCE(J+(NETAPT-1)*NUMSCA)=(WDOTJ+
1336         1     RSPACE(I_RCQ+NETAPT-1)*(RSPACE(I_CETA2+NETAPT-1)*
1337         2     Q(J+(NETAPT-1)*NUMSCA)+RSPACE(I_BETA2+NETAPT-1)*
1338         3     Q(J+(NETAPT-2)*NUMSCA)+RSPACE(I_FETA2+NETAPT-1)*
1339         4     Q(J+(NETAMX-1)*NUMSCA)))/RSPACE(I_RUQ+NETAPT-1)
1340   1750     CONTINUE
1341            QSORCE(NETAPT*NUMSCA)=RSPACE(I_RCQ+NETAPT-1)*
1342         1     (RSPACE(I_CETA2+NETAPT-1)*Q(NETAPT*NUMSCA)+
1343         2     RSPACE(I_BETA2+NETAPT-1)*Q((NETAPT-1)*NUMSCA)+
1344         3     RSPACE(I_FETA2+NETAPT-1)*Q(NETAMX*NUMSCA))/
1345         4     RSPACE(I_RUQ+NETAPT-1)
1346   C
1347   C     Calculate source terms for SVODE away from boundaries.
1348   C
1349           DO 1602 I=2,NETAPT-1
1350            IPT=I
1351            IP=I+1
1352            IM=I-1
1353            CALL CKWYP(PRESSQ,RSPACE(I_T+I-1),
1354         1    Q(1+(I-1)*NUMSCA),ISPACE(J_CKWK),RSPACE(I_CKWK),
1355         2    RSPACE(II_SCR))
1356            CALL CKRHOY(PRESSQ,RSPACE(I_T+I-1),Q(1+(I-1)*NUMSCA),
1357         1    ISPACE(J_CKWK),RSPACE(I_CKWK),RSPACE(II_SCR+NSCAMX+I-1))
1358            RRHOI=1./RSPACE(II_SCR+NSCAMX+I-1)
1359            DO 1602 J=1,NUMSCA-1
1360             WDOTJ=RSPACE(II_SCR+J-1)*RSPACE(I_WT+J-1)*1.E3
1361             QSORCE(J+(I-1)*NUMSCA)=(WDOTJ+RSPACE(I_RCQ+I-1)*
1362         1     (RSPACE(I_CETA2+I-1)*Q(J+(I-1)*NUMSCA)+
1363         2     RSPACE(I_BETA2+I-1)*Q(J+(IM-1)*NUMSCA)+
1364         3     RSPACE(I_FETA2+I-1)*Q(J+(IP-1)*NUMSCA)))/
1365         4     RSPACE(I_RUQ+I-1)
1366   1602     CONTINUE
1367   C
1368           DO 1600 I=2,NETAPT-1
1369            IP=I+1
1370            IM=I-1
1371            QSORCE(NUMSCA+(I-1)*NUMSCA)=(RSPACE(I_RCQ+I-1)*
1372         1   (RSPACE(I_CETA2+I-1)*Q(I*NUMSCA)+
1373         2    RSPACE(I_BETA2+I-1)*Q(IM*NUMSCA)+
1374         3    RSPACE(I_FETA2+I-1)*Q(IP*NUMSCA)))/RSPACE(I_RUQ+I-1)
1375   1600    CONTINUE
1376   C
1377           RETURN
1378           END
1379   C=============================================================
1380   C
1381   C+++++++++++++++++++++++++++++++++++++++++++++++++++++++++++++
1382         SUBROUTINE RHSFN2(NMXQ,XSTEP,Q,QSORCE,RSPACE,ISPACE)
1383   C
1384   C     This subroutine is passed as an external to the PDE solver
1385   C     SVODE.  RHSFN2 is distinct from RHSFN0,1 in that it calculates
1386   C     the right hand side term of each o.d.e. for reactive radiative
1387   C     mixing cases.
```

```
1388   C
1389   C     INPUT:
1390   C
1391   C     NMXQ   An integer which describes the size of the arrays
1392   C             Q and QSORCE
1393   C     XSTEP  A real variable which describes the size of the
1394   C             current step
1395   C     Q(NMXQ) An array of reals that contains the value of
1396   C              species mass fractions and temperature at each
1397   C              point in mixture fraction space
1398   C              (Units: dimensionless or ergs per gram     )
1399   C              (depending on whether the entry is a mass  )
1400   C              (fraction or a standardized enthalpy       )
1401   C
1402   C     OUTPUT:
1403   C
1404   C     QSORCE(NMXQ)  An array of reals that contains the value
1405   C                    of the finite change in Q that will occur
1406   C                    over the step of size XSTEP
1407   C                    (Units: per metre or ergs per gram metre )
1408   C                    (depending whether the entry corresponds to a)
1409   C                    (change of species mass fraction or enthalpy)
1410   C
1411   C
1412         IMPLICIT REAL (A-H,O-Z), INTEGER(I-N)
1413   C
1414         PARAMETER(NETAMX=50,NSPCMX=15,NSCAMX=NSPCMX+1,NMAXQ=NSCAMX*NETAMX,
1415        1  LENIWK=600,LENWK=600,LENCWK=20,NOUTMX=99,NSPOUT=7,NELMX=6,
1416        2  NEXMX=50,LIMRSC=MAX(6*NSCAMX,(NEXMX+3)*NETAMX),LIMISC=2*NETAMX,
1417        3  GASCON=8.314E4)
1418         PARAMETER(LIMIWK=30+NMAXQ,LIMRWK=22+11*NMAXQ+10*NMAXQ*NSCAMX)
1419   C
1420         PARAMETER( I_PRESS=1, I_XNDF=I_PRESS+1, I_XON=I_XNDF+1,
1421        1  I_XTRX=I_XON+1, I_BACKT=I_XTRX+1, I_QPRNT=I_BACKT+1,
1422        2  I_QPRAY=I_QPRNT+1, I_ETA=I_QPRAY+NOUTMX,
1423        3  I_CETA1=I_ETA+NETAMX, I_FETA1=I_CETA1+NETAMX,
1424        4  I_BETA1=I_FETA1+NETAMX, I_CETA2=I_BETA1+NETAMX,
1425        5  I_FETA2=I_CETA2+NETAMX, I_BETA2=I_FETA2+NETAMX,
1426        6  I_RUQ=I_BETA2+NETAMX, I_RCQ=I_RUQ+NETAMX, I_T=I_RCQ+NETAMX,
1427        7  I_CMRHO=I_T+NETAMX, I_Q=I_CMRHO+NETAMX, I_PDFS=I_Q+NMAXQ,
1428        8  I_PDF0=I_PDFS+NEXMX*NETAMX, I_PDF1=I_PDF0+NEXMX,
1429        9  I_UCLM=I_PDF1+NEXMX,I_UCLV=I_UCLM+NEXMX,
1430        X  I_CK=I_UCLV+NEXMX, I_PATM=I_CK, I_WT=I_PATM+1,
1431        1  I_CKWK=I_WT+NSPCMX, I_SV=I_CKWK+LENWK, I_RTOL=I_SV,
1432        2  I_ATOL=I_RTOL+1, I_SVWK=I_ATOL+1, I_SCR=I_SVWK+LIMRWK,
1433        3  I_END=I_SCR+LIMRSC )
1434   C
1435         PARAMETER( J_NETA=1, J_NMSCA=J_NETA+1, J_COUNT=J_NMSCA+1,
1436        1  J_FINDEX=J_COUNT+1, J_IGN=J_FINDEX+1, J_RAD=J_IGN+1,
1437        2  J_CHI=J_RAD+1, J_DELAY=J_CHI+1, J_STOIC=J_DELAY+1,
1438        3  J_NMOUT=J_STOIC+1, J_H2O=J_NMOUT+1, J_CO2=J_H2O+1,
1439        4  J_SPC=J_CO2+1, J_CK=J_SPC+NSPOUT, J_NMEL=J_CK,
1440        5  J_NMSPC=J_NMEL+1, J_NMRC=J_NMSPC+1, J_NCF=J_NMRC+1,
1441        6  J_CKWK=J_NCF+NELMX*NSPCMX, J_SV=J_CKWK+LENIWK,
1442        7  J_STATE=J_SV, J_TASK=J_STATE+1, J_OPT=J_TASK+1,
1443        8  J_ITOL=J_OPT+1, J_MF=J_ITOL+1, J_LIMRWK=J_MF+1,
1444        9  J_SVWK=J_LIMRWK+1, J_SCR=J_SVWK+LIM1WK,
1445        1  J_END=J_SCR+LIMISC )
1446   C
1447   C     Radiation model constants in SI units (m,s,kg,K ... W, Pa etc)
1448         PARAMETER(SIGMA=5.6697E-8,B1=2.E-5,B2=6.4E-9,B3=4.6E-5,B4=1.3E-8,
1449        1 CONV=1.E0,XEMIS=4.*SIGMA*CONV) ! CONV allows for pressure in
1450   C      dyn/cm**2 instead of Pa, and produces a radiative loss in units of
1451   C      erg/cm**3.s instead of W/m**3.  When divided by the density (in
1452   C      units of g/cm**3) this produces the desired result in erg/g.s which
1453   C      is the units of the dissipation terms.
1454         PARAMETER(XLN10=2.30258509)
1455   C
1456         INTEGER ISPACE(*)
1457         REAL RSPACE(*),Q(*),QSORCE(*)
1458         REAL A(10)
1459   C
1460         COMMON/COMLNE/REFH,IPT
```

```
      SAVE /COMLNE/
C
C     Unpack some integer and real variables and realign real scratchspace
      NUMSCA=ISPACE(J_NMSCA)
      NETAPT=ISPACE(J_NETA)
      PRESSQ=RSPACE(I_PRESS)
      BACKT4=RSPACE(I_BACKT)**4
      IRAD=ISPACE(J_RAD)
      IPH2O=ISPACE(J_H2O)
      IPCO2=ISPACE(J_CO2)
      II_SCR=I_SVWK+ISPACE(J_LIMRWK) ! variable starting address
C
C      DATA A/-1.288,1.927,0.13,-0.809,-0.345,0.642,-0.991,
C     1  0.636,-0.6583,0.55634/
C
      DO 1595 I=1,NETAPT
      TI=RSPACE(I_T+I-1)
      DELTAT=0.0
      IPT=I
      REFH=Q(I*NUMSCA)
 1594 CONTINUE
      TI=TI-DELTAT
      CALL CKHBMS(TI,Q(1+(I-1)*NUMSCA),ISPACE(J_CKWK),
     1  RSPACE(I_CKWK),HBML)
      CALL CKCPBS(TI,Q(1+(I-1)*NUMSCA),ISPACE(J_CKWK),
     2  RSPACE(I_CKWK),CP)
      DELTAT=(HBML-Q(I*NUMSCA))/CP
      IF(ABS(DELTAT).GT.1.) GOTO 1594
      RSPACE(I_T+I-1)=TI
 1595 CONTINUE
C
C     Calculate SVODE source terms at boundaries.
C
        IPT=1
        CALL CKWYP(PRESSQ,RSPACE(I_T),Q(1),ISPACE(J_CKWK),
     1    RSPACE(I_CKWK),RSPACE(II_SCR))
        CALL CKRHOY(PRESSQ,RSPACE(I_T),Q(1),ISPACE(J_CKWK),
     1    RSPACE(I_CKWK),RHOI)
        RRHOI=1./RHOI
        DO 1700 J=1,NUMSCA-1
         WDOTJ=RSPACE(II_SCR+J-1)*RSPACE(I_WT+J-1)*RRHOI
         QSORCE(J)=WDOTJ/RSPACE(I_RUQ)
 1700   CONTINUE
        QSORCE(NUMSCA)=0.
C
        IPT=NETAPT
        CALL CKWYP(PRESSQ,RSPACE(I_T+NETAPT-1),Q(1+(NETAPT-1)*NUMSCA),
     1    ISPACE(J_CKWK),RSPACE(I_CKWK),RSPACE(II_SCR))
        CALL CKRHOY(PRESSQ,RSPACE(I_T+NETAPT-1),Q(1+(NETAPT-1)*NUMSCA),
     1    ISPACE(J_CKWK),RSPACE(I_CKWK),RHOI)
        RRHOI=1./RHOI
        DO 1750 J=1,NUMSCA-1
         WDOTJ=RSPACE(II_SCR+J-1)*RSPACE(I_WT+J-1)*RRHOI
         QSORCE(J+(NETAPT-1)*NUMSCA)=(WDOTJ+RSPACE(I_RCQ+NETAPT-1)*
     1      (RSPACE(I_CETA2+NETAPT-1)*Q(J+(NETAPT-1)*NUMSCA)+
     2      RSPACE(I_BETA2+NETAPT-1)*Q(J+(NETAPT-2)*NUMSCA)+
     3      RSPACE(I_FETA2+NETAPT-1)*Q(J+(NETAMX-1)*NUMSCA)))/
     4      RSPACE(I_RUQ+NETAPT-1)
 1750   CONTINUE
        CALL CKYTX(Q(1+(NETAPT-1)*NUMSCA),ISPACE(J_CKWK),
     1   RSPACE(I_CKWK),RSPACE(II_SCR))
        EM=RSPACE(II_SCR+IPH2O-1)*(B1-B2*RSPACE(I_T+NETAPT-1))*
     1   PRESSQ+(IRAD-1)*RSPACE(II_SCR+IPCO2-1)*
     2   (B3-B4*RSPACE(I_T+NETAPT-1))*PRESSQ
        THNRAD=XEMIS*EM*(RSPACE(I_T+NETAPT-1)**4-BACKT4)*RRHOI
        QSORCE(NETAPT*NUMSCA)=(RSPACE(I_RCQ+NETAPT-1)*
     1      (RSPACE(I_CETA2+NETAPT-1)*Q(NETAPT*NUMSCA)+
     2      RSPACE(I_BETA2+NETAPT-1)*Q((NETAPT-1)*NUMSCA)+
     3      RSPACE(I_FETA2+NETAPT-1)*Q(NETAMX*NUMSCA))-THNRAD)/
     4      RSPACE(I_RUQ+NETAPT-1)
C
C     Calculate SVODE source terms away from boundaries.
C
```

```
        DO 1602 I=2,NETAPT-1
         IPT=I
         IP=I+1
         IM=I-1
         CALL CKWYP(PRESSQ,RSPACE(I_T+I-1),
     1     Q(1+(I-1)*NUMSCA),ISPACE(J_CKWK),RSPACE(I_CKWK),
     2     RSPACE(II_SCR))
         CALL CKRHOY(PRESSQ,RSPACE(I_T+I-1),Q(1+(I-1)*NUMSCA),
     1     ISPACE(J_CKWK),RSPACE(I_CKWK),RSPACE(II_SCR+NSCAMX+I-1))
         RRHOI=1./RSPACE(II_SCR+NSCAMX+I-1)
         DO 1602 J=1,NUMSCA-1
          WDOTJ=RSPACE(II_SCR+J-1)*RSPACE(I_WT+J-1)*RRHOI
          QSORCE(J+(I-1)*NUMSCA)=(WDOTJ+RSPACE(I_RCQ+I-1)*
     1      (RSPACE(I_CETA2+I-1)*Q(J+(I-1)*NUMSCA)+
     2      RSPACE(I_BETA2+I-1)*Q(J+(IM-1)*NUMSCA)+
     3      RSPACE(I_FETA2+I-1)*Q(J+(IP-1)*NUMSCA)))/
     4      RSPACE(I_RUQ+I-1)
 1602   CONTINUE
C
        DO 1600 I=2,NETAPT-1
C
         IP=I+1
         IM=I-1
C
C       Calculate Emissivity and radiation loss using various models
        CALL CKYTX(Q(1+(I-1)*NUMSCA),ISPACE(J_CKWK),
     1    RSPACE(I_CKWK),RSPACE(II_SCR))
        EM=RSPACE(II_SCR+IPH2O-1)*(B1-B2*RSPACE(I_T+I-1))*
     1    PRESSQ+(IRAD-1)*RSPACE(II_SCR+IPCO2-1)*
     2    (B3-B4*RSPACE(I_T+I-1))*PRESSQ
C
C        THETA=1.E-3*RSPACE(I_T+I-1)-1.
C        EMH2O=0.
C        DO 1001 II=1,7
C         EMH2O=(EMH2O+A(II))*THETA
C1001    CONTINUE
C        P2000=REAL(INT(THETA))
C        EMH2O=(1.-P2000)*(EMH2O+A(8))+P2000*(A(9)*THETA+A(10))
C        EMH2O=EXP(EMH2O*XLN10)
C        EM=PRESSQ*EMH2O*RSPACE(II_SCR+IPH2O-1)/RSPACE(I_PATM)
C
        THNRAD=XEMIS*EM*(RSPACE(I_T+I-1)**4-BACKT4)/
     1     RSPACE(II_SCR+NSCAMX+I-1)
C
        QSORCE(NUMSCA+(I-1)*NUMSCA)=(RSPACE(I_RCQ+I-1)*
     1    (RSPACE(I_CETA2+I-1)*Q(I*NUMSCA)+
     2    RSPACE(I_BETA2+I-1)*Q(IM*NUMSCA)+
     3    RSPACE(I_FETA2+I-1)*Q(IP*NUMSCA))-THNRAD)/
     4    RSPACE(I_RUQ+I-1)
 1600   CONTINUE
C
        RETURN
        END
C=============================================================
C
C+++++++++++++++++++++++++++++++++++++++++++++++++++++++++++++
C
      SUBROUTINE UCHIGAU(NMAX,N,XMFRC,XMFRCV,YPOSN,VEL,VELY,CHI,
     1  RHOIN,CRRNTX,OLDX,NETAMX,ETA,PDF,PDF0,PDF1,UCLM,UCLV,
     2  PDFSTR,SCR1,SCR2,USCHI,RUQ,RCQ,XTREMX,IZ,IDELAY,
     3  ISTOIC,NETAPT,IMODE,LDERF,LDIAGN)
C
C     This subroutine calculates conditional mean scalar
C     dissipation by double integrating time derivatives
C     (or length derivatives when premultiplied by velocity)
C     of mixture fraction PDFs across mixture fraction space.
C
C     PDFs and their derivatives are calculated using a
C     clipped gaussian function assumed form.
C
      IMPLICIT REAL (A-H,O-Z), INTEGER (I-N)
C
      PARAMETER(VSML=1.E-10)
```

```
1607  C
1608        INTEGER NMAX,N,IZ(*),NETAMX,NETAPT,IDELAY,ISTOIC,IMODE,LDERF
1609        REAL XMFRC(*),XMFRCV(*),VEL(*),RHOIN(*),CHI(*),YPOSN(*),
1610       1  VELY(*),PDF(*),PDF0(*),PDF1(*),PDFSTR(*),SCR1(*),SCR2(*),
1611       2  USCHI(*),ETA(*),RUQ(*),RCQ(*),UCLM(*),UCLV(*),
1612       3  CRRNTX,OLDX,XTREMX
1613  C
1614  C     Determine step size in x space,
1615  C     if this is the first call then
1616  C     no calculation of scalar dissipation
1617  C     can be made.
1618        IF(CRRNTX.GT.0..AND.CRRNTX.NE.OLDX) THEN
1619         XSTEP=CRRNTX-OLDX
1620         IDELAY=0
1621         INIT=1     ! Flag to GAUDI
1622  C
1623         PDFAC0=0.
1624         PDFAC1=0.
1625         RVAC0=0.
1626         RVAC1=0.
1627         CHIACC=0.
1628         OY=0.
1629         OPDF0=0.
1630         OPDF1=0.
1631         ORV=0.
1632         OCHI=0.
1633         ORHO=0.
1634         RHACC=0.
1635  C
1636         DO 10 J=1,N
1637  C
1638          VMAX=XMFRC(J)*(1.-XMFRC(J))
1639          XMFRVJ=MIN(MAX(0.,XMFRCV(J)),VMAX)
1640          CHIJ=MAX(0.,CHI(J))
1641          IF(VMAX.EQ.0.) CHIJ=0.
1642          TSTEP=XSTEP/VEL(J)
1643          HSTEP=CHIJ*TSTEP
1644          HALFB=MIN(XMFRVJ+HSTEP,VMAX)
1645          HALFF=MAX(XMFRVJ-HSTEP,0.)
1646          RVJ=RHOIN(J)/TSTEP
1647          XMFP=XMFRC(J)
1648          XMFM=XMFRC(J)
1649  C
1650  C       Call GAUDIM to get PDF, and PDF*CHI
1651          CALL GAUDIM(XMFRC(J),XMFRVJ,HALFF,HALFB,NETAMX,ETA,
1652       1   PDF(1+(J-1)*NETAMX),PDF0(J),PDF1(J),UCLM(J),UCLV(J),
1653       2   USCHI(1+(J-1)*NETAMX),SCR1,SCR2,RVJ,INIT,IMODE,
1654       3   LDERF,LDIAGN)
1655          IF(IMODE.EQ.3) RETURN
1656  C
1657          DELY=YPOSN(J)-OY
1658          PDFAC1=PDFAC1+0.5*(RHOIN(J)*PDF1(J)*YPOSN(J)+
1659       1     OPDF1*OY*ORHO)*DELY
1660          PDFAC0=PDFAC0+0.5*(RHOIN(J)*PDF0(J)*YPOSN(J)+
1661       1     OPDF0*OY*ORHO)*DELY
1662          RV=RHOIN(J)*VEL(J)
1663          RVAC0=RVAC0+0.5*(PDF0(J)*RV*YPOSN(J)+OPDF0*ORV*OY)*DELY
1664          RVAC1=RVAC1+0.5*(PDF1(J)*RV*YPOSN(J)+OPDF1*ORV*OY)*DELY
1665          CHIACC=CHIACC+0.5*(RHOIN(J)*CHI(J)*YPOSN(J)+
1666       1    OCHI*ORHO*OY)*DELY
1667          RHACC=RHACC+0.5*(RHOIN(J)*YPOSN(J)+OY*ORHO)*DELY
1668  C
1669          OY=YPOSN(J)
1670          OPDF1=PDF1(J)
1671          OPDF0=PDF0(J)
1672          ORV=RV
1673          OXMF=XMFRC(J)
1674          OXMFV=XMFRCV(J)
1675          ORHO=RHOIN(J)
1676          OCHI=CHI(J)
1677  C
1678  10     CONTINUE
1679         RHARA=1./RHACC
```

```
1680         IF(PDFAC0.GT.0.) RVAC0=RVAC0/PDFAC0
1681         IF(PDFAC1.GT.0.) RVAC1=RVAC1/PDFAC1
1682         PDFAC0=PDFAC0*RHARA
1683         PDFAC1=PDFAC1*RHARA
1684         CHIACC=CHIACC*RHARA
1685  C
1686  C     Integrate USCHI, PDF values and mass flux
1687  C     across the width of the flow.
1688         DO 50 J=1,NETAMX
1689          OY=YPOSN(1)
1690          ORV=RHOIN(1)*VEL(1)
1691          OPY=PDF(J)*YPOSN(1)
1692          OV=VEL(1)
1693          OUSCHI=USCHI(J)
1694          USCACC=0.
1695          PYACC=0.
1696          URPYAC=0.
1697          RPYACC=0.
1698          ORHO=RHOIN(1)
1699  C
1700          DO 60 I=2,N
1701           DELY=0.5*(YPOSN(I)-OY)
1702           RV=RHOIN(I)*VEL(I)
1703           PY=PDF(J+(I-1)*NETAMX)*YPOSN(I)
1704           USCACC=USCACC+(USCHI(J+(I-1)*NETAMX)*
1705       1       YPOSN(I)+OUSCHI*OY)*DELY
1706           RPYACC=RPYACC+(PY*RHOIN(I)+ORHO*OPY)*DELY
1707           URPYAC=URPYAC+(RV*PY+ORV*OPY)*DELY
1708  C
1709           OY=YPOSN(I)
1710           OV=VEL(I)
1711           OUSCHI=USCHI(J+(I-1)*NETAMX)
1712           ORV=RV
1713           OPY=PY
1714           ORHO=RHOIN(I)
1715  60      CONTINUE
1716  C
1717  C       Normalize by area
1718          RUQ(J)=URPYAC*RHARA            ! divided by integ. pdf at later stage
1719          RCQ(J)=USCACC*RHARA            !   "      "  "    "  "
1720          PDFSTR(J)=RPYACC*RHARA
1721  50     CONTINUE
1722  C
1723  C     RCQ must be divided by the integrated PDF to
1724  C     yield the conditional mean (flow integrated)
1725  C     scalar dissipation.
1726  C     Since integrated PDF values can be zero
1727  C     or very small, it is necessary to guard
1728  C     against overflow errors in the division.
1729  C
1730         OPDF=0.
1731         OETA=0.
1732         PDFACC=0.
1733         CHECK=0.
1734         OETA=ETA(1)
1735         ORCQ=0.
1736         COR0=RCQ(1)
1737         COR1=RCQ(NETAMX)-COR0
1738         DO 70 J=1,NETAMX
1739          PDFACC=PDFACC+0.5*(PDFSTR(J)+OPDF)*(ETA(J)-OETA)
1740          RCQ(J)=RCQ(J)-COR0-ETA(J)*COR1
1741          CHECK=CHECK+0.5*(ETA(J)-OETA)*(RCQ(J)+ORCQ)
1742          ORCQ=RCQ(J)
1743          OPDF=PDFSTR(J)
1744          OETA=ETA(J)
1745  70      CONTINUE
1746         WRITE(LDIAGN,*) 'CHIACC ',CRRNTX,CHIACC,CHECK
1747         WRITE(LDIAGN,444) 'INT ',CRRNTX,PDFACC,PDFAC0,PDFAC1
1748  444    FORMAT(A4,4(1X,E15.8))
1749  C
1750         IC=1
1751         IZ(1)=1
1752         BIGCHI=0.
```

```
1753          WRITE(LDIAGN,*) 'EPRC ',CRRNTX
1754          DO 75 J=1,NETAMX
1755           PDFSTJ=MAX(PDFSTR(J),VSML)
1756           IF(RUQ(J).LE.VSML) RUQ(J)=0.
1757           RCQ(J)=2.*RCQ(J)/PDFSTJ
1758           RUQ(J)=RUQ(J)/PDFSTJ
1759           IF(RUQ(J).NE.0.) THEN
1760            IZ(IC)=J
1761            IC=IC+1
1762           ENDIF
1763           IF(RCQ(J).LT.0.) IDELAY=-1
1764           IF(RCQ(J)/RHOIN(J).GT.BIGCHI) BIGCHI=RCQ(J)/RHOIN(J)
1765           WRITE(LDIAGN,999) 'EPR ',ETA(J),PDFSTJ,RCQ(J),RCQ(J)*PDFSTJ
1766   999     FORMAT(A4,4(1X,E15.7))
1767   75     CONTINUE
1768   C
1769          IF(PDFAC0.GT.0.) RUQ(1)=RVAC0
1770          IF(PDFAC1.GT.0.) THEN
1771           RUQ(NETAMX)=RVAC1
1772           IZ(IC)=NETAMX
1773           IC=IC+1
1774          ENDIF
1775   C
1776   C      Fix holes in RUQ profile by interpolation
1777          CALL FIXRUQ(ETA,RUQ,IZ,IC-1,NETAMX,VEL(1))
1778   C
1779   C      Set calculation delay flag to zero
1780   C      thereby allowing CMC calculations to
1781   C      take place, but check for extreme
1782   C      scalar dissipation values in the
1783   C      reaction range.  An extreme value requires
1784   C      a delay.
1785          IF(IDELAY.EQ.0) THEN
1786           XLIMIT=MIN(XTREMX,1.E20)
1787           IF(BIGCHI.GT.XLIMIT) IDELAY=1
1788          ENDIF
1789   C
1790   C      Determine rich bound on calculation zone
1791          J=NETAMX
1792          IF(PDFAC1.EQ.0.) THEN
1793   80      CONTINUE
1794           IF(PDFSTR(J).LT.VSML) THEN
1795            J=J-1
1796            GOTO 80
1797           ENDIF
1798          ENDIF
1799          NETAPT=J
1800   C
1801         ELSE
1802   C
1803   C      No CMC calc is to be made, but GAUDI requires initialization
1804          INIT=0
1805          DUM=0.    !  Dummy variables not used during initialization
1806          CALL GAUDIM(DUM,DUM,DUM,DUM,NETAMX,ETA,PDF,DUM,DUM,DUM,DUM,
1807        1   USCHI,SCR1,SCR2,DUM,INIT,IMODE,LDERF,LDIAGN)
1808          IF(IMODE.EQ.3) RETURN
1809          IDELAY=1
1810   C
1811         ENDIF    ! end of integration option
1812   C
1813         RETURN
1814         END
1815   C=====================================================================C
1816   C
1817   C+++++++++++++++++++++++++++++++++++++++++++++++++++++++++++++++++++++C
1818   C
1819          SUBROUTINE FIXRUQ(ETA,FRUQ,IZ,NC,NETAMX,RUQC)
1820   C
1821          IMPLICIT REAL (A-H,O-Z), INTEGER (I-N)
1822          INTEGER NC,IZ(*),NETAMX
1823          REAL FRUQ(*),ETA(*)
1824   C
1825          IF(NC.GT.1) THEN
```

```
1826           DO 1000 I=1,NC-1
1827            IF(IZ(I)+1.NE.IZ(I+1).AND.IZ(I).NE.IZ(I+1)) THEN
1828             ETA0=ETA(IZ(I))
1829             FRUQ0=FRUQ(IZ(I))
1830             FAC=(FRUQ(IZ(I+1))-FRUQ0)/(ETA(IZ(I+1))-ETA0)
1831             DO 2000 J=IZ(I)+1,IZ(I+1)-1
1832              FRUQ(J)=(ETA(J)-ETA0)*FAC+FRUQ0
1833   2000      CONTINUE
1834            ENDIF
1835   1000     CONTINUE
1836   C
1837           IF(IZ(NC).LT.NETAMX) THEN
1838            DO 3000 I=IZ(NC)+1,NETAMX
1839             FRUQ(I)=RUQC
1840   3000      CONTINUE
1841           ENDIF
1842          ELSE
1843           DO 4000 I=1,NETAMX
1844            FRUQ(I)=RUQC
1845   4000     CONTINUE
1846          ENDIF
1847   C
1848          RETURN
1849          END
1850   C+++++++++++++++++++++++++++++++++++++++++++++++++++++++++++++++++++++C
1851   C
1852   C=====================================================================C
1853         SUBROUTINE Q2UCV(NETAMX,NUMSCA,ETA,Q,T,NPTS,NPTMX,
1854        1  PDF,PDF0,PDF1,GASCON,PRESS,RHO,DRHODF,UCTEMP,UCENTH,SPEC1,
1855        2  SPEC2,SPEC3,SPEC4,SPEC5,SPEC6,SPEC7,WT,CMRHO,CMDRDF,CETA1,
1856        3  FETA1,BETA1,XMFRC,XMFRCV,SCR0,SCR1,SCR2,UCLM,UCLV,ISP,IMODE,
1857        4  LDERF,LSCOUT,LDIAGN)
1858   C
1859   C       This subroutine converts conditional mean data into
1860   C       unconditional data for output to QKIN3's calling code.
1861   C
1862          IMPLICIT REAL(A-H,O-Z), INTEGER(I-N)
1863          REAL ETA(*),Q(*),T(*),PDF(*),PDF0(*),
1864        1   PDF1(*),RHO(*),DRHODF(*),SPEC1(*),SPEC2(*),
1865        2   SPEC3(*),SPEC4(*),SPEC5(*),SPEC6(*),SPEC7(*),
1866        3   CMRHO(*),CMDRDF(*),WT(*),CETA1(*),FETA1(*),
1867        4   BETA1(*),UCTEMP(*),UCENTH(*),XMFRC(*),XMFRCV(*),
1868        5   SCR0(*),SCR1(*),SCR2(*),UCLM(*),UCLV(*)
1869          INTEGER NETAMX,NUMSCA,NPTS,NPTMX,ISP(*),IMODE,
1870        1   LDIAGN,LDERF,LSCOUT
1871   C
1872   C       If only new PDF values are desired, and no CMC calculation
1873   C       has been made then.....
1874          IF(IMODE.EQ.4.OR.IMODE.LE.1) THEN
1875           DO 2000 J=1,NPTS
1876            INIT=1
1877            VMAX=XMFRC(J)*(1.-XMFRC(J))
1878            XMFRVJ=MIN(MAX(0.,XMFRCV(J)),VMAX)
1879            DUM=0.
1880            CALL GAUDIM(XMFRC(J),XMFRVJ,XMFRVJ,XMFRVJ,NETAMX,ETA,
1881        1    PDF(1+(J-1)*NETAMX),PDF0(J),PDF1(J),UCLM(J),UCLV(J),SCR0,
1882        2    SCR1,SCR2,DUM,INIT,IMODE,LDERF,LDIAGN)
1883            IF(IMODE.EQ.3) THEN
1884             WRITE(LSCOUT,*)
1885             WRITE(LSCOUT,*) 'Error encountered in unconditional mean'
1886             WRITE(LSCOUT,*) 'data calculation.'
1887             RETURN
1888            ENDIF
1889   2000     CONTINUE
1890          ENDIF
1891   C
1892   C       Calculate conditional mean density reciprocal
1893          DO 1994 I=1,NETAMX
1894           SUM=0.
1895           INUM=(I-1)*NUMSCA
1896           DO 1990 J=1,NUMSCA-1
1897            SUM=SUM+Q(J+INUM)/WT(J)
1898   1990     CONTINUE
```

```
1899            CMRHO(I)=GASCON*T(I)*SUM/PRESS
1900  1994    CONTINUE
1901  C
1902  C     Calculate derivative of reciprocal density wrt mixture fraction
1903          SCR1(1)=(CMRHO(1)*CETA1(1)+CMRHO(2)*FETA1(1))/CMRHO(1)
1904          DO 1995 I=2,NETAMX-1
1905           SCR1(I)=(CMRHO(I+1)*FETA1(I)+CMRHO(I)*CETA1(I)+
1906         1   CMRHO(I-1)*BETA1(I))/CMRHO(I)
1907  1995    CONTINUE
1908          SCR1(NETAMX)=(CMRHO(NETAMX)*CETA1(NETAMX)+
1909         1   CMRHO(NETAMX-1)*BETA1(NETAMX))/CMRHO(NETAMX)
1910  C
1911  C     Calculate second derivative of reciprocal density wrt mixture fraction
1912          CMDRDF(1)=0.
1913          DO 1996 I=2,NETAMX-1
1914           CMDRDF(I)=(SCR1(I+1)*FETA1(I)+SCR1(I)*CETA1(I)+
1915         1   SCR1(I-1)*BETA1(I))*CMRHO(I)
1916  1996    CONTINUE
1917          CMDRDF(NETAMX)=0.
1918  C
1919  C       Unpack output species indices
1920          IS1=ISP(1)
1921          IS2=ISP(2)
1922          IS3=ISP(3)
1923          IS4=ISP(4)
1924          IS5=ISP(5)
1925          IS6=ISP(6)
1926          IS7=ISP(7)
1927  C
1928  C       At each radial point, convolve the conditional mean scalars
1929  C       of interest with the available PDF to produce unconditional
1930  C       mean point values.  In some instances, the PDF will have zero
1931  C       value at all grid points.  This is because it is a delta
1932  C       function between grid points.  The correct remedy is to linearly
1933  C       interpolate between adjacent conditional mean data
1934  C       values.
1935  C
1936          DO 1000 I=1,NPTS
1937  C
1938  C        Get PDF moments
1939           CALL GOODI(NETAMX,ETA,UCLM(I),UCLV(I),SCR1,SCR2,LDIAGN)
1940           INET=(I-1)*NETAMX
1941  C
1942           PDFACC=PDF0(I)*ETA(1)
1943           RHOACC=CMRHO(1)*PDF0(I)
1944           TEMPAC=T(1)*PDF0(I)
1945           ENTHAC=Q(NUMSCA)*PDF0(I)
1946           DRDFAC=CMDRDF(1)*PDF0(I)
1947           SAC1=Q(IS1)*PDF0(I)
1948           SAC2=Q(IS2)*PDF0(I)
1949           SAC3=Q(IS3)*PDF0(I)
1950           SAC4=Q(IS4)*PDF0(I)
1951           SAC5=Q(IS5)*PDF0(I)
1952           SAC6=Q(IS6)*PDF0(I)
1953           SAC7=Q(IS7)*PDF0(I)
1954  C
1955           DO 1200 J=2,NETAMX
1956            JNUM=(J-1)*NUMSCA
1957  C
1958            PDFACC=PDFACC+SCR2(J)*ETA(J)+SCR1(J)*ETA(J-1)
1959            RHOACC=RHOACC+CMRHO(J)*SCR2(J)+CMRHO(J-1)*SCR1(J)  ! Density
1960            TEMPAC=TEMPAC+T(J)*SCR2(J)+T(J-1)*SCR1(J)  ! Temp.
1961            ENTHAC=ENTHAC+Q(J*NUMSCA)*SCR2(J)+Q((J-1)*NUMSCA)*SCR1(J)
1962            DRDFAC=DRDFAC+CMDRDF(J)*SCR2(J)+CMDRDF(J-1)*SCR1(J)
1963            SAC1=SAC1+Q(JNUM+IS1)*SCR2(J)+Q(IS1+JNUM-NUMSCA)*SCR1(J)
1964            SAC2=SAC2+Q(JNUM+IS2)*SCR2(J)+Q(IS2+JNUM-NUMSCA)*SCR1(J)
1965            SAC3=SAC3+Q(JNUM+IS3)*SCR2(J)+Q(IS3+JNUM-NUMSCA)*SCR1(J)
1966            SAC4=SAC4+Q(JNUM+IS4)*SCR2(J)+Q(IS4+JNUM-NUMSCA)*SCR1(J)
1967            SAC5=SAC5+Q(JNUM+IS5)*SCR2(J)+Q(IS5+JNUM-NUMSCA)*SCR1(J)
1968            SAC6=SAC6+Q(JNUM+IS6)*SCR2(J)+Q(IS6+JNUM-NUMSCA)*SCR1(J)
1969            SAC7=SAC7+Q(JNUM+IS7)*SCR2(J)+Q(IS7+JNUM-NUMSCA)*SCR1(J)
1970  C
1971  1200    CONTINUE
```

```
1972  C
1973           PDFACC=PDFACC+PDF1(I)
1974           RHO(I)=1./(RHOACC+CMRHO(NETAMX)*PDF1(I))
1975           DRHODF(I)=(DRDFAC+CMDRDF(NETAMX)*PDF1(I))*RHO(I)**2
1976           UCTEMP(I)=TEMPAC+T(NETAMX)*PDF1(I)
1977           UCENTH(I)=ENTHAC+Q(NETAMX*NUMSCA)*PDF1(I)
1978           SPEC1(I)=SAC1+Q(IS1+(NETAMX-1)*NUMSCA)*PDF1(I)
1979           SPEC2(I)=SAC2+Q(IS2+(NETAMX-1)*NUMSCA)*PDF1(I)
1980           SPEC3(I)=SAC3+Q(IS3+(NETAMX-1)*NUMSCA)*PDF1(I)
1981           SPEC4(I)=SAC4+Q(IS4+(NETAMX-1)*NUMSCA)*PDF1(I)
1982           SPEC5(I)=SAC5+Q(IS5+(NETAMX-1)*NUMSCA)*PDF1(I)
1983           SPEC6(I)=SAC6+Q(IS6+(NETAMX-1)*NUMSCA)*PDF1(I)
1984           SPEC7(I)=SAC7+Q(IS7+(NETAMX-1)*NUMSCA)*PDF1(I)
1985           WRITE(LDIAGN,555) 'RDU ',XMFRC(I),XMFRCV(I),
1986         1    PDF0(I),RHO(I),
1987         2    DRHODF(I)
1988  C
1989  1000    CONTINUE
1990  C
1991  555     FORMAT(A4,1X,E18.11,4(1X,E12.5))
1992  C
1993          RETURN
1994          END
1995  C=============================================================
1996  C
1997  C+++++++++++++++++++++++++++++++++++++++++++++++++++++++++++++
1998  C
1999        SUBROUTINE AVERUX2(NMAX,N,XMFRC,XMFRCV,YPOSN,VEL,CHI,
2000       1  RHOIN,NETAMX,ETA,PDF,PDF0,PDF1,UCLM,UCLV,PDFSTR,
2001       2  SCR0,SCR1,SCR2,RUQ,RCQ,IZ,NETAPT,IMODE,LDERF,LDIAGN)
2002  C
2003  C     This subroutine calculates conditional mean scalar by
2004  C     PDF weighted averaging of the unconditional mean profile.
2005  C     PDFs and their derivatives are calculated using a
2006  C     clipped gaussian function assumed form.
2007  C
2008          IMPLICIT REAL (A-H,O-Z), INTEGER (I-N)
2009  C
2010          PARAMETER(VSML=1.E-10)
2011  C
2012          INTEGER NMAX,N,IZ(*),NETAMX,IMODE,LDERF
2013          REAL XMFRC(*),XMFRCV(*),VEL(*),RHOIN(*),CHI(*),YPOSN(*),
2014       1  PDF(*),PDF0(*),PDF1(*),PDFSTR(*),SCR1(*),SCR2(*),
2015       2  SCR0(*),ETA(*),RUQ(*),RCQ(*),UCLM(*),UCLV(*)
2016  C
2017          IF(IMODE.GT.1) THEN
2018           INIT=1
2019  C
2020           PDFAC0=0.
2021           PDFAC1=0.
2022           RVAC0=0.
2023           RVAC1=0.
2024           OY=0.
2025           OPDF0=0.
2026           OPDF1=0.
2027           ORV=0.
2028           ORHO=0.
2029           RHACC=0.
2030  C
2031           DO 10 J=1,N
2032  C
2033            VMAX=XMFRC(J)*(1.-XMFRC(J))
2034            XMFRVJ=MIN(MAX(0.,XMFRCV(J)),VMAX)
2035            DUM=0.
2036  C
2037            CALL GAUDIM(XMFRC(J),XMFRVJ,XMFRVJ,XMFRVJ,NETAMX,ETA,
2038       1    PDF(1+(J-1)*NETAMX),PDF0(J),PDF1(J),UCLM(J),UCLV(J),SCR0,
2039       2    SCR1,SCR2,DUM,INIT,IMODE,LDERF,LDIAGN)
2040            IF(IMODE.EQ.3) RETURN
2041  C
2042           DELY=YPOSN(J)-OY
2043           PDFAC1=PDFAC1+0.5*(RHOIN(J)*PDF1(J)*YPOSN(J)+
2044       1      OPDF1*OY*ORHO)*DELY
```

```
2045          PDFAC0=PDFAC0+0.5*(RHOIN(J)*PDF0(J)*YPOSN(J)+
2046         1     OPDF0*OY*ORHO)*DELY
2047          RV=RHOIN(J)*VEL(J)
2048          RVAC0=RVAC0+0.5*(PDF0(J)*RV*YPOSN(J)+OPDF0*ORV*OY)*DELY
2049          RVAC1=RVAC1+0.5*(PDF1(J)*RV*YPOSN(J)+OPDF1*ORV*OY)*DELY
2050          RHACC=RHACC+0.5*(RHOIN(J)*YPOSN(J)+OY*ORHO)*DELY
2051  C
2052          OY=YPOSN(J)
2053          OPDF1=PDF1(J)
2054          OPDF0=PDF0(J)
2055          ORV=RV
2056          OXMF=XMFRC(J)
2057          OXMFV=XMFRCV(J)
2058          ORHO=RHOIN(J)
2059  C
2060  10     CONTINUE
2061          RHARA=1./RHACC
2062          IF(PDFAC0.GT.0.) RVAC0=RVAC0/PDFAC0
2063          IF(PDFAC1.GT.0.) RVAC1=RVAC1/PDFAC1
2064          PDFAC0=PDFAC0*RHARA
2065          PDFAC1=PDFAC1*RHARA
2066  C
2067  C     Integrate PDF values,  CHI, and mass flux
2068  C     across the width of the flow.
2069          DO 50 J=1,NETAMX
2070  C
2071           OY=YPOSN(1)
2072           ORV=RHOIN(1)*VEL(1)
2073           OPY=PDF(J)*YPOSN(1)
2074           OCHI=RHOIN(1)*CHI(1)
2075           CHIACC=0.
2076           RPYACC=0.
2077           URPYAC=0.
2078           ORHO=RHOIN(1)
2079  C
2080           DO 60 I=2,N
2081            DELY=0.5*(YPOSN(I)-OY)
2082            RV=RHOIN(I)*VEL(I)
2083            PY=PDF(J+(I-1)*NETAMX)*YPOSN(I)
2084            CHIACC=CHIACC+(CHI(I)*RHOIN(I)*PY+
2085         1     OCHI*OPY)*DELY
2086            RPYACC=RPYACC+(PY*RHOIN(I)+ORHO*OPY)*DELY
2087            URPYAC=URPYAC+(RV*PY+ORV*OPY)*DELY
2088  C
2089            OY=YPOSN(I)
2090            ORV=RV
2091            OPY=PY
2092            OCHI=CHI(I)*RHOIN(I)
2093            ORHO=RHOIN(I)
2094  60       CONTINUE
2095  C
2096  C        Normalize by area
2097           RUQ(J)=URPYAC*RHARA          ! divided by integ. pdf at later stage
2098           RCQ(J)=2.*CHIACC*RHARA         !   *      *  *       *  *
2099           PDFSTR(J)=RPYACC*RHARA
2100  50       CONTINUE
2101  C
2102          IC=1
2103          IZ(1)=1
2104          DO 75 J=1,NETAMX
2105           PDFSTJ=MAX(PDFSTR(J),VSML)
2106           IF(RUQ(J).LE.VSML) RUQ(J)=0.
2107           RCQ(J)=RCQ(J)/PDFSTJ
2108           RUQ(J)=RUQ(J)/PDFSTJ
2109           IF(RUQ(J).NE.0.) THEN
2110            IZ(IC)=J
2111            IC=IC+1
2112           ENDIF
2113  75       CONTINUE
2114  C
2115          IF(PDFAC0.GT.0.) RUQ(1)=RVAC0
2116          IF(PDFAC1.GT.0.) THEN
2117           RUQ(NETAMX)=RVAC1
2118           IZ(IC)=NETAMX
2119           IC=IC+1
2120          ENDIF
2121  C
2122  C     Fix holes in RUQ profile by interpolation
2123           CALL FIXRUQ(ETA,RUQ,IZ,IC-1,NETAMX,VEL(1))
2124  C
2125  C     Determine rich bound on calculation zone
2126           J=NETAMX
2127           IF(PDFAC1.EQ.0.) THEN
2128  80        CONTINUE
2129            IF(PDFSTR(J).LT.VSML) THEN
2130             J=J-1
2131             GOTO 80
2132            ENDIF
2133           ENDIF
2134           NETAPT=J
2135  C
2136          ELSE
2137  C
2138  C     GAUDI requires initialization
2139           INIT=0
2140           DUM=0.    !  Dummy variables not used during initialization
2141           CALL GAUDIM(DUM,DUM,DUM,DUM,NETAMX,ETA,PDF,DUM,DUM,DUM,DUM,
2142         1   SCR0,SCR1,SCR2,DUM,INIT,IMODE,LDERF,LDIAGN)
2143           IF(IMODE.EQ.3) RETURN
2144  C
2145          ENDIF    ! end of integration option
2146  C
2147          RETURN
2148          END
2149  C=============================================================
2150  C
2151  C+++++++++++++++++++++++++++++++++++++++++++++++++++++++++++++
2152          SUBROUTINE TWZONE(ETA,NETAMX,NETAPT,
2153         1    CETA,FETA,BETA,IMODE,LSCOUT,LDIAGN)
2154  C
2155  C     This subroutine is designed to handle those
2156  C     regions of mixture fraction space where
2157  C     scalar mixing rates are indeterminate.  In this
2158  C     Twilight Zone, no CMC calculations are made
2159  C     and instead the last determinate point mixes
2160  C     with the values at the rich boundary.
2161  C
2162          IMPLICIT REAL(A-H,O-Z), INTEGER(I-N)
2163          REAL ETA(*),CETA(*),FETA(*),BETA(*)
2164          INTEGER NETAMX,NETAPT,IMODE,LDIAGN,LSCOUT
2165  C
2166          IF(NETAPT.EQ.NETAMX) RETURN
2167          IF(NETAPT.EQ.1) THEN
2168           IMODE=3
2169           WRITE(LSCOUT,*) ' No active grid points left.'
2170           RETURN
2171          ENDIF
2172  C
2173  C     Modify difference grids to mix last point with ETA=1
2174          ETAI=ETA(NETAPT)
2175          ETAM1=ETA(NETAPT-1)
2176          ETAP1=ETA(NETAPT+1)
2177          ETAMX=ETA(NETAMX)
2178          TOT=1./(ETAP1-ETAM1)
2179          FETA(NETAPT)=2.*TOT/(ETAMX-ETAI)
2180          BETA(NETAPT)=2.*TOT/(ETAI-ETAM1)
2181          CETA(NETAPT)=-1.*(FETA(NETAPT)+BETA(NETAPT))
2182  C
2183          RETURN
2184          END
```